UNIVERSITY of CALIFORNIA

Santa Barbara

Tunable dielectric response, resistive switching, and unconventional transport in SrTiO$_3$

A Dissertation submitted in partial satisfaction of the

requirements for the degree

Doctor of Philosophy

in

Materials

by

Evgeny Mikheev

Committee in charge:

Professor Susanne Stemmer, Chair

Professor Robert A. York

Professor Chris J. Palmstrom

Professor Anton Van der Ven

December 2016

The dissertation of Evgeny Mikheev is approved.

Professor Robert A. York

Professor Chris J. Palmstrom

Professor Anton Van der Ven

Professor Susanne Stemmer, Committee Chair

October 2016

Tunable dielectric response, resistive switching, and unconventional transport

in SrTiO$_3$

Copyright © 2016

by

Evgeny Mikheev

Curriculum Vitæ

Evgeny Mikheev

Education

2011–2016	Ph.D. in Materials, University of California, Santa Barbara, CA, USA.
2009–2011	M.Sc. in Materials Science and Engineering, Ecole Polytechnique Fdrale de Lausanne, Switzerland.
2006–2009	B.Sc. in Materials Science and Engineering, Ecole Polytechnique Fdrale de Lausanne, Switzerland.

Awards

2015	Ovshinsky Student Travel Award for the 2015 March APS Meeting.
2014	Materials Research Society (MRS) Graduate Student Gold Award.

2011	Best Master Thesis Prize of Materials Science and Engineering department at EPFL.
2010	Travel fellowship for European Cooperation in Science and Technology (COST) workshop in Hasselt Belgium.
2010	European Cooperation in Science and Technology (COST) grant for a short term scientific mission (two weeks) at the School of Physics and Astronomy, University of Nottingham.
2010	Runner-up prize in the student poster competition at conference International Symposium on the Applications of Ferroelectrics (ISAF), Edinburgh.
2009-2011	Research assistant scholarship (Materials Science and Engineering department, EPFL).

Publications

25. P. B. Marshall, **E. Mikheev**, S. Raghavan, S. Stemmer, "Pseudogaps and emergence of coherence in two-dimensional electron liquids in $SrTiO_3$", *Physical Review Letters* 117, 046402 (2016).

24. J. Y. Zhang, H. Kim, **E. Mikheev**, A. J. Hauser, S. Stemmer, "Key role of lattice symmetry in the metal-insulator transition of $NdNiO_3$ films", *Scientific Reports* 6, 23652 (2016).

23. A. J. Hauser, **E. Mikheev**, A. P. Kajdos, A. Janotti, "Small polaron-related recombination in $Ba_xSr_{1-x}TiO_3$ thin films by cathodoluminescence spectroscopy", *Applied Physics Letters* 108, 102901 (2016).

22. **E. Mikheev**, S. Raghavan, J. Y. Zhang, P. B. Marshall, A. P. Kajdos, L. Balents, S. Stemmer, "Carrier density independent scattering rate in $SrTiO_3$-based electron liquids", *Scientific Reports* 6, 20865 (2016).

21. **E. Mikheev**, A. J. Hauser, B. Himmetoglu, N. E. Moreno, A. Janotti, C. G. Van de Walle, S. Stemmer, "Tuning bad metal and non-Fermi liquid behavior in a Mott material: rare earth nickelate thin films", *Science Advances* 1, e1500797 (2015).

20. D. Lee, H. Lu, Y. Gu, S.-Y. Choi, S.-D. Li, S. Ryu, T. R. Paudel, K. Song, **E. Mikheev**, S. Lee, S. Stemmer, D. A. Tenne, S. H. Oh, E. Y. Tsymbal, X. Wu,

L.-Q. Chen, A. Gruverman, C. B. Eom, "Emergence of room-temperature ferroelectricity at reduced dimensions", *Science* 349, 1314 (2015).

19. **E. Mikheev**, S. Raghavan, S. Stemmer, "Dielectric response of metal/SrTiO$_3$/two-dimensional electron liquid heterostructures", Applied Physics Letters 107, 072905 (2015).

18. **E. Mikheev**, J. Hwang, A. P. Kajdos, A. J. Hauser, S. Stemmer, "Tailoring resistive switching in Pt/SrTiO$_3$ junctions by stoichiometry control", *Scientific Reports* 5, 11079 (2015).

17. **E. Mikheev**, C. R. Freeze, B. J. Isaac, T. A. Cain, S. Stemmer, "Separation of transport lifetimes in SrTiO$_3$-based two-dimensional electron liquids". *Physical Review B* 91, 165125 (2015).

16. A. J. Hauser, **E. Mikheev**, N. E. Moreno, J. Hwang, J. Y. Zhang, S. Stemmer, "Correlation between stoichiometry, strain, and metal-insulator transitions of NdNiO$_3$ films". *Applied Physics Letters* 106, 092104 (2015).

15. S. J. Allen, A. J. Hauser, **E. Mikheev**, J. Y. Zhang, N. E. Moreno, J. Son, D. G. Ouellette, J. Kally, A. Kozhanov, L. Balents, S. Stemmer, "Gaps and Pseudogaps in Perovskite Rare Earth Nickelates". *APL Materials* 3, 062503 (2015). ArXiv: 1404.2544.

14. **E. Mikheev**, B. Himmetoglu, A. P. Kajdos, P. Moetakef, T. A. Cain, C. G.

Van de Walle, S. Stemmer, "Limitations to the room temperature mobility of two- and three-dimensional electron liquids in SrTiO$_3$". *Applied Physics Letters* 106, 062102 (2015).

13. W. J. Hardy, H. Ji, **E. Mikheev**, S. Stemmer, D. Natelson, "Nanostructure investigations of nonlinear differential conductance in NdNiO$_3$ thin films. *Physical Review B* 90, 205117 (2014). ArXiv: 1411.1776.

12. V. Chobpattana, **E. Mikheev**, J. Y. Zhang, T. E. Mates, S. Stemmer, "Extremely scaled high-k/In$_{0.53}$Ga$_{0.47}$As gate stacks with low leakage and low interface trap densities. *Journal of Applied Physics* 116, 124104 (2014).

11. **E. Mikheev**, B. D. Hoskins, D. B. Strukov, S. Stemmer, "Resistive switching and its suppression in Pt/Nb:SrTiO$_3$ junctions. *Nature Communications* 5, 3990 (2014).

10. A. J. Hauser, **E. Mikheev**, N. E. Moreno, T. A. Cain, J. Hwang, J. Y. Zhang, S. Stemmer, "Temperature-dependence of the Hall coefficient of NdNiO$_3$ thin films. *Applied Physics Letters* 103, 182105 (2013).

9. **E. Mikheev**, A. P. Kajdos, A. J. Hauser, S. Stemmer, "Electric field-tunable Ba$_x$Sr$_{1-x}$TiO$_3$ films with high figures of merit grown by molecular beam epitaxy. *Applied Physics Letters* 101, 252906 (2012).

8. **E. Mikheev**, I. Stolichnov, E. De Ranieri, J. Wunderlich, H. J. Trodahl, A. W.

Rushforth, S. W. E. Riester, R. P. Campion, K. W. Edmonds, B. L. Gallagher, N. Setter, "Magnetic domain wall propagation under ferroelectric control". *Physical Review B* 86, 235130 (2012).

7. **E. Mikheev**, I. Stolichnov, A. K. Tagantsev, N. Setter: "Polarization screening in polymer ferroelectric films: uncommon bulk mechanism. *Applied Physics Letters* 101, 132905 (2012).

6. **E. Mikheev**, I. Stolichnov, Z. Huang, A. W. Rushforth, J. Haigh, R. P. Campion, K. W. Edmonds, B. L. Gallagher, N. Setter, "Non-volatile ferroelectric gating of magnetotransport anisotropy in (Ga,Mn)(As,P)". *Applied Physics Letters* 100, 262906 (2012).

5. I. Stolichnov, P. Maksymovych, **E. Mikheev**, S. Kalinin, A. Tagantsev, N. Setter, "Cold-field switching in PVDF-TrFE ferroelectric polymer nanomesas". *Physical Review Letters* 108, 027603 (2012)

4. **E. Mikheev**, S.W.E. Riester, I. Stolichnov, N. Setter: "Polarization screening in multiferroic (Ga,Mn)As/P(VDF-TrFE) transistors. *Ferroelectrics* 421, 98 (2011).

3. I. Stolichnov, S. W. E. Riester, **E. Mikheev**, N. Setter, A. W. Rushforth, K. W. Edmonds, R. P. Campion, C. T. Foxon, B. L. Gallagher, T. Jungwirth, H. J. Trodahl, "Ferroelectric polymer gates for non-volatile field effect control of

ferromagnetism in (Ga,Mn)As layers," *Nanotechnology* 22, 254004 (2011).

2. I. Stolichnov, S. W. E. Riester, **E. Mikheev**, N. Setter, A. W. Rushforth, K. W. Edmonds, R. P. Campion, C. T. Foxon, B. L. Gallagher, T. Jungwirth, H. J. Trodahl: "Enhanced Curie temperature and nonvolatile switching of ferromagnetism in ultrathin (Ga,Mn)As channels. *Physical Review B* 83, 115203 (2011).

1. B. Ketterer, **E. Mikheev**, E. Uccelli, A. Fontcuberta i Morral: "Compensation mechanism in silicon-doped gallium arsenide nanowires. *Applied Physics Letters* 97, 223103 (2010).

Acknowledgements

I would like to thank my advisor, professor Susanne Stemmer, for giving me the opportunity to pursue a Ph.D. and for her invaluable guidance and support along the way.

I am very grateful to the members of my thesis committee: Chris Palmstrom, Anton Van der Ven, and Bob York.

I want to offer many thanks to my colleagues from the Stemmer group for their help, support, advice, and friendship: Santosh, Pouya, Tyler, Gift, Brandon, Chris, Mandi, Timo, Manik, Omor, Kaveh, David, Nelson, and Ryota. In particular, I would like to express gratitude to Adam Kajdos, who taught me so much about MBE growth and was an equal contributor to the work on tunable dielectrics described in Chapter 2. I want to thank Adam Hauser, for his help with the sputtering systems, RBS analysis, and for being a big driving force in the projects on rare earth nickelates. I am very grateful to Patrick Marshall for growing many samples for gated device processing and diligently fixing the shortcomings of my English proficiency in this thesis. I am very thankful to Junwoo Son for his help with sputtering of epitaxial platinum and cleanroom processing. I am also extremely grateful to Jinwoo Hwang and Jack Zhang for TEM imaging.

Abstract

Tunable dielectric response, resistive switching, and unconventional transport

in $SrTiO_3$

by

Evgeny Mikheev

The first section of this thesis discusses integration of $SrTiO_3$ grown by molecular beam epitaxy (MBE) in vertical device structures. One target application is as a tunable dielectric. Parallel plate capacitors based on epitaxial Pt(001) bottom electrodes and $(Ba,Sr)TiO_3$ dielectric layers grown by MBE are demonstrated. Optimization of structural quality of the vertical stack is shown to produce very low dielectric loss combined with very high tunability of the dielectric constant by DC bias. This results in considerable improvement of common figures of merit for varactor performance in comparison to previous reports.

Another target application for transition metals oxides is in resistive switching memories, which are based on the hysteretic current-voltage response observed in many oxide-based Schottky junctions and capacitors. A study on the role of metal/oxide interface quality is presented. In particular, the use of epi-

taxial Pt(001) as Schottky contacts to Nb:SrTiO$_3$ is shown to suppress resistive switching hysteresis by eliminating unintentional contributions to interface capacitance. Such uncontrolled factors are discussed as a probable root cause for poor reproducibility in resistive switching memories, currently a ubiquitous challenge in the field. Potential routes towards stabilizing reproducible switching through intentional control of defect densities in high-quality structures are discussed, including a proof of concept demonstration using Schottky junctions incorporating intentionally non-stoichiometric SrTiO$_3$ interlayers grown by MBE.

The second section of this thesis is concerned with unconventional electronic transport in SrTiO$_3$. A systematic description of scattering mechanisms will be presented for three related material systems: uniformly-doped SrTiO$_3$, two-dimensional electron liquids (2DEL) at SrTiO$_3$/RTiO$_3$ interfaces (R = Gd, Sm) and confined 2DELs in RTiO$_3$/SrTiO$_3$/RTiO$_3$ quantum wells. In particular, the prevalence of a well-defined T^2 scattering rate in doped SrTiO$_3$ will be discussed as being incompatible with its traditional assignment as electron-electron scattering in a Fermi liquid.

In the case of ultrathin SrTiO$_3$ quantum wells bound by RTiO$_3$, evidence will be presented for the existence of a quantum critical point. This refers to a quantum phase transition at zero temperature towards an ordered phase in

SrTiO$_3$. This transition is driven by increasing confinement of the 2DEL, with a critical point located at the 5 SrO layer thickness of SrTiO$_3$. It is manifested in anomalous temperature exponents of the power law resistivity. Additionally, a well-defined trend for the separation of the Hall and longitudinal scattering rates will be presented, analogously to a similar effect observed in the normal state of high-T_c superconductors. In particular, a unique pattern of residual scattering separation was documented, consistent with a quantum critical correction to the Hall lifetime that is divergent at the quantum critical point.

Contents

List of Figures

List of Tables

Chapter 1

Introduction: SrTiO$_3$-based vertical devices

1.1 Overview of SrTiO$_3$

A central material of interest for this thesis is SrTiO$_3$. Its room temperature crystal structure is an undistorted cubic perovskite with a lattice constant of 3.905 (Å) [1]. A unique aspect of this material is the very wide tunability of its electrical conductivity and dielectric response.

In its pure, stoichiometric form, SrTiO$_3$ is an insulator with an indirect band gap of 3.3 eV and a direct band gap of 3.8 eV [2]. One can induce n-type conductivity via doping. This is generally achieved by substituting the divalent Sr ion with a trivalent rare-earth ion (e.g. La, Gd, Sm), substituting the tetravalent Ti ion with a pentavalent ion such as Nb, or inducing oxygen vacancies [3].

SrTiO$_3$ has a very large dielectric constant, with a room temperature value of 350. This value can be tuned across many orders of magnitude (between $\sim$ 20 and 10^4) using combinations of temperature, chemical substitution, epitaxial strain and electric field [4]–[7].

1.2 Dielectric response of SrTiO$_3$ and (Ba,Sr)TiO$_3$

The very large dielectric response of SrTiO$_3$ is one of the distinguishing characteristics of this material. It is also of wide practical interest as it translates into

large capacitance densities. The most common geometry is that of the parallel plate capacitor, where an insulator of thickness d and area A is sandwiched between two metallic plates. By applying a voltage V to the capacitor, opposite charges $\pm Q$ are accumulated at the bounding plates. The capacitance C is the proportionality constant defined as $C = Q/V$. C is determined by the dielectric constant of the insulator material ε_r, a dimensionless quantity that defines the dielectric permittivity of a material in relation to that of the vacuum (ε_0):

$$\frac{C}{A} = \frac{\varepsilon_r \varepsilon_0}{d} \tag{1.1}$$

For bulk SrTiO$_3$ in the low-electric field limit at room temperature, $\varepsilon_r = 350$. This value is very large in comparison with other commonly used insulating oxides: SiO$_2$ ($\varepsilon_r = 3.9$), Al$_2$O$_3$ (9), ZrO$_2$ and HfO$_2$ (25) [8], [9].

The physical origin of the very large dielectric response of SrTiO$_3$ lies in its proximity to a ferroelectric transition. This can be illustrated using a conventional phenomenological description, based on the Landau-Ginzburg expansion of the Gibbs free energy potential (ΔG) with respect to macroscopic polarization P as the order parameter [5], [6], [10]. For a one-dimensional case where the electric field E is aligned with P:

$$\Delta G = \alpha_0 + \frac{\alpha_1}{2} P^2 + \frac{\alpha_2}{4} P^4 - EP \tag{1.2}$$

where $\alpha_{1,2}$ are expansion coefficients. A stable solution corresponds to a mini-

mum of the thermodynamical potential, requiring $\partial G/\partial P = 0$:

$$E = \alpha_1 P + \alpha_2 P^3 \tag{1.3}$$

A key assumption of this description is the linearity of α_1 with temperature:

$$\alpha_1 = \frac{(T - T_C)}{C_{CW}} \tag{1.4}$$

Where T_C is the ferroelectric instability temperature and C_{CW} the Curie-Weiss constant. This assumption can be justified to be strictly valid in direct vicinity of T_C and remains accurate across much wider T ranges for typical ferroelectrics [6], [11]. For $T > T_C$ and in the limit of very small E, the dielectric constant is thus given by the first term in Equation 1.3:

$$\varepsilon_r(E = 0) = \frac{1}{\varepsilon_0} \left.\frac{\partial P}{\partial E}\right|_{E=0} = \frac{1}{\varepsilon_0 \alpha_1} = \frac{C_{CW}}{T - T_C} \tag{1.5}$$

This is the well known Curie-Weiss law, which describes the divergence of the dielectric response at the ferroelectric instability (see Figure 1.1(a)). In addition, titanate perovskites such as $BaTiO_3$ and $SrTiO_3$ are known to have particularly high Curie-Weiss constants ($C_{CW} \approx 10^5$ K [11]), leading to fairly large dielectric response even at temperatures far removed from T_C.

The occurrence of ferroelectric order, i.e. the presence of a non-zero spontaneous polarization $P_s = P(E = 0)$, is also described by Equation 1.2. For the simple case of a second order transition ($\alpha_2 > 0$), $P_s = 0$ is the only possible

4

solution for the paraelectric state at $T > T_C$. Below T_C, a finite spontaneous polarization emerges:

$$P_S = \sqrt{-\frac{\alpha_1}{\alpha_2}} \sim \sqrt{T_C - T} \qquad (1.6)$$

The ferroelectric order corresponds to a bistable potential well (Figure 1.1(b)). Below T_C the polarization can be switched between these two states by applying an electric field, leading to the ferroelectric hysteresis loop.

An important aspect of the dielectric response in proximity of a ferroelectric instability is its electric field dependence. This effect can be illustrated by
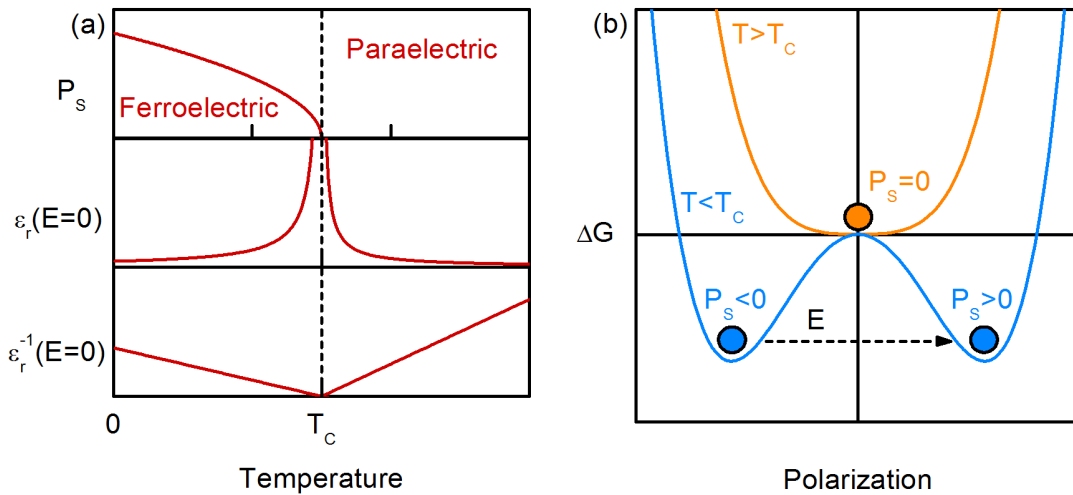
Figure 1.1. (a) Illustration of temperature dependence for spontaneous polarization P_S and low-field dielectric constant $\varepsilon_0(E)$ near a ferroelectric transition at $T = T_C$. (b) Bistable thermodynamic potential implied by Equation 1.2 near a second order transition.

differentiating Equation 1.3 for $T > T_C$:

$$\varepsilon_r = \frac{1}{\varepsilon_0}\frac{\partial P}{\partial E} = \frac{1}{\varepsilon_0}\frac{1}{\alpha_1 + 3\alpha_2 P^2} = \frac{\varepsilon_r(E=0)}{1 + 3\varepsilon_r(E=0)\alpha_2\varepsilon_0 P^2} \tag{1.7}$$

Application of an electric field induces a finite polarization even in the paraelectric state, which in turn reduces the dielectric constant below its zero field value. The possibility of tuning the dielectric constant with voltage is of high practical interest, as discussed further in Chapter 2. In particular, it is often desirable to maximize the tunablility of ε_r, which can be written in the small field limit as:

$$\eta(E) \equiv \frac{\varepsilon_r(E=0)}{\varepsilon_r(E)} = 1 + 3\varepsilon_r(E=0)\alpha_2\varepsilon_0 P^2 \approx 1 + 3\alpha_2(\varepsilon_0\varepsilon_r(E=0))^3 E^2 \tag{1.8}$$

This expression implies that the tunability scales very strongly with the magnitude of the dielectric response: $\eta \sim \varepsilon_r(E=0)^3$. Consequently, it is maximized in proximity to the ferroelectric instability, where $\varepsilon_r(E=0)$ is divergent.

The $\eta \sim E^2$ dependence in Equation 1.8 only holds for small E. At higher E, the tuning scales less sharply [5], [6], [12], [13]. The full field dependence of the dielectric response for SrTiO$_3$ can be described as [14]:

$$\varepsilon_r(E) = \frac{\varepsilon_r(E=0)}{2\cosh\left(\frac{2}{3}\sinh^{-1}\left(\frac{2E}{E_2}\right)\right) - 1} \tag{1.9}$$

where E_2 is the "2:1" voltage at which $\varepsilon_r(E_2) = \varepsilon_r(E=0)/2$.

A common empirical approximation to describe the for this dependence is

[15], [16]:

$$\varepsilon_r(E) = \frac{b}{\sqrt{a + E^2}} \tag{1.10}$$

where a and b are temperature dependent empirical parameters.

The above discussion presented the origin of the large dielectric response near ferroelectric transitions from a macroscopic phenomenological view. On the microscopic level it can be described in terms of instabilities of vibrational modes of the perovskite lattice. In particular, a structural transition can be characterized in terms of a "soft" phonon mode, whose normal frequency tends to zero as the temperature approaches T_C [17]–[19]. In the case of pervoskite ferroelectrics, this is the transverse optical (TO) mode, which corresponds to displacement of Ti cations within the TiO_6 octahedra. The softening of this phonon mode is directly related to the divergent dielectric response:

$$\frac{\varepsilon_r(T)}{\varepsilon_\infty} = \frac{\omega_{LO}^2}{\omega_{TO}^2(T)}, \tag{1.11}$$

where ω_{TO} and ω_{LO} are normal frequencies for the transverse and longitudinal phonon modes, and ε_∞ is the high-frequency dielectric constant. The phonon spectrum is highly sensitive to structural distortions of the perovskite lattice. Consequently, ferroelectric transitions are tunable by pressure, epitaxial strain and chemical substitution [17], [20], [21].

$(Ba,Sr)TiO_3$ is a prominent example of a system where the ferroelectric in-

stability can be tuned across a wide temperature range. It is a perovskite solid solution between ferroelectric $BaTiO_3$ and paraelectric $SrTiO_3$. In $BaTiO_3$, ferroelectric order appears below a transition point at $T_C = 120$ °C. At higher temperatures, $BaTiO_3$ is a cubic paraelectric, analogous to $SrTiO_3$. Below T_C, $BaTiO_3$ undergoes a series of additional structural transitions, with the full sequence being: cubic $\rightarrow$ tetragonal at $T_C = 120$ °C, tetragonal $\rightarrow$ orthorombic at 5 °C and orthorombic $\rightarrow$ rhombohedral at -70 °C [22].

By substituting Sr for Ba in the $Ba_xSr_{1-x}TiO_3$ solid solution, the transition point T_C is gradually shifted to lower temperatures [6], [12], [23], [24]. Near $x = 0.7$, the ferroelectric T_C is at room temperature. In the limit of pure $SrTiO_3$ there is no ferroelectric transition, and the $T = 0$ K ground state is paraelectric [4], [11]. A ferroelectric T_C at finite temperature does appear at a very small level of Ba substitution ($x_C \sim 0.002 - 0.1$ [25]). However, even below x_C, $\varepsilon_r(T)$ maintains a strong peak-like behavior around $T = 0$ K: for $x = 0$, there is a smooth increase from $\varepsilon_r(300$ K$) = 350$ to $\varepsilon_r(0$ K$) \sim 10^4$. Near x_C, this gradual increase develops into a finite-T peak reaching $\varepsilon_r \approx 10^4$ at T_C. With the very high $\varepsilon_r(300$ K$)$ of $SrTiO_3$ being due to proximity to ferroelectric order, this material is commonly referred to as an incipient ferroelectric.

The ferroelectric transition in $SrTiO_3$ can also be induced by epitaxial strain. Distortions induced by both tensile and compressive strain are generally ex-

pected to increase the transition point T_C [26]. Experimentally, room-temperature ferroelectricity has been demonstrated by growing tensile strained $SrTiO_3$ films on $DyScO_3$ [27] and below $\approx$150 K in compressively strained $SrTiO_3$ films on $(LaAlO_3)_{0.3}(Sr_2AlTaO_6)_{0.7}$ (LSAT) [28], [29].

1.3   Schottky barriers at $SrTiO_3$/metal interfaces

1.3.1   Band diagram

The Schottky junction between n-type doped $SrTiO_3$ and high work function metals is a heavily investigated material system, largely in the context of potential applications in resistive switching memories (see Chapter 3). In addition, commercial availability of high quality single crystals of $SrTiO_3$ doped with Nb (or oxygen vacancies) enables easy fabrication, contributing to the popularity of this system in academic research on complex oxides.

The generic band diagram for such a junction [30]–[32] is shown in Figure 1.2. Bringing an n-type semiconductor and a metal in close contact enables charge flow between the two layers and alignment of their respective Fermi levels. As a result, the conduction band of $SrTiO_3$ is bent in vicinity of the interface with the metal, creating a depletion width W_D: a region where the

electrons originating from doping are depleted via transfer to the metal contact

An important consequence for electron transport across such an interface is the presence of a Schottky barrier. The barrier height ϕ_B is the mismatch between the conduction band of the semiconductor and the Fermi level of the metal. In the ideal case, their positions with respect to the vacuum level are defined by the electron affinity of χ_s of SrTiO$_3$ and the work function ϕ_M of the metal, both intrinsic material properties. To the first approximation, the barrier
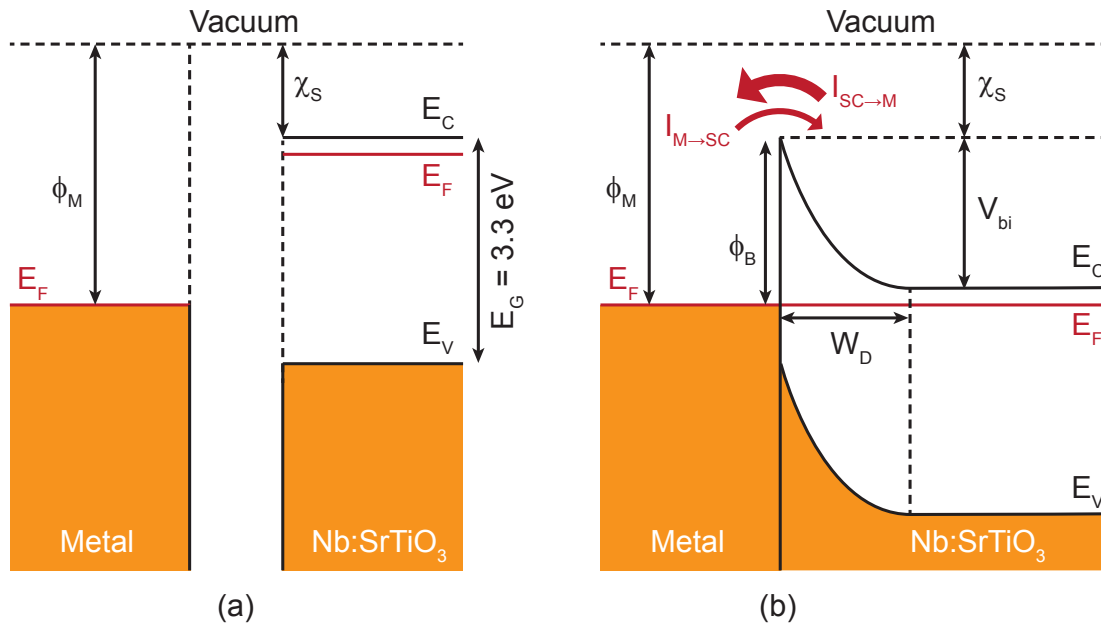
Figure 1.2. Band diagrams of an interface between an n-type semiconductor and a high work function metal, when separated by vacuum (a) and in direct contact (b).

height is $\phi_B = \phi_M - \chi_s$.

1.3.2 Current-voltage response

The resulting current-voltage $(I - V)$ characteristics are highly asymmetric, reflecting the fact that it is much harder for an electron to cross from the metal to the semiconductor than in reverse (see Figure 1.3). The process of electron transport over the barrier is described by thermionic emission theory. It treats the case of forward bias (voltage $V > 0$ applied to the metal), where the current
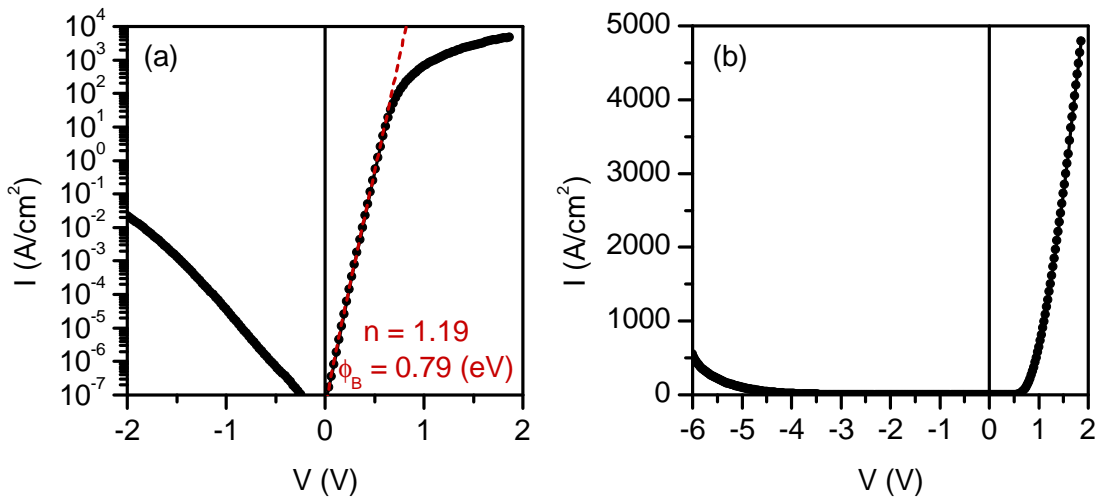
Figure 1.3. Current-voltage (I-V) characteristics for a Nb:SrTiO$_3$/Pt Schottky junction in (a) log-linear scale and (b) linear scale. Dashed red line corresponds to the thermionic emission model (eq. 1.12)

from the semiconductor to the metal is limited by diffusion across the depletion width. The full treatment of this problem [30], [33] yields:

$$I(V) = A^* T^2 \exp\left(-\frac{e\phi_B}{k_B T}\right) \exp\left(\frac{eV}{n k_B T}\right) \tag{1.12}$$

where A^* is the Richardson constant, an intrinsic material property ($A^*(\text{SrTiO}_3)=$ 156 Acm^{-2}K^{-2} [34]), T is the temperature, e is the electron charge, k_B is the Boltzmann constant, and n is the ideality factor, which represents the deviation of the experimental $I - V$ curve from the ideal thermionic emission case $n = 1$. Mathematically, n accounts for a voltage-dependent barrier height, which can be illustrated by differentiating Equation 1.12:

$$\frac{1}{n} = \frac{k_B T}{e} \frac{d\ln I}{dV} = 1 - \frac{d\phi_B}{dV} \tag{1.13}$$

For the case of an ideality factor that is constant with voltage, this is equivalent to:

$$\phi_B = \phi_{B,0} + \left(1 - \frac{1}{n}\right) V \tag{1.14}$$

Physically, $n > 1$ can be interpreted as a consequence of an interface layer: an arbitrary insulator with a dielectric constant ε_i and thickness δ inserted between the semiconductor and the metal (Figure 1.4) [30]–[32].

In the absence of this additional layer, any applied voltage V_i would be entirely converted into a potential difference across the depletion width (V_d). The

additional insulating layer absorbs a portion of the applied bias (V_i). The partitioning of V into V_d and V_i can be shown to follow the ideality factor [15], [16]:

$$V = V_i + V_d \tag{1.15}$$

$$V_i = \left(1 - \frac{1}{n}\right) V \tag{1.16}$$

$$V_d = \frac{V}{n} \tag{1.17}$$

The explicit connection [15], [16], [30], [35] between the ideality factor and the interface layer is governed by the charge neutrality condition, that also in-
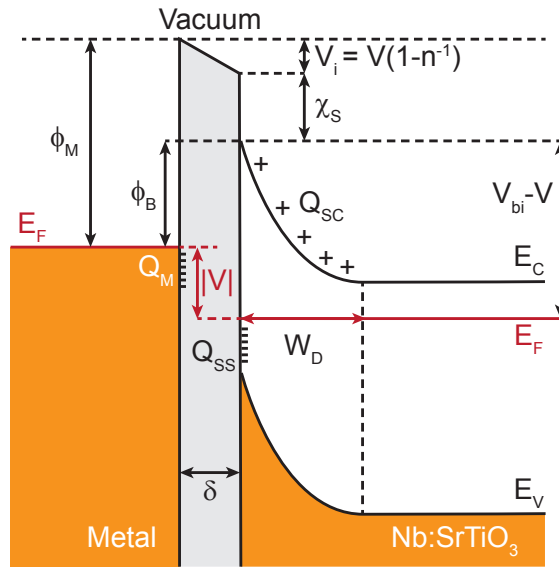
Figure 1.4. Band diagram of a Schottky junction in the presence of an insulating interface layer.

cludes trapped charges in the interface states:

$$Q_M(V) = Q_{SS}(V) + Q_{SC}(V) + Q_F \tag{1.18}$$

where Q_F is the fixed charge, the only contribution that is not altered by applied bias. Q_M is the charge projected on the metal, given by the interface layer capacitance C_i:

$$C_i = \frac{\partial Q_M}{\partial V_i} = \frac{\varepsilon_i \varepsilon_0}{\delta} \tag{1.19}$$

where Q_{SC} is the space charge in the depletion width of the semiconductor, which can be expressed via the depletion region capacitance C_d:

$$C_d = \frac{\partial Q_{SC}}{\partial V_d} = \frac{\varepsilon_r \varepsilon_0}{W} \tag{1.20}$$

where Q_{SS} is the charge filling the interface states, split into two contributions as $Q_{SS} = Q_{SSa} + Q_{SSb}$. Q_{SSa} is in equilibrium with the metal and Q_{SSb} with the semiconductor, leading to:

$$\frac{\partial Q_{SSa}}{\partial V_i} = e D_{sa} \tag{1.21}$$

$$\frac{\partial Q_{SSb}}{\partial V_d} = q D_{sb} \tag{1.22}$$

By differentiating Equation 1.18, an expression for the ideality is obtained:

$$n = 1 + \frac{C_d + e D_{Sb}}{C_i + e D_{Sa}} \tag{1.23}$$

A common assumption is to neglect the surface states, particularly in the context of capacitive measurements at frequencies that are high enough that Q_{SS} cannot

follow the AC voltage signal [36]:

$$n = 1 + \frac{C_d}{C_i} \tag{1.24}$$

The simplified expression illustrates that the ideal case $n = 1$ physically corresponds to the limit of a very thin interface layer ($\delta << W$, $C_i >> C_d$). On the other hand, high ideality factor values ($n > 1$) can correspond to combinations of high thickness (δ) and low dielectric constant (ε_i) in the interface layer, short depletion width (W) and high dielectric constant (ε_r) in the semiconductor.

A separate contribution to the junction current and ideality factor can arise from electron tunneling through the barrier, as opposed to thermionic emission over the barrier. This is usually described by the thermionic-field emission model [35]:

$$I(V) = I_S \exp\left(\frac{V}{E_0}\right) \tag{1.25}$$

where I_S is the saturation current, which is a function of temperature, barrier height, and material parameters [37]. E_0 is defined as:

$$E_0 = E_{00} \coth\left(\frac{eE_{00}}{k_B T}\right) \tag{1.26}$$

$$E_{00} = \frac{eh}{4\pi}\sqrt{\frac{N_D}{m^* \varepsilon_r}} \tag{1.27}$$

with m^* being the effective electron mass in the semiconductor. Tunneling contribution to the current becomes non-negligible when $eE_{00} \approx k_B T$, i.e. at high doping and low temperatures.

15

The functional forms of thermionic and thermionic-field emission are similar. In the context of Equation 1.12, significant tunneling current result in a signficantly increased ideality factor (often $n > 10$, see e.g. [37], [38]).

1.3.3 Capacitive response

Another important aspect of a Schottky junction is its dielectric response, which is generally dominated by the depleted region of the semiconductor. In the abrupt approximation of a depletion width W_D within which the depleted charge corresponds to the doping level N_D, one can write [30]:

$$W_D = \sqrt{\frac{2\varepsilon_0\varepsilon_r}{qN_D}\left(V_{bi} - V\right)}.$$

(1.28)

where V_{bi} is the built-in voltage, which corresponds to the potential drop measured from the top of the Schottky barrier to the conduction band level in the bulk of the semiconductor. The measured capacitance can then be written using $C = C_d = \varepsilon_r\varepsilon_0/W_d$ as:

$$\frac{1}{C^2} = 2 \cdot \frac{V_{bi} - V}{\varepsilon_0\varepsilon_r qN_D}.$$

(1.29)

This expression is a commonly used approximation for experimental analysis of Schottky junctions. It is a convenient description for the often observed linear dependence between C^{-2} and V, and allows for experimental measurement of V_{bi} and N_D from the zero intercept and slope of the curve. It ignores, however

the above discussion of the presence of an insulating interface layer. Given Equation (1.23), one can use the ideality factor to make a correction for the interface capacitance placed in series with the depletion width [35], [36], [39]. The measured capacitance is then $C = C_d/n$ or:

$$\frac{1}{C^2} = 2n^2 \cdot \frac{V_{bi} - V/n}{\varepsilon_0 \varepsilon_r q N_D}. \tag{1.30}$$

In the case of Schottky junctions using doped SrTiO$_3$ as the semiconductor, an additional complication arises from the electric field-tunable nature of the dielectric constant. As discussed in Chapter 1.2, an adequate description can be obtained using the following empirical approximation:

$$\varepsilon_r(E) = \frac{b}{\sqrt{a + E^2}}, \tag{1.31}$$

$$\varepsilon_r(E = 0) = \frac{b}{\sqrt{a}}. \tag{1.32}$$

This field dependence results in a reduced ε_r within the depletion region, owing to the built-in electric field of the Schottky junction. This modifies the potential distribution, and the new expressions for the depletion width and measured capacitance are [15], [16]:

$$W_D = \frac{b\varepsilon_0}{qN_D} \cosh^{-1}\left(1 + \frac{qN_D\varepsilon(E=0)}{b^2\varepsilon_0}\left(V_{bi} - \frac{V}{n}\right)\right). \tag{1.33}$$

$$\frac{1}{C^2} = \frac{2n^2\left(V_{bi} - V/n\right)}{qN_D\varepsilon_0\varepsilon_r(E=0)} + \left(\frac{n}{b\varepsilon_0}\right)^2\left(V_{bi} - \frac{V}{n}\right)^2. \tag{1.34}$$

An important consequence for the analysis of experimental data is the departure from linearity in the C^{-2} and V plot. The first term is now also bias dependent, and it leads to a positive curvature for $C^{-2}(V)$ [15].

1.4 Growth of SrTiO$_3$ by molecular beam epitaxy

The technique of molecular beam epitaxy (MBE) is widely recognized for its ability to produce thin films of exceptional structural quality [40]–[42]. It relies on creating a highly controlled environment for thin film growth within an ultra-high vacuum (UHV) chamber. Directional beams of the intended thin films constituents are individually generated by evaporation or sublimation from high purity sources. Owing to the very large mean free paths between collisions in the UHV environment, these molecular beams can be delivered within line-of-sight onto a heated single crystal substrate.

One distinct advantage of the MBE technique is its low energetic nature [43]. The energy of the incident molecular beam is substantially lower in comparison to other popular growth techniques, such as pulsed laser deposition (PLD, reliant on target ablation by a laser) and RF magnetron sputtering (reliant on target sputtering by a plasma). The low energy of the incident beam minimizes the undesirable formation of structural defects.

The MBE technique also enables unprecedented control of thin film properties, and in particular, their stoichiometry. In MBE, stoichiometry optimization is enabled by the presence of a "growth window". This refers to the range of constituent supply fluxes within which the film stoichiometry is self-regulating. A wide growth window is promoted by high growth temperatures and high volatility of one of the thin film constituents. [44], [45].

Practically accessible growth windows were originally demonstrated for III-V semiconductors, most notably for GaAs and other arsenides. Due to the high volatility of As, the growth window for practical growth temperatures is several order of magnitude wide in terms of III/V flux ratios [40], [44], [46], [47].

A major challenge associated with the growth of many complex oxides and transition metal perovskites is the comparatively low volatility of their constituents. This shifts the growth windows for these materials to impractically high temperatures [45], [47]. In its absence, one needs to optimize the growth conditions around a singular stoichiometric point in the elemental flux phase space [48]. Due to practical limitations on the stability of fluxes from standard solid source effusion cells, it is extremely challenging to control it with precision higher then $\approx$0.1 % - 1 % [49], [50], which corresponds to large defect densities. For instance, in the context of semiconductor doping 1 % substitution is equivalent to a volume concentration of $\approx 10^{20}$ cm^{-3}.

A recent innovation that enabled practically achievable growth windows for complex oxides was the use of a highly volatile metal-organic precursor instead of a solid source effusion cell to supply one of the film constituents [45], [51]. These precursors have been developed in the context of high vapor pressure film growth methods such as chemical vapor deposition (CVD) and atomic layer deposition (ALD) [52], [53]. The hybrid MBE method was demonstrated for the growth of SrTiO$_3$ by combining Sr from a solid source and Ti supplied by the metal-organic precursor titanium tetra-isopropoxide (TTIP). Its chemical formula is Ti(OCH(CH$_3$)$_2$)$_4$, with the central Ti^{4+} cation being bonded to four oxygen atoms. It decomposes above 260 °C (i.e. much lower than typical oxide MBE substrate temperatures of $\approx$ 600-950 °C) into titanium oxide and volatile organic components [54].

The use of TTIP to supply Ti enables a growth window for SrTiO$_3$ at practically achievable substrate temperatures ($>$ 700 °C) [45]. This is illustrated in Figure 1.5 for the case of 20-30 nm thick SrTiO$_3$ films homoepitaxially grown on (001)-oriented Nb:SrTiO$_3$ substrates, with a substrate temperature of 900 °C [55]. The stoichiometry of SrTiO$_3$ films can be checked ex-situ by measuring the out-of-plane lattice parameter c with X-ray diffracion (XRD). Both Sr and Ti excess in this material result in lattice constant expansion above the stoichiometric value of $c = 3.905$ (Å) [45], [48], [56].
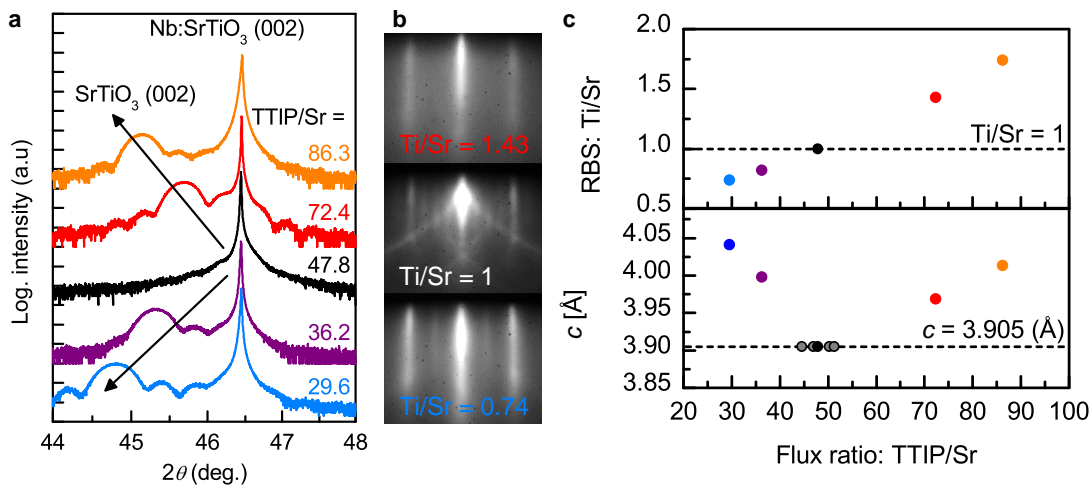
Figure 1.5. Structural characterization of $SrTiO_3$ films grown on $Nb:SrTiO_3(001)$ substrates by hybrid MBE using different TTIP/Sr flux ratios: (a) XRD spectra, (b) in-situ RHEED diffraction patterns, (c) Ti/Sr stoichiometry as determined by RBS and the corresponding lattice expansion of the out-of-plane lattice constant. Reprinted from [55], licensed under CC BY 4.0.

In Figure 1.5, the $SrTiO_3$ film peaks overlap with the substrate peak In the flux range of TTIP/Sr $\approx$ 45 - 55. This indicates that the film lattice parameter is bulk-like, and therefore these flux conditions fall within the self-regulating growth window. When the fluxes are tuned outside of this window, Ti or Sr-rich films are obtained, which is signaled by the expansion of the lattice constant in XRD. The stoichiometry of these films can be quantitatively confirmed (also ex-situ) within approximately ± 1 % by Rutherford backscattering spectrometry (RBS, analysis courtesy of Adam Hauser), as shown in Figure 1.5(c).

Another important aspect of MBE growth is the ability to monitor the film quality in-situ using reflection high-energy electron diffraction (RHEED). This technique relies on diffraction of an electron beam incident at a very small angle with respect to the film. The resulting diffraction pattern is sensitive to the structure of the film surface. In particular, the surface reconstructions carry information about the film stoichiometry [46], [57], [58]. For the case of $SrTiO_3$, perfectly stoichiometric films with Ti/Sr = 1 show a characteristic c(4×4) reconstruction in the RHEED pattern [45], [59], as shown in Figure 1.5(b). This reconstruction pattern disappears as one moves away from the center and towards the edges of the growth window. This evolution of RHEED patterns with film stoichiometry can be reliably used to quickly identify the optimal growth conditions [59].

Another important use of RHEED is for film thickness control. During layer-by-layer film growth the diffracted pattern intensity shows periodic oscillations. This corresponds to progressive filling of each successive layer, and their period corresponds to one unit cell of the film material [45], [48]. This can be used to monitor the growth rate in-situ and to accurately define extremely small layer thicknesses in heterostructures, see e.g. [60]–[62].

The hybrid MBE method has been extended to materials systems other than $SrTiO_3$. The TTIP precursor has been used to grow rare earth titanates ($RTiO_3$, R

22

= Gd, Sm, Nd) [63]–[65], BaTiO$_3$ [66], [67], the (Ba,Sr)TiO$_3$ alloy system (see Chapter 2), and CaTiO$_3$ [68]. The precursor Zirconium tert-butoxide (ZTB) has been analogously used to grow SrZrO$_3$ and Sr(Ti,Zr)O$_3$ [69]. Other examples include the use of hexamethylditin (HDMT) to grow BaSnO$_3$ [70] and vanadium oxytriisopropoxide (VTIP) to grow SrVO$_3$ [71].

Chapter 2

(Ba,Sr)TiO$_3$ films as tunable dielectrics

2.1 Performance requirements for tunable dielectric applications

As outlined in Chapter 1.2, a distinguishing feature of the $(Ba,Sr)TiO_3$ solid solution system is its high and electric field-tunable dielectric constant, which originates from proximity to the ferroelectric ordering transition.

The possibility of electrically tuning the capacitance of a device is of great interest for practical applications in microwave circuits, i.e. systems designed to manipulate high frequency (>1 GHz) AC signals. For example, a tunable capacitor (or varactor) can be used to tune the resonance in a frequency filter (tunable filter devices), or to manipulate the microwave signal by applying a controlled phase shift to it (tunable phase shifter devices) [6], [14], [72].

The engineering problem addressed in this Chapter[1] is the simultaneous requirement for high dielectric tunability and low dielectric loss. As outlined in greater detail in the following discussion of dielectric loss mechanisms, these two requirements are often in direct competition. There is thus a materials science-oriented challenge to produce a recipe for a basic tunable device (a varactor) with the best compromise of dielectric tunability and loss [72], [74]–

---

[1]The results discussed in this Chapter have been previously published in [73]. I would like to acknowledge the contributions of Adam Kajdos, who was an equal contributor to this work and had a lead role in optimizing the MBE growth of $(Ba,Sr)TiO_3$.

[76].

The tunability is generally quantified using the ratio of the AC dielectric constant at zero and operating DC electric field, giving the tunability η [6], [14]:

$$\eta = \frac{\varepsilon_r(0)}{\varepsilon_r(E)}.$$ (2.1)

Alternatively, the relative tunability η_r is defined as:

$$\eta_r = \frac{\varepsilon_r(0) - \varepsilon_r(E)}{\varepsilon_r(0)} = 1 - \frac{1}{\eta}$$ (2.2)

The term dielectric loss reflects the non-ideal nature of the tunable capacitance. The energy of the high frequency input AC signal is partially dissipated, which is classically modeled by expressing the dielectric constant as a complex quantity with a real and an imaginary component: $\varepsilon = \varepsilon' + i\varepsilon''$. The loss tangent $\tan(\delta)$ and its reciprocal, the quality factor Q, are defined as the ratio of the real to the imaginary parts of the dielectric constant:

$$Q = \frac{1}{\tan(\delta)} = \frac{\varepsilon''}{\varepsilon''}$$ (2.3)

Q and $\tan(\delta)$ are convenient metrics that define the amount of electromagnetic dissipation taking place in a device. For instance, the power converted into heat scales directly as $P \sim \tan(\delta)$.

The performance requirement for high η and low $\tan(\delta)$ is formulated by defining figures of merit (FOM) for a tunable capacitor. The simplest way to

express the compromise requirement is through the product of Q and tunability. One of the most commonly used FOM takes the zero-bias value of Q and the relative tunability at the maximum operating field:

$$\text{FOM}(E) = \eta_r(E) \cdot Q(0). \tag{2.4}$$

An alternative way to evaluate device performance is to use the commutation quality factor (CQF). This quantity can be shown to be maximized when the insertion loss of a device into a microwave circuit is minimized [77]. In its generalized version, CQF is defined for a two state switchable device as the ratio of the on and off state impedances. For a tunable dielectric, the two states are the zero field and maximum operating field, leading to:

$$\text{CQF}(E) = \frac{(\eta - 1)^2}{\eta} \cdot Q(E)Q(0) \tag{2.5}$$

In comparison to Equation (2.4), CQF is a more rigorously defined quantity that optimizes a single device element for application in a larger microwave circuit. It also has the advantage of accounting for the fact that dielectric loss can both significantly increase or decrease with applied electric field [78], [79].

Tables 2.1 and 2.2 provide a summary of previous reports on (Ba,Sr)TiO$_3$ thin films and their dielectric performance, in terms of zero-field dielectric constant and loss, maximum achieved tunability and CQF. All references in Table 2.2 are for parallel-plate capacitor structures, i.e. metal/(Ba,Sr)TiO$_3$/metal. As

Material	f(GHz)	T(K)	ε_r	η	Q	CQF	Ref.
$SrTiO_3$ on $LaAlO_3$	11	4	920	1.7	20	$\approx463^*$	[80]
$Ba_{0.5}Sr_{0.5}TiO_3$ on MgO	1-20	300	770	1.5	15	85	[81]
$Ba_{0.5}Sr_{0.5}TiO_3$ on $LaAlO_3$	1-20	300	2545	2.2	6	71	[81]
$Ba_{0.03}Sr_{0.97}TiO_3$ on MgO	4	15	430	1.2	53	187	[82]
$Ba_{0.3}Sr_{0.7}TiO_3$ on Al_2O_3	1	300	n/a	2	83	16000	[83]
$SrTiO_3$ on MgO (as grown)	8	78	900	1.5	196	7600	[78]
$SrTiO_3$ on MgO (annealed)	8	78	600	1.25	263	3209	[78]
$Ba_{0.5}Sr_{0.5}TiO_3$ on MgO	20	300	900	1.2	200	600	[84]
$Ba_{0.5}Sr_{0.5}TiO_3$ on MgO	20	300	1800	2	18	275	[85]
$SrTiO_3$ on $DyScO_3$	10	300	3500	2.6	20	98	[86]
$Ba_{0.5}Sr_{0.5}TiO_3$ on $LaAlO_3$	1	300	1429	1.74	102	420	[87]
$Ba_{0.25}Sr_{0.75}TiO_3$ on $LaAlO_3$	1	300	715	1.42	213	331	[87]
$Sr_7Ti_6O_{19}$ on $DyScO_3$	10	300	400	1.2	250	$\approx3125^*$	[88]

Table 2.1. Overview of previous reports on dielectric performance of $(Ba,Sr)TiO_3$ thin films grown on insulators and characterized in planar electrode configurations. The table indicates $E = 0$ values of ε_r and Q. η and CQF are the maximum achieved at high E. * indicates CQF estimated from zero bias Q, with no field dependence provided, most likely resulting in overestimation of CQF. Adapted from [75].

Material	f(GHz)	T(K)	ε	η	Q	CQF	Ref.
$Ba_{0.25}Sr_{0.75}TiO_3$ on Si/Pt	20	300	164	1.7	10	5228	[89]
$Ba_{0.25}Sr_{0.75}TiO_3$ on Si/Pt	2	300	728	1.4	45	208	[75]
$Ba_{0.5}Sr_{0.5}TiO_3$ on Si/Pt	1	300	368	1.43	60	501	[87]
$Ba_{0.25}Sr_{0.75}TiO_3$ on Si/Pt	1	300	208	1.27	65	281	[87]
$(Ba,Sr)TiO_3$ on Si/Pt	0.5	300	291	1.34	80	5521	[90]
$Mg:(Ba,Sr)TiO_3$ on Si/Pt	0.5	300	201	1.17	200	988	[90]
$SrTiO_3$ on $SrTiO_3/SrRuO_3$	10^{-6}	190	600	1.85	1060	443470	[91]
$Ba_{0.5}Sr_{0.5}TiO_3$ on Si/Pt	10^{-5}	300	153	1.9	213	$\approx$19574*	[92]
$SrTiO_3$ on Al_2O_3/Pt	10^{-2}	300	240	n/a	300	n/a	[93]
$Ba_{0.48}Sr_{0.52}TiO_3$ on Al_2O_3/Pt	10^{-3}	300	455	13.71	75	$\approx$66280*	[94]
$Ba_{0.48}Sr_{0.52}TiO_3$ on Al_2O_3/Pt	10^{-3}	300	241	7.88	161	$\approx$155700*	[94]
$Ba_{0.19}Sr_{0.81}TiO_3$ on $SrTiO_3$/Pt	10^{-3}	300	457	3.3	4030	1130000	[73]
$Ba_{0.35}Sr_{0.65}TiO_3$ on $SrTiO_3$/Pt	10^{-3}	300	709	5.6	1550	500000	[73]
$Ba_{0.46}Sr_{0.54}TiO_3$ on $SrTiO_3$/Pt	10^{-3}	300	1260	6.5	160	52000	[73]

Table 2.2. Overview of previous reports on dielectric performance of $(Ba,Sr)TiO_3$ thin films grown metallics bottom electrodes and characterized in parallel-plate capacitor configurations. Presented quantities are same as in Table 2.1. Adapted from [75]. Reference [73] is the work presented in Chapter 2.4

discussed in Chapter 2.2, a big challenge in this geometry is to minimize loss from electrode series resistance, which tends to severely limit the maximum operating frequency. Its advantage is the possibility to apply very high electric fields. Table 2.1 presents studies of (Ba,Sr)TiO$_3$ films grown on insulators and characterized by measuring the in-plane dielectric response between planar interdigitated electrodes [95]. The advantage of this geometry is the comparative ease of growing on an insulator, and the possibility to easily measure high frequency response. The disadvantage is the difficulty in achieving high tunability, with only small applied fields being possible due to fringing fields and inherently larger lateral electrode spacing [74], [75].

Experimental efforts have largely focused on paraelectric Ba$_x$Sr$_{1-x}$TiO$_3$ films with $x = 0.2$-0.5. In this composition range, the films are in proximity to a ferroelectric T_C at cryogenic temperatures, thus maximizing the dielectric tunability (η).

High quality bulk single crystals and ceramics with low x can have Q above 1000 [6], [23], [96]–[98]. In contrast, values of Q in thin films are much smaller. Generally $Q < 100$, in particular for films with high tunability. This discrepancy is thought to stem from extrinsic losses, i.e. linked to structural imperfections resulting from the thin film growth process [6], [72], [74], [75]. This Chapter will present a tunable capacitor fabrication procedure based on

MBE growth of $Ba_xSr_{1-x}TiO_3$ and high temperature sputtering of an epitaxial Pt bottom electrode. This process was designed to maximize the structural quality of the capacitor stack, which will be shown to translate into very high Q, η, CQF and n_rQ.

2.2   Dielectric loss mechanisms

In the context of a tunable dielectric capacitor based on $(Ba,Sr)TiO_3$, the mechanisms for dielectric loss can be classified into three categories: intrinsic (interaction between phonons in a perfect crystal with the AC electric field), extrinsic (interaction between imperfections of the crystal and the AC electric field) and loss originating from the device layout [6], [14], [93].

Most practical settings for measurement of a tunable dielectric can be modeled by an equivalent circuit consisting of a tunable capacitance C, a parallel resistance R_P and a series resistance R_S (Figure 2.1). In the context of a paral-
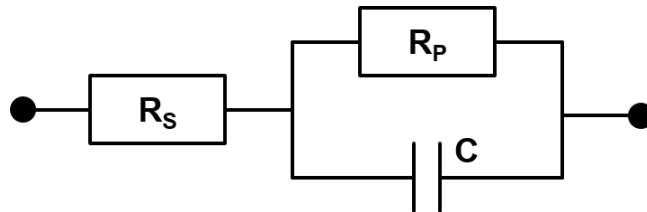
Figure 2.1. Equivalent circuit of a parallel plate capacitor.

lel plate capacitor, R_S includes the bottom and top electrode resistance and R_P represents leakage currents. The impedance of this equivalent circuit is:

$$Z = R_S + R_P \cdot \frac{1 - i\omega R_P C}{1 + \omega^2 R_P^2 C^2},$$
(2.6)

with ω being the angular frequency ($\omega = 2\pi f$). The dielectric loss quality factor of the circuit is given by $Q = Z''/Z'$. Its frequency dependence is conveniently described by considering the low and high frequency limits:

- In the **low frequency limit**, the dielectric loss is dominated by leakage, represented by R_P in the equivalent circuit. A simplified expression for Q at low ω is:

$$Q(\text{low } \omega) = \omega R_P C.$$
(2.7)

- In the **high frequency limit**, the dielectric loss is dominated by the series resistance (R_S), resulting in a decreasing Q:

$$Q(\text{high } \omega) = \frac{1}{\omega R_s C}.$$
(2.8)

The resulting dependence of Q on frequency is illustrated in Figure 2.2, using representative experimental data for a Pt/(Ba,Sr)TiO$_3$/Pt parallel-plate capacitor. The plot shows a well defined roll-off at high frequency that follows Equation (2.8).

32

To extend the operational regime with high Q to higher f, it is important to minimize the series resistance R_S. Lower R_S shifts the roll off to higher frequencies. In the context of device design, this corresponds to using high metal thicknesses for both top and bottom contacts. Another avenue to minimize R_S is to use metals with high conductivity. The ideal choice is Au (highest conductivity), but Pt is often preferred as it is much more resistant to oxidation and thus more compatible with growth and processing at high temperatures.

At low frequency, Q is dominated by R_P according to Equation (2.7), which emphasizes the need for leakage currents to be low enough (particularly for
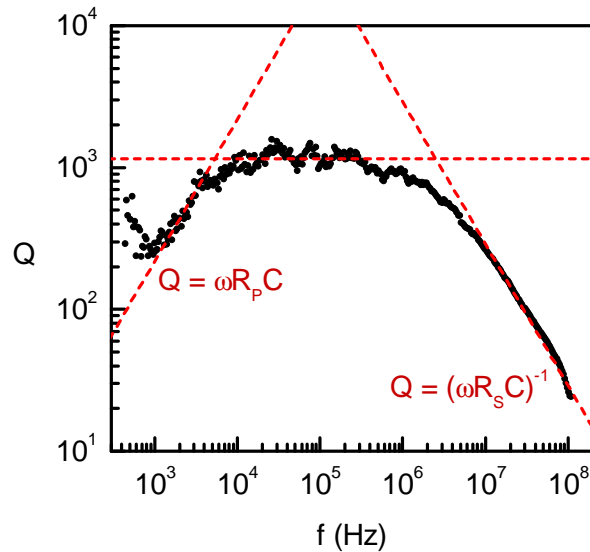
Figure 2.2. Representative example for frequency dependence of dielectric loss quality factor in a metal/(Ba,Sr)TiO$_3$/metal parallel plate capacitor.

devices with high capacitance densities) that it does not interfere with the operating regime.

The intermediate frequency regime has the highest Q. It is approximately flat and does not correspond to losses related to R_P or R_S. This is the ceiling of Q that corresponds to dielectric losses within the (Ba,Sr)TiO$_3$ layer. Minimizing them is an important engineering challenge, given the goal of optimizing the device figures of merit. In the following, the various possible mechanisms are outlined.

Intrinsic dielectric losses originate from interactions between the AC signal and the thermal phonon spectrum of the insulator crystal. Three possible mechanisms that satisfy the energy conservation requirements are [6], [79], [99]:

- The **three quantum mechanism** refers to the interaction between one quantum of energy from the AC electromagnetic field and two quantums from the phonons. The full theoretical description is quite sensitive to the details of the phonon dispersion. For the case of a paraelectric in proximity to ferroelectricity (i.e. in the presence of a low frequency soft phonon mode), this mechanism leads to:

$$\tan(\delta)(3\hbar\omega) \sim \omega T^2 \varepsilon_r^{1.5}. \tag{2.9}$$

This expression is for the case of $\omega << \Gamma$, with Γ being the phonon damp-

ing ($\Gamma \approx 100$ GHz in SrTiO$_3$).

- The **four quantum mechanism** is largely analogous to the three quantum one, but involves three phonons and one electromagnetic field quantum. It can also be shown to scale very simlarly for $\omega < \Gamma$:

$$\tan(\delta)(4\hbar\omega) \sim \omega T^2 \varepsilon_r^{1.5}. \tag{2.10}$$

- The **Quasi-Debye mechanism** is related to the electric field dependence of the phonon spectrum. In non-centrosymmetric crystals, phonon frequencies are field dependent and are modulated by the AC input signal. Their relaxation to the zero field state generates dielectric loss.

  In the case of paraelectric (Ba,Sr)TiO$_3$ with cubic (and centrosymmetric) symmetry, there is no Quasi-Debye loss at zero bias. However, a finite electric field does break centrosymmetry and activates the Quasi-Debye mechanism. For a small electric field and $\omega < \Gamma$, the corresponding dielectric loss can be expressed using the relative tunablity:

$$\tan(\delta)(\text{Q.-D.}) \sim \omega \eta_r. \tag{2.11}$$

Intrinsic dielectric loss mechanisms represent the ceiling of Q inherent to a particular crystal structure. They can only be manipulated by changing the insulator material. In contrast, **extrinsic loss mechanisms** are related to in-

teractions with the imperfections of the material. These mechanisms can be mitigated by improving the material quality:

- The **charged defect mechanism** is related to the motion of such defects induced by the AC electric field, which in turn generates acoustic waves in the material [6]. The dielectric loss related to this process can be approximately calculated for the case of materials with high ε_r:

$$\tan(\delta)(\text{C.D.}) \sim N(\text{defects}) \cdot \omega\varepsilon_r \left(1 - \frac{1}{1 + \omega^2/\omega_c^2} \right), \qquad (2.12)$$

where $N(\text{defects})$ is the charged defect density and ω_c is a characteristic frequency.

- The **local polar region mechanism** is caused by the presence of local inhomogeneous strain and disorder [6]. Broken centrosymmetry in such regions locally activates the Quasi-Debye mechanism. It can be demonstrated that this mechanism scales very strongly with the dielectric constant:

$$\tan(\delta)(\text{L.P.R.}) \sim \varepsilon_r^{4.5-d}. \qquad (2.13)$$

where $d = 0, 1, 2$ corresponds to the dimensionality of the polar structural defect (point, linear, planar).

- The **universal relaxation law mechanism** is linked to the low frequency relaxation of the dielectric constant [100]. It is similar for both its real and

36

imaginary component:

$$\varepsilon_r'' = \varepsilon_r' \cot(m\pi/2) \sim \omega^{m-1}. \tag{2.14}$$

From Kramers-Kronig relations, this relaxation is equivalent to a frequency independent contribution to loss [100], [101]:

$$\tan(\delta)(\text{U.R.L.}) = \frac{\varepsilon_r''}{\varepsilon_r'} = \cot(m\pi/2). \tag{2.15}$$

Table 2.3 summarizes the various loss mechanisms and their scaling with

Type	Mechanism	$\tan(\delta)$ vs f	$\tan(\delta)$ vs ε_r
Device	Low-f leakage	$\sim f^{-1}$	$\sim \varepsilon_r^{-1}$
Device	High-f roll-off	$\sim f$	$\sim \varepsilon_r$
Intrinsic	3-Quantum	$\sim f$	$\sim \varepsilon_r^{1.5}$
Intrinsic	4-Quantum	$\sim f$	$\sim \varepsilon_r^{1.5}$
Intrinsic	Quasi-Debye	$\sim f$	$\sim \eta_r(E) \sim E$
Extrinsic	Charged defects	$\sim f$	$\sim \varepsilon_r$
Extrinsic	Local polar region	?	$\sim \varepsilon_r^{4.5-d}$ $(d = 0, 1, 2)$
Extrinsic	Universal relaxation	constant	?

Table 2.3. Dielectric loss mechanism relevant to (Ba,Sr)TiO$_3$ and theoretical predictions for their scaling with frequency dielectric constant. Adapted from [6].

frequency and dielectric constant.

2.3   Fabrication of parallel-plate capacitors

This Chapter will detail the fabrication of Pt/Ba$_x$Sr$_{1-x}$TiO$_3$/Pt parallel-plate capacitors using a combination of MBE and sputtering for film growth and standard contact photolithography techniques for device definition. The procedure can be briefly outlined as follows:

1. Growth of the 100 nm thick Pt(001) epitaxial bottom electrode on a SrTiO$_3$ single crystal substrate by sputtering at 825 °C.

2. Post-growth anneal of SrTiO$_3$ / Pt(001) at 1000 °C for 30 minutes in oxygen

3. MBE growth of 300 nm thick (Ba,Sr)TiO$_3$ on SrTiO$_3$ / Pt(001) at a substrate temperature of 750 °C in an oxygen plasma

4. Mesa etch though the (Ba,Sr)TiO$_3$ using hydrofluoric acid (HF)

5. Lift-off process for a 100 nm thick top Pt electrode (45x45 μm^2 squares)

6. Post-processing anneal of the SrTiO$_3$ / Pt(001) / (Ba,Sr)TiO$_3$ / Pt stack at 800 °C for 20 minutes in oxygen.

Step 1 follows the procedure developed in [102]. Prior to Pt depostion the SrTiO$_3$(001) single crystal substrate is in-situ annealed in the sputtering growth chamber at 825 °C for 2 hours in 10 mTorr O$_2$. It is immediately followed by the deposition of Pt by DC magnetron sputtering at the same substrate temperature, using 10 mTorr Ar as a sputter gas.

The pre-growth anneal in O$_2$ is necessary to clean the SrTiO$_3$ surface from undesirable contamination (see also Chapter 3.2 for a more in-depth discussion). It was found to stabilize the Pt(001) orientation that follows a cube-on-
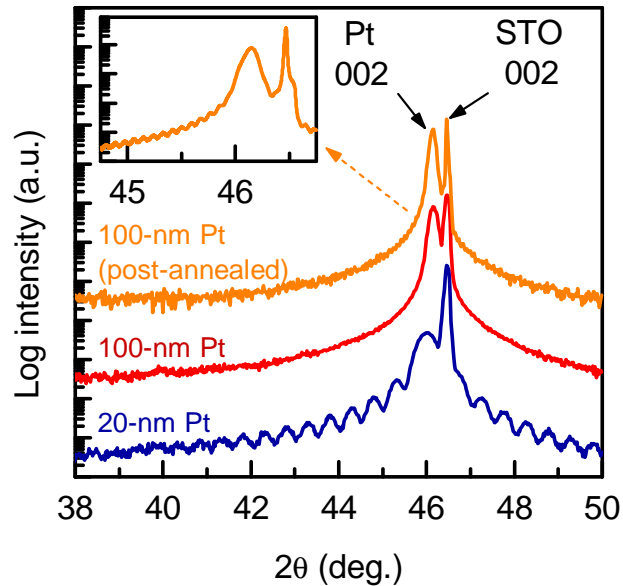
Figure 2.3. XRD 2θ-ω spectra of epitaxial 20 and 100-nm thick Pt films grown on SrTiO$_3$ substrates. The orange curve and the inset show a 100-nm thick Pt film after post growth annealing at 1000 °C in oxygen.

cube epitaxial relationship with SrTiO$_3$ [102]. This is in contrast with the preferential Pt(111) orientation that is stable for low temperature growth, yielding a polycrystalline film on SrTiO$_3$. High T growth without a pre-growth anneal in O$_2$ also yields a polycrystalline Pt(111) film [102], [103].

XRD scans of 20 and 100 nm thick Pt(001) films on SrTiO$_3$ are shown in Figure 2.3. In both cases, prominent Pt 002 peaks are observed near $2\theta = 46.24$ °. No Pt 111 peaks were detected near $2\theta = 39.77$ °. 20-nm thick films show thickness fringes around Pt(002). Their disappearance in the 100 nm thick films is consistent with strain relaxation by twinning [102].

For parallel plate capacitors, fairly thick bottom electrodes are needed to minimize series resistance, which encouraged the use of thicker Pt layers with fully relaxed strain. Another challenge was to maintain stability of the Pt(001) orientation during the MBE growth step, which exposes the Pt film to high temperatures in a UHV environment. These conditions favor the formation of Pt(111). As-grown Pt layers were found to perform poorly in such conditions, with mixed orientations Pt(001)/(111) being observed during substrate temperature ramp-up via in-situ RHEED and ex-situ XRD.

Step 2 addresses this issue by incorporating a post-growth anneal for the Pt(001) layer. Figure 2.4 shows the optimization test for this step, where three
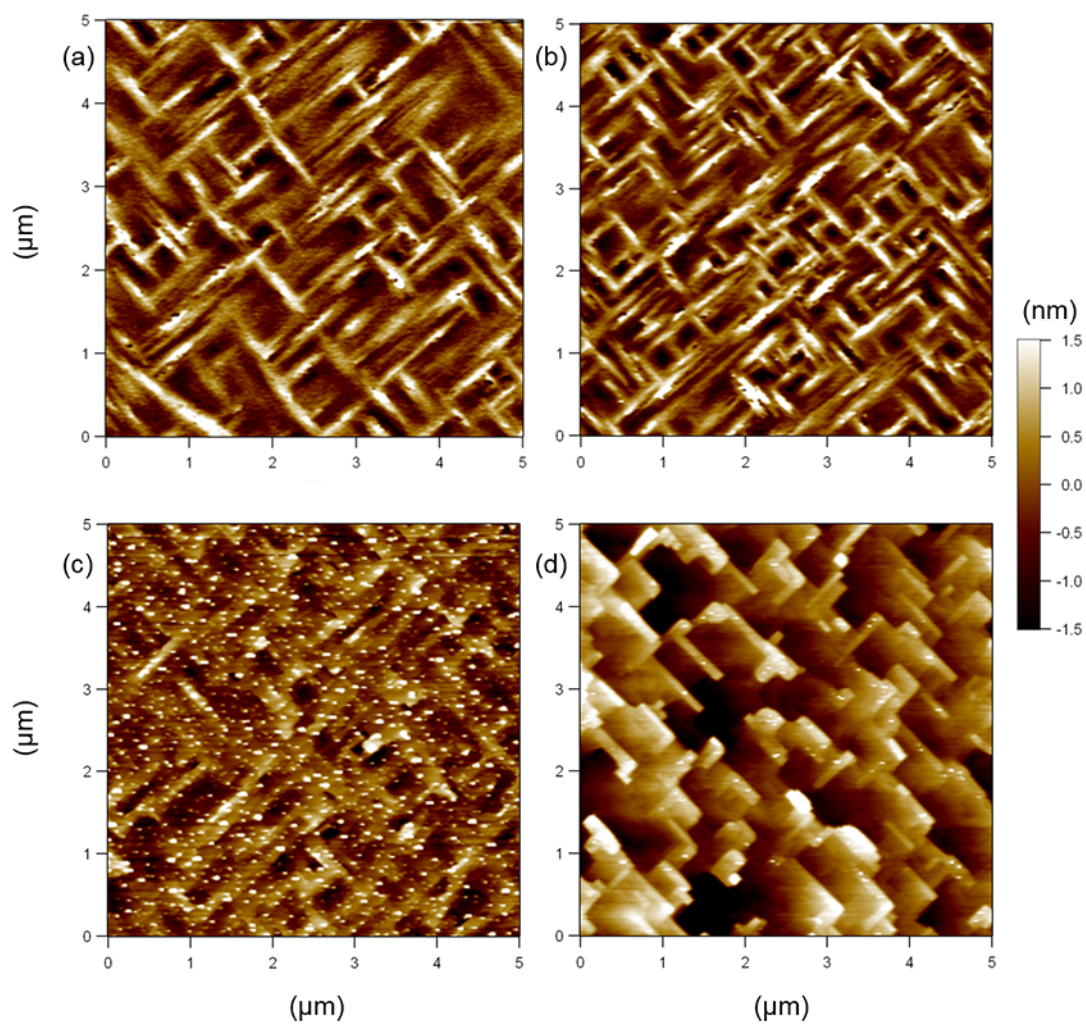
Figure 2.4. Atomic force microscopy (AFM) images of the 100-nm Pt(001) surface on SrTiO₃: as grown (a) and after a 30 minute-long anneal in oxygen at 600 (b), 750 (c) and 1000 (d) °C.

pieces of a single SrTiO$_3$ / Pt(001) sample were annealed at different temperatures (600, 750 and 1000 °C) in flowing O$_2$ for 30 minutes. The Pt surface imaged by atomic force microscopy (AFM) is shown. The as grown Pt has a fairly smooth surface (root mean square roughness ≈ 0.4 nm) with a cross-hatch pattern indicative of strain relaxation by twinning.

Annealing at very high temperatures in oxygen modifies the surface morphology of Pt. Figures 2.4(b-d) show a transition towards a smooth terraced surface for Pt annealed at 1000 °C. This annealing treatment was found to be beneficial in terms of stabilizing the structural integrity of Pt in the high temperature and low oxygen pressure environment of the MBE growth chamber. As shown in the inset of Figure 2.4, faint XRD thickness fringes around the Pt 002 peak were recovered for post-annealed samples, consistent with their smoother surface. No change in the bulk structure of Pt was detected, as its (001) orientation was preserved.

Step 3 is the growth of 300-nm thick Ba$_x$Sr$_{1-x}$TiO$_3$ on SrTiO$_3$ / Pt(001) by MBE. To preserve the structural integrity of the bottom electrode, the substrate temperature was kept at 750 °C (minimum required for a narrow growth window). The sample heat-up, growth and cool-down were performed in an O$_2$ plasma environment (background pressure $\approx 4 \times 10^{-6}$ Torr). Calibration growths of Ba$_x$Sr$_{1-x}$TiO$_3$ on SrTiO$_3$ substrates were used to optimize the Ti/(Ba,Sr)

cation stoichiometry, following the standard procedure of minimizing the out-of-plane plane lattice parameter as a function of the TTIP/(Ba+Sr) ratio. This optimization was performed separately for three different Ba/Sr compositions, which were measured by RBS to be $x = 0.19$, 0.35 and 0.46 (courtesy of Adam Hauser). The exact $Ba_xSr_{1-x}TiO_3$ layer thicknesses for these three samples were 322, 264 and 269 nm, respectively (as measured by cross-section TEM, courtesy of Jack Zhang).

Figure 2.5 shows XRD scans of $SrTiO_3/Pt(001)/Ba_xSr_{1-x}TiO_3$ stacks after the MBE growth. The orange, red and blue curves correspond to $Ba_xSr_{1-x}TiO_3$ films ($x = 0.19$, 0.35 and 0.46) grown $SrTiO_3$ / Pt(001) annealed at 1000 °C in step 2. For comparison, the overlayed black curves in (a) show films with the same composition grown on $SrTiO_3$ / Pt(001) with no annealing in step 2. The wide-angle scans reveal the polycrystalline nature of these films, with peaks present near $2\theta = 32.2$ (BST 110) and $2\theta = 39.8$ (Pt and BST 111). The films grown on pre-annealed Pt show a considerable reduction of the (111) orientation peaks, consistent with in-situ RHEED observation of better Pt(001) stability. These films are predominantly (001) cube-one-cube oriented (also confirmed in phi angle scans).

Figure 2.6 shows representative AFM scans for the $x = 0.46$ sample (with annealed Pt). It reveals a smooth surface corresponding to the dominant BST

(001) orientation with minority (110) and (111) grain inclusions. Their orientation can be identified by the shape: (110) grains are rectangular and (111) are triangular, as expected from the surface energies in the perovskite crystal structure.

Figure 2.5(b) shows high resolution scans around the BST / Pt / STO 002 peaks. The thickness fringes correspond to the 100 nm thick Pt bottom elec-
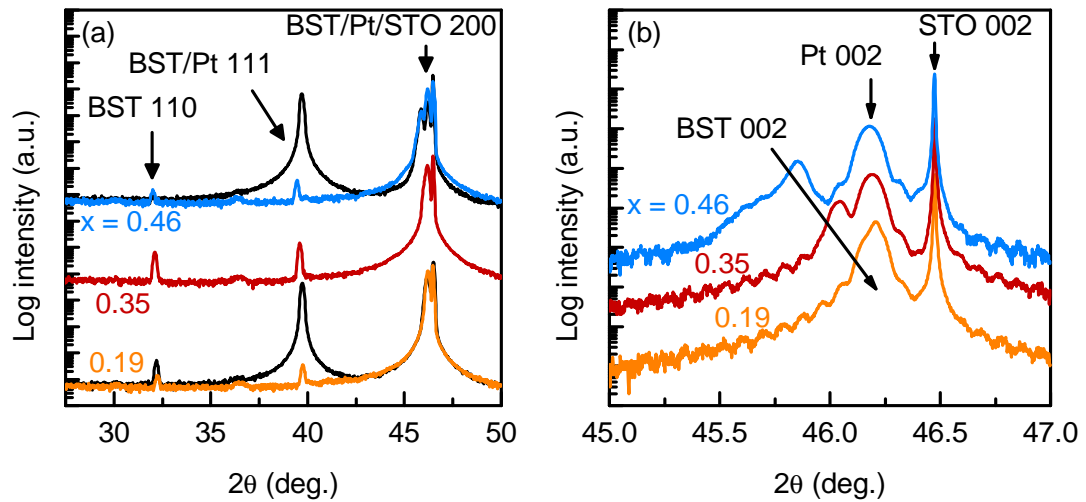
Figure 2.5. XRD scans of $Ba_xSr_{1-x}TiO_3$ films with three different compositions grown on $SrTiO_3$/Pt(001). (a) Wide range scans. Overlayed black curves correspond to films with same composition, but grown on $SrTiO_3$/Pt(001) without the 1000 °C anneal ("step 2"), illustrating the suppression of (111) oriented grains. (b) High resolution scans near the (002) reflections of the substrate and films, with the thickness fringes corresponding to 100-nm thick Pt.

trodes. The shift of the $Ba_xSr_{1-x}TiO_3$ peak with composition corresponds to an increased lattice constant. This is expected for the solid solution of perovskites with mismatched lattice constants: $a = 3.905$ (Å) for $SrTiO_3$ and ≈ 4.0 (Å) in the pseudocubic approximation for $BaTiO_3$ [22].

Steps 4 and 5 pattern the blanket $SrTiO_3$ / Pt(001) / $Ba_xSr_{1-x}TiO_3$ stack into the parallel-plate capacitor device illustrated in Figure 2.7. The optimization of the device pattern design is described in detail in [104]. The initial mesa etch is required to uncover the buried bottom Pt electrode. The wet etch with 1:20 diluted trace metal grade HF is selective: it removes $Ba_xSr_{1-x}TiO_3$ and stops
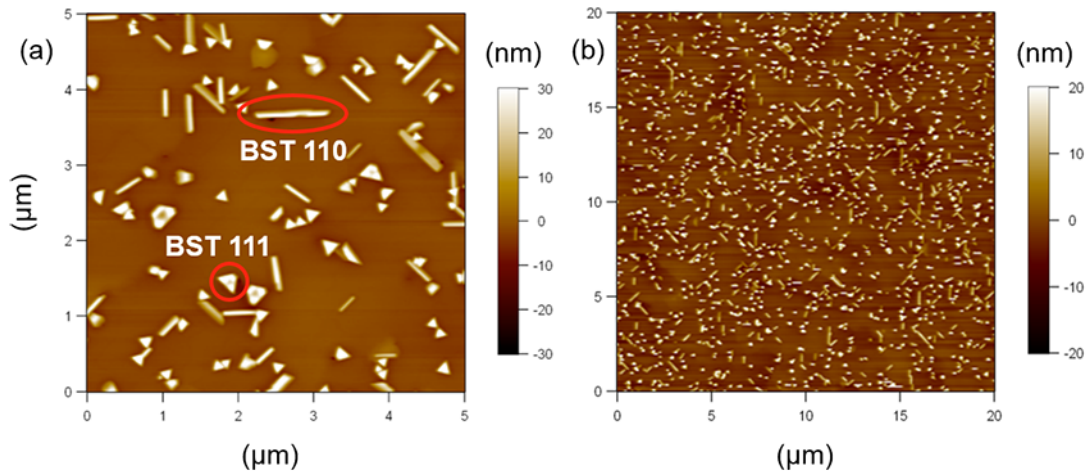
Figure 2.6. AFM images of the $Ba_{0.46}Sr_{0.54}TiO_3$ surface after growth on $SrTiO_3$/Pt(001), highlighting the (111) and (110) oriented grains embedded in a majority matrix of (001) oriented (Ba,Sr)TiO_3.

at the Pt electrode. The lift-off process in step 4 defines a 100-nm thick top electrode and the contact pads for the bottom electrode. These contacts pads are oriented in a ground-signal-ground geometry (GSG) with a 100 μm pitch.

Step 6 is a 20 minute-long anneal at 800 °C in oxygen. Its primary purpose is to mitigate oxygen deficiency inherent to the low-pressure growth environment of MBE. It was also found to improve the leakage characteristics of the devices, with 20-30 minutes being the optimal anneal duration.
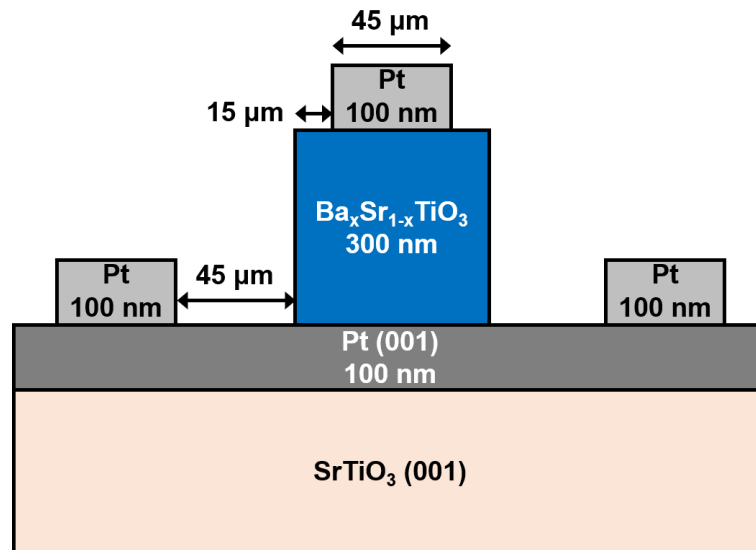
Figure 2.7. Parallel plate capacitor device geometry for dielectric measurements in a ground-signal-ground (GSG) configuration.

2.4 Dielectric performance

This Chapter presents the dielectric performance of the parallel plate capacitors described above. It was performed using 100-μm pitch GSG probes and an HP 4294A impedance analyzer. The frequency dispersion of the dielectric constant and loss is shown in Figure 2.8. The frequency region of interest is 10 kHz - 10 MHz, where the dielectric loss is dominated by the $(Ba_xSr_{1-x})TiO_3$ material, instead of leakage (below 1 kHz) or series resistance (above 10 MHz).

In the intermediate frequency regime, the trend with composition x illus-
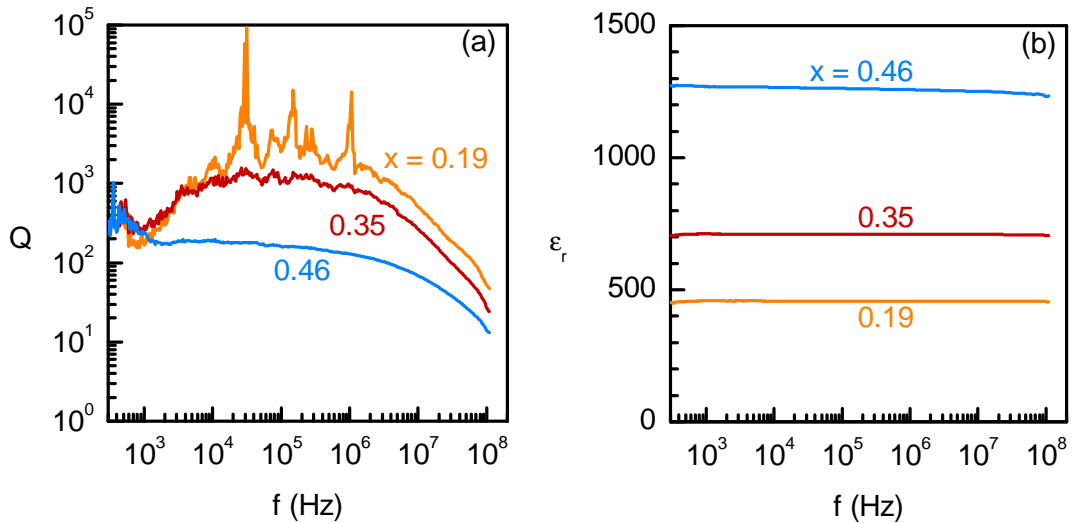
Figure 2.8. Frequency dependence of (a) dielectric quality factor Q and (b) dielectric constant ε_r of $SrTiO_3$/Pt/$(Ba_xSr_{1-x})TiO_3$/Pt parallel plate capacitors.

trates the ubiquitous trade-off between Q and ε_r. For the most Ba-rich sample ($x = 0.46$), proximity to the ferroelectric transition results in very high $\varepsilon_r = 1260$ at 1 MHz, but its $Q < 200$ is significantly lower in comparison to the other two samples. For $x = 0.19$ and 0.35, Q plateaus above 1000 in the intermediate frequency range.

Figure 2.9(a) compares the dielectric loss of these films with values reported
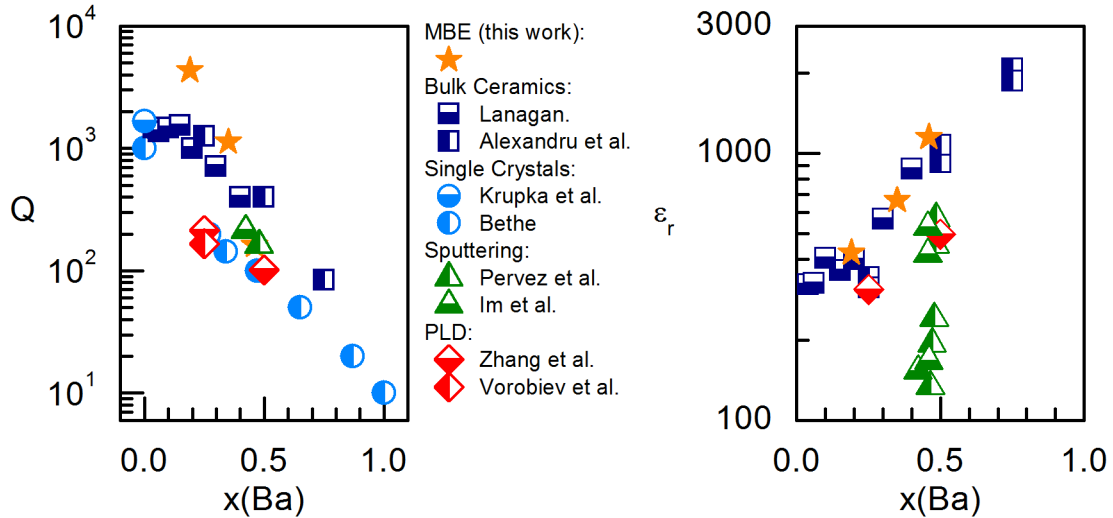
Figure 2.9. Comparison of (a) dielectric loss quality factors Q and (b) dielectric constants ε_r in $Ba_xSr_{1-x}TiO_3$ at zero field and room temperature for MBE - grown films (from Figure 2.8) with values reported using other growth techniques by Lanagan [97], Alexandru et al. [98], Krupka et al. [96], Bethe [23], Pervez et al. [94], Im et al. [92], Vorobiev et al. [89], and Zhang et al. [87]. Reprinted with permission from [73]. Copyright 2012, AIP Publishing LLC.

previously in the literature. For the MBE-grown films, the average in the 100 kHz - 1 MHz range is plotted, given the large frequency dependent fluctuations. By comparison of $Ba_xSr_{1-x}TiO_3$ samples with similar composition, it is clear that the use of the MBE technique yields considerably higher Q than other thin film growth techniques (pulsed laser deposition, sputtering) and even bulk ceramics and single crystals.

Figure 2.9(b) makes a similar comparison for ε_r of $Ba_xSr_{1-x}TiO_3$. The magnitude of the dielectric response in MBE-grown films is on par with bulk material and much higher in comparison with typical thin films. This attests to the measured capacitance in our case being dominated by the tunable dielectric film. The influence of parasitic capacitances at the metal/oxide interfaces is minimized. This is due to the high quality of the epitaxial bottom interface (Pt(001) / $Ba_xSr_{1-x}TiO_3$) and the fairly high thickness of $Ba_xSr_{1-x}TiO_3$.

The second important aspect for device applications is the tuning of ε_r with applied electric field. The field dependence of Q and ε_r at 1 MHz is shown in Figure 2.10. This Figure showcases a large and continuous tuning of ε_r, and the corresponding tunability η is shown in Figure 2.12. η reaches above 3, 5, and 7 for $x = 0.19$, 0.35, and 0.46, respectively. This compares very favorably with the previously reported tunability values, which are generally in the range $\eta \approx$ 1.5-2.5 (Tables 2.1 and 2.2).
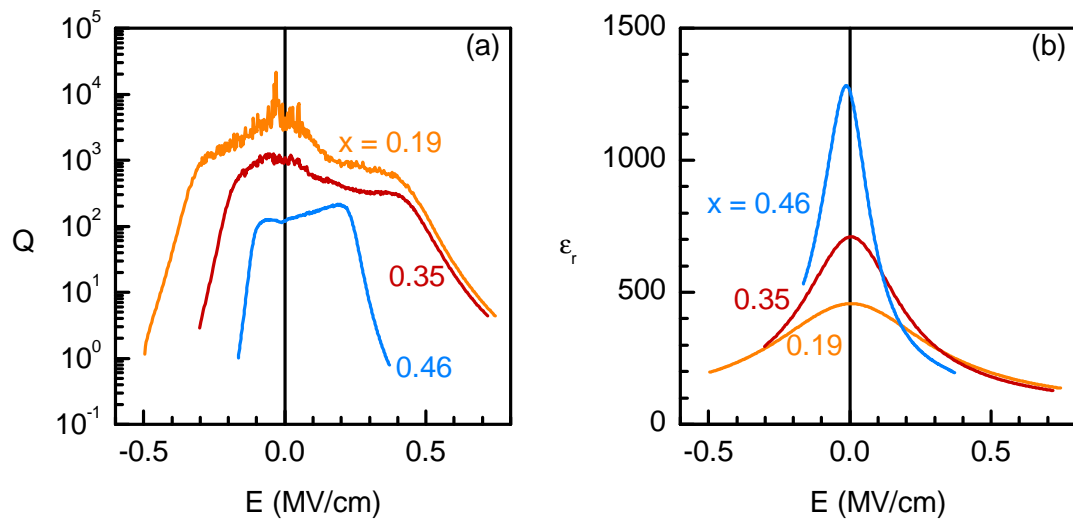
Figure 2.10. Electric field dependence of Q and ε_r at $f = 1$ MHz for all Ba$_x$Sr$_{1-x}$TiO$_3$ compositions
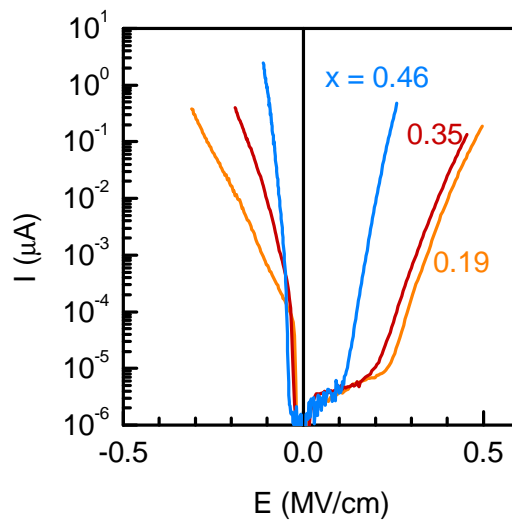
Figure 2.11. DC leakage current for all Ba$_x$Sr$_{1-x}$TiO$_3$ compositions

The maximum achievable tunability for these samples is limited by the onset of DC leakage current, which is clearly seen in the field dependence of Q in Figure 2.10. It results in a sharp drop off at $E = 0.4$ (MV/cm) for $x = 0.19$, 0.35 and at $E = 0.2$ (MV/cm) for $x = 0.46$. This decrease in Q can be rationalized in terms of the equivalent circuit in Figure 2.1 and Equation 2.7, by evoking a decrease of R_P at high E, as expected for highly non-linear leakage current. The observed trend for higher leakage at high Ba content is consistent with the direct two-probe DC measurement of leakage current, shown in Figure 2.11.

To assess the overall combined performance for dielectric tunability and loss as a function of field, it is customary to use figures of merit, most notably the commutation quality factor (Equation 2.5) [75], [77]. In Figure 2.12, CQF it is plotted as a function of E, where it reaches a peak value before decreasing at high E due to leakage. The plateau reaches CQF $= 10^6$, $5 \cdot 10^5$, and $5 \cdot 10^4$ for $x = 0.19$, 0.35 and 0.46, respectively. These values are orders of magnitude larger than the previous reports (Tables 2.1 and 2.2), with the highest previously measured CQF at room temperature being $1.6 \cdot 10^4$. The very high CQF values for MBE grown films showcase the simultaneous presence of very high tunability and very low loss, as is necessary for device applications.

Another common figure of merit is the product $n_r(E)Q(0)$ (Equation 2.4), which is also shown in Figure 2.12. The highest achived values are $n_r(E)Q(0) =$
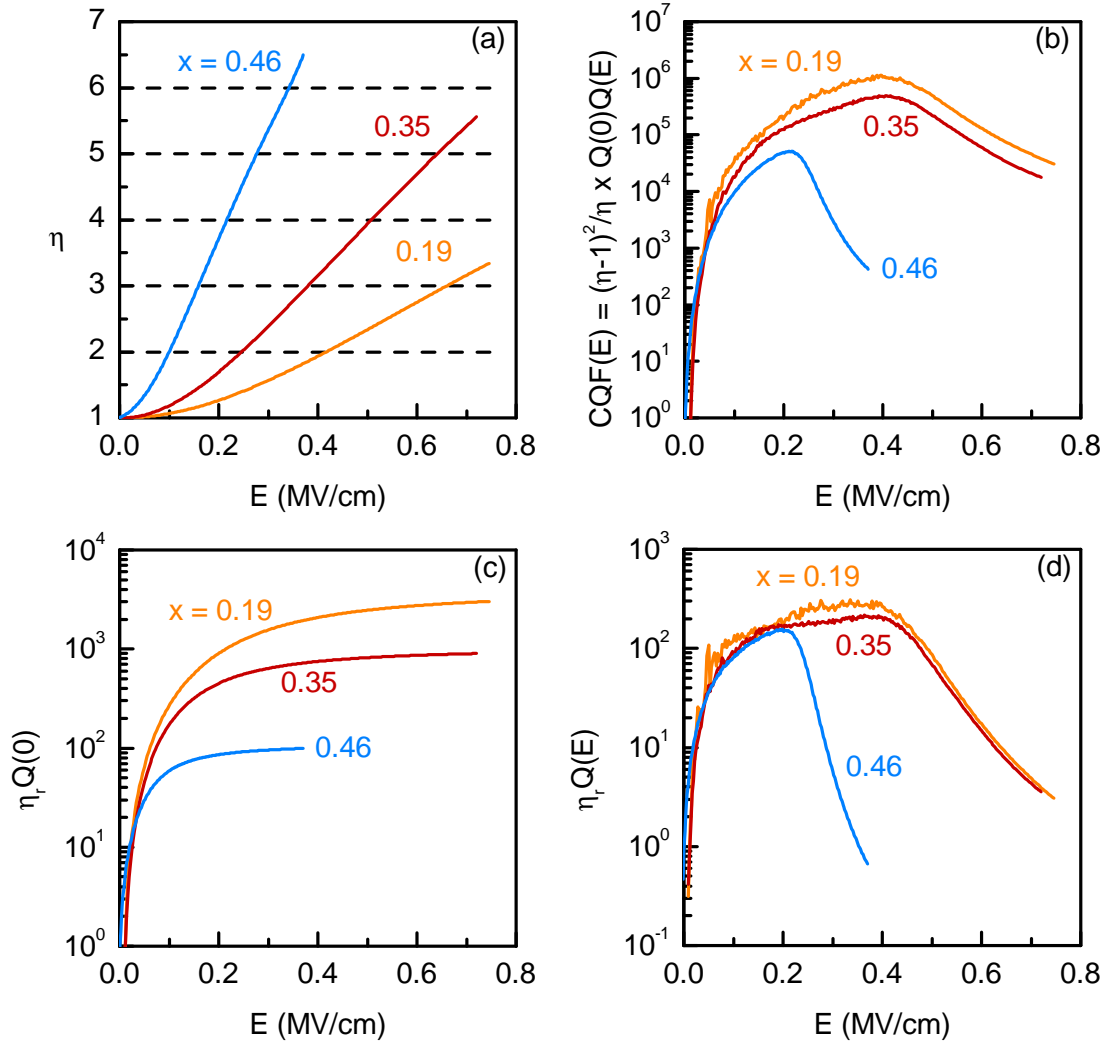
Figure 2.12. Electric field dependence of (a) relative tunability $\eta(E) \equiv \varepsilon(E)/\varepsilon(0)$, (b) commutation quality factor, (c) $n_r(E)Q(0)$, (d) $n_r(E)Q(E)$ for all Ba$_x$Sr$_{1-x}$TiO$_3$ compositions.

3020, 900, and 100 for $x = 0.19$, 0.35 and 0.46 respectively. Again, this compares very favorably with other reports, e.g. $n_r(E)Q(0) = 140$ [94] and 400 [88]. Additionally, Figure 2.12 shows the field-dependent equivalent of the previous figure of merit: $n_r(E)Q(E)$. This accounts for the field dependence of Q and displays the same peak behavior as the CQF.

In conclusion of this Chapter, we discuss the loss mechanisms in the medium-frequency, high-Q regime. It is instructive to compare the field dependence of Q in Figure 2.10(a) with the theoretical predictions in Table 2.3. Most loss mechanisms are predicted to decrease if ε_r is reduced at higher E. This is observed for the most lossy sample ($x = 0.46$) at low E (before the onset of leakage), where Q is increased above its zero field value. This trend with E is very often observed in the literature [78], [79], [87], [89], [92], [94], and is particularly strong for films with low Q. In such settings, Q is likely to be dominated by extrinsic mechanisms, namely the dissipation related to charged defects, for which $\tan(\delta)$ scales with ε_r.

For the samples with high Q ($x = 0.19$ and 0.35), its dependence on E is monotonously decreasing. The only loss mechanism in Table 2.3 consistent with this trend is Quasi-Debye, which increases in intensity as the applied field breaks the centrosymmetry of the paraelectric perovskite. Figure 2.13 illustrates that for $x = 0.19$, the low field region is approximately consistent with the

theoretical prediction of $\tan(\delta)$(Q.-D.) scaling with the relative tunability η_r [6]. This implies that Q in these MBE-grown samples is dominated by an intrinsic loss mechanism.

The increased Q in MBE-grown $Ba_xSr_{1-x}TiO_3$ in comparison to previous reports (see Figure 2.9) is consistent with improved material quality minimizing extrinsic loss mechanisms. One possible explanation for the extrinsic loss is the charged defect mechanism, which is consistent with the observed trends for Q with field and materials quality. It is, however, predicted to scale with frequency $(\tan(\delta)$(C.D.) $\sim f)$ [6], which is inconsistent with the medium frequency plateau
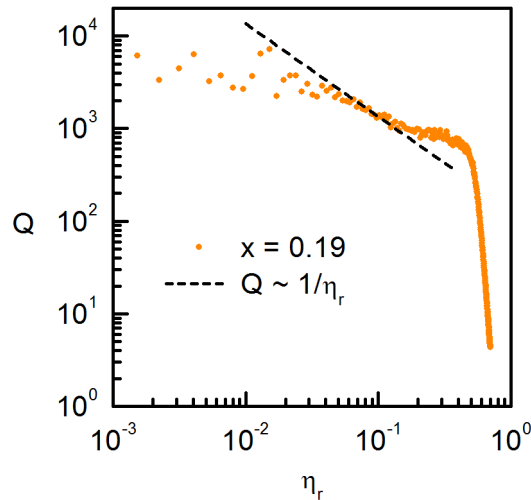
Figure 2.13. Comparison between the experimental data for $x = 0.19$ and the Quasi-Debye mechanism prediction for inverse scaling between Q and the relative tunability η_r (dashed line).

of Q. The universal relaxation mechanism [100] has been discussed to be applicable to $Ba_xSr_{1-x}TiO_3$ grown by sputtering [101]. It accurately describes the frequency independence of Q. This framework is, however, agnostic with respect to the microscopic mechanism. It is nevertheless quite clear that this loss mechanism scales with structural quality of the material and can be minimized by appropriate stack design and the use of low energy deposition techniques, such as MBE.

It is important to note that all intrinsic mechanisms (including Quasi-Debye) were predicted to scale with frequency (see Table 2.3), while experimentally the overall shape of Q is always approximately constant in the medium frequency range. It is at present unclear whether such discrepancies are an artifact of approximations in the theoretical derivations of the frequency dependence or if alternate loss mechanisms need to be considered.

With respect to the intrinsic ceiling of loss, another open question concerns the resonant-like features in the frequency dependence of Q (see $x = 0.19$ in Figure 2.8(a)). These features do not come from measurement noise: they are repeatable and do not appear to originate from the measurement setup.

Chapter 3

Hysteresis in vertical transport across SrTiO$_3$/Pt interfaces

3.1 Oxide-based resistive switching memories

The central topic of this Chapter[1] is the hysteretic nature of the DC current-voltage response in Schottky junctions between doped $SrTiO_3$ and high work function metals (such as Pt, Au, Ni, $SrRuO_3$). The context of these studies is in the applications of such structures as resistive switching memories and addressing the issues of their reliability and reproducibility.

The term resistive switching refers to voltage-induced modulation of the electrical resistance in a two-terminal device, such as a Schottky junction or a parallel-plate capacitor.

Figure 3.1 illustrates the practical manifestation of this effect, showing one cycle of switching between the high and the low resistance states (HRS and LRS, respectively). The initial (virgin) state of $SrTiO_3$-based Schottky junctions is generally equivalent to the HRS. Starting from that point, the ramping of voltage to positive values generates an exponential increase in current. Beyond a certain threshold voltage, the two terminal-resistance is decreased in a non-volatile manner (switching to LRS). This is manifested in the appearance of hysteresis upon ramping the voltage back down to $V = 0$. Comparison of resistances in the $V = 0$ limit for the HRS and LRS reveals a difference of several orders mag-

---

[1]The results discussed in this Chapter have been previously published in [55], [105].

nitude. This effect can be reversed by applying a voltage of opposite polarity: the negative voltage cycle in Figure 3.1 brings the junction back to the HRS.

Resistive switching devices are of interest for memory applications, where one seeks to use the HRS and LRS as the distinct memory states [106]–[113]. One clear advantage of this concept is the simplicity of the corresponding device. A two terminal junction or capacitor can be downscaled to very small lateral dimensions in comparison to three terminal devices such as transistors. One particularly exciting concept is the possibility of assembling resistive switching devices into "crossbar" arrays, which have the potential to offer unprecedented
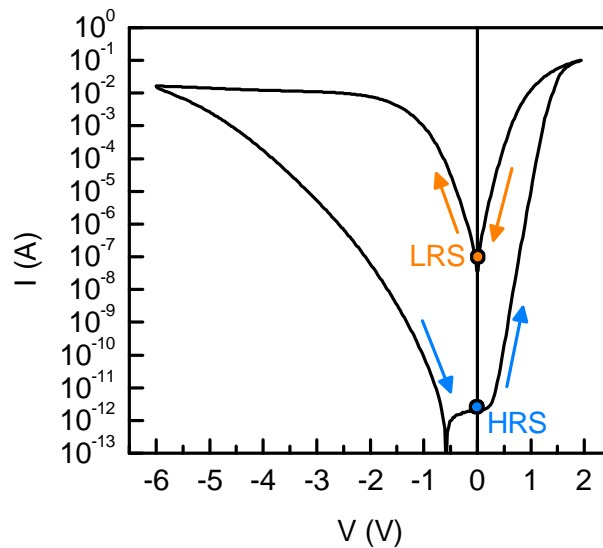
Figure 3.1. Example of DC current-voltage (I-V) hysteresis in a doped SrTiO$_3$/Pt junction

58

lateral integration density [109], [114]–[116].

A second exciting aspect of the resistive switching memory is its non-binary, continuously tunable nature. A typical switching event is not discrete, but continuous. By adjusting the parameters of the switching voltage cycle (shape, amplitude, ramp speed, etc), an arbitrary resistance state can be obtained [117]–
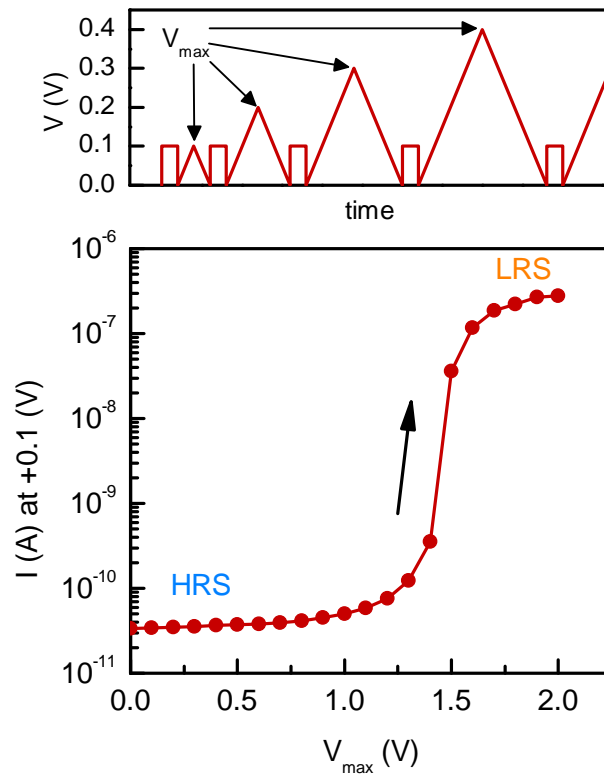
Figure 3.2. Progressive switching of a SrTiO$_3$/Pt junction from the HRS to the LRS. Top: applied pulse shape. Bottom: small signal current versus switching pulse amplitude. Reprinted from [105], licensed under CC BY 3.0.

[119]. This is illustrated in Figure 3.2, where a progressive switching cycle is applied to a typical SrTiO$_3$-based Schottky junction. Rectangular read pulses (+0.1 V) are alternated with triangular switching cycles with increasingly high maximum voltage V_{max}. The plot shows small signal current read out against V_{max}, demonstrating the progressive nature of resistive switching. For small V_{max}, the magnitude of the effect is negligible. Near a threshold of $V_{max} \approx 1$ (V) the read out current progressively increases, which corresponds to switching towards the LRS.

The possibility of continuously (and reversibly) tuning the resistance states of a two-terminal device can enable its use as a multi-state memory. This implies a new computing architecture that is radically different from the standard boolean logic (on/off states as "1" and "0") and instead uses the full spectrum of intermediate logic states between "1" and "0". Such alternative computation techniques have the potential to be much more efficient for certain complex tasks. Pattern recognition and classification is one such example [111], [120], [121].

The physical mechanisms behind resistive switching effects are a contested issue. It is largely recognized to be a structural defect-driven phenomenon [106], [108], [122], [123], as suggested by the numerous observations of very robust resistive switching hysteresis in polycrystalline and amorphous thin film

systems with high point and/or extended defect densities, see e.g. [124]–[126].

One common distinction in terms of mechanism is between **interface-based** and **filamentary** switching. It is generally recognized [107] that the switching effects in Schottky junctions between doped single crystal oxides and conventional or oxide metals are **interface-based**. The most heavily studied type of system is the interface between electron-doped $SrTiO_3$ and high work function metals, such as Pt [117], [127]–[143], Au [129], [144]–[149], Ni [129], [150], $SrRuO_3$ [151], [152] and $YBa_2Cu_3O_{6+x}$ [153]. Interfaces between p-type doped manganites and low workfunction metals also show resistive switching [107], [154]–[156]. In such cases, the electrical modulation of the two-terminal resistance is thought to be driven by a reversible and laterally uniform modification of the entire interface [107]. Interface-type switching is usually of bipolar type, as described in Figure 3.1: the polarity of the voltage determines whether the resistance is increased towards the HRS or lowered towards the LRS.

In contrast, the **filamentary** switching mechanism implies voltage-induced formation of a conductive short circuit through the resistive switching device, which often results in very sharp transitions between the HRS and LRS [107]. This generally requires an initial "electroforming" step, where application of a large voltage induces partial dielectric breakdown and creation of one or several conductive filaments [107], [109]. These filaments can then be reversibly ma-

nipulated with smaller voltages, pinching off and recreating the short-circuit. This type of switching is commonly found in polycrystalline and amorphous metal/oxide/metal stacks, usually involving simple binary oxides such as TiO_x [157], [158] and NiO_x [158], [159].

Filamentary switching is often unipolar: the direction of resistance change is determined by voltage magnitude, rather than polarity. Each voltage polarity has two distinct thresholds: SET and RESET. At the SET voltage, the device abruptly switches to the LRS (short-circuit creation). At the RESET voltage, it goes back to the HRS (short-circuit disruption). While such unipolar systems can also generally be quite unambiguously classified as filamentary, some bipolar switching cases are debated to be either filamentary or interface-based, see e.g. [113], [118], [124], [125].

Beyond this generally accepted distinction between the two macroscopic mechanism types, the microscopic mechanisms are unclear in both cases. Prominent proposed mechanisms include:

- **Charge trapping**, which refers to capture of a fraction of the electrical current flowing through a junction or a capacitor. This is a well-documented phenomenon in the context of gate dielectric technology [160]–[162]. In a Schottky junction, the build up of this charge will alter the electrostatic

potential distribution and band bending near the interface, which directly translates into transport characteristics (see Chapter 1.3).

- **Electromigration of oxygen vacancies**, referring to voltage-induced vertical drift towards/away from the interface or lateral segregation into filaments [108], [113], [122].

- **Electrodiffusion of the electrode metal**. This mechanism is particularly relevant for several very particular parallel plate capacitor systems where the electrode metal (usually Ag) is highly soluble in the insulator material. Voltage-induced diffusion of the electrode metal into the insulator enables reversible formation of conductive filaments. Such Ag-based filaments have been extensively documented using both electron and optical microscopy [108], [122], [163]–[165].

- **Local valence state change**, often speculated to be linked to oxygen vacancy migration, has been proposed as a microscopic mechanism for the formation of conductive filaments in several oxide systems with resistive switching, notably TiO_x and $SrTiO_3$ [108], [123], [166].

- **Ferroelectric polarization switching** is a separate mechanism that is applicable to device structures involving ferroelectrics, such as $BaTiO_3$ or $Pb(Zr,Ti)O_3$. A voltage-induced reversal of polarization can distort the

band profile of a Schottky barrier, thus modulating vertical transport in a capacitor or a Schottky junction [167]–[169].

The current major roadblock for resistive switching memory technology is directly related to this lack of understanding of the microscopic mechanisms: it is currently very difficult to fabricate such devices in a uniform and reproducible manner. Existing recipes for device processing yield functioning devices, but suffer from very low yield and large statistical scatter in switching parameters [107], [109], [113], [116]. This is particularly true for the case of resistive switching requiring initialization by electroforming steps [109], [116].

The studies presented in this Chapter aim to address the reproducibility and variability problems by studying the influence of material quality on the resistive switching phenomena. By using MBE growth of oxides and epitaxial sputtering of Pt metal contacts, idealized device stacks are constructed aiming to unambiguously tune the structural parameters responsible for the switching effects. Such explicit control is a key first step towards stabilizing a resistive switching memory processing route that is repeatable and reproducible.

3.2 The importance of oxide/metal interface quality

This Chapter presents a study on the role oxide/metal interface quality in resistive switching at the doped $SrTiO_3$/Pt Schottky junction. The study uses commercial Nb:$SrTiO_3$ single crystals with 0.7 wt % Nb doping, which corresponds to an electron density $N_D = 10^{20}$ cm^{-3}. This choice was made to ensure uniform doping levels and $SrTiO_3$ quality across the sample series.

The tuned parameter was the Pt metalization quality. This was accomplished by modifying the growth parameters for Pt growth on Nb:$SrTiO_3$, as summarized in Table 3.1. The four studied samples were labeled "A", "B", "C" and "D" in order of decreasing metalization quality:

- Device "A" was grown using the standard method for epitaxial growth of Pt

Sample	A	B	C	D
Deposition method	DC Sputtering			E-beam evaporation
In-situ anneal	2h, 825 °C		5min, 120 °C	none
Growth temperature	825 °C		Room temperature	
Metal quality	Epitaxial Pt		Polycrystalline Pt	

Table 3.1. Differences in preparation of the studied Nb:$SrTiO_3$/Pt junctions

on $SrTiO_3$ described in Chapter 2.3. The 2 hour in-situ pre-growth anneal at a substrate temperature of 825 °C in a 10 mTorr O_2 atmosphere is necessary in order to clean the $Nb:SrTiO_3$ surface. It is immediately followed by the deposition of epitaxial (001)-oriented Pt at the same temperature of 825 °C.

- For the device "B", the same in-situ pregrowth anneal at 825 °C was kept, but it was followed by bringing the substrate back to room temperature for the Pt deposition. This aims at intentionally degrading the quality of the Pt metalization.

- For the case of device "C", the pre-growth anneal was done for a shorter time (5 minutes) and at a lower temperature (120 °C), thus reducing the effectiveness of the $SrTiO_3$ surface cleaning effect.

- Device "D" was grown using a different technique: e-beam evaporation, with no in-situ anneal. This growth technique is known to be highly energetic and damaging for the underlying thin films [170]. This was expected to yield the most disorder and structural damage and the least clean metal/oxide interface.

In all cases, the Pt thickness was close to 100 nm. The variations in Pt quality are illustrated in Figure 3.3, which shows the X-ray diffraction scans of the four

Nb:SrTiO$_3$/Pt junctions after the deposition and before device patterning. It confirms the epitaxial growth of Pt(001) in the case of sample "A". Samples "B", "C" and "D" show much weaker Pt(111) peaks, which is the commonly observed preferential orientation for Pt deposited at low temperatures [102], [171]. The much lower Pt peak intensity is consistent with a degraded crystal quality.

X-ray diffraction gives information about the structural quality of the Pt bulk. It is, however, only an indirect measurement of the quality of the Nb:SrTiO$_3$/Pt interface, which is arguably the more important aspect in the context of resistive switching. A secondary ion mass spectrometry (SIMS) measurement can
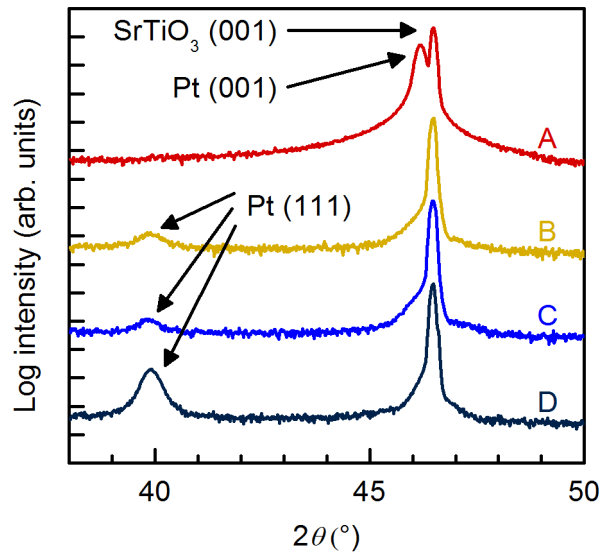
Figure 3.3. XRD spectra for SrTiO$_3$/Pt samples "A"-"D" with different structural quality. Reprinted from [105], licensed under CC BY 3.0.

give information about the interface quality, in particular about the levels of contamination (the author would like to acknowledge Tom Mates for assistance with the measurement and analysis). This technique uses an ion beam to sputter the surface of a sample and uses a mass spectrometer to analyze the ejected secondary ions. A measurement of intensity of secondary emission of a certain
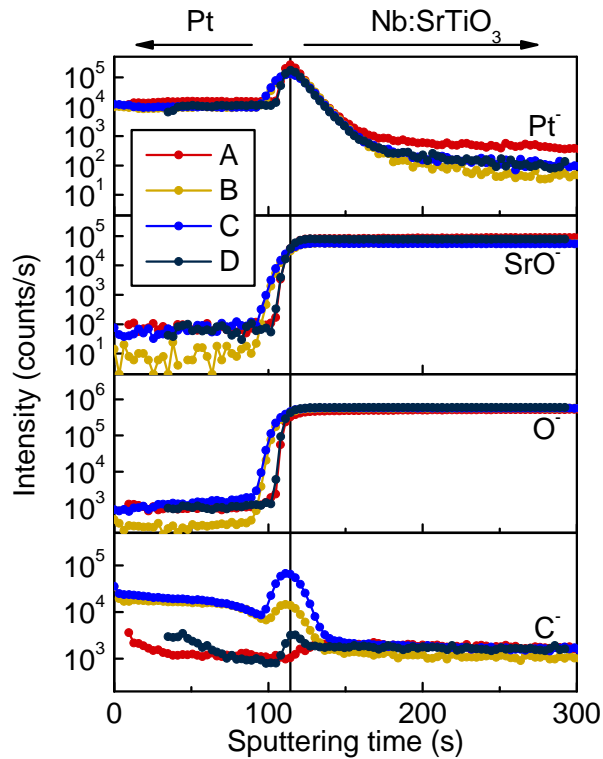
Figure 3.4. SIMS depth profiles of Pt^-, SrO^-, O^- and C^- for all $SrTiO_3$/Pt samples, highlighting the absence the of a carbon peak at the oxide/metal interface for the highest quality sample "A". Reprinted from [105], licensed under CC BY 3.0.

ion mass as a function of time is equivalent to probing its thickness profile, as the ion beam progressively digs deeper into the film. Figure 3.4 shows thickness profiles of several relevant secondary ions (Pt^-, SrO^-, O^-, C^-) for all samples ("A"-"D"). SrO^- and O^- intensities show an expected sharp increase at the $Nb:SrTiO_3/Pt$ interface. Pt^- has an increased intensity at the interface, most likely related to an increased ionization yield of Pt^- in the presence of oxygen sputtered from the oxide substrate. These three emissions are largely equivalent across all samples. This is not the case for the carbon emission: polycristalline samples "B", "C" and "D" show a detectable C^- peak at the interface, which is absent for the epitaxial sample "A". This indicates suppression of unintentional contamination with hydrocarbons in the case of high temperature growth with an in-situ pre-growth anneal. This is consistent with the known tendency of oxide surfaces (including $SrTiO_3$) to chemiosorb carbon-hydroxyl groups upon exposure to air. Their removal requires high temperatures and/or oxygen containing atmospheres [172]–[174].

Prior to further processing, these samples were annealed at 800 °C in flowing O_2. The goal of this ex-situ post deposition anneal was to eliminate oxygen vacancies that might form in $Nb:SrTiO_3$ during Pt growth. The uniformity of this final annealing across the entire sample treatment removes the possibility of variability due to uncontrolled concentrations of oxygen vacancies. Blanket

Pt on Nb:SrTiO$_3$ was then patterned into Schottky contacts of different sizes (illustrated in Figure 3.5(a)). The data presented below is for 30x30 μm^2 squares. The pattern was defined by standard photolithography combined with selective oxidation of the Pt surface with a 100 W plasma in 300 mTorr O$_2$ at room temperature. The oxidized Pt surface was used as a hard mask for selective wet etching of Pt in Aqua Regia heated to 60 °C [175]. This etch removes Pt until the Nb:SrTiO$_3$ substrate is exposed, except for areas with an oxidized Pt surface, which form the contact pads. Ohmic contacts were formed by e-beam evaporation of Al/Ni/Au on the Nb:SrTiO$_3$ substrate.

Figure 3.5(b) shows the $I - V$ characteristics for all samples. Device "D" shows a very large resistive switching hysteresis, with an on/off ratio between the HRS and LRS that exceeds five orders of magnitude. This is similar to many other experiments on SrTiO$_3$-based Schottky junctions (see e.g. [129], [149], [152]). However, as the quality of the metalization is increased (samples "C", "B" and "A"), the hysteresis progressively shrinks. For the fully epitaxial junction "A", it is almost completely suppressed. As described above, this progression from very large to nearly suppressed resistive switching is driven entirely by modification of structural quality of the Pt metalization and of the Nb:SrTiO$_3$/Pt interface.

The mechanism of the switching effect can be described in terms of standard
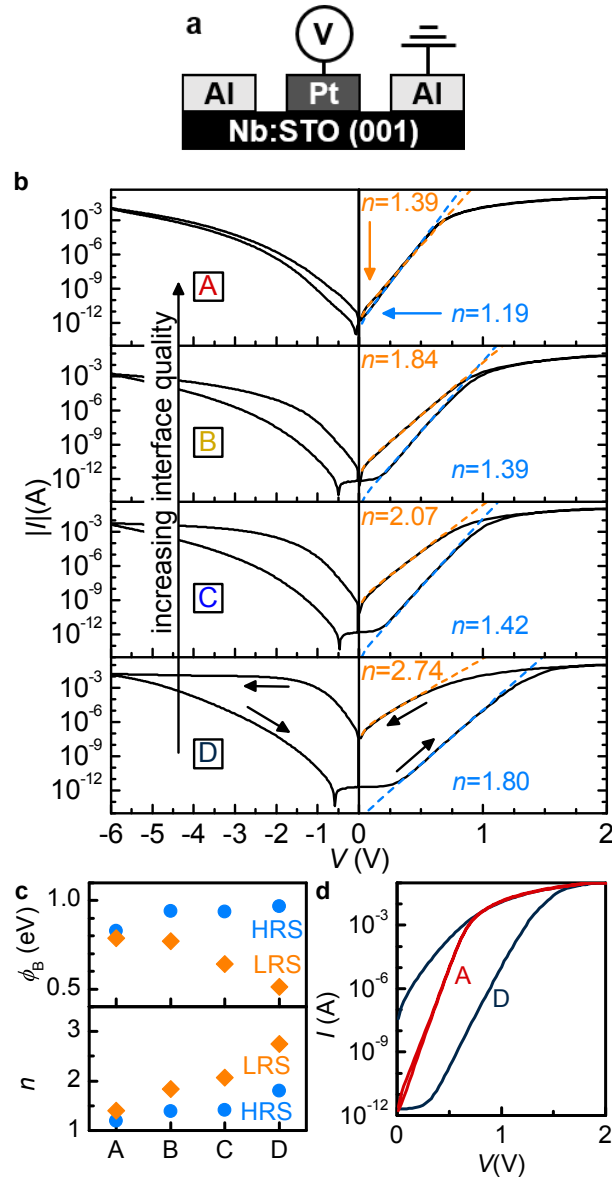
Figure 3.5. (a) Device schematic, (b) DC *I-V* characteristics for all samples, blue and orange line are fits to thermionic emission (Equation 1.12) for the HRS and LRS, (c) corresponding barrier height and ideality factors, (d) comparison of forward bias current in samples "A" and "D". Reprinted from [105], licensed under CC BY 3.0.

thermionic emission. Dashed lines in Figure 3.5(b) in the forward bias region correspond to fits to Equation 1.12, with the fitting parameters being the Schottky barrier height ϕ_B and the ideality factor n. The blue and orange correspond to fits in the HRS and LRS states, respectively.

Figure 3.5(c) shows the extracted ϕ_B and n. It highlights that switching from the HRS to LRS is accomplished by the lowering of the barrier height, which points to an interface-based mechanism. The trend of the suppression of switching in high quality devices is also clear in the evolution of the ϕ_B parameter, as its modulation between the HRS and LRS shrinks similarly to the $I - V$ hysteresis.

Another relevant trend is in the ideality factor as a function of device quality. For the epitaxial junction "A", $n = 1.19$ in the HRS, which is close to the ideal value $n = 1$. This is particularly remarkable in comparison with the previous reports on SrTiO$_3$-based Schottky junctions, where ideality factors are typically above 1.4 and often close to $n = 2$, similar to junctions "B", "C", and "D" in this study [129], [152]. The lowest reported value was $n = 1.14$ for an Nb:SrTiO$_3$/Au that was ozone cleaned in-situ with the metal deposition [176]. This was, however, for much lower Nb doping ($N_D = 10^{18}$ cm^{-3}). Ideality factors tend to increase significantly at higher doping [35], [152], [177] due to smaller depletion widths (see Equation 1.24).

With respect to the physical origin of increased n in low quality junctions, one can exclude the possibility of it being related to electron tunneling through the barrier: by comparing the HRS of junctions "A" in "D" in Figure 3.5(d), it is clear that the increased n in "D" is associated with decreased forward current. A tunneling mechanism would be associated with increased forward current.

A more appropriate description for this trend is given by the framework of insulating interface layers, as described in detail in Chapter 1.3.2. In our case, the interface layers are associated with a combination of unintentional contamination and growth-induced damage at the $SrTiO_3$/Pt interface. The contribution of carbon contamination was documented in the SIMS experiment in figure 3.4. A contribution from growth damage is suggested by the large ideality factor of sample D, where the SIMS carbon peak at the interface is relatively small, but the deposition energetics are expected to be high [170]. It is possible that there is also an intrinsic contribution to the interface layer arising from surface reconstruction [178].

Following Equation 1.24, the relation between the ideality factor and the capacitances of the depletion width (C_D) and the interface layer (C_i) can be written as:

$$n = 1 + \frac{C_d}{C_i} = 1 + \frac{\delta}{W_D} \cdot \frac{\varepsilon_r}{\varepsilon_i} \tag{3.1}$$

In the approximation of C_D being constant across the "A"-"D" series, higher n corresponds to lower C_i, which can be a combination of larger interface layer thickness δ and its dielectric constant ε_i being lower. It is quite intuitive to ascribe high n in low quality junctions to thicker unintentional interface layer thickness as a combined consequence of higher hydrocarbon contamination and more severe Pt growth-induced damage and disorder.

It is, however, quite possible that ε_i has a larger value in high quality samples. The ratio $\varepsilon_r/\varepsilon_i$ is expected to be particularly high when $SrTiO_3$ is used as a semiconductor, given its very high $\varepsilon_r \approx 350$ in bulk. Unintentional interface layers are likely to be equivalent to very defective/contaminated $SrTiO_3$ (structural defects tend to severely decrease ε) or to a binary oxide with a high-K dielectric-like dielectric constant of 10-25. High metalization quality can result in an interface layer that is more $SrTiO_3$-like and thus has a higher ε_i. Dielectric response in the titanates is known to be highly sensitive to point defect levels and residual stresses [179], [180]. Furthermore, it should be noted that high $\varepsilon_r/\varepsilon_i$ ratios explain the very high ideality factors usually observed in $SrTiO_3$-based Schottky junctions [129], [152], in particular when compared to typical III-V and Si-based junctions (see e.g. [35]).

A more accurate quantification of these trends can be achieved by pairing the $I-V$ measurement with the $C-V$ characteristics, which allows the extraction

of the depletion width capacitance C_D. These measurements were performed in a ground-signal-ground geometry at a frequency of 1 MHz (before the high frequency series resistance roll-off). The DC voltage sweep orientation was from negative to positive, consequently the measured junction state is equivalent to the HRS in Figure 3.5. Its voltage dependence is plotted in Figure 3.6 as $C^{-2} - V$ for comparison with Equations 1.30 and 1.34.

Equation 1.30 is the simpler model that assumes a field-independent dielec-
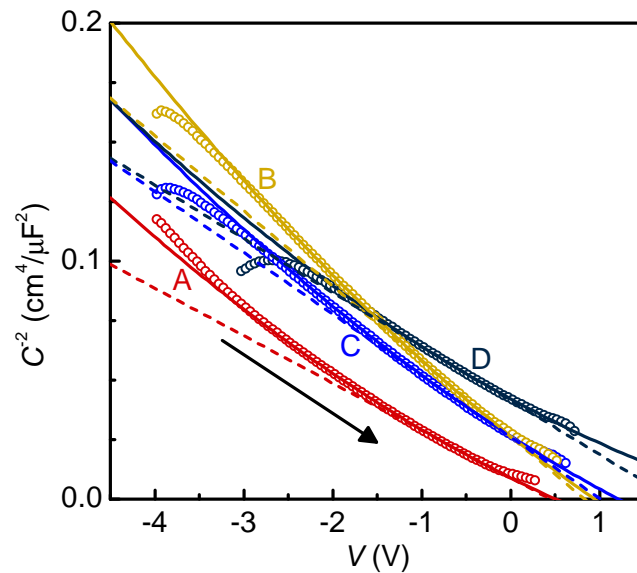
Figure 3.6. Capacitance-voltage characteristics for all samples in the HRS at 1 MHz. Dashed and solid lines are fits to Equations 1.30 and 1.34 (constant and field-dependent ε_r, respectively). Reprinted from [105], licensed under CC BY 3.0.

tric response in SrTiO$_3$. It accounts for the presence of an interface layer and the resulting partitioning of applied bias between C_d and C_i by including the ideality factor n. For the purpose of this fit, the values of n were taken from the DC measurement in the HRS in Figure 3.5. These fits are shown as dashed lines in Figure 3.6, with the adjustable parameters being ε_r and V_{bi}.

The extracted values are shown in Table 3.2, along with the corresponding depletion width thickness W_D at zero bias. This table reflects a clear trend of smaller V_{bi} and shorter depletion widths in higher quality junctions. This can also be seen through visual inspection of the data in Figure 3.6: device "A" clearly has a much smaller voltage intercept, which corresponds to V_{bi}, than device "D". The applicability of this linear model is questionable, however, as

Sample	Linear $\varepsilon_r(E)$ model		
	ε_r	V_{bi} (eV)	W_D (nm)
A	80.4	0.4	5.9
B	59.0	0.63	6.4
C	73.8	0.74	7.7
D	106.6	1.04	11.0

Table 3.2. Summary of dielectric properties extracted from C-V data in Figure 3.6, using the linear dielectric response model and Equation 1.30.

76

the experimental data shows clear deviations from linearity as one expects in the case of a field-dependent ε_r.

The more accurate model of Equation 1.34 requires a quantitative description of the $\varepsilon_r(E)$ dependence. We adopt the procedure from references [15], [16], which use the common phenomenological assumption that this dependence is quadratic:

$$\varepsilon_r^{-2}(E) = \varepsilon_r^{-2}(E=0) + \left(\frac{E}{b}\right)^2 \tag{3.2}$$
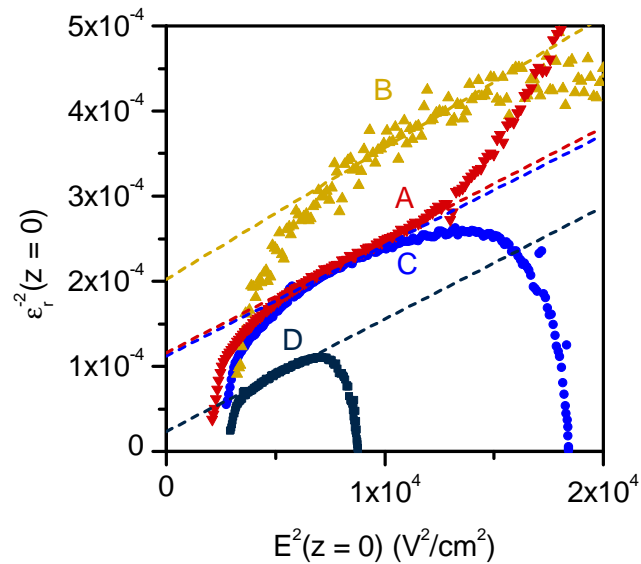
Figure 3.7. Scaling of dielectric constant with field at the interface ($z = 0$), extracted using Equations 3.3 and 3.4 and data in Figure 3.6. Dashed lines are the quadratic scaling from Equation 3.2. Reprinted from [105], licensed under CC BY 3.0.

This non-linearity of $\varepsilon_r(E)$ modifies the spatial distribution of the electric field as a function of distance from the interface (z). The voltage dependence of capacitance can be connected to the boundary condition: the value of ε_r and E at the metal/SrTiO$_3$ interface ($z = 0$):

$$E(z = 0) = -\frac{eN_D}{nC} \tag{3.3}$$

$$\varepsilon_r(z = 0) = -\frac{\partial C^{-2}}{\partial V}\frac{2n}{eN_D} \tag{3.4}$$

Using these two relations, one can reconstruct a $\varepsilon_r(z = 0)$ vs $E(z = 0)$ curve, using a locus of capacitance points at different voltages, as shown in Figure 3.7. The dashed lines are fits to Equation 3.2, giving the values for b and $\varepsilon_r(E = 0)$ shown in Table 3.3. The chosen fitting ranges corresponds to voltages with low leakage in proximity of zero bias.

Using these descriptive parameters for the dielectric non-linearity, one can use Equation 1.34 to fit the $C^{-2} - V$ data in Figure 3.6 (solid lines). The only remaining adjustable parameter is V_{bi} (Table 3.3). The ideality factors n from the DC measurement in the HRS were used. This model offers a significant improvement in terms of describing the deviation from linearity in the $C^{-2} - V$ plot.

It is important to emphasize that a key ingredient of this description is the ideality factor n extracted from the DC $I - V$ measurement. Its relevance for the

model of the $C - V$ response is in accounting for the redistribution of applied voltage between the depletion width ($V_d = V/n$) and the interface layer ($V_i = V \cdot (1 - n^{-1})$). The smaller n for junction "A" results in a higher proportion of V being dropped across the depletion width, which results in a higher tuning of ε_r. This can also be seen qualitatively in Figure 3.6 as the larger positive curvature of $C^{-2} - V$ for higher quality junctions. The quantitative correspondence between the ideality factors in the DC and AC measurements is strong evidence to justify the framework of insulating interface layers in the case of SrTiO$_3$/metal Schottky junctions.

Another outcome of the above modeling of $C - V$ data is the possibility of quantifying the interface layer capacitance using Equation 3.1. The results are

Sample	b (V/cm)	$\varepsilon_r(E = 0)$	V_{bi} (eV)	W_D (nm)
		Non-linear $\varepsilon_r(E)$ model		
A	2.75·10^5	92.9	0.45	6.6
B	2.77·10^5	70.3	0.71	7.1
C	2.54·10^5	94.4	0.88	9.2
D	2.75·10^5	206.4	1.51	17.1

Table 3.3. Summary of dielectric properties extracted from C-V data in Figure 3.6, using the non-linear dielectric response model and Equation 1.34.

shown in Table 3.4. The raw outcome of inserting the values of n from the DC measurement in the HRS and W_D from Table 3.3 is $\delta \cdot (\varepsilon_r/\varepsilon_i)$, the interface layer thickness weighted by the ratio of dielectric constants. Given the expectation that $\varepsilon_r > \varepsilon_i$, this value overestimates the actual physical interface layer thickness.

Assuming the value of ε_r from Table 3.2, the weighted thickness can be converted into interface layer capacitance. It is shown in Table 3.4 as δ/ε_i (in nm) and C_i (in μF/cm^2). There is a clear trend for higher interface capacitance in high quality junctions, as expected for thinner interface layers with higher ε_i. While it is not possible to definitively decouple δ and ε_i, Table 3.4 includes the values of δ calculated for two realistic assumptions of $\varepsilon_i = 10$ and 25. This

Sample	$\delta \cdot (\varepsilon_r/\varepsilon_i)$	δ/ε_i	C_i	$\delta(\varepsilon_i = 10)$	$\delta(\varepsilon_i = 25)$
	(nm)	(nm)	(μF/cm^2)	(nm)	(nm)
A	1.3	0.016	55.8	0.16	0.40
B	2.8	0.047	18.9	0.47	1.17
C	3.8	0.052	17.1	0.52	1.30
D	13.6	0.13	6.9	1.28	3.20

Table 3.4. Summary of unintentional interface layer properties extracted from the combined C-V and I-V data for all samples.

corresponds to typical interface layers that are several atomic layers thick.

The above discussion of interface layer capacitance focused on the HRS, which is equivalent to the initial as grown state of the device. It is thus representative of the trends with structural quality of the samples "A"-"D". We now turn to the discussion of the relevance of this interface capacitance for the band structure of the Schottky junction. The goal of this discussion will be to clarify the connection between the interface layers and the HRS - LRS switching effect. There is a clear correlation between these two concepts, as shown in the plot of δ/ε_i versus on/off ratio in Figure 3.8(a).

The presence of an interface capacitance changes the electrostatics of a Schottky junctions, as the voltage drop Δ across this layer modifies the Schottky barrier:

$$\phi_B = \phi_M - \chi_{STO} - \Delta \tag{3.5}$$

This is also illustrated in Figure 3.8(b). Even in the absence of applied bias, a non-zero voltage Δ appears in presence of static charge separation. One intrinsic source is the space charge in the depletion width ($Q_{SC} = qN_DW_D$). To satisfy charge neutrality, it is compensated by Q_M, the projected charge on the metal plate. The resulting profiles of charge density, electric field and band energy levels are illustrated in Figure 3.8(b) (black lines).
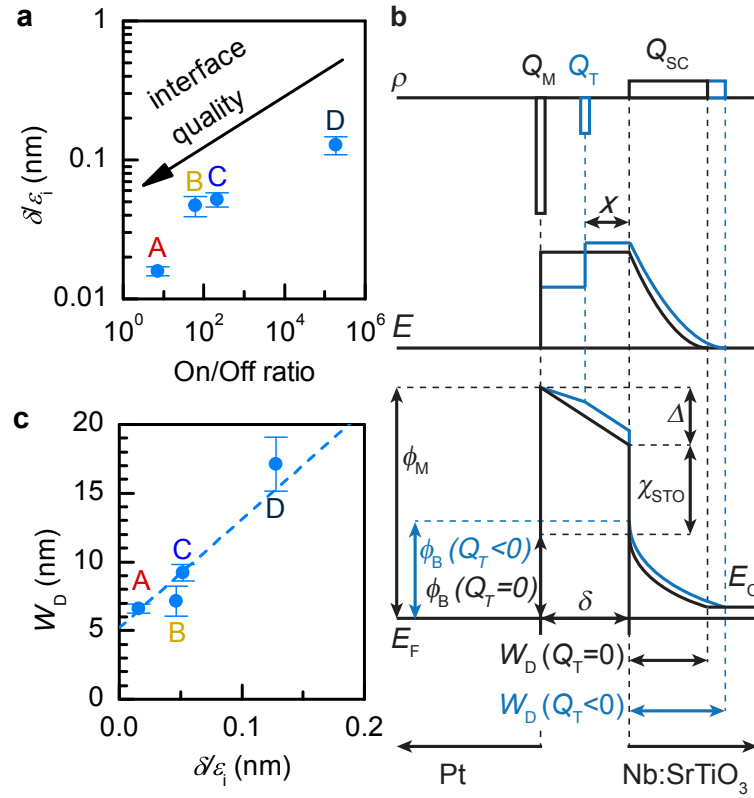
Figure 3.8. (a) Correlation between unintentional interface layer capacitance and the magnitude of the resistive switching effect. (b) charge density, electric field and band profile at the Nb:SrTiO$_3$ interface. Blue curves illustrate the effect of a negative trapped charge within the interface layer. (c) Correlation between the depletion width at zero bias and the interface layer capacitance. Reprinted from [105], licensed under CC BY 3.0.

82

The second type of contribution to Δ is extrinsic trapped charge. Blue lines in Figure 3.8(b) illustrate the influence of a negative trapped charge centroid Q_T placed at a distance x from Nb:SrTiO$_3$. The degree to which Q_T affects the electric field and band profiles is sensitive to its placement. Mathematically, this can be expressed as:

$$\Delta = \frac{\delta}{\varepsilon_i \varepsilon_0} \cdot q N_D W_D + \frac{\delta - x}{\varepsilon_i \varepsilon_0} \cdot Q_T \tag{3.6}$$

In equations 3.5 and 3.6, three out of four terms are known: $\phi_M = 5.65$ (eV) [181], $\chi_{STO} = 3.9$ (eV) [182], ϕ_B has been extracted from the DC $I-V$ measurement, δ/ε_i and W_D have been quantified in the above C_V analysis. This allows the extraction of the total voltage projected by the trapped charge: $(\delta - x)/\varepsilon_i \cdot Q_T$. This is illustrated in Figure 3.9(a), which shows the respective contributions of each term in Equations 3.5 and 3.6 for the HRS state of all samples. $\phi_M - \chi_{STO} =$ 1.75 (eV) is a constant quantity. The space charge in the depletion width projects a positive contribution to Δ, which is increased for low quality junctions owing to their larger W_D (see Figure 3.8(c)).

The balance of the above contributions corresponds to trapped charges. The sign of this last contribution is not the same across the series: it is positive for samples "A" and "B", while it is negative for samples "C" and "D" (see the red bars in Figure 3.9(a)). This sign crossover implies superposition of two separate
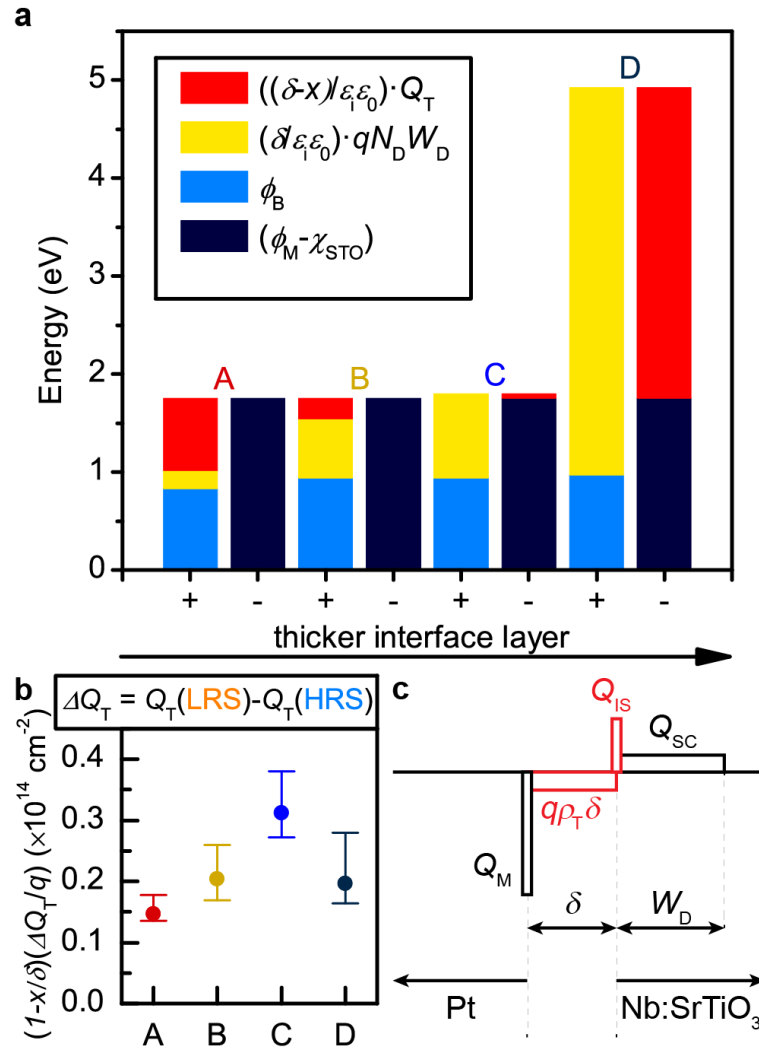
Figure 3.9. (a) Summary of positive and negative contributions in Equations 3.5 and 3.6 for all junctions in the HRS. (b) Modulation of the trapped charge centroid corresponding to the resistive switching effects observed in Figure 3.5. (c) Simplified trapped charge profile implied by the crossover in the sign of the trapped charge centroid in (a). Reprinted from [105], licensed under CC BY 3.0.

contributions with opposite signs that are lumped together as an effective charge centroid in the above calculation. Figure 3.9(c) illustrates the simplest trapped charge profile that can produce this situation: positive trapped charge Q_{is} in the interface states combined with ρ_T, a volume density of negative trapped charge in the interface layer. The positive sign of Q_{is} is expected for highly doped SrTiO$_3$ [182], [183]. Assuming that the volume trapped charge density ρ_T is approximately uniform across the interface layer, the total corresponding charge is $q\rho_T\delta$, i.e. it is proportional to interface layer thickness. The progressive increase in δ between samples "A" and "D" adds more negative trapped charge, which eventually overtakes the positive Q_{is} as the larger contribution.

While the actual profile of trapped charge is likely to be more complex, its effective contribution to the electrostatics of the Schottky junction will be accurately captured by the effective centroid Q_T in Equation 3.6.

From the analysis above, it is clear that the trapped charge Q_T can have a direct impact on Schottky junction parameters. In the context of resistive switching between the HRS and LRS, the very high applied voltages necessary for this effect to occur can be reasonably expected to modify the trapped charge profile. If one assumes that the lowering of the barrier height in the LRS ($\Delta\phi_B = \phi_B(\text{LRS}) - \phi_B(\text{HRS})$) is entirely driven by a change in trapped charge density

85

$(\Delta Q_T = Q_T(\text{LRS}) - Q_T(\text{HRS}))$, then from Equations 3.5 and 3.6:

$$\Delta\phi_B = \frac{\delta - x}{\varepsilon_i \varepsilon_0} \cdot \Delta Q_T \tag{3.7}$$

It is reasonable to assume that W_D is not altered upon HRS-LRS switching, as $C-V$ measurements in SrTiO$_3$/metal junctions show very little hysteresis [129], [138]. By multiplying the above Equation by the interface capacitance from Table 3.4, the experimental values of $\Delta\phi_B$ (between the HRS and LRS) from Figure 3.5(c) can be converted into a corresponding change in trapped charge. Figure 3.9(b) shows ΔQ_T multiplied by a dimensionless term $(1 - x/\delta)$ that accounts for the spatial positioning of the charge centroid within the interface layer.

The magnitude of $\Delta Q_T (1 - x/\delta)$ is approximately similar for all junctions. This is in stark contrast with the results shown in Figure 3.5, where the resistive switching effect is tuned from very large ("D") to small ("A"). The natural explanation is that the trend for $\Delta\phi_B$ versus SrTiO$_3$/Pt interface quality is driven entirely by the change in interface capacitance. If the role of trapped charge centroid positioning is neglected, Equation 3.7 becomes:

$$\Delta\phi_B \sim \frac{\delta}{\varepsilon_i \varepsilon_0} \cdot \Delta Q_T. \sim \Delta Q_T / C_i \tag{3.8}$$

This illustrates that the observed change in barrier height corresponds to a change in voltage projected by the trapped charge via the interface capaci-

tance. At this point it is important to re-emphasize that C_i in this context is not a quantity that is explicitly controlled in typical processing recipes for resistive switching devices. It is rather a product of contamination and Pt growth-induced damage and disorder. One can naturally expect a large statistical scatter for C_i, both between separate devices on the same sample and between different processing runs. Equation 3.8 illustrates that these statistical deviations will directly translate into the resistive switching magnitude. This is consistent with the ubiquitous observations of very poor statistical reproducibility of switching parameters [107], [109], [113], [116].

The possibility of growing epitaxial Pt metalization with very high C_i offers an interesting route towards fighting this statistical scatter. It is possible to replace unintentional and uncontrolled interface layers with intentionally placed insulating layers. The corresponding well-defined capacitance will dominate the poorly controlled C_i if the latter is large enough.

A final aspect of resistive switching in these Nb:SrTiO$_3$ junctions to be highlighted is the state retention, which will be shown to also be consistent with a charge trapping based picture of HRS - LRS switching. This is another common problem for resistive switching devices, in particular for the SrTiO$_3$-based systems [138], [143], [150], [153].As illustrated in Figure 3.10(a), the HRS is stable with time after the switching voltage pulse (t). In contrast, the small sig-

nal current in the LRS progressively decays back towards the HRS. In the limit of high t, it follows a power law: $I \sim t^\beta$. The normalized decay behavior shown in Figure 3.10(b) is similar for all samples, with $\beta \approx 0.35$ for "B", "C" and "D", and $\beta = 0.23$ for "A". This is consistent with the picture of switching presented above (similar ΔQ_T in all cases).

This power law dependence of small signal current on time is known as the Curie-von-Schweidler law [184]. It is typical for capacitive charging and it is
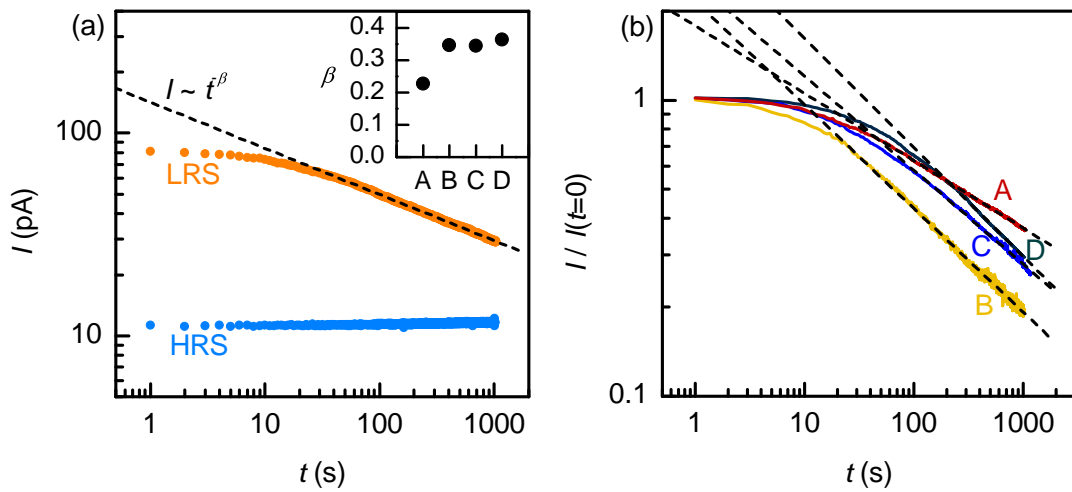
Figure 3.10. Dependence of the small signal current (measured at +0.1 V) on time after the HRS-LRS switching cycle. (a) HRS and LRS of the sample "A". The dashed line is a fit to a power law. The inset shows the corresponding exponents for all junctions. (b) Normalized LRS decay for all samples. Reprinted from [105], licensed under CC BY 3.0.

88

ubiquitously observed for charge trapping under bias in high-k dielectrics [160], [185]. This suggests a likely mechanism for the modification of the trapped charge profile (Figure 3.9(c)) upon switching from the HRS to LRS: high applied bias reduces the amount of negative trapped charge in the interface layer (ρ_T). The decay of the LRS towards HRS corresponds to progressive re-trapping of this negative charge under the built-in electric field (following the Curie-von-Schweidler law), bringing ρ_T to its original level. An alternative mechanism would involve an increase in the positive trapped charge in the interface states Q_{IS} upon switching to the LRS, with the power law decay corresponding to de-trapping of these charges.

3.3 Resistive switching based on defect-engineered interface layers

This Chapter presents an exploratory study on resistive switching based on intentional placement of structural defects in $SrTiO_3$. It combines epitaxial growth of Pt (to minimize the role of unintentional interface capacitance) and MBE growth of $SrTiO_3$ interlayers that are intentionally off-stoichiometric. These $SrTiO_3$ interlayers are inserted between the $Nb:SrTiO_3$ substrate and Pt, with the

goal of substituting them for the unintentional interface layers (based on contamination and disorder).

The rationale for this study is based on the above result that the magnitude of the resistive switching effect is governed by the amount of charge trapping and the interface layer capacitance. As summarized in Equation 3.8, the modulation of the Schottky barrier height between the HRS and LRS is $\Delta\phi_B \sim \Delta Q_T/C_i$. In a device with controlled and reproducible resistive switching, one needs to explicitly control both C_i and Q_T.

In the studied Nb:SrTiO$_3$/SrTiO$_3$/Pt stack, the MBE-grown SrTiO$_3$ interlayer aims to set both these quantities. Given the atomic layer level control over the layer thickness, its capacitance can be reproducibly defined. In order for it to be the dominant interface capacitance, one needs to minimize the unintentional contributions from the subsequent growth, which can be accomplished by using the epitaxial Pt contacts described in Chapter 3.2.

Reproducible control of Q_T involves introducing a well defined concentration of charge trapping centers. For it to be the dominant contribution to resistive switching, this concentration has to be large, and the levels for other defects need to be minimized. The route explored in this Chapter relies on intentionally introducing large Ti/Sr off-stoichiometry into the MBE-grown SrTiO$_3$ interlayer.

The details of the growth and structural characterization of $SrTiO_3$ interlayers can be found in Chapter 1.4. In particular, see Figure 1.5 for XRD, RHEED and RBS characterization of these films. Five different films were grown for this study. By adjusting the TTIP and Sr fluxes, their stoichiometry was tuned across a wide range from Sr-rich, to perfectly stoichiometric, to Ti-rich. Based on RBS measurements, their stoichiometry was Ti/Sr = 0.74, 0.82, 1.00, 1.43 and 1.74. All films are epitaxial and have well defined crystal structures, despite the very large deviations from ideal stoichiometry. Their thicknesses were between 20 and 30 nm.
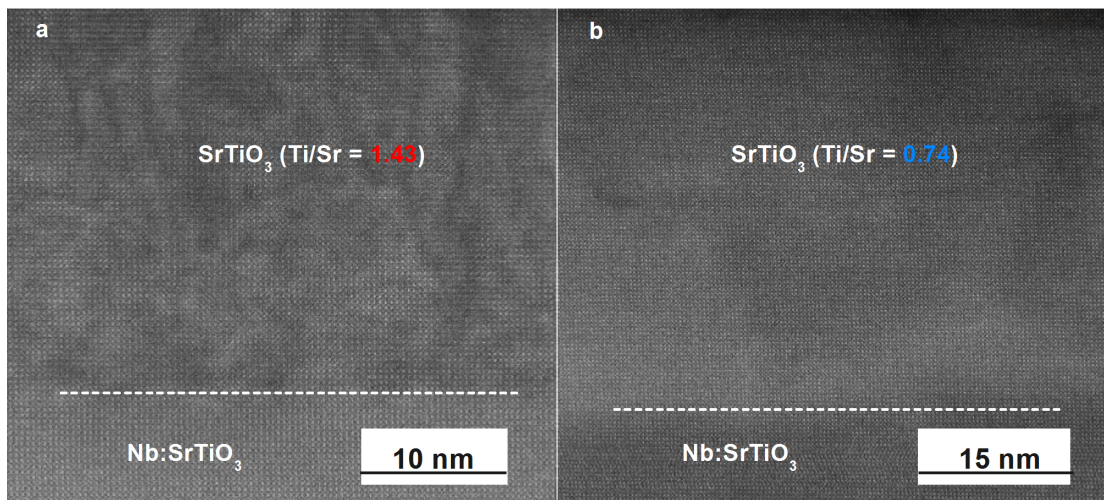
Figure 3.11. HAADF STEM cross-section images of (a) Ti-rich and (b) Sr-rich $SrTiO_3$ films on $Nb:SrTiO_3$ substrates. Reprinted from [55], licensed under CC BY 4.0.

Additionally, Figure 3.11 presents cross sectional high-angle annular dark-field (HAADF) scanning transmission electron microscopy (STEM) images for the highly non-stoichiometric samples (Ti/Sr = 1.43 and 0.74), courtesy of Jin-woo Hwang. For the Ti-rich interlayer, local changes in contrast indicate the presence of locally disordered regions. These are likely to be nanoscale amorphous inclusions accommodating the large Ti excess in the form of titanium oxide [48], [186], [187]. In the Sr-rich case, the film crystallinity was better preserved and no significant extended defects were detected. These observations are different from previous studies of Sr-rich SrTiO$_3$ films grown by solid-source MBE, PLD and sputtering [48], [56], [187], where Sr excess is accommodated by formation of planar Ruddlesden-Popper (RP) defects. This discrepancy is likely linked to the very high growth rates ($\approx$ 150 nm/hour) in the hybrid method of oxide MBE, which could kinetically limit the formation of RP-type planes. Another possibility is related to the high volatility of the TTIP precursor used to supply Ti, which may favor the formation of Ti vacancies. In both cases, the significant Sr excess appears to be accommodated by point defects, of which Ti vacancies are the most likely. The alternate candidate is the Sr interstitial, but this defect has a very high formation energy [188]. With the intent of the study being to isolate resistive switching based on a specific defect population, the Sr-rich interlayers are thus of particular interest in this context.

Two pieces of each sample were processed into Schottky junction devices using two different methods (ten devices in total). One piece was processed equivalently to junction "A" (see Table 3.1), using the epitaxial growth of Pt(001) to achieve a Nb:SrTiO$_3$/SrTiO$_3$/Pt(001) stack of the highest possible quality. A second piece of each sample was processed using standard e-beam evaporation for Pt deposition, which is equivalent to the lowest quality junction "D" in Table 3.1. In the following, this polycrystalline low quality metalization is referred to as Pt(PC). These devices were included in the study to illustrate the superposition of intentional (Ti/Sr off-stoichiometry) and unintentional (contamination, growth-induced damage and disorder) contributions to resistive switching.

Figure 3.12 shows the forward bias $I - V$ characteristics for the ten resulting devices. Horizontally, the panels are ordered according to the Ti/Sr stoichiometry of the SrTiO$_3$ interlayers. The top and bottom rows are for Pt(PC) and PT(001) metalization, respectively.

For the simplest case of Ti/Sr = 1.00, the behavior is consistent with the observations for the Nb:SrTiO$_3$/Pt junctions discussed in the previous Chapter. The Pt(PC)-based device has a very large $I - V$ hysteresis. Both the HRS and LRS can be described by standard thermionic emission (Equation 1.12), and the corresponding fits are shown as blue and orange dashed lines. The extracted values of ϕ_B and n are shown in Figure 3.13. For stoichiometric SrTiO$_3$ com-
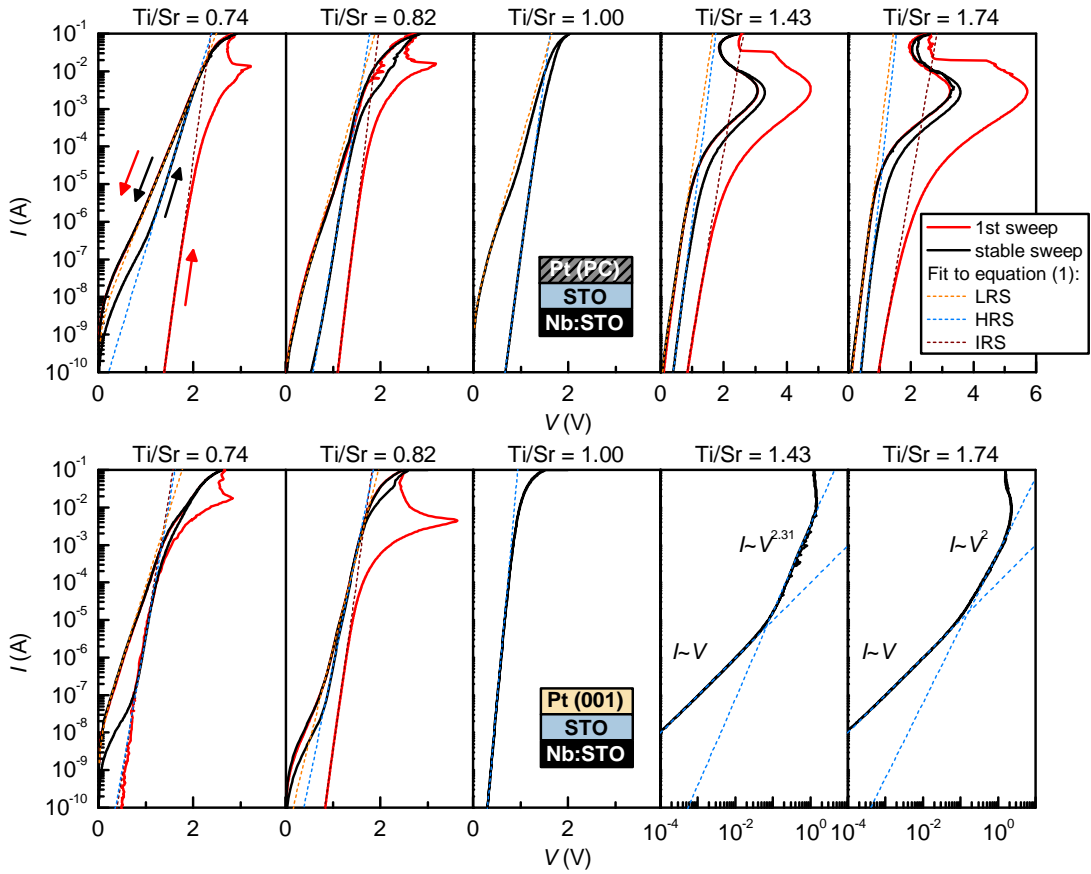
Figure 3.12. Hysteretic current-voltage characteristics of all Nb:SrTiO$_3$/SrTiO$_3$/Pt devices. The SrTiO$_3$ interlayer stoichiometry is tuned from Sr-rich (left) to Ti-rich (right). The top and bottom rows correspond to polycrystalline and epitaxial Pt metalization, respectively. Black curves are reversible HRS/LRS sweeps. Red curves are irreversible first steps, if present (IRS to LRS). Dashed lines are fits to thermionic emission (Equation 1.12). Reprinted from [55], licensed under CC BY 4.0.

94

bined with Pt(001) (highest quality junction), the resistive switching hysteresis is fully suppressed. For both these cases, ϕ_B and n are similar to the results shown in Figure 3.5. This is consistent with the mobile carriers spreading from Nb:SrTiO$_3$ into the undoped SrTiO$_3$ interlayer due to the absence of a conduction band offset. These samples are thus equivalent to the simple Nb:SrTiO$_3$/Pt Schottky junctions.

The resistive switching behavior is heavily altered upon introduction of off-
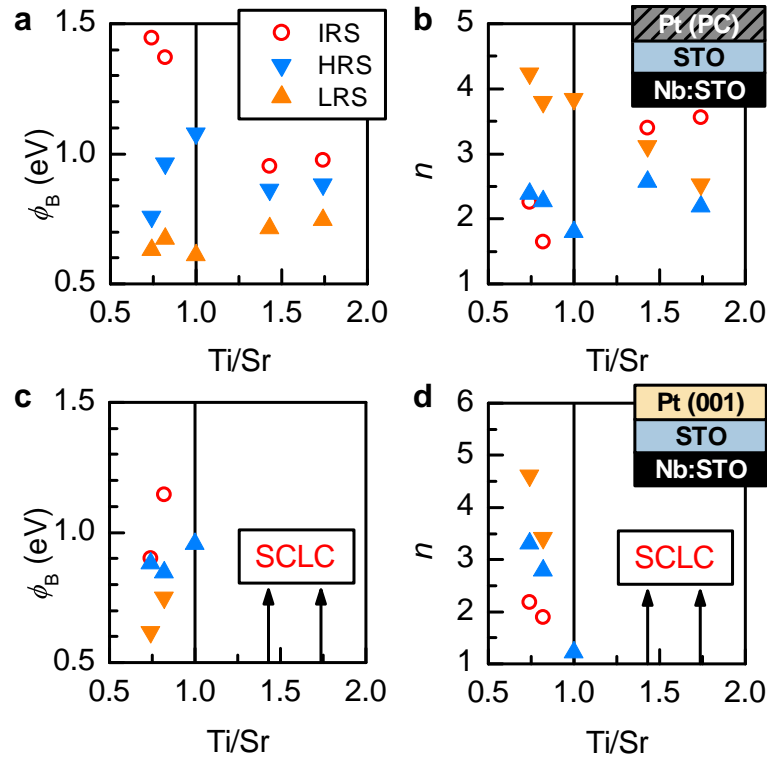
Figure 3.13. (a,c) Barrier heights and (b,d) ideality factors extracted from the data in Figure 3.12. Reprinted from [55], licensed under CC BY 4.0.

stoichiometry into the SrTiO$_3$ interlayers. For the case of the top row (Pt(PC)-based devices), both the Ti and Sr excess result in the appearance of an irreversible first step. This initial voltage cycle (red lines in Figure 3.12) switches the device from an initial resistance state (IRS) to the LRS. Subsequent voltage cycles are reversible, switching the devices between stable HRS and LRS. This irreversible first cycle is reminiscent of the "forming" steps necessary for resistive switching in many other parallel plate capacitor systems [109], [116]. Additionally, many of these off-stoichiometric devices show negative differential resistance (NDR) at high forward bias, particularly for the first IRS-LRS switching step.

Of particular interest is the bottom row in Figure 3.12, where the use of Pt(001) aims to isolate resistive switching effects based on intentional Ti/Sr off-stoichiometry. For the case of Ti excess (Ti/Sr = 1.43 and 1.74), resistive switching is suppressed and these junctions have very high leakage. By plotting this data on a log-log scale, the conduction mechanism can be identified as space charge limited conduction (SCLC). SCLC represents bulk-limited conduction and implies that the Schottky barrier was lowered to the point where it is no longer the dominant limiting step for the vertical current. The SCLC mechanism is generally signaled by the crossover between two power laws [189]: linear $I \sim V$ at low bias, and $I \sim V^2$ at high bias. This pattern is observed for Ti/Sr =

1.74. For Ti/Sr = 1.43, a slightly different power law is found at high voltage: $I \sim V^{2.31}$.

The most interesting case is the one of Pt(001) combined with Sr-rich $SrTiO_3$ interlayers (Ti/Sr = 0.74 and 0.82). The role of unintentional interface capacitance in these devices is minimized. Resistive switching here is thus expected to be dominated by the intentional Sr excess. As seen in Figure 3.12, a reduced but stable $I - V$ hysteresis is maintained. The character of this switching bears similarity with the Sr-rich devices with Pt(PC), including the irreversible IRS-LRS switching step and NDR at high voltage.

One subtle but potentially important aspect of transport in Sr-rich devices is the small forward bias regime, where a large excess current in comparison to the thermionic emission fit is seen. This low-V shoulder can be modeled using the same Equation 1.12, but with very large ideality factors ($n = 7-10$). Such excess current with high n is typical for the case of tunneling current (field emission process, see Equation 1.25 and [152]). Additionally, given the expected large intentional defect densities in the $SrTiO_3$ layers, this is likely to be defect state-assisted tunneling through the Schottky barrier [33]. It should also be noted that this feature again indicates an interface effect. It is not consistent with an ohmic conductive shunt behavior (see [190], [191]) that one would expect in the case of filamentary switching.

Figure 3.14 shows LRS retention characteristics for all devices that have a detectable $I - V$ hysteresis. For device based on Pt(PC), the normalized current follows a power law with time after switching: $I \sim t^{\beta}$. It is very similar to the previous observations for the Nb:SrTiO$_3$/Pt junctions, including the $\beta = 0.35$ exponent value for Ti/Sr = 1.00.

There is, however, an intriguing trend with off-stoichiometry: for both Ti and Sr-rich interlayers, the LRS decay is slowed down, with the power law exponent
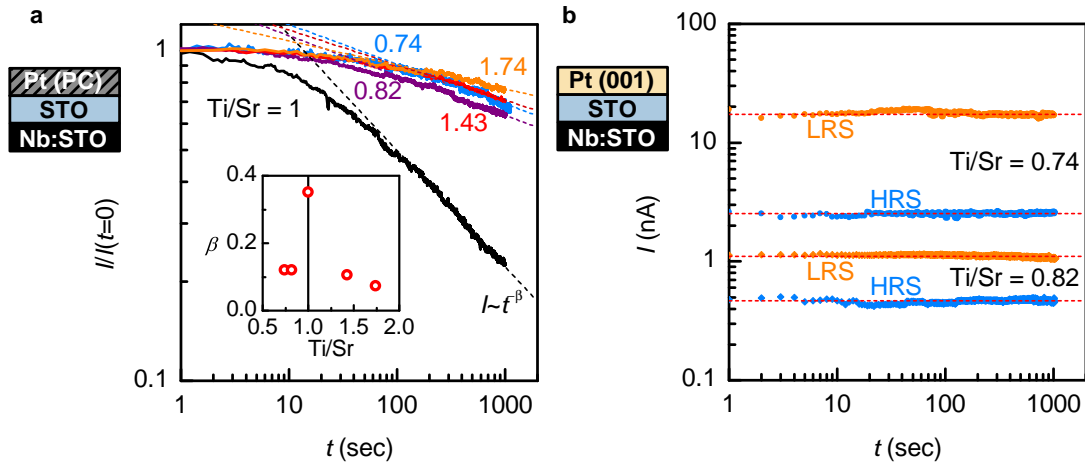
Figure 3.14. (a) Normalized time decay for the small-signal current in the LRS (at +0.1 V) for devices with Pt(PC). Dashed lines are power law fits. The corresponding exponents are shown in the inset. (b) State retention for both the HRS and LRS in Pt(001)-based devices with Sr-rich interlayers. Reprinted from [55], licensed under CC BY 4.0.

being reduced to $\beta \approx 0.1$. Moreover, in the case of Sr-rich devices with Pt(001) contacts, the LRS is stable with time within the noise level of the experiment (Figure 3.14(b)). This corresponds to an even further reduction of the decay exponent to $\beta \approx 0$.

The combined $I - V$ and LRS retention data in Figures 3.12 and 3.14 is consistent with an overlap of two distinct contributions to resistive switching. One corresponds to switching within the unintentional interface layers associated with Pt(PC). It produces a very large switching effect, and is characterized by a rapid time decay of the LRS with $\beta \approx 0.35$. The second type of contribution is related to Sr (or Ti) excess. The corresponding on/off ratio is considerably smaller, but it is much more stable with time. The most likely point defects associated with Sr excess are Ti vacancies, which are deep acceptors within the bandgap [188]. This would be consistent with a very long lifetime of trapped charge and thus improved state retention. The switching behavior of devices in the top row of Figure 3.12 is complicated by the mixing of both archetypes of switching, giving fairly large on/off ratios and an intermediate decay speed.

The above discussion highlights intentional control of defect levels as a route towards stabilizing controlled and reproducible resistive switching effects. The last piece of data presented in this Chapter is the frequency relaxation of capacitance in these junctions. This measurement also shows a strong correlation

with intentional off-stoichiometry in SrTiO$_3$ and can be used as a metric and diagnostic tool for controlling defect populations in resistive switching devices.

Figures 3.15(a) and (b) show junction capacitances (C) versus frequency (f). Besides the low-f deviations due to leakage, the frequency relaxation follows a power law: $C \sim f^{m-1}$. Red dashed lines are fits to this power law, and the extracted exponents $(1 - m)$ are plotted in Figure 3.15(c). These exponents show clear continuous trends with off stoichiometry and Pt quality. While the physical interpretation of m is not straightforward, it is generally agreed that it correlates with structural defect levels [192], [193].

A helpful framework is provided by considering a random interconnected
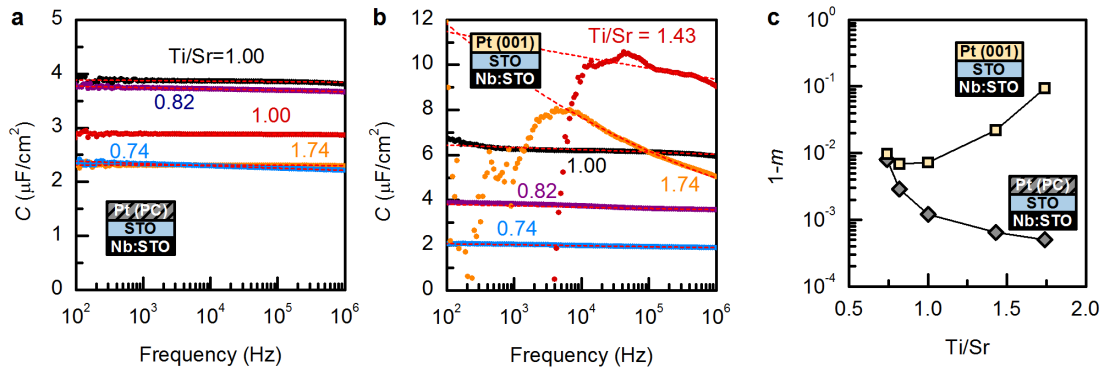
Figure 3.15. Frequency dependence of the IRS junction capacitance for devices with (a) Pt(PC) and (b) Pt(001). Dashed lines are fits to $C \sim f^{m-1}$. The corresponding exponents are shown in (c). Reprinted from [55], licensed under CC BY 4.0.

network of capacitors and resistors [194], [195]. For the case where m is the majority population of capacitors and $1-m$ the minority population of resistors, the global network capacitance follows a f^{m-1} relaxation. While the intuitive interpretation is to assign the resistor population $1-m$ to the point defect density, the trends in Figure 3.15 are more complex.

One robust trend is the increase of $1-m$ upon replacing Pt(PC) with Pt(001). This implies that the unintentional interface layers related to Pt(PC) growth act in a capacitor-like manner in the context of dielectric relaxation, increasing m. Their suppression in the case of Pt(001) increases the resistor-like population $1-m$. Sr excess consistently increases $1-m$, consistent with the picture of it being incorporated as resistor-like point defects (e.g. Ti vacancies). The combination of Ti excess and Pt(PC) very heavily decreases $1-m$, which is likely associated with the TiO_x observed in STEM (Figure 3.11(a)). Conversely, the combination of Ti excess and Pt(001) corresponds to a very large increase in $1-m$, which correlates with a very strong suppression of the Schottky barrier and increased SCLC-type DC leakage.

In conclusion of this Chapter, the ensemble of data presented above is a proof of concept for tailoring resistive switching using intentional structural defects. This is guided by the premise that the switching effect is proportional to trapped charge density and interface capacitance ($\Delta \phi_B \sim \Delta Q_T / C_i$). This work estab-

lishes the control of interface capacitance through the use of advanced growth techniques for both the insulating interlayer and the metal of the Schottky junction. It also establishes control of charge trapping center density via intentional introduction of non-stoichiometry into the interlayer.

One possible avenue for improving the resistive switching magnitude is to reduce the interlayer capacitance, e.g. by using epitaxial insulators with a lower dielectric constant then $SrTiO_3$, or by increasing its thickness. It would also be interesting to explore alternative ways to control the dominant trapping center population. In particular, it has been suggested that deep level dopants (such as Cr and Fe) may stabilize robust resistive switching with good state retention in $SrTiO_3$ and $SrZrO_3$ [166], [196]–[200]. Such point defects might offer a cleaner way to control Q_T.

Chapter 4

Introduction: electronic transport in titanate perovskites

The second part of this thesis deals with electronic transport behavior in SrTiO$_3$. It will present systematic studies of electrical resistivity in SrTiO$_3$ tuned by doping and heterostructuring [201]–[203]. It will seek to establish phenomenological descriptions and identify features that show departure from electrical transport in conventional semiconductors and metals.

This introductory Chapter will start by outlining the electronic phases in SrTiO$_3$ and the relevant carrier scattering mechanisms. A basic overview of Mott insulators (in particular, the rare earth titanates), SrTiO$_3$-based heterostructures, and 2D electron liquid formation at oxide interfaces will be given. This Chapter will also present the concept of quantum criticality and the current understanding the different types of unconventional transport phenomena, such as non-Fermi liquid behavior and scattering rate separation.

4.1 The electronic phase diagram of R_xSr$_{1-x}$TiO$_3$

Undoped SrTiO$_3$ is a band insulator, with an indirect gap of 3.3 eV [2] separating the filled oxygen $2p$ bands and the empty Ti $3d$ bands [204]–[206]. As illustrated in Figure 4.1(a), the tenfold degeneracy of the $3d$ states is lifted by the anisotropic crystal field within the TiO$_6$ octahedra of the perovskite structure [207].

SrTiO$_3$ at room temperature is a cubic perovskite, and the lowest states relevant for electron doping are within the sixfold degenerate t_{2g} manifold. This degeneracy is lifted by the spin-orbit coupling combined with the tetragonal distortion occurring near 110 K. The t_{2g} orbital is split into d_{xy}, d_{yz} and d_{xz} states. The momentum space dispersion of the three resulting bands is illustrated in Figure 4.1(b) [204]–[206].

The trend with electron doping can be summarized as follows: in the low density limit, only one band is partially filled. It is labeled as heavy electron ("he") because of its higher effective mass in the xy plane. Above a critical electron density $N_{c1} \approx 10^{18}$ cm^{-3} [206], [208], [209], a second band becomes occupied, labeled light electron ("le"). A third, split-off ("so") band is also a light electron band, which starts being filled above $N_{c1} \approx 2 \times 10^{19}$ [206], [209].

Another notable aspect of SrTiO$_3$ is the wide range of electronic states that can be accessed in this material. This is highlighted using the example of the R_xSr$_{1-x}$TiO$_3$ solid solution system, with R = La, Gd, Sm. There is no solubility limit for these rare earth ions in the perovskite structure of SrTiO$_3$. One can continuously tune x across the entire composition range between SrTiO$_3$ (a band insulator) and RTiO$_3$ (a Mott insulator, see Chapter 4.2) [210]–[212]. For other types of n-type dopants (oxygen vacancies, Nb on the Ti site), the phase diagram is largely equivalent in terms of carrier density (N) dependence. The maximum

achievable carrier density in these cases is, however, limited to $\approx 5 \times 10^{20}$ cm^{-3} [3], [213], [214], which is equivalent to $x \approx 0.03$ for rare earth doping.

The electronic phase diagram as a function of x is illustrated in Figure 4.2. It is dominated by a very wide composition range with metallic conductivity (re-
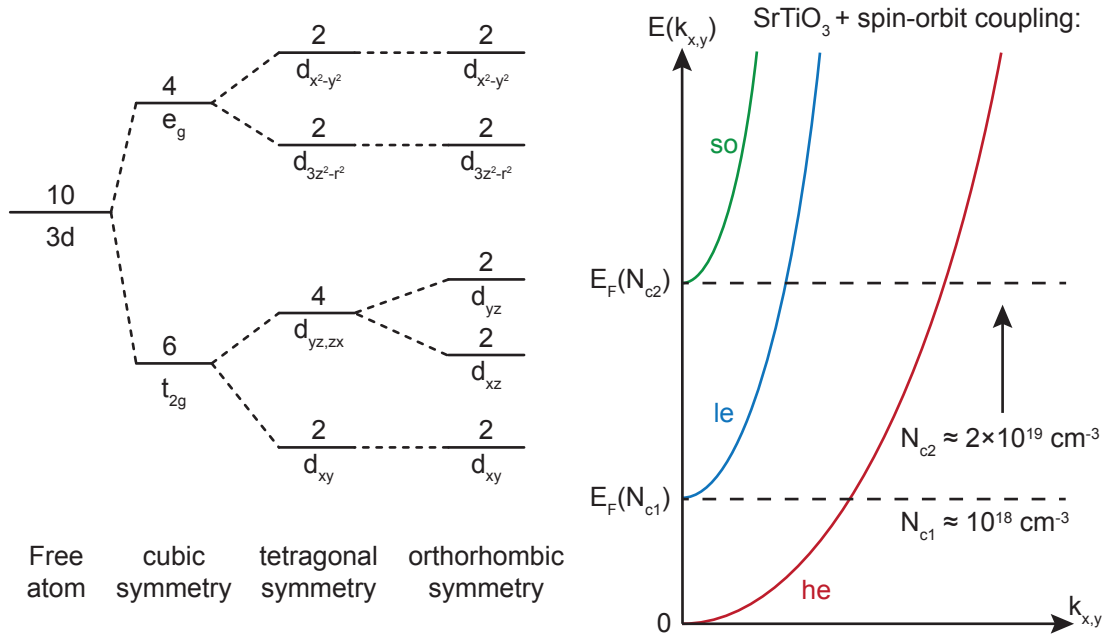
Figure 4.1. (a) Crystal field splitting of the $3d$ orbital states for the perovksite structures with various symmetries. Numbers indicate the state degeneracy (including spin). (b) Sketch of the lowest-lying conduction band dispersion in tetragonal SrTiO$_3$ in presence of spin-orbit coupling, with $k_{x,y}$ being the momentum orthogonal to the tetragonal axis. The dashed horizontal lines indicate the critical doping levels for partial filling of higher-lying bands.

sistivity increases with temperature), where R acts as an n-type dopant donating one electron. On the low x side of the phase space it extends down to extremely low doping densities. The metallic conductivity and T-independent carrier density (no freeze-out at low T) are preserved for carrier densities as low as $\approx 10^{15}$ cm^{-3} [3], [214].

Another prominent feature of the phase diagram is the superconducting dome that is found in the $N \approx 10^{18}$-10^{21} cm^{-3} range , with a critical temperature that plateaus near 300 mK [209], [213], [215]. These carrier densities are
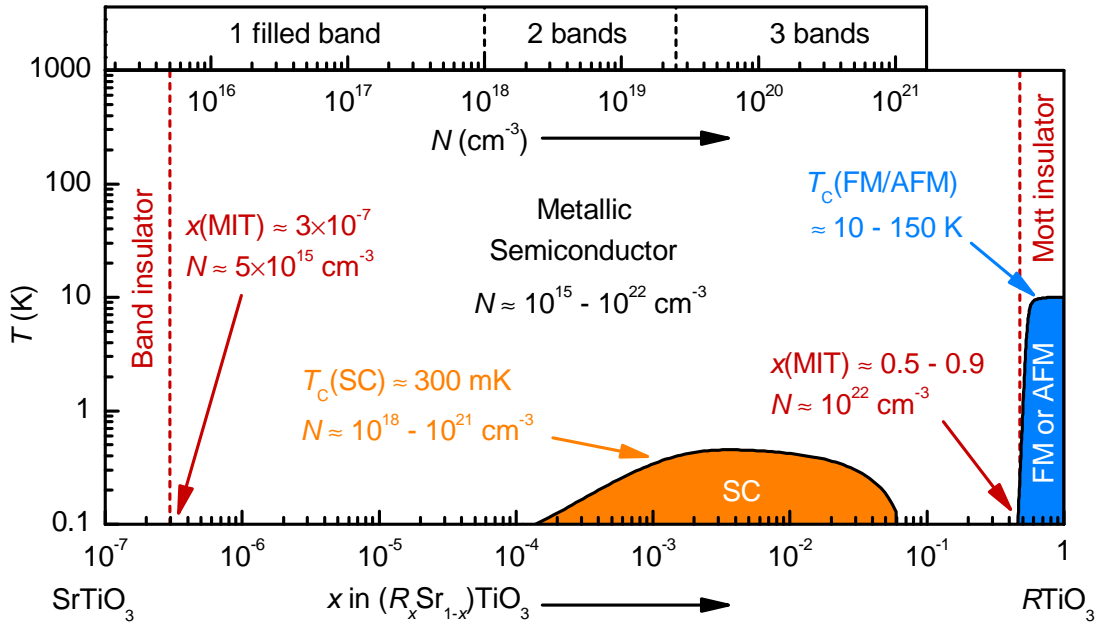
Figure 4.2. Electronic phase diagram of the R_xSr$_{1-x}$TiO$_3$ system. The phase boundaries summarize the results from references [3], [209], [211]–[216].

very low in comparison to typical superconductors, which are generally metals having close to one electron or hole per unit cell and $N > 10^{21}$ cm^{-3}. In contrast, doped SrTiO$_3$ is an unusually dilute superconductor [217]. The electron pairing mechanism has been described in terms of classic BCS coupling to the transverse optical phonons [218]. It has also been proposed that the pairing is unconventional and related to quantum criticality originating from proximity to suppression of ferroelectric order [219], [220].

In the ultra-high doping limit of $x \approx 0.5$, R_xSr$_{1-x}$TiO$_3$ undergoes a transition to a Mott insulator. As detailed further in Chapter 4.2, this is an insulating state induced by strong electron correlations. It is characteristic of rare earth titanates RTiO$_3$ with R = Yb, Y, Gd, Sm, Nd, La, etc [221]. These are heavily distorted perovskites with orthorhombic symmetry. Depending on the size of the R cation the ground state is either ferromagnetic (T_C = 10 - 60 K) or antiferromagnetic (T_N = 10 - 150 K) [216], [221].

4.2   Mott insulators

Mott insulators are a classic example of a strongly correlated phenomenon, i.e., effects that are missed within the classical approximation of independent electrons.

A good illustration is provided by considering the simplest case of a single band Hubbard model [207], [222]–[224]:

$$\mathcal{H}_H = -t \sum_{<i,j>,\sigma} \left(c_{i\sigma}^\dagger c_{j\sigma} + c_{j\sigma}^\dagger c_{i\sigma} \right) + U \sum_i n_{i\uparrow} n_{i\downarrow} + \mu_C \sum_{i,\sigma} n_{i,\sigma} \qquad (4.1)$$

where i and j are crystal lattice site indices and $\sigma =\uparrow\downarrow$ are the electron spins. $c_{i\sigma}^\dagger$ and $c_{i\sigma}$ are the electron particle creation and annihilation operators, and $n_{i\sigma} \equiv c_{i\sigma}^\dagger c_{i\sigma}$ is the number operator.

The first term is the kinetic energy. It is defined by t, the energy scale for electron hopping between two lattice sites. The notation $< i,j >$ emphasizes that hopping is only allowed between adjacent sites. The second term is the on-site repulsion, characterized by the electron interaction U. This is the added energy cost of putting two electrons with a repulsive interaction on the same lattice site. The third term describes the role of band filling. It is characterized by the chemical potential μ_C.

The classic band theory setting corresponds to the case $t \gg U$, i.e., when the second term is negligible. The opposite limit $t \ll U$ corresponds to an isolated free atom. Of particular interest is the intermediate case, when the interaction scale U is comparable to hopping t. Such systems are commonly referred to as strongly correlated. The interplay between U and t can lead to transitions between metallic and insulating states and stabilize various forms of magnetic

ordering [207].

The emergence of a Mott insulating state is one well-known effect that is driven by U. It is illustrated in Figure 4.3 for the case of d-electron transition metal oxides. These materials are predicted by classic band theory ($t \gg U$) to be metals with a conduction band near half-filling. In reality, they are insulators as a consequence of the interaction term. A non-negligible U causes the d-electron band to split into upper and lower Hubbard bands (UHB and LHB), with the Fermi level being in the gap. The simplest case is the Mott-Hubbard insulator, where the gap is given by U. Notable examples include oxide compounds with light $3d$ transition metals, e.g. rare earth titanates [210], [211], [225] and vanadates [226].

A second possible case is the charge transfer insulator. It is largely similar to the Mott-Hubbard case, with the conventional band theory treatment giving a metal close to half-filling. The difference is in the oxygen-derived p-electron band lying higher with respect to the d band. If the p-d charge transfer energy (Δ) is smaller than the d site interaction, the gap is determined by Δ (see Figure 4.3). Oxide compounds of heavier $3d$ transition metals tend to have smaller Δ and thus are thus more likely to be charge transfer insulators. This is thought to be the case for many rare earth nickelates [227]–[229] and cuprates [230].
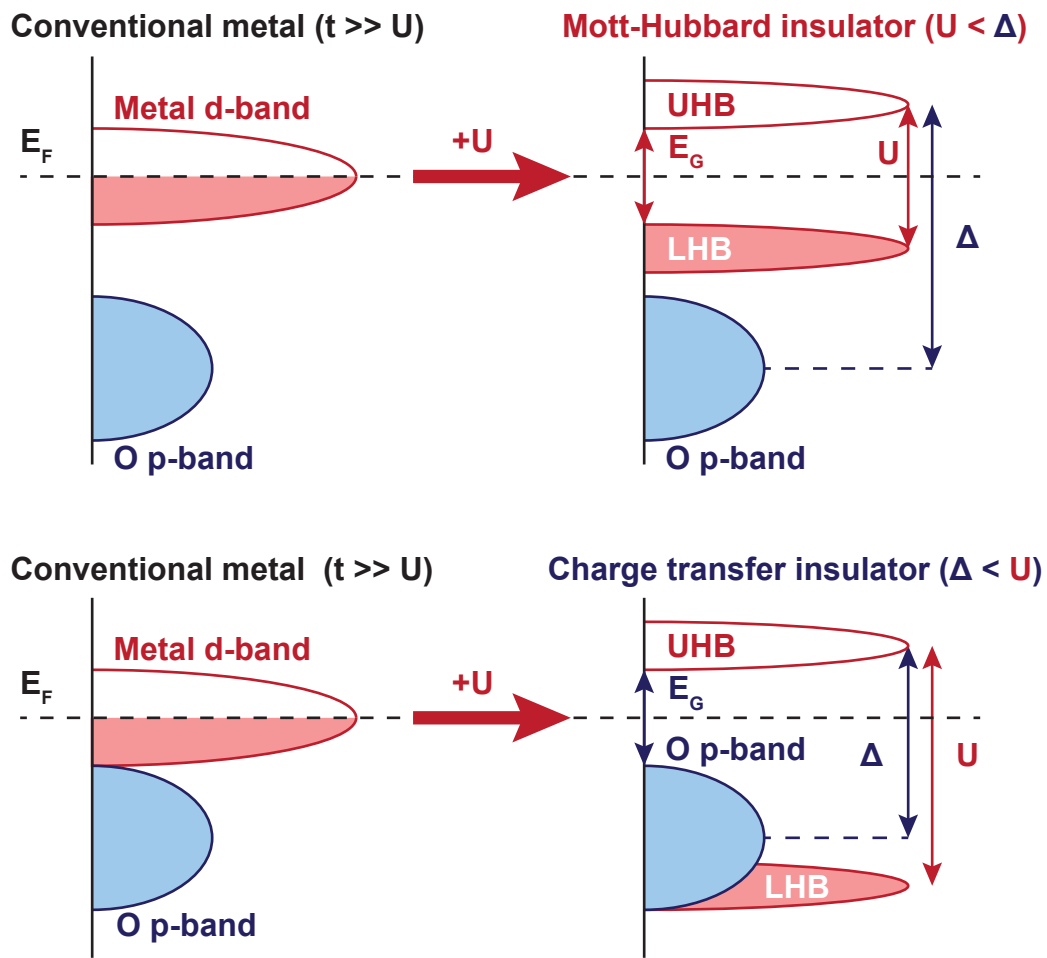
Figure 4.3. Schematic illustration of energy levels in Mott-Hubbard insulators (top) and charge transfer insulators (bottom) induced by d electron interactions. Adapted from [207].

As mentioned above, the band filling is an important aspect of the Hubbard model (see the third term in Equation 4.1). The Mott insulating state is stable only near half filling of the d band, i.e., when there is close to 1 electron per site. This can be simplistically illustrated as the case where an electron hopping to a nearby lattice site will have the highest probability of finding it occupied by another electron. This costs an energy U, thus promoting an insulating state.

As illustrated in Figure 4.4, moving away from half-filling destroys the Mott insulating state. This is the filling-controlled metal-insulator transition (MIT). It
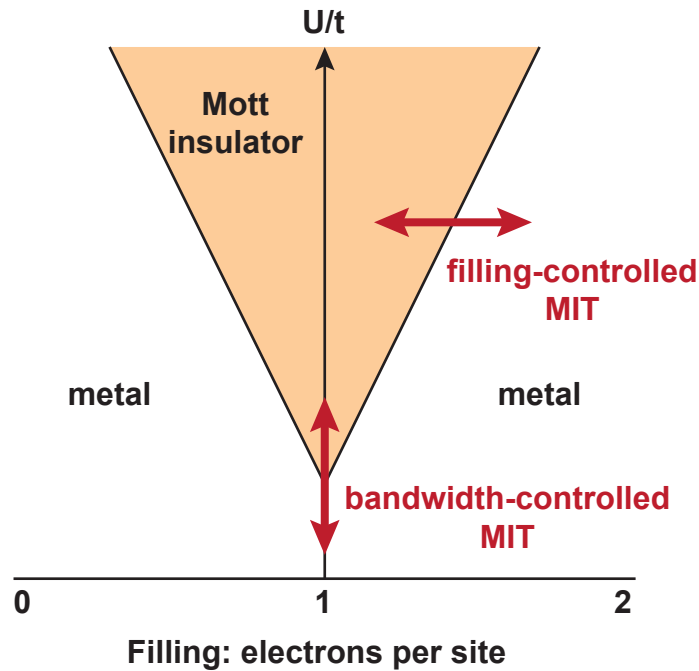
Figure 4.4. Filling and bandwidth-controlled Mott MIT within the single band Hubbard model. Adapted from [207].

has been observed experimentally by chemically doping Mott insulators. Examples include Sr doping of GdTiO$_3$ [225] and LaTiO$_3$ [210], [211], Ca doping of YTiO$_3$, Sr, Ca and Th doping of NdNiO$_3$ [227], and hole or electron doping of the cuprates leading to high-T_C superconductivity [230]. The filling controlled MIT is also relevant for the phase diagram of the R_xSr$_{1-x}$TiO$_3$ solid solution in Figure 4.2.

Figure 4.4 also illustrates a different route towards inducing a Mott MIT: control of bandwidth, which in the classic band theory is proportional to the hopping scale t. The destruction of the insulating state at low U/t can be illustrated by considering the Mott-Hubbard insulator in Figure 4.3: higher t increases the bandwidth of the UHB and LHB, reducing the gap below U. The case of $t \gg U$ is also the classic band theory limit that predicts a metal at half filling.

The bandwidth and hopping scales can be tuned by changing the overlap between d orbitals. This can be achieved experimentally by modulating structural distortions in a Mott insulator via hydrostatic pressure, isovalent doping with ions of different size, or epitaxial strain. Rare earth nickelates RNiO$_3$ (R = La, Pr, Nd, Sm, Eu, ...) are an established system for bandwidth control of a Mott MIT [228], [229].

4.3   2D electron liquids

Study of emergent phenomena at oxide interfaces has been a very active research direction for more than a decade. The discovery of conductive interfaces between two oxide insulators generated much of this excitement [231]–[234].

Figure 4.5 illustrates the polar discontinuity mechanism for formation of a two-dimensional electron liquid (2DEL) at a polar/non-polar oxide perovskite interface [61], [235]–[237]. It treats the case of a $SrTiO_3/RTiO_3$ interface.

A (001) oriented $SrTiO_3$ layer consists of alternating atomic planes with zero net charge: $Sr^{2+}O^{2-}$ and $Ti^{4+}O_2^{4-}$. There is no electric dipole between these planes and the layer surface is non-polar. In contrast, the $R^{3+}O^{2-}$ and $Ti^{3+}O_2^{4-}$ planes of the $RTiO_3$ layer have unequal +1/-1 net charges. This creates a net dipole within each repeat unit and the layer surfaces are thus polar.

This type of interface is unstable due to a divergent electrical potential. In order to stabilize this interface, its charge needs to be compensated, which can be accomplished either by charged surface defects or by electronic reconstruction. The latter mechanism involves a transfer of 1/2 of an electron per lateral unit cell from $R^{3+}O^{2-}$ planes to each adjacent $Ti^{3+}O_2^{4-}$ plane, as illustrated in Figure 4.5. The resulting $RTiO_3$ layer is largely equivalent to the unreconstructed one, with the exception of the surface planes that have an extra 1/2 of an elec-

tron per unit cell. In particular, this is the case of the $Ti^{3+/4+}O_2^{4-}$ plane at the SrTiO$_3$/RTiO$_3$ interface, which acquires a mixed valence character.

For oxide perovskites with a cubic unit cell parameter of $\approx$0.4 Å, 1/2 of an electron per unit cell corresponds to a sheet density of $\approx 3 \times 10^{14}$ cm^{-2}. In the case where these electrons fill the Ti d-orbital states (as implied by writing $Ti^{3+/4+}$), this sheet charge can be mobile and the polar discontinuity acts as an interface n-type doping mechanism.

It is important to note the magnitude of this sheet density: 3×10^{14} cm^{-2} distributed over a vertical thickness of one unit cell corresponds to a very large volume density of $\approx 8 \times 10^{21}$ cm^{-3}. In reality, the vertical spread of mobile
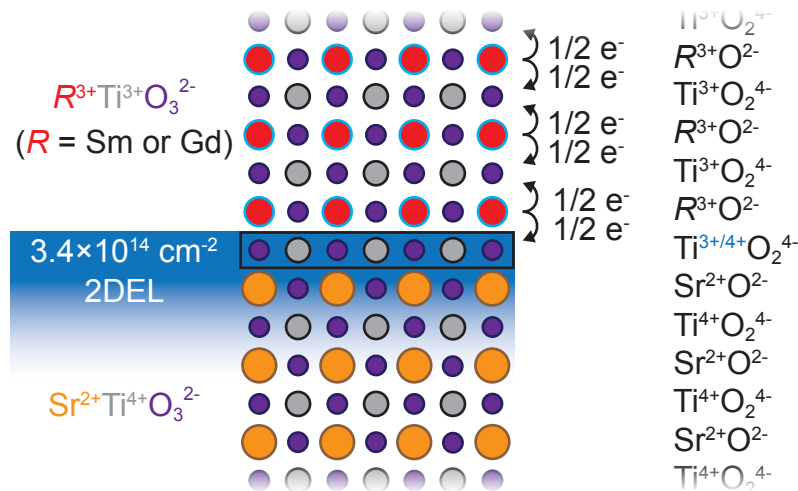
Figure 4.5. Formation of a two-dimensional electron liquid (2DEL) at a SrTiO$_3$/RTiO$_3$ interface

electrons into $SrTiO_3$ is usually across several nanometers [61], [238], but this still corresponds to volume densities close to 10^{21} cm^{-3}.

This kind of heterostructure system with extremely high sheet carrier densities induced by a polar discontinuity is referred to as a two-dimensional electron liquid (2DEL). This term is largely analogous to two-dimensional electron gas (2DEG), but emphasizes the increased importance of strong electron correlations in the high carrier density regime.

Chapters 5 and 6 will focus on scattering mechanisms and confinement effects in 2DELs at $SrTiO_3/RTiO_3$ interfaces grown on $(LaAlO_3)_{0.3}(Sr_2AlTaO_6)_{0.7}$ (LSAT) substrates. Previous work established that such interfaces consistently produce sheet electron densities of $N = 3.4\times10^{14}$ cm^{-2} per interface [61]. This exactly corresponds to the number expected for a polar discontinuity mechanism, given the 3.86 Å lattice constant of LSAT.

The $SrTiO_3/RTiO_3$ system has many similarities with the interface between Ti-terminated $SrTiO_3$ and $LaAlO_3$, which was the platform for the original studies of oxide 2DELs and continues to be the most heavily investigated oxide interface system [239]–[242]. The polar discontinuity mechanism at this interface is analogous to the one in Figure 4.5 if $R^{3+}O^{2-}$ planes are replaced with $La^{3+}O^{2-}$, and $Ti^{3+}O_2^{4-}$ with $Al^{3+}O_2^{4-}$. The $SrTiO_3/RTiO_3$ system has, however, several im-

portant distinguishing characteristics:

- The sheet carrier density measured by the Hall effect at $SrTiO_3$/$RTiO_3$ interfaces is consistently 3.4×10^{14} cm^{-2}, i.e., 1/2 of an electron per lateral unit cell [61], [243], [244]. For $SrTiO_3$/$LaAlO_3$ interfaces there is a very large variability in observed sheet densities, usually dependent on the $LaAlO_3$ growth parameters. In most reports, the measured values are $\approx 1 - 5 \times 10^{13}$ cm^{-2}, which is only a small fraction of the value expected in the polar discontinuity model [240], [242].

- Both regular ($RTiO_3$ on $SrTiO_3$) and inverted ($SrTiO_3$ on $RTiO_3$) interfaces display the same full sheet carrier density [61]. In contrast, measurable mobile carrier densities are observed for $LaAlO_3$ layers grown on $SrTiO_3$, but not for the inverted interfaces [245].

- Repeated $SrTiO_3$ and $RTiO_3$ layers can be stacked into superlattices, where the measured total carrier concentration is always the number of interfaces multiplied by 3.4×10^{14} cm^{-2}. In contrast, generally only the first $SrTiO_3$/$LaAlO_3$ interface shows an appreciably high carrier density [241], [245].

The $SrTiO_3$/$RTiO_3$ interface is arguably a more conceptually intuitive system, where the predictions of the polar discontinuity model are exactly valid. It

offers more possibilities in terms of engineering strong correlations by producing very high volume carrier densities by quantum confinement of the 2DELs in RTiO$_3$/SrTiO$_3$/RTiO$_3$ quantum wells [237].

Finally, it is important to draw a distinction between polar discontinuity systems and the various interfaces systems based on oxygen reduction of SrTiO$_3$. Growth processes carried out at very low oxygen pressures and involving Al (a strong oxygen getter) can produce extremely high sheet carrier densities ($N \approx 10^{15} - 10^{17}$ cm^{-2}) by generating oxygen vacancies in SrTiO$_3$ that act as n-type dopants. The polar discontinuity picture does not apply in such cases. Notable examples include low pressure-grown SrTiO$_3$/LaAlO$_3$ [242], [246], SrTiO$_3$/Al$_2$O$_3$ (crystalline γ-alumina [247]) and SrTiO$_3$/AlO$_x$ (amorphous alumina [248], [249]). The very large sheet carrier concentrations of these systems are distributed over fairly large SrTiO$_3$ thicknesses, strongly reducing the corresponding volume concentrations.

4.4 Carrier scattering mechanisms in SrTiO$_3$

4.4.1 Basic definitions

The basic definitions of electrical conductivity σ and resistivity ρ [250], [251] are given by Ohm's law, the linear relationship between between current density J and electric field E:

$$J = eNv_D = \sigma E \tag{4.2}$$

For n-type conduction (electrons as charge carriers), v_D is the electron drift velocity, e the electron charge and N the charge carrier density. The electron drift mobility μ is defined as :

$$\mu \equiv \frac{v_D}{E} \tag{4.3}$$

It describes how quickly an electron in a material can be accelerated by an electric field. A classic approximation for μ assumes an average time τ between scattering events. After each such collision, the electron velocity is randomized and averages to zero. From classical mechanics, the velocity at time τ after a collision is $v_D = eE\tau/m^*$, with m^* being the effective electron mass. This is equivalent to defining the electron mobility as:

$$\mu = \frac{e\tau}{m^*} \tag{4.4}$$

The mobility μ incorporates both the electronic band structure effects (through m^*) and the various carrier scattering mechanisms (through τ). This quantity is convenient for interpretation of experimental data, as it is also the proportionality constant between the measured resistivity and carrier density:

$$\rho = \frac{1}{\sigma} = \frac{1}{e\mu N} = \frac{m^*}{e^2 \tau N} \tag{4.5}$$

Two common geometries for measurement of electrical transport in thin films are illustrated in Figure 4.6. These four terminal measurement methods eliminate the contact resistance to isolate the sheet resistance R_{xx} (with units of Ω/square). For a conducting film with vertical thickness z, the volume resistivity in Ωcm is $\rho = z R_{xx}$.

In the **Hall bar geometry** [251] (Figure 4.6(a)), a conducting channel with width W and length L needs to be defined by photolithography (or appropriate cutting of a sample piece). A current I_{SD} is applied between the source and drain contacts. The voltage drops measured between contact pads 1-4 give the sheet resistance and the Hall coefficient (with magnetic field B applied orthogonally to the sample plane). With $V_{ij} \equiv V_j - V_i$:

$$R_{xx} = \frac{W}{L} \cdot \frac{V_{12}}{I_{SD}} = \frac{W}{L} \cdot \frac{V_{34}}{I_{SD}} \tag{4.6}$$

$$R_H = \frac{R_{xy}}{B} = \frac{V_{13}}{I_{SD} B} = \frac{V_{24}}{I_{SD} B} \tag{4.7}$$
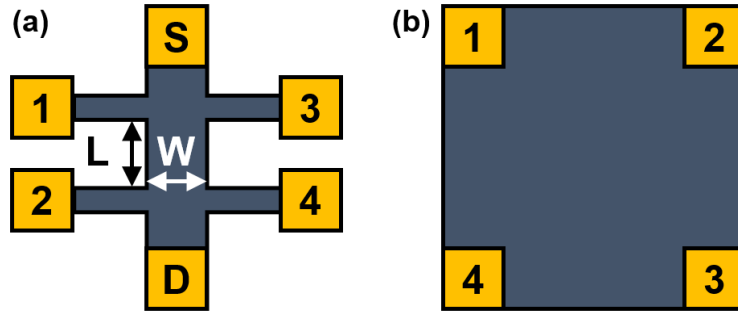
Figure 4.6. Illustration of the (a) Hall bar and (b) van der Pauw geometries for four-terminal measurements of electrical resistivity.

The **van der Pauw geometry** (Figure 4.6(b), [251]–[253]) consists of four ohmic contacts at the corners of a square sample. Its main advantage is the simplicity of fabrication. It does not require mesa definition and thus avoids any potential interference from damage by the etch or cutting processes.

For a four-terminal measurement, one contact pair is used to apply current I_{kl} and the voltage drop V_{ij} is measured across a second pair. With $R_{ij,kl} \equiv V_{ij}/I_{kl}$, the sheet resistance can be iteratively calculated from the following expression:

$$\exp\left(-\pi \cdot \frac{R_{43,12}}{R_{xx}}\right) + \left(-\pi \cdot \frac{R_{23,14}}{R_{xx}}\right) = 1 \qquad (4.8)$$

A special case of interest is $R_{43,12} = R_{23,14}$, i.e., when the measured resistances are equal in both directions, as expected for perfectly symmetric square samples

and contact positioning. In this case, the sheet resistance is simply:

$$R_{xx} = \frac{\pi}{\ln(2)} \cdot R_{43,12} = 4.532 \cdot R_{43,12} \qquad (4.9)$$

The Hall effect is given by the transverse measurement geometry:

$$R_H = \frac{R_{xy}}{B} = \frac{V_{42}}{I_{13}B} = \frac{V_{31}}{I_{42}B} \qquad (4.10)$$

The classic relationship between the measured Hall coefficient and carrier density is $N = (eR_H)^{-1}$, which is valid for the linear Hall signal at small magnetic field in the presence of a single type of charge carriers [250], [251].

4.4.2 Electron-phonon scattering

One major source of charge carrier scattering in metals and semiconductors is the interaction with phonons, i.e., the quantized vibrations of the crystal lattice induced by temperature.

The classic treatment of this scattering mechanism follows the Debye model, which treats phonons as particles in a box [250], [254], [255]. The phonon spectrum is characterized by the Debye temperature:

$$\Theta_D = \frac{h\nu_D}{k_B} = \frac{h}{k_B} = \left(\frac{3}{4\pi} \cdot N(\text{atoms})\right)^{1/3} \cdot v_s, \qquad (4.11)$$

where ν_D is the Debye frequency, which has the physical meaning of a theorerical maximum frequency for a given crystal structure. It is given by the speed of

sound in the solid v_s and the volume density of atoms in the crystal structure (N(atoms)). h and k_B are the Planck and Boltzmann constants.

The electron-phonon scattering cross section can be approximated as the amplitude of thermal atom displacement caused by phonons, leading to an increased scattering rate at high temperature. The full treatment of this problem leads to the generalized Bloch-Grüneisen formula:

$$\rho_{e-ph}(T) = K_{BG} \cdot \left(\frac{T}{\Theta_D}\right)^5 \cdot \int_0^{\Theta_D/T} \frac{z^5 dz}{(e^z - 1)(1 - e^{-z})}, \tag{4.12}$$

with K_{BG} being a material-dependent electron-phonon coupling constant. Of particular use are the low and high T limits of this expression with respect to the Debye temperature scale:

$$\rho_{e-ph} \sim T^5 \quad (T \ll \Theta_D) \tag{4.13}$$

$$\rho_{e-ph} \sim T \quad (T \gg \Theta_D) \tag{4.14}$$

In SrTiO$_3$ Θ_D is fairly high: the estimate based on measured elastic constants is 693 K [256]. The estimate from heat capacity is 513 K [257]. Therefore, in most practical settings (in particular the cryogenic T range), the $T \ll \Theta_D$ limit is applicable. However, the sharp T^5 power law is never observed in doped SrTiO$_3$. As discussed in more detail below, the experimental resistivity follows a much more gradual increase, consistent with T^2 or T^3 power laws.

4.4.3 Polaron-phonon scattering

While the Bloch-Grüneisen result is not directly applicable to the case of SrTiO$_3$, the polaron-phonon scattering picture was very successful in describing the high-T range above $\approx$200 K, where resistivity scales approximately as T^3 [3], [258].

A polaron is a quasiparticle that describes the motion of an electron in a polar or highly ionic crystal. It accounts for the non-rigid nature of the lattice, in which an electron can induce a local polarization, which will in turn distort the electron's motion. This interaction is mediated by phonons, which can be described by the dimensionless electron-phonon coupling constant [259]:

$$K_{ep} = \frac{e^2}{\hbar} \cdot \sqrt{\frac{m^*}{2\hbar\omega}} \cdot \left(\frac{1}{\varepsilon_\infty} - \frac{1}{\varepsilon} \right), \qquad (4.15)$$

where ω is the phonon frequency, m^* the effective electron mass, ε_∞ is the high frequency electronic dielectric constant and ε the static dielectric constant. The polaron quasiparticle mass is then approximately:

$$m_P = m^* \cdot \left(1 + \frac{K_{ep}}{6} \right) \qquad (4.16)$$

The full treatment of the scattering process between polarons and phonons gives the following contribution to electron mobility:

$$\mu_{\text{polaron}}(T) = \frac{1}{2K_{ep}\omega} \frac{e}{m_P} \left(\frac{m^*}{m_P} \right)^2 f(K_{ep}) \left(\exp\left(\frac{\hbar\omega}{k_B T} \right) - 1 \right), \qquad (4.17)$$

where $f(\beta) \approx 1$ is a dimensionless function that is weakly dependent on β. For SrTiO$_3$, the relevant phonons are the two highest lying longitudinal optical (LO) branch modes, with $\hbar\omega_{LO} = 99$ and 58 meV [260]. Their respective coupling constants are $K_{ep} = 2.6$ and 0.7 [261]. Assuming that their contributions to scattering add up according to the Matthiessen rule, this gives $K_{ep} = 3.3$ and $m_P = 1.55m^*$. Under these assumptions, Equation 4.17 describes fairly well the carrier mobility of electron doped SrTiO$_3$ above $\approx$200 K [3], [258].

4.4.4 Electron-electron scattering

One well-known signature of electron-electron scattering in a metallic solid is the T^2 scaling of resistivity [250], [254], [255], [262]–[264]:

$$\rho_{e-e} \sim \frac{1}{\tau_{e-e}} \sim AT^2, \qquad (4.18)$$

where τ_{e-e} is the corresponding scattering rate. The origin of the T^2 dependence lies in the Pauli exclusion principle and the applicability of Fermi-Dirac statistics for electrons in a solid. This can be illustrated in a simplified way [250] by considering a scattering event between two non-interacting electrons in the context of a Fermi sphere at $T = 0$, which is thus filled up to the Fermi level E_F. An excited electron with an energy $E_1 \geq E_F$ interacts with a second electron within the Fermi sphere ($E_2 \leq E_F$) and they are scattered into

unoccupied states $E_{3,4} > E_F$. The energy conservation requirements is:

$$E_1 + E_2 = E_3 + E_4 \tag{4.19}$$

In the absence of thermal activation at $T = 0$, $E_1 = E_F$. This in turn requires that $E_{2,3,4} = E_F$. Consequently, the phase space for electron-electron scattering is a vanishing volume around the Fermi surface. This results in an infinite lifetime of an electron at the Fermi surface at $T = 0$, as also implied by Equation 4.18.

At finite $T > 0$, the phase space for scattering becomes a shell of approximate width $k_B T$ around the Fermi surface. The probability of a scattering event for the excited electron (E_1) is obtained by double integration over the phase space, as knowing $E_{1,2,3}$ sets E_4 by energy conservation. This leads to a scattering rate that scales as T^2.

The above argument relies on treating electrons as independent and non-interacting, which is a poor approximation for a metal. Justification for its validity is provided by the Landau Fermi liquid framework [250], [264]. It treats strongly interacting electrons as renormalized quasiparticles, which can be shown to also obey the Pauli exclusion principle and Fermi-Dirac statistics. Consequently, the above derivation holds as a description of a quasiparticle scattering process. It is, however, now restricted to low temperatures, where the quasiparticles are well-defined ($k_B T \ll E_F$).

An important consideration for electron-electron scattering concerns momentum conservation. For an electron-only process as described above, the total momentum of conduction electrons is preserved:

$$\vec{k_1} + \vec{k_2} + \vec{k_3} + \vec{k_4} = 0 \tag{4.20}$$

This implies that such scattering mechanism should not contribute to the electrical resistivity. A non-zero contribution can be obtained for an Umklapp process [262], [263], which involves the reciprocal lattice vector $\vec{G}$:

$$\vec{k_1} + \vec{k_2} + \vec{k_3} + \vec{k_4} = \vec{G} \tag{4.21}$$

This leads to a change of the total momentum after the scattering process. A notable restriction on such processes is the requirement for the Fermi surface size to be comparable with the Brillouin zone size. From Equation 4.21, the momenta for involved electrons need to be larger than $\approx G/4$, leading to a necessary condition $k_F > G/4$ for Umklapp processes to be possible [265].

4.4.5 Electron-impurity scattering

In the low temperature limit, both electron-phonon and electron-electron scattering mechanisms vanish. The residual resistivity at $T = 0$ is generally dominated by the T-independent disorder scattering of electrons. These disor-

der scatterers can be point defects in the lattice, dislocations or grain boundaries. At finite temperature, residual scattering is generally assumed to add up with other mechanisms according to the Matthiessen rule [251], [255]:

$$\tau^{-1}(T) = \tau_0^{-1} + \sum_i \tau_i^{-1}(T) \tag{4.22}$$

where i is an index that runs across all T-dependent scattering mechanisms. The quantity τ_0 is the residual scattering rate. The corresponding residual resistivity and mobility are:

$$\rho_0 = \frac{1}{\mu_0 e N} = \frac{m^*}{e^2 \tau_0 N} \tag{4.23}$$

In the context of single crystals of $SrTiO_3$ doped with electron donors (e.g. La^{3+} on the Sr^{2+} site or Nb^{5+} on the Ti^{4+} site), the dominant residual scattering is by ionized impurities. They are usually modeled as screened Coulomb potentials [3], [266]:

$$V_C(r) = \frac{Ze^2}{\varepsilon_0 \varepsilon_r} \frac{1}{r} \exp\left(-\frac{r}{a}\right) \tag{4.24}$$

where r is the distance from the impurity, Ze is the impurity charge ($Z = 1$ for La and Nb), ε_r is the dielectric constant and a is the screening length. The corresponding scattering rate is:

$$\tau_0^{-1} = N_I v_F \cdot \sigma_T \tag{4.25}$$

where N_I is the volume concentration of scatterers, v_F is the Fermi velocity ($v_F^2 m^* = 2E_F$) and σ_T is the total scattering cross section. By assuming $ka \ll 1$,

one can express σ_T for a screened interaction potential as [3]:

$$\tau_0^{-1} = N_I v_F \cdot 4\pi a^2 \cdot f(\gamma a) \tag{4.26}$$

where γ and the screening correction factor f are given by:

$$\gamma \equiv \frac{2m^*}{\hbar^2} \frac{Ze^2}{\varepsilon_0 \varepsilon_r} \tag{4.27}$$

$$f(\gamma a) = \frac{16(\gamma^2 a^2 + 8\gamma a)}{\gamma^2 a^2 + 20\gamma a + 32} \tag{4.28}$$

For the screening length, a common assumption in the small wavelength limit is the Thomas-Fermi approximation:

$$a_{TF} = \sqrt{\frac{\varepsilon_0 \varepsilon_r}{4\pi e^2 N(E_F)}} \cong \sqrt{\frac{\varepsilon_0 \varepsilon_r \hbar^2}{4m^* e^2} \left(\frac{\pi}{3N}\right)^{1/3}} \tag{4.29}$$

Experimentally, the low temperature mobility in SrTiO$_3$ is $\mu_0 \approx 10^4$ cm^2/Vs for low doping concentrations ($N \approx 10^{18}$ cm^{-3}) [3], [266]–[268]. A good agreement can be obtained by using Equations 4.26 and 4.29, $N_I = N$, $m^* = 2m_e$ and $\varepsilon_r = 5$ [3] or $m^* = 6.5m_e$ and $\varepsilon_r = 4$ [258]. The low value of ε_r is the high-frequency (optical) dielectric constant. This choice is necessary for quantitative agreement and to satisfy the assumption $ka \ll 1$. At low carrier densities, this gives $k_F a_{TF} \approx 0.1$ [3].

If one was to use the static dielectric constant of SrTiO$_3$, which in the low T limit is $\varepsilon_r \approx 10^4$, the opposite assumption of $ka \gg 1$ is valid. This is known as the Born approximation. The full treatment of this case gives $\tau_0 \sim$

$N/(Z^2 N_I \ln(N^{1/3}))$. For $N_I = N$, μ_0 is $\approx 10^6$ cm^2/Vs and is weakly dependent on N. This is at least two order of magnitude higher than the experimentally observed values [3], [266].

The choice of appropriate values of a, m^* and ε_r is further complicated if one considers the fairly strong electron-phonon coupling in SrTiO$_3$. By comparing the estimates of the Thomas-Fermi screening length and the polaron radius (r_p), one finds $r_p > a_{TF}$. The polaronic interaction range being longer can justify the relevant electron mass being enhanced. It can also rationalize a crossover in the applicable ε_r for screening of the impurity potential: the low optical value for $r < r_p$ and the high static value for $r > r_p$ [3], [258].

4.5   Quantum phase transitions, quantum critical-ity, and non-Fermi liquids

A quantum phase transition (QPT) refers to a crossing of an ordered phase boundary at zero temperature, driven by a non-thermal tuning parameter δ [269]–[272]. Examples include chemical doping, magnetic fields, and hydrostatic pressure ($\delta = x, B, P$). For a phase transition occurring at $\delta = \delta_c$ and $T = 0$, the proximity to it is conventionally defined by a normalized tuning

parameter:

$$r \equiv \frac{\delta - \delta_c}{\delta_c} \tag{4.30}$$

This definition emphasizes a distinction from classical phase transitions (CPT) driven by temperature ($\delta = T$). Their phenomenology was discussed in Chapter 1.2.

The common ground for both types of transitions is their critical nature: they describe a suppression of an ordered phase, which has an order parameter (magnetization, ferroelectric polarization, etc.) with a finite correlation length ξ_L for $r < 0$. For a second order phase transition, ξ_L diverges at $r = 0$ according to a critical exponent ν:

$$\xi_L \sim |r|^{-\nu} \tag{4.31}$$

For the classical T-driven case, this corresponds to the destruction of the ordered phase by thermal fluctuations. In contrast, for a QPT at $T = 0$ these order parameter fluctuations are quantum mechanical in nature.

A second dynamical critical exponent z describes the divergence of the correlation time ξ_τ and the vanishing of the energy scale E of the order parameter:

$$\xi_\tau \sim \xi_L^z \sim |r|^{-\nu z} \tag{4.32}$$

$$E \sim \xi_L^{-z} \sim |r|^{\nu z} \tag{4.33}$$

131

The critical scaling exponents are associated with the idea of universality [273]. Material systems with very different properties are often found to follow similar patterns near criticality, corresponding to universal exponents. For example, $\nu = 1/2$ in standard mean field-type theories for the thermally driven phase transitions.

While a true QPT at $T = 0$ cannot be accessed experimentally, the associated
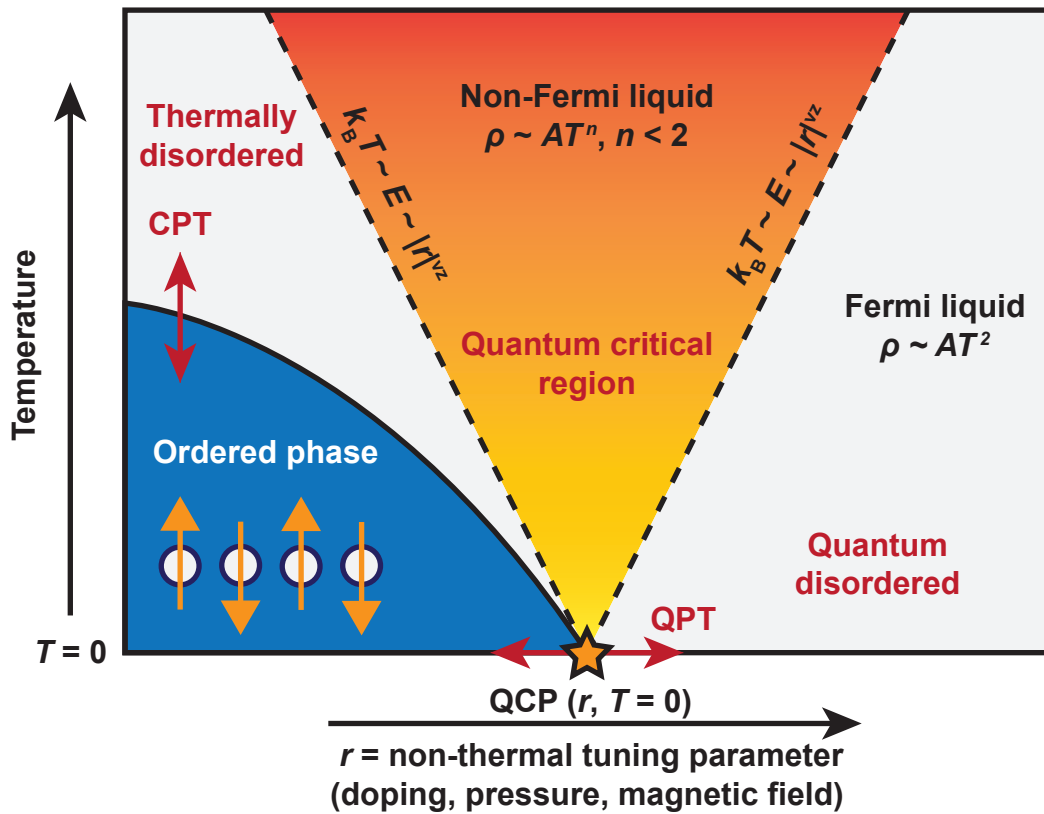
Figure 4.7. Generic phase diagram near a quantum critical point. Adapted from [271].

quantum critical fluctuations of the order parameter can be relevant at $T > 0$. This is illustrated in Figure 4.7, which shows a generic $r - T$ phase diagram in proximity of a quantum critical point (QCP) at $r, T = 0$. The QCP is generally the end point of a classic phase transition, which is suppressed to $T = 0$ by a non-thermal r.

The distinctive feature of this phase diagram is the "quantum critical fan" above the QCP. It is defined by the vanishing energy scale E of the order parameter fluctuations. If $E < k_B T$, the associated time scale ξ_τ is longer than the thermal one. This results in E and the associated microscopic physics becoming irrelevant within the critical fan region (defined by $k_B T \approx E \sim |r|^{\nu z}$), similar to the situation directly at the QCP with $r, T = 0$. In this case, the system is governed by a different, "quantum critical" spectrum of fluctuations. This is thought to give rise to anomalous temperature dependencies of physical observables near the QCP and potentially stabilize unconventional states of matter [269]–[272].

There is a large body of experimental evidence [269], [271], [274], [275] for anomalous temperature scaling of electronic properties (heat capacity C, electrical resistivity ρ, order parameter susceptibility χ) in vicinity of suppressed ferro- and antiferromagnetic order. Such phenomena often take the shape of deviations from the predictions of the Landau Fermi liquid theory that apply at

133

low T outside of the quantum critical region:

$$\rho_{FL}(T) \sim AT^2 \tag{4.34}$$

$$C_{FL}(T) = \gamma T \tag{4.35}$$

"Non-Fermi liquid" (NFL) behavior refers to anomalous scaling of observable properties in proximity to a QCP, usually in the form of unusual power law exponents in resistivity, non-linear heat capacity or modified non-Curie-Weiss susceptibility:

$$\rho_{NFL}(T) \sim AT^n, 1 \leq n < 2 \tag{4.36}$$

$$C_{NFL}(T) \sim T \log(T) \quad \text{or} \quad C_{NFL}(T) \sim T^{1+\lambda}, \lambda \neq 0 \tag{4.37}$$

$$\chi_{NFL}^{-1}(T) = \chi_0^{-1} + T^\beta, \beta < 1 \tag{4.38}$$

Constructing a universal microscopic description of non-Fermi liquids has been a major challenge in theoretical condensed-matter physics, and this problem is still arguably unresolved [271], [276]–[278].

One established theory is the Hertz-Millis model [279]–[282], which considers the emergence of the NFL state out of a Fermi liquid (at $r > 0$) in proximity to a magnetic QCP. The relevant correlation length is $\xi_L = k_F^{-1}$ and the energy scale is the Fermi energy. The crossover to the quantum critical region corresponds to the dampening of ferromagnetic or antiferromagnetic fluctuations.

The results for physical observable scaling above the QCP within this model are summarized in Table 4.1.

Experimentally, prominent NFL systems are heavy fermion materials and high-T_c cuprate superconductors. Heavy fermions are intermetallic compounds incorporating $4f$ or $5f$ electron elements, typically Ce, U and Yb. These materials are known for their very high effective masses ($m^* = 10 - 1000$). There is a great diversity of doping, field and pressure-induced QCPs with AFM order (e.g. CeRh$_2$Si$_2$ [283], CeCu$_6$ [284], CeRhIn$_5$ [285]). Somewhat less common

		AFM 3D	AFM 2D	FM 3D	FM 2D
[281]	$\rho \sim$	$T^{3/2}$	T	T	
[282]	$\rho \sim$	$T^{3/2}$	T	$T^{5/3}$	$T^{4/3}$
[281]	$C/T \sim$	$T^{1/2}$	$-\log(T)$	$-\log(T)$	$T^{-1/3}$
[282]	$C/T \sim$	$T^{1/2}$	$-\log(T)$	$-\log(T)$	$T^{-1/3}$
[281]	$\chi \sim$	$T^{3/2}$			
[282]	$\chi \sim$	$T^{-3/2}$	$-\log(T)/T$	$T^{-4/3}$	$-T^{-1}/\log(T)$

Table 4.1. Hertz-Millis model predictions for the low-temperature limit scaling of resistivity, heat capacity, and spin susceptibility in the quantum critical region for the cases of antiferromagnetic and ferromagnetic QCPs in two and three dimensions. Adapted from [269].

for heavy fermions are FM QCPs ($Th_{1-x}U_xCu_2Si_2$ [286]). Several notable QCPs have been found in d-electron intermetallics $ZrZn_2$ [287], [288], MnSi [289], (Cr,V) [290] and in the ruthenate perovskites $Sr_3Ru_2O_7$ [291] and $Sr_xCa_{1-x}RuO_3$ [292].

The experimental trends for the NFL behavior in these systems are very diverse. In many systems near AFM QCPs, resistivity scales as T^n with $n \approx 1-1.6$, including essentially all intermediate values. Concurrent logarithmic scaling of heat capacity is common [269], [276]. Systematic comparison with the predictions of the Hertz-Millis model (Table 4.1) reveal approximate agreement but also numerous inconsistencies. In particular, many three dimensional AFM systems with T linear resistivity behave according to the 2D predictions. A partial explanation for the large scatter in observed NFL dependencies has been provided by subsequent works that noted the very large sensitivity of the predicted resistivity exponents to disorder and impurity scattering [293], [294]. As discussed in [269], [271], [276], [277], there is a lot of debate on whether accounting for the full range of complexity in materials can salvage the Hertz-Millis-type models.

The QCP systems that generated the most excitement and activity are the high T_c superconductors, most notably the cuprates [230], [295] and more recently the iron-based superconductors [296]. These are the most striking exam-

ples of the emergence of an exotic state of matter at the QCP: unconventional (non-BCS) superconductivity.

The cuprates are layered perovskite compounds in which CuO_2 planes are alternated with insulating spacer layers. While the structure and stacking sequences can be very diverse, the electronic structure is dominated by the CuO_2 sheets, producing a quasi-two-dimensional Fermi surface. Notable examples of

Temperature

AFM Mott insulator

"Strange metal"
$\rho \sim AT$

Pseudogap phase

Crossover region
$\rho \sim AT^n, 1 < n < 2$
or $\rho \sim A_1 T + A_2 T^2$

Fermi liquid
$\rho \sim AT^2$

High-T_c superconductivity

QCP

Doping
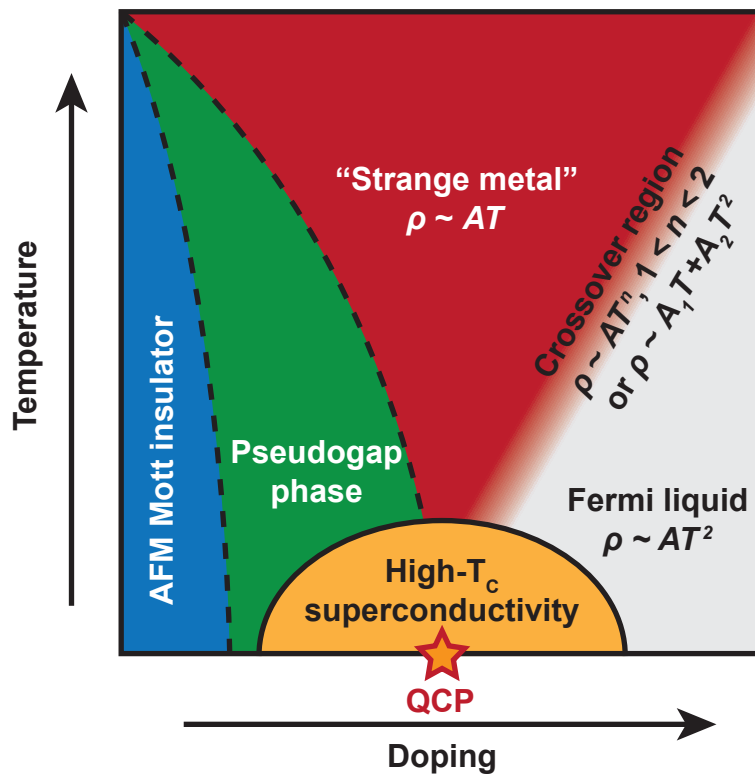
Figure 4.8. Simplified generic phase diagram of a cuprate high-T_c superconductor.

such materials are $YBa_2Cu_3O_{6+\delta}$ (YBCO), $HgBa_2CaCu_2O_{6+\delta}$ (Hg1212), $HgBa_2CuO_{4+\delta}$ (Hg1201), and $La_{2-x}Sr_xCuO_4$ (LSCO) [230], [295].

The phase diagrams of these materials follow a general universal trend, illustrated in Figure 4.8. The parent compound of these materials is an AFM Mott insulator, which is suppressed by doping (with holes or electrons). A notable feature of this underdoped region (in hole-doped cuprates) is the pseudogap phase, which corresponds to a large suppression of the single-particle density of states near the Fermi level [297]–[300]. It appears to be linked to incipient order (spin or charge density wave, electron nematic order) and is often speculated to be a precursor or competitor to unconventional superconductivity [295], [300].

In vicinity of the QCP one finds the superconducting dome, with transition temperatures as high as 135 K in Hg1212 [301] (150 K under pressure[302]). These T_c values are much higher than conceivable within a conventional BCS-type mechanism for Cooper pair formation mediated by phonon interaction. High T_c superconductivity is thus thought to be driven by unconventional pairing mechanisms, likely connected to the underlying quantum critical point [277], [296].

Another striking feature of this phase diagram is the famous T-linear resis-

tivity ("strange metal") regime, which is arguably the most famous example of non-Fermi liquid behavior. This is a very robust $\rho \sim T$ scaling that is found above the superconducting dome near the optimal doping. It can extend to temperatures as high as ≈ 1000 K [303]. In the overdoped regime beyond the superconducting dome, resistivity is also metallic and crosses over to a Fermi liquid $\rho \sim T^2$ dependence at low T [303]–[305].

4.6 Scattering rate separation

One subtle aspect of Non-Fermi liquid behavior is the concurrent phenomenon of scattering rate separation. This refers to a situation where the measured longitudinal and transverse scattering rates behave differently [274], [306]–[308]. It stands in contrast with standard transport models, where only one scattering rate is usually defined.

The electrical transport at small electrical fields (E) is conventionally described by the conductivity tensor: $J_i = \sigma_{ij} E_j$, where J is the current density. The standard isotropic in-plane conductivity can be written as:

$$\sigma = \begin{pmatrix} \sigma_{xx} & -\sigma_{xy} \\ \sigma_{xy} & \sigma_{xx} \end{pmatrix} = \frac{Ne^2\tau}{m^*} \cdot \frac{1}{1+\omega_c^2\tau^2} \cdot \begin{pmatrix} 1 & \omega_c\tau \\ -\omega_c\tau & 1 \end{pmatrix}, \tag{4.39}$$

where $\omega_c = eH/m^*$ is the cyclotron frequency. The corresponding inverted ten-

sor is the resistivity ($E_i = \rho_{ij} I_j$):

$$\rho = \begin{pmatrix} \rho_{xx} & -\rho_{xy} \\ \rho_{xy} & \rho_{xx} \end{pmatrix} = \frac{m^*}{Ne^2\tau} \cdot \begin{pmatrix} 1 & -\omega_c\tau \\ \omega_c\tau & 1 \end{pmatrix}. \tag{4.40}$$

The experimentally measured Hall effect is:

$$R_H = \frac{\rho_{xy}}{H} = \frac{1}{H} \cdot \frac{\sigma_{xy}}{\sigma_{xx}^2 + \sigma_{xy}^2} \cong \frac{1}{H} \cdot \frac{\sigma_{xy}}{\sigma_{xx}^2} = \frac{1}{eN}. \tag{4.41}$$

This is the widely used Hall effect expression routinely used to measure charge carrier concentrations in electronic materials [251]. The above derivation implies a cancellation of the scattering rate, as $\sigma_{xx} \sim \tau$ and $\sigma_{xy} \sim \tau^2$.

The experimental situation in many non-Fermi liquids is consistent with the existence of two distinct scattering rates τ_{xx} and τ_H that scale differently with temperature. This is known as the "two-lifetime" ansatz [306], [307]: $\sigma_{xx} \sim \tau_{xx}$ and $\sigma_{xy} \sim \tau_H \tau_{xx}$. It was originally postulated in the context of optimally doped cuprate superconductors, where the longitudinal scattering rate above the superconducting transition follows the "strange metal" T-linear dependence: $\rho_{xx} \sim \tau_{xx}^{-1} \sim T$. It was contrasted with the T^2 scaling of the Hall angle, a quantity that isolates the Hall scattering rate: $\cot(\theta_H) = \sigma_{xx}/\sigma_{xy} \sim \tau_H^{-1} \sim T^2$ [307], [309]–[315] (this definition of the Hall angle is essentially equivalent to the Hall mobility, with $\mu_H^{-1} = H \cdot \cot(\theta_H)$). The clear discrepancy in the temperature scaling implies $\tau_H \neq \tau_{xx}$. One direct consequence is the lack of scattering rate

140

cancellation in the Hall effect:

$$R_H = \frac{1}{H} \cdot \frac{\sigma_{xy}}{\sigma_{xx}^2} = \frac{1}{eN} \cdot \frac{\tau_H}{\tau_{xx}}. \tag{4.42}$$

The measured Hall effect now includes not only the carrier density, but also the scattering rate ratio $(\tau_H/\tau_{xx}) \neq 1$. The distinct T dependencies for τ_H and τ_{xx} translate into the Hall coefficient, even in the absence of any T-dependent change of the actual carrier density N.

Experimentally, many non-Fermi liquid systems have been documented to follow the pattern of scattering rate separation with $\tau_{xx}^{-1} \sim T^n$ ($n < 2$) and $\tau_H^{-1} \sim T^2$: most cuprate superconductor variants [307], [309]–[316], several heavy fermion materials [275], [285], [317], and V_2O_{3-x} [318]. One common trait among these materials is proximity to antiferromagnetic order [275].

While the two lifetime ansatz was remarkably successful as an empirical description for large amounts of transport data across many different materials, providing a satisfying microscopic description for it has remained challenging [274], [275], [308], [319]. In a conventional isotropic metal, there is no microscopic distinction between the scattering that sets longitudinal and transverse current. The original proposal by Anderson in 1991 invoked the decoupling of charge and spin degrees of freedom into holon and spinon quasiparticles [306], [319], by analogy with the Luttinger liquid behavior found in one-dimensional
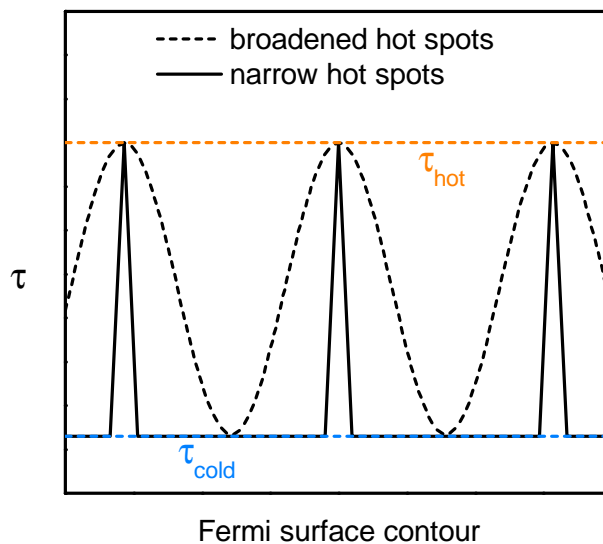
Figure 4.9. Illustration of the hot spot scenario for the scenario of anisotropic scattering across the Fermi surface contour.

systems. It is, however, quite questionable whether such a state can be stable in a two or three dimensional setting [274].

An alternative and more conservative theory postulates one single scattering rate that is anisotropic across the Fermi surface contour. It requires the existence of contour sections with high and low scattering rates ("hot" and "cold" spots). In the context of cuprates, scattering of antiferromagnetic fluctuations was invoked as a microsopic origin for this anisotropy. The "hot" spots are thus found in the vicinity of intersections between the Fermi surface and the antiferromagnetic order wavevector [320]–[322].

The simplest case to consider is a Fermi surface with an isotropic scattering rate τ_{cold} and local hot spot regions with increased scattering rate τ_{hot} (illustrated in Figure 4.9). The longitudinal conductivity is proportional to the integrated average of τ across the Fermi surface, and the contributions of hot spots become negligible if they are very narrow: $\sigma_{xx} \sim \tau_{cold}$. In contrast, σ_{xy} is approximately proportional to the product of the two scattering rate extrema: $\sigma_{xy} \sim \tau_{cold}\tau_{hot}$. This results in the appearance of scattering rate separation with $\tau_{xx} = \tau_{cold}$ and $\cot(\theta_H) \sim \tau_H = \tau_{hot}$ [316], [323], [324].

The simplicity of this result breaks down if the "hot spots" are broadened in any way. This is the case in cuprates, where the scattering rate along the Fermi surface contour is cosine-like [321], [325]. This results in mixing of τ_{cold} and τ_{hot} in the transport integrals. Integration over realistic Fermi surface contours gives approximately $\sigma_{xx} \sim \sqrt{\tau_{cold}\tau_{hot}}$, which can be consistent with the experimentally observed T scaling of σ_{xx} and $\cot(\theta_H)$ [325]–[327]. This model does, however, imply a very high sensitivity of the scattering rate separation and its scaling to broadening of hot spots from disorder. This will be found to be inconsistent with experiment in the discussion of Chapter 6.

Chapter 5

T^2 resistivity in SrTiO$_3$

5.1   Scattering mechanisms in uniformly doped SrTiO$_3$

This Chapter presents a phenomenological description of scattering rates in electron doped SrTiO$_3$[1]. The materials systems presented here are uniformly doped thick R:SrTiO$_3$ (R = La, Gd) films and interface-doped SrTiO$_3$/RTiO$_3$ heterostructures (R = Gd, Sm). In particular, the discussion will focus on the robust $\rho \sim T^2$ regime observed in all these systems. It will be based on electrical transport data from thick films of La and Gd-doped SrTiO$_3$ grown by MBE, previously published in [268] and [212] (data courtesy of Adam Kajdos, Tyler Cain and Pouya Moetakef), as well as additional data from similar films courtesy of

---

[1]The results discussed in this Chapter have been previously published in [201], [203].

Brandon Isaac. Growth procedures have been outlined in [45], [61], [267] and Chapter 1.4. Chapter 5.2 will present an analysis of the electrical transport in SrTiO$_3$/GdTiO$_3$ heterostructures, originally published in [61]. Chapter 6 will focus on the special case of SrTiO$_3$ confined in narrow RTiO$_3$/SrTiO$_3$/RTiO$_3$ quantum wells.

Figure 5.1(a) shows the temperature dependence of the Hall mobility for La-doped SrTiO$_3$ with a low carrier density ($N = 8 \times 10^{17}$ cm^{-3}). $\mu(T)$ shows an overlap of three distinct scattering contributions that add according to the classic Mathiessen's rule:

$$\mu^{-1}(T) = \mu_0^{-1} + \alpha T^2 + \mu_{LO}^{-1}(T) \tag{5.1}$$

where μ_0 is the approximately T-independent contribution that dominates in the low-T limit. Across many material systems μ_0 is nearly universally associated with disorder. In this context, a likely explanation is scattering between electrons and ionized impurities [3].

Phonon scattering dominates in the high-T limit. This contribution can be described [3], [259] as scattering between the longitudinal optical (LO) phonon branch and polarons. Following the discussion in Chapter 4.4.3:

$$\mu_{LO}(T) = \frac{K_{LO}}{\hbar\omega_{LO}} \left(\exp\left(\frac{\hbar\omega_{LO}}{k_B T}\right) - 1 \right) \tag{5.2}$$

$$K_{LO} = \frac{\hbar}{2K_{ep}} \frac{e}{m_p} \left(\frac{m^*}{m_p}\right)^2 f(K_{ep}) \tag{5.3}$$
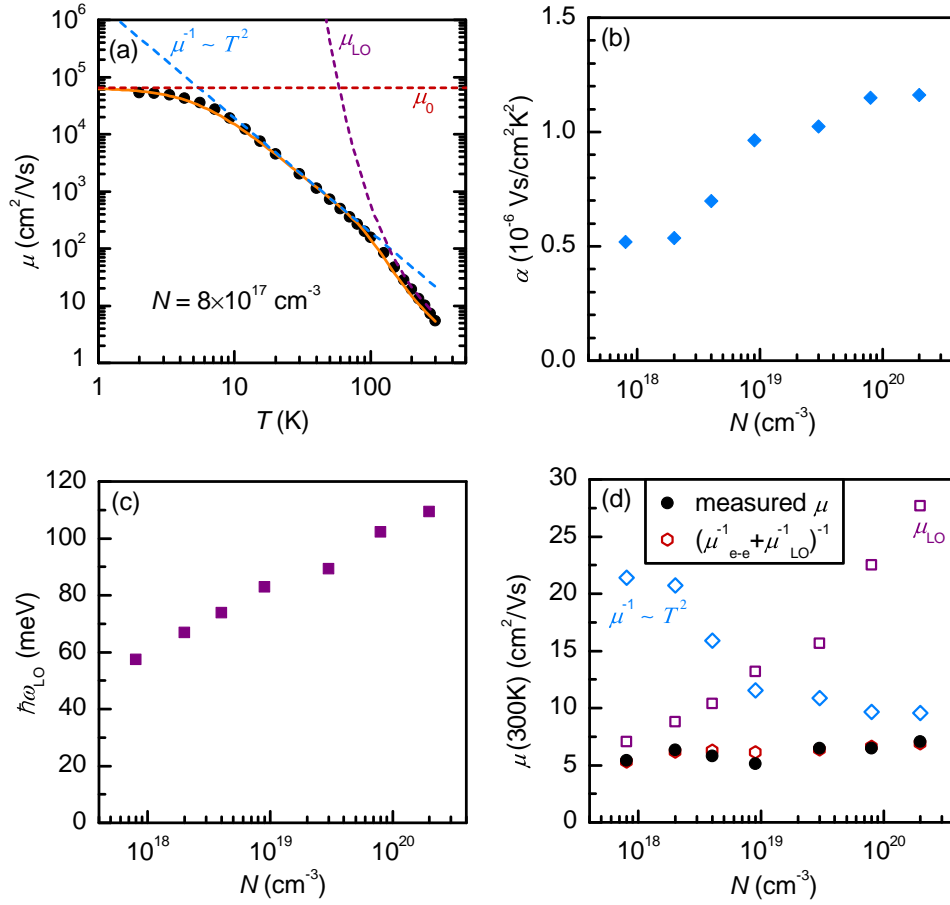
Figure 5.1. (a) T dependence of the Hall mobility for La:SrTiO$_3$ with a carrier density of $N = 8 \times 10^{17}$ cm^{-3}. The solid line is a fit to Equation 5.1, the dashed lines are the contributions of the different scattering mechanisms. The fit parameters α (b) and ω_{LO} (c) are shown as a function of the doping level. (d) Comparison of the measured electron mobility at room temperature (solid circles), the limiting contributions from the μ_{LO} (squares) and αT^2 (diamonds) terms extracted by fitting, as well as their sum (hexagons). Reprinted with permission from [201]. Copyright 2015, AIP Publishing LLC.

146
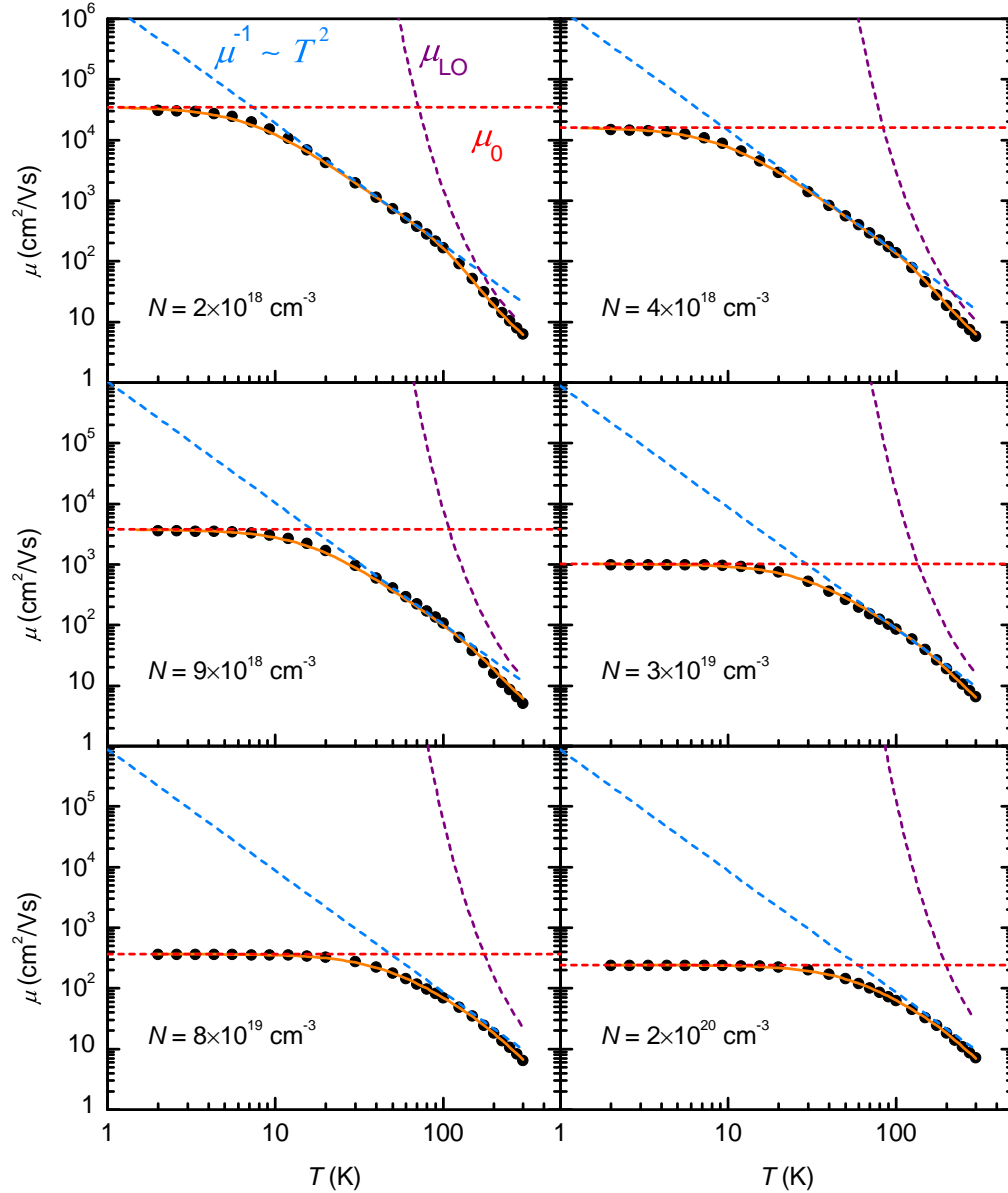
Figure 5.2. Temperature dependence of Hall mobility in La:SrTiO$_3$ with fits to Equation 5.1 for different doping levels. Reprinted with permission from [201]. Copyright 2015, AIP Publishing LLC.

where ω_{LO} is the LO phonon frequency, K_{ep} is the electron-phonon coupling constant, m^* and m_p are the effective electron and polaron masses. For $K_{ep} = 2.6$ [3] and an effective electron mass of 1.8 times the free electron mass [208], $K_{LO} \approx 0.12$ cm^2/Vs.

The intermediate temperature range is dominated by a T^2 power law. It should be noted that given the approximately T-independent carrier density in SrTiO$_3$, this αT^2 scaling of mobility is equivalent to the AT^2 scaling of resistivity, with $\alpha = AeN$.

These three scattering contributions describe the entire cryogenic T range for doped SrTiO$_3$, as shown in Figures 5.1(a) and 5.2 for several (La,Sr)TiO$_3$ films with $N = 8 \times 10^{17} - 2 \times 10^{20}$ cm^{-3}. The solid orange lines show fits to Equation 5.1, with μ_0, α and ω_{LO} used as adjustable parameters. Red, blue and purple dashed lines plot the individual contributions of μ_0, $\mu \sim \alpha T^2$ and μ_{LO}, respectively.

Figures 5.1(b) and (c) show the doping dependence for α and ω_{LO}. The extracted values of $\hbar\omega_{LO}$ are in the 60-110 meV range. This is consistent with the previous understanding that this scattering range is coupled to the two highest lying LO phonon modes at 99 and 58 meV [3], [328]. The experimentally extracted values of ω_{LO} represent a weighted average value.

In the high N limit, the increased ω_{LO} corresponds to higher μ_{LO}, i.e. the associated ceiling for μ in this T range is increased. This can be seen qualitatively in Figure 5.2: μ_{LO} is exclusively dominant above 200 K at low N, but the crossover between $\mu \sim \alpha T^2$ and μ_{LO} progressively moves to higher T with increasing N. For $N > 10^{19}$, μ_{LO} is not the dominant scattering mechanism even at room temperature. This crossover is illustrated in Figure 5.1(d), which compares $\mu \sim \alpha T^2$ and μ_{LO} contributions at 300 K.

The increased μ_{LO} at high N is in agreement with first-principle calculations [328] that predict higher electron-phonon scattering rates near the center of the Brillouin zone. For a larger Fermi surface at high N, the smaller scattering rates at higher momentum dominate, increasing μ_{LO}. Another potential contribution is a higher screening of the electron-phonon interaction at high electron density.

It is interesting to note that due to the simultaneous increase of α and ω_{LO}, the overall mobility at 300 K stays at ≈ 6 cm^2/Vs. While the constant nature of the trend for μ(300K) versus N in Figure 5.1 can be used as an argument for one single limiting scattering mechanism, a crossover is clearly apparent when considering the full T dependence at different values of N in Figure 5.2.

The following discussion will focus on the $\mu \sim \alpha T^2$ region. As discussed in Chapter 4.4, the traditional explanation for T^2 resistivity is electron-electron

scattering, as it is consistent with the prediction of Fermi liquid theory. The same assignment was also made for the T^2 resistivity observed in the intermediate T range in doped SrTiO$_3$ [206], [265]. However, several issues with this explanation are outlined below.

Figure 5.3 recasts the transport data in the form of temperature derivative of resistivity ρ. In addition to the data for La:SrTiO$_3$ analyzed above, it incorporates data from Gd-doped of SrTiO$_3$ films, including the very high doping limit before the Mott metal-insulator transition.

The above description of mobility based on Equation 5.1 is equivalent to:

$$\rho(T) = \rho_0 + AT^2 + \frac{1}{e\mu_{LO}N} \tag{5.4}$$

$$\frac{d\rho(T)}{dT} = 2AT + \frac{1}{eN}\frac{d\mu_{LO}^{-1}}{dT} \tag{5.5}$$

where $A = \alpha/(eN)$. Plotting the derivative $d\rho/dT$ against T on a log-log scale is a common procedure [255] for characterizing power laws in resistivity ($\rho = AT^n$). Any such scaling gives a straight line on this plot. With $d\rho/dT = nAT^{n-1}$, the exponent value corresponds to the slope of the straight line. The A parameter sets the vertical position of the curve.

The straight black dashed lines in Figure 5.3 correspond to the T^2 resistivity. They closely follow the experimental data in the intermediate region across a little under a decade of temperature. Depending on the doping level, the lower

boundary is at 10-30 K and the upper boundary is between 100 and 300 K. At higher, T, the increase of $d\rho/dT$ corresponds to a crossover towards LO phonon scattering (Equation 5.2). The deviations in the low T limit are, however, not described by Equation 5.5, according to which the disorder contribution is expected to be removed in this plot. As discussed in more detail in Chapter 6.3, this is likely a consequence of a T-dependent μ_0 contribution.

Figure 5.4 shows the doping dependence of A, a quantity that represents the amplitude of the T^2 scattering rate. To emphasize the generality of the trend for A versus N, this plot includes data from MBE-grown films as well as from the
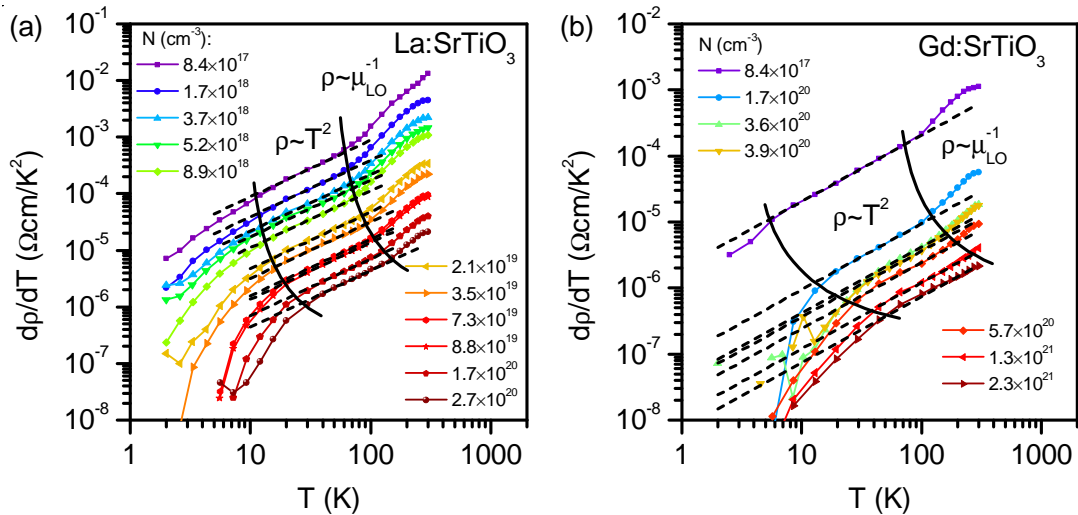
Figure 5.3. Logarithmic plots for the temperature derivatives of resistivity in La:SrTiO$_3$ (a) and Gd:SrTiO$_3$ (b). Dashed lines correspond to the T^2 scaling of resistivity.
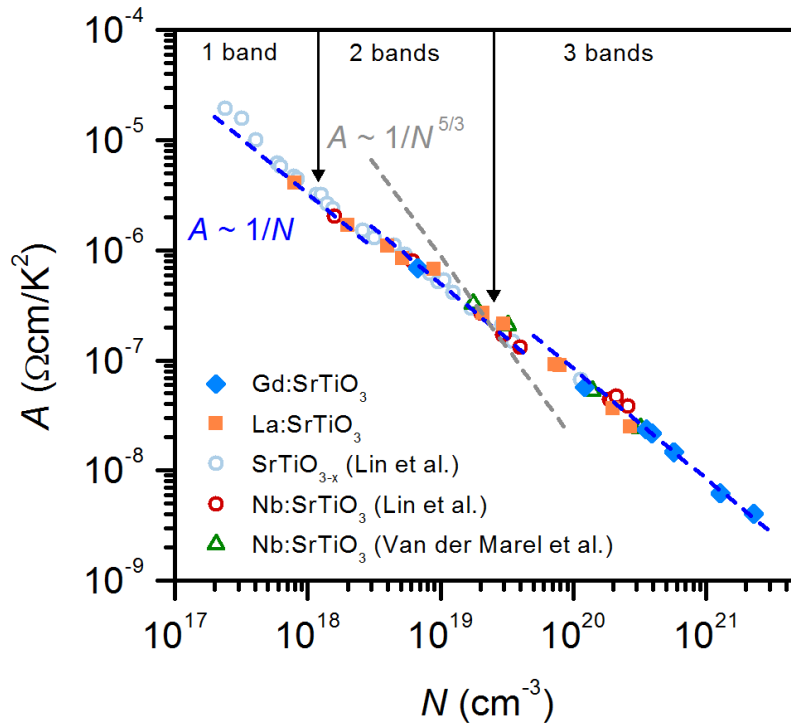
Figure 5.4. Doping dependence of the amplitude coefficient of the T^2 resistivity. The plot shows data from La:SrTiO$_3$ and Gd:SrTiO$_3$ thin films and bulk single crystal data from [206], [329]. Blue dashed lines correspond to the $A \sim N^{-1}$ scaling (carrier density independent scattering). The grey dashed line is the $A \sim N^{-5/3}$ scaling from [262], [330]. Reprinted from [203], licensed under CC BY 4.0.

literature: oxygen deficient and Nb-doped single crystals [206], [329].

This plot makes a case for $A \sim 1/N$ scaling that dominates across four orders of magnitude of N (blue dashed lines in Figure 5.4). In the Drude picture of conductivity, this is equivalent to a carrier density independent scattering rate:

$$AT^2 = \frac{m^*}{Ne^2} \cdot \Gamma(T^2), \tag{5.6}$$

where $\Gamma(T^2)$ is the scattering rate that increases as T^2. Using a simple dimensional analysis argument, one can write [250]:

$$\Gamma(T^2) = B \cdot \frac{(k_B T)^2}{\hbar E}, \tag{5.7}$$

where B is a dimensionless constant. Given that Γ has units of inverse time, the right side of this Equation must contain $\hbar$ (in eV·sec) and an energy scale E.

In the case of electron-electron scattering within the Fermi liquid framework, this energy scale is the Fermi energy E_F [250], [254], [262], [264]. This is inconsistent with a carrier density-independent Γ. Adding charge carriers to the material inevitably results in the expansion of the Fermi surface, i.e. E_F is a monotonously increasing function of N. This would inevitably translate in a strong N dependence of Γ, which is not the case experimentally.

Figure 5.4 does shows weak steps in the $A(N)$ curve near $N = 10^{18}$ and 3×10^{19} cm^{-3}. They may be associated with the thresholds for filling of higher

lying t_{2g} bands (see Chapter 4.1). Given that the heavy electron band is expected to be the lowest lying one [188], [208], the increased A is inconsistent with a change of the effective mass. One can, however, reasonably expect a change in the density of states at the Fermi level or a different multi-band effect to affect the scattering rate Γ.

One aspect to consider is the potential carrier density dependence of the dimensionless pre-factor B, which incorporates the effects of screening. For instance, in the case of Thomas-Fermi type screening of the electron-electron scattering and a spherical Fermi surface, one expects $A \sim N^{-5/3}$ [262]. This dependence holds true for the T^2 regime in TiS$_2$ [330]. This scaling is, however, not applicable for doped SrTiO$_3$, as illustrated by the grey dashed line in Figure 5.4. While one can make different assumptions for screening, an accidental cancellation of the N scaling between B and Γ is unlikely, particularly across four orders of magnitude of carrier density.

Beyond the inconsistency in carrier density scaling, another way to illustrate the inapplicability of Fermi liquid theory with $E = E_F$ is to compare the magnitudes of these energy scales. Figure 5.5(a) contrasts the experimentally extracted energy scale E of the T^2 regime and E_F in the approximation of a

simple spherical Fermi surface:

$$E = B \cdot \frac{k_B^2}{\hbar e^2} \cdot \frac{m^*}{AN} = B \cdot \frac{k_B^2}{\hbar e} \cdot \frac{m^*}{\alpha}, \qquad (5.8)$$

$$E_F = \frac{\hbar^2}{2m^*} \cdot \left(3\pi^2 N\right)^{2/3}. \qquad (5.9)$$

For both scales, the approximation $m^* = 1$ was taken. Moreover, the prefactor B was also assumed to be unity by analogy with the T-linear resistivity [331], an approximation that is further justified in Chapter 6.2. Under these assumptions, the implied energy scale of the T^2 resistivity is approximately 10 meV. While
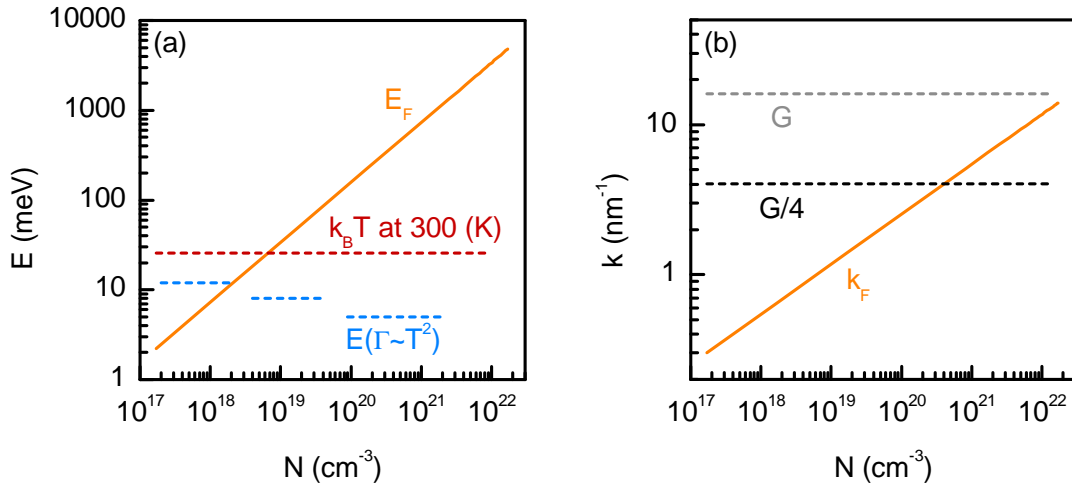
Figure 5.5. (a) Comparison of energy scales in uniformly doped SrTiO$_3$: temperature $k_B T$, energy scale E for the T^2 scattering (Equation 5.8), and Fermi energy E_F (Equation 5.9). (b) Comparison of the Fermi wave vector k_F, SrTiO$_3$ Brillouin zone size G, and the required Fermi surface size for Umklapp scattering processes ($G/4$).

this approximately corresponds to E_F at low carrier densities, the discrepancy reaches almost two orders of magnitude for $N = 10^{20} - 10^{21}$ cm^{-3}. The ensemble of the discussion above implies that $E \neq E_F$.

Figure 5.5(a) illustrates another inconsistency with Fermi liquid theory which only holds at low temperatures ($k_B T \ll E_F$) [250], [254], [262], [264]. Experimentally, the T^2 region extends up to room temperature. As shown in Figure 5.1, it is dominant for $N > 10^{19}$ cm^{-3}. For lower N, the electron-phonon scattering is larger, but the T^2 contribution is still detectable at 300 K. The comparison between E_F and $k_B T$ at 300 K reveals a crossover at $N \approx 10^{19}$ cm^{-3}. E_F is much larger only at very high N. There is a very large carrier density range below $N \approx 10^{20}$ cm^{-3} where it is difficult to justify the assumption $k_B T \ll E_F$.

As originally discussed in [329], a separate dilemma concerns the necessary conditions for momentum dissipation in electron-electron scattering. As discussed in Chapter 4.4.4, Umklapp processes can occur only if the Fermi surface is large than approximately a quarter of the Brillouin zone width ($k_F > G/4$). With $G = 2\pi/a$ for a cubic crystal, Figure 5.5(a) compares $G/4$ with k_F (estimated using $\hbar^2 k_F^2 = 2m^* E_F$). It illustrates that there is a large range of low carrier densities ($N < 10^{20}$ cm^{-3}) where the Fermi surface is too small to allow Umklapp scattering. Given that they are allowed at high N, one expects a sharp increase in the corresponding scattering contribution near $N \approx 10^{20}$

cm^{-3} [265]. As discussed above, this is not observed experimentally, where α is approximately constant with N across many orders of magnitude.

An alternative mechanism for momentum dissipation is Baber scattering [254], which involves scattering between light and heavy electrons. Such multi-band scattering has been argued to contribute to resistivity, even for normal (non-Umklapp) processes [254], [265]. It should not, however, be applicable in the extremely low N limit ($N < 10^{18}$ cm^{-3}) of single band occupancy [329].

5.2 T^2 resistivity in 2D electron liquids

This Chapter presents an analysis of the electrical transport in SrTiO$_3$/GdTiO$_3$ heterostructures, originally published in [61]. As outlined in Chapter 4.3, the polar discontinuity at the SrTiO$_3$/RTiO$_3$ interface creates a 2DEL with a mea-sured carrier density of $N = 3.4 \times 10^{14}$ cm^{-2}. This very large sheet density is largely confined in the SrTiO$_3$ layer within a few nanometers from the inter-face. The LSAT/SrTiO$_3$/GdTiO$_3$ heterostructures discussed below were grown by MBE, with SrTiO$_3$ layer thicknesses ranging from 2 to 88 nm and the top GdTiO$_3$ layer being either 10 or 20 nm [61], [63], [64], [237].

Such heterostructures exhibit metallic conduction. It can be measured by depositing Ti/Au contacts on the top GdTiO$_3$ surface. Figure 5.6 shows the Hall

mobility in the $T = 2 - 300$ K range. The temperature dependence can be described as:

$$\mu^{-1}(T) = \mu_0^{-1} + \alpha T^2 \qquad (5.10)$$

The LO phonon scattering contribution at high T is undetectable. The T dependence is dominated by the T^2 resistivity up to room temperature. Disorder scattering (μ_0) dominates at low T, in particular when the SrTiO$_3$ layer is thin.
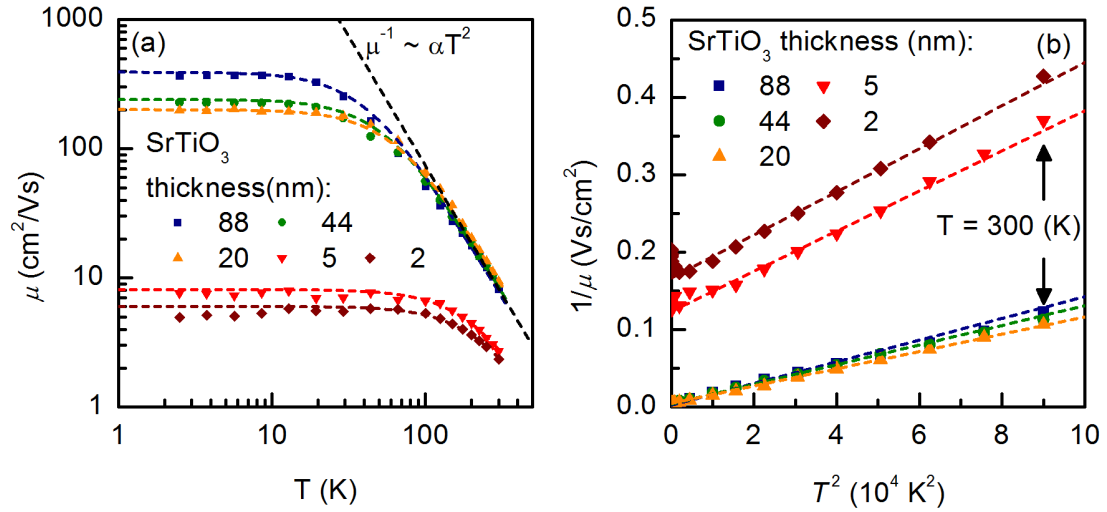
Figure 5.6. (a) Hall mobility in LSAT/SrTiO$_3$/GdTiO$_3$ heterostructures with different SrTiO$_3$ thicknesses. The black dashed line is the T^2 scaling observed in highly doped bulk SrTiO$_3$ (3 partially filled bands region in Figure 5.4). (b) Same data replotted as μ^{-1} against T^2, illustrating the dominance of T^2 scattering at high T. Reprinted with permission from [201]. Copyright 2015, AIP Publishing LLC.

This situation is analogous to that of uniformly doped SrTiO$_3$ in the high N limit. If ones assumes that the 2DEL is uniformly spread across the first 3 nm of the SrTiO$_3$ layer, the volume density can be estimated to be $\approx 10^{21}$ cm^{-3}. This is a rough estimate, as the vertical profile of the volume carrier density of the 2DEL is expected to be highly non-uniform. It does, however reflect the extremely high density nature of the electrical transport.

The fairly low value of μ_0 is consistent with the high volume carrier density and a contribution from interface roughness scattering. The latter is expected to dominate in ultrathin conducting layers [332] and is consistent with a strong increase of μ_0 when the SrTiO$_3$ layer is thin.

Figures 6.1(a) and (b) compares α, the T^2 scattering amplitude pre-factor, for the cases of uniform doping interface-doped 2DELs. For 2DELs in thick SrTiO$_3$ it is approximately constant at $\alpha \approx 1 - 1.5 \times 10^{-6}$ Vs/cm^{2}K^2, which is similar to bulk doped SrTiO$_3$ with $N > 10^{20}$ cm^{-3}.

The increase of α for 2 and 5 nm thick SrTiO$_3$ has been interpreted as an effect of strong correlations in the extremely high carrier density limit [237]. An analogy can be made with the phase diagram of bulk R_xSr$_{1-x}$TiO$_3$ (Figure 4.2), where α is known to increase in vicinity of the Mott metal-insulator transition [210]–[212], [237]. The effects of 2DEL confinement in narrow SrTiO$_3$

quantum wells will be discussed further in Chapter 6.

The main message of this Chapter is the similarity of the scattering amplitude α in uniform and interface-doped SrTiO$_3$. This implies a common origin of T^2 resistivity in both cases. Therefore, the above discussion of the inconsistencies between Fermi liquid theory and experimental transport data in bulk and bulk-like R_xSr$_{1-x}$TiO$_3$ also applies to 2DEL-based heterostructures such as LSAT/SrTiO$_3$/RTiO$_3$ and LSAT/RTiO$_3$/SrTiO$_3$/RTiO$_3$.

Additionaly, we note the absence of the LO phonon scattering contribution
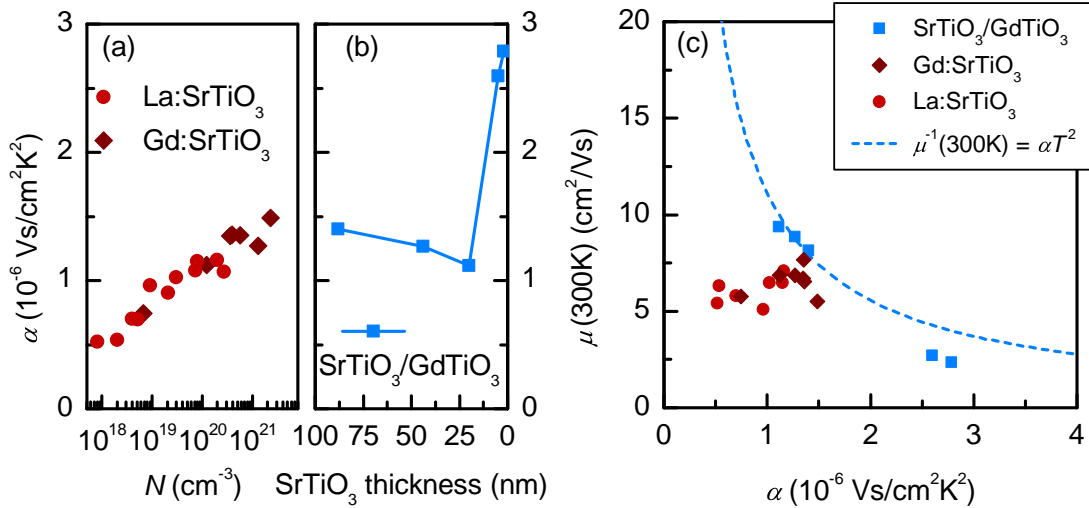
Figure 5.7. Comparison of the α parameters of T^2 mobility in (a) uniformly doped SrTiO$_3$ and (b) SrTiO$_3$/GdTiO$_3$ heterostructures. (c) Measured electron mobilities at room temperature as a function of the α parameter. Reprinted with permission from [201]. Copyright 2015, AIP Publishing LLC.

in SrTiO$_3$/RTiO$_3$ heterostructures. Figure 6.1(c) shows the measured room temperature mobility against α, the extracted T^2 region slope. In heterostructures with thick SrTiO$_3$, μ at 300 K corresponds exactly to the value expected from T^2 slope, signaling the complete absence of any interference from the LO phonon. When comparing samples with same α, the mobility in the heterostructures is higher than in uniformly doped SrTiO$_3$, where the mobility is degraded by the LO phonon. One possible explanation for this discrepancy is enhanced screening of the LO phonon due to the large density of states in the confined 2DEL [201].

An intriguing prospect is illustrated by the dashed blue line in 6.1(c): in the absence of LO phonon scattering, the 300 K mobility ceiling corresponding to the T^2 region can be quite high. For values of α typical in low doped bulk SrTiO$_3$, this ceiling could exceed 20 cm^2/Vs. It is an open question whether it is feasible to isolate low α while simultaneously screening out the LO phonon (for example, in heterostructures with low electron doping levels), leading to enhanced electron mobility at room temperature.

Chapter 6

Quantum criticality, T^n resistivity, and scattering rate separation in confined electron liquids

6.1 Tuning of quantum criticality by confinement in a heterostructure

This Chapter will focus on the $RTiO_3/SrTiO_3/RTiO_3$ (R = Gd, Sm) quantum well system[1]. It will make a case for the existence of a quantum critical point (QCP) that is crossed by tuning the $SrTiO_3$ well thickness.

Figure 6.1 illustrates the quantum well structure. When $SrTiO_3$ is sandwiched between two $RTiO_3$ layers, high carrier density 2DELs are formed at both the top and bottom $SrTiO_3/RTiO_3$ interfaces, with $N = 3.4 \times 10^{14}$ cm^{-2} for each interface. This produces a total sheet density of 6.8×10^{14} cm^{-2}, which is largely confined within the $SrTiO_3$ layer within a few nanometers from the interface, and partially spread further into $SrTiO_3$ [238].

As the $SrTiO_3$ layer thickness is reduced to the point where it is comparable to the vertical spread of the 2DELs, quantum confinement effects become relevant. The sheet density remains constant, but its vertical spread is reduced and the corresponding volume density is increased.

The growth of these heterostructures by MBE enables atomic layer-level control of $SrTiO_3$ thickness. In the following, this thickness is defined in terms of the

---

[1]The results discussed in this Chapter have been previously published in [202], [203].
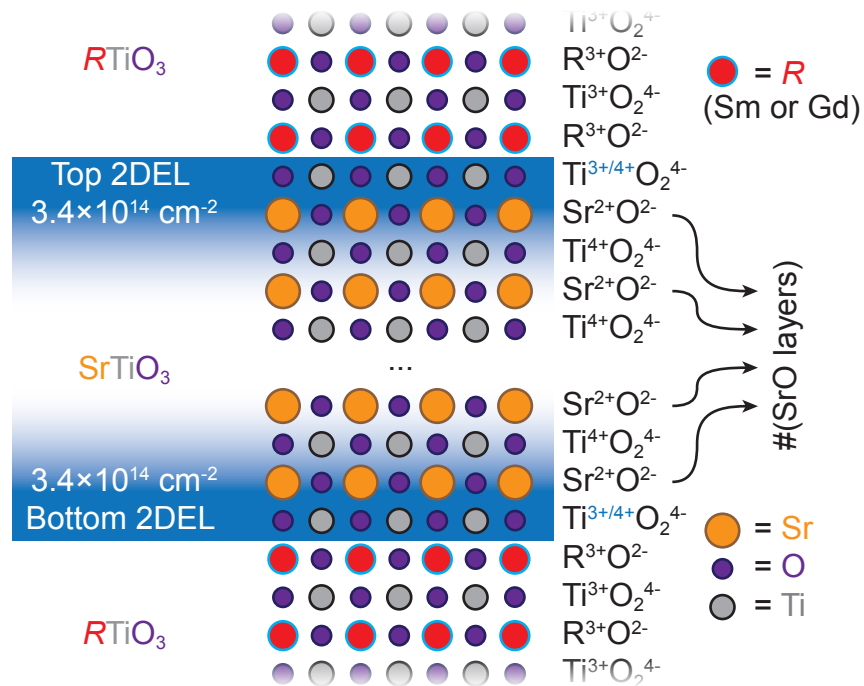
Figure 6.1. Illustration of 2DEL confinement in $R\text{TiO}_3/\text{SrTiO}_3/R\text{TiO}_3$ quantum wells. Reprinted with permission from [202]. Copyright 2015, American Physical Society.

number of SrO layers sandwiched between thicker $R\text{TiO}_3$, as illustrated in Figure 6.1. Details of quantum well growth can be found in [61], [63], [64], [237], transport data analyzed in the following is courtesy of Tyler Cain, Christopher Freeze and Brandon Isaac.

Figure 6.2 presents a temperature - quantum well thickness phase diagram for $\text{GdTiO}_3/\text{SrTiO}_3/\text{GdTiO}_3$ and $\text{SmTiO}_3/\text{SrTiO}_3/\text{SmTiO}_3$ heterostructures. The key common feature in both these cases is a quantum phase transition towards
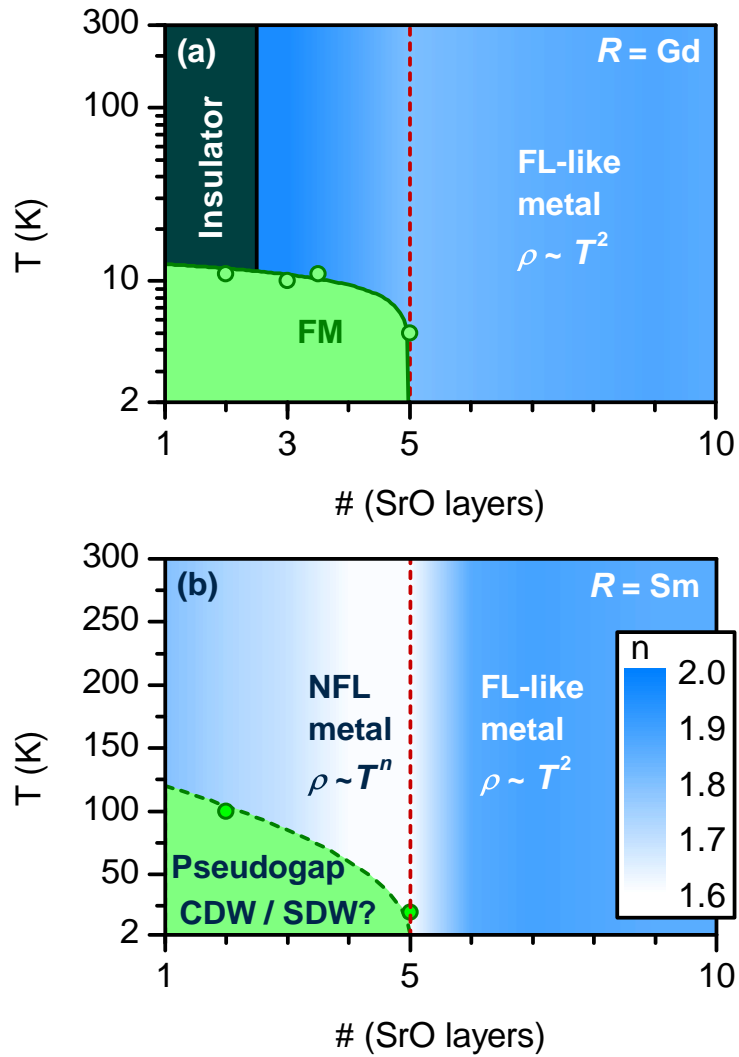
Figure 6.2. Temperature - quantum well thickness phase diagram for $SrTiO_3$ embedded in (a) $GdTiO_3$ and (b) $SmTiO_3$. The red lines indicates the QCP at 5 SrO layer thickness. Ferromagnetic ordering temperatures are from [333], [334]. Approximate pseudogap emergence points from [335].

an ordered phase in the limit of ultrathin $SrTiO_3$. The QCP is at a thickness of 5 SrO layers. The argument for this statement relies on four separate pieces of evidence, briefly summarized as follows:

- Anomalous resistivity exponents ($\rho \sim T^n$, $n \approx 1.6$)) in vicinity of the QCP for $R =$ Sm

- Separation of the longitudinal and Hall scattering rates ($\tau_{XX} \neq \tau_H$) that peaks at the QCP for both $R =$ Gd and Sm, consistent with a quantum critical correction to the Hall scattering rate.

- QPT towards ferromagnetic order in ultrathin $SrTiO_3$ bound by $GdTiO_3$

- QPT towards an ordered phase (spin or charge density wave) with a pseudogap in ultrathin $SrTiO_3$ bound by $SmTiO_3$

The first two items are a result of a systematic description of electrical transport in these heterostructures within the framework of scattering rate separation. It will be the major focus of this Chapter.

Observation of ferromagnetic order in $GdTiO_3/SrTiO_3/GdTiO_3$ quantum wells was originally documented in [333]. For thin $SrTiO_3$ wells (3 or 4 SrO layers), the longitudinal magnetoresistance shows well-defined hysteretic features. An example is shown in Figure 6.3(a) for a 3 SrO layer thick quantum well at $T =$
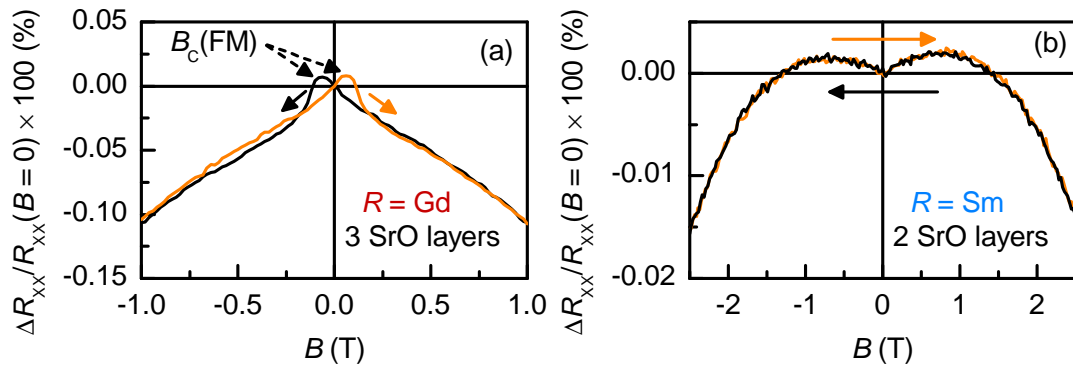
Figure 6.3. Magnetoresistance at $T = 2$ K for ultrathin $SrTiO_3$ quantum wells embedded in (a) $GdTiO_3$ and (b) $SmTiO_3$

2 K. These decrease in magnitude and move to smaller magnetic field at higher T. They disappear completely above $T \approx 10$ K

The hysteretic peaks near ± 0.1 Tesla are attributed to magnetization reversal in $SrTiO_3$. This ferromagnetic order is distinct from the ferrimagnetism in the bounding $GdTiO_3$ layers. The existing evidence for this assignment is three-fold: (1) the electrical conduction and thus magnetoresistance is dominated by $SrTiO_3$, while $GdTiO_3$ is insulating and should not contribute to magnetoresistance. (2) there is a discrepancy between the ordering temperature observed in magnetoresistance (≈ 10 K, dominated by $SrTiO_3$) and in the SQUID (super-conducting quantum interference device) measurement (≈ 20 K, dominated by $GdTiO_3$). (3) Polarized neutron reflectivity measurements on $[GdTiO_3/SrTiO_3]$ superlattices are consistent with the presence of two distinct magnetic moments

in $GdTiO_3$ and $SrTiO_3$, which is consistent with the thickness and temperature dependence inferred from magnetoresistance measurements [334].

Another argument in favor of the interface-induced ferromagnetism picture is based on substituting the ferrimagnetic $GdTiO_3$ bounding layer for $SmTiO_3$, which is an antiferromagnet in bulk [216], [221]. Magnetoresistance in $SmTiO_3$/ $SrTiO_3$/ $SmTiO_3$ quantum wells is very different and does not show any hysteresis (Figure 6.3(b)). This indicates the absence of ferromagnetic order in $SrTiO_3$. The exact nature of the magnetic ground state of ultrathin $SrTiO_3$ embedded in $SmTiO_3$ is at present unclear, as discussed further below and in [335].

Another important aspect of the phase diagram for $R = Gd$ in Figure 6.2(a) is the metal-insulator transition (MIT) between the 2 and 3 SrO layer thicknesses. Above this critical thickness, the longitudinal resistance of these heterostructures is metallic. This abrupt transition to insulating character was documented to occur simultaneously with a structural distortion in $SrTiO_3$ [336]. The orthorhombic octahedral distortion inherent to the bounding $GdTiO_3$ layer propagates into $SrTiO_3$ if it is only 1 or 2 atomic layers thick. In contrast, the propagation of the octahedral distortion into $SrTiO_3$ is minimal when it is bound by $SmTiO_3$. These structures remain metallic even when the quantum well contains only 1 SrO layer.
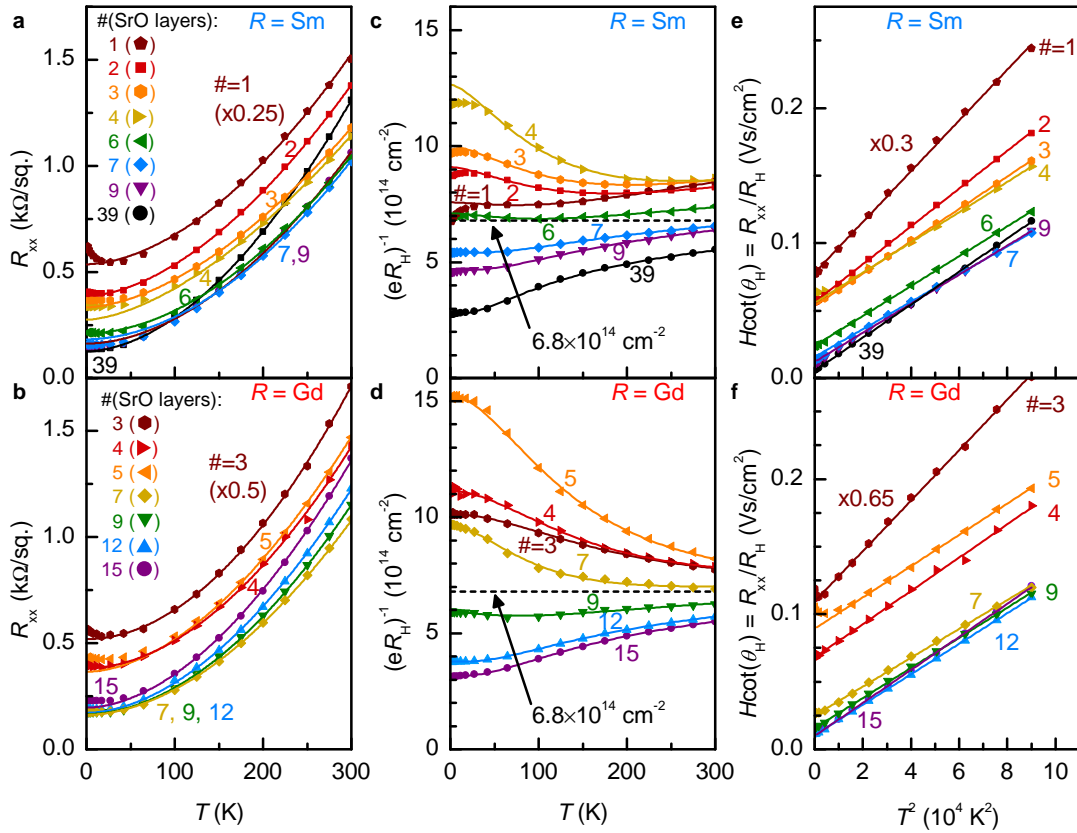
Figure 6.4. Transport data for RTiO$_3$/SrTiO$_3$/RTiO$_3$ quantum wells in SmTiO$_3$ (top row) and GdTiO$_3$ (bottom row). Labels indicate the different SrTiO$_3$ thicknesses. (a,b) Longitudinal resistance, (c,d) inverse Hall coefficient, (e,f) Hall angle or, equivalently, inverse Hall mobility. All solid lines are fits to Equations 6.1, 6.2 and 6.3, using a single set of adjustable parameters for each sample. Reprinted with permission from [202]. Copyright 2015, American Physical Society.

Figure 6.4 shows a full data set of the electrical transport in SmTiO$_3$/ SrTiO$_3$/ SmTiO$_3$ (top row) and GdTiO$_3$/SrTiO$_3$/GdTiO$_3$ (bottom row) quantum well structures. The quantities shown are the longitudinal sheet resistance R_{XX}, the inverse Hall coefficient $(eR_H)^{-1}$, and the inverse Hall mobility $\mu_H^{-1} = R_{XX}/R_H$. Qualitatively, all these heterostructures are metallic and show a complex evolution of Hall effect with both temperature and SrTiO$_3$ thickness.

The framework of scattering rate separation discussed in Chapter 4.6 provides a remarkably simple empirical description of this data, using the ansatz $\tau_{xx} \sim T^n$ and $\tau_{xx} \sim T^2$. In this picture the longitudinal sheet resistance follows a temperature exponent n that can take non-Fermi liquid values ($1 \leq n \leq 2$):

$$R_{xx} = \frac{m^*}{e^2 N \tau_{xx}} = \frac{1}{eN\mu_{xx}} = R_0 + AT^n. \tag{6.1}$$

This expression accounts for the presence of disorder scattering in form of a T-independent residual ($R_0^{-1} = e^2 N \tau_{xx}(T=0)/m^*$). The Hall scattering rate is isolated in the Hall angle $\cot(\theta_H)$, or equivalently the inverse Hall mobility:

$$\mu_H^{-1} = H \cot(\theta_H) = \frac{R_{xx}}{R_H} = \frac{m^*}{e\tau_H} = H(C + \alpha T^2) \tag{6.2}$$

The distinction between "longitudinal" mobility $\mu_{xx} = e\tau_{xx}/m^*$ and the "Hall" mobility μ_H lies in the choice of assumption for the carrier density N. The standard calculation of Hall mobility contains the conventional assumption that $N = (eR_H)^{-1}$, including its strong T dependence. In contrast, Equation 6.1

contains an implicit assumption that the true carrier density $N = 6.8 \times 10^{14}$ cm^{-2} is independent of temperature. Under the second assumption, the measured Hall effect is no longer strictly given by the carrier density, but also the ratio of the two scattering rates (μ_{xx}/μ_H). Combining Equations 6.1 and 6.2, the measured Hall coefficient can be modeled as a ratio of two distinct power laws:

$$\frac{1}{eR_H} = N \cdot \frac{\mu_{xx}}{\mu_H} = \frac{H}{e} \frac{C + \alpha T^2}{R_0 + AT^n} \qquad (6.3)$$

The implication of this expression is that the measured temperature dependence of $(eR_H)^{-1}$ is contained in the scattering rate ratio μ_{xx}/μ_H, which causes deviations from $(eR_H)^{-1} = 6.8 \times 10^{14}$ cm^{-2}.

All solid lines in Figure 6.4 are self-consistent fits to Equations 6.1, 6.2 and 6.3, using a single set of adjustable parameters for each sample. The first step in the fitting procedure used Equation 6.2 to extract C and α that describe the $\mu_H^{-1} - T^2$ scaling. It should be noted that while the temperature exponent was fixed in this case, fitting with a free exponent gave very similar results to a strict T^2 dependence. The second step used Equation 6.3 to fit the $(eR_H)^{-1} - T$ data using fixed values of C and α from the first step. R_0, A and n were the adjustable parameters.

Self-consistency of this description was checked for R_{xx} by plotting the Equation 6.1 in Figures 6.4(a) and (b) using the values of R_0, A and n extracted in

the last fitting step. No fitting on R_{xx} data was performed in this procedure.

A key component of the scattering rate separation is the appearance of NFL exponents $n < 2$ in the longitudinal resistance. The exponent values extracted from the procedure above are shown in Figure 6.5(a). For thick quantum wells (R = Gd and Sm), n is close to 2. This is consistent with data on single interface 2DELs with thick SrTiO$_3$ (see Chapter 5.2). A pronounced dip towards $n \approx 1.6$ appears for R = Sm near the 5 SrO layer thickness. This is coincident with the location of the QCP discussed above (see Figure 6.2), which is consistent with the general trend of NFL behavior emerging in immediate proximity of quantum phase transitions (see Chapter 4.5).

It should be emphasized here that the transport signature used to extract these exponents is in the Hall effect (not R_{xx}). In particular, $n < 2$ manifests itself most clearly in the high T limit of Equation 6.3, where the residuals C and R_0 can be neglected:

$$\frac{1}{eR_H(\text{high } T)} = \frac{H}{e}\frac{\alpha}{A} \cdot T^{2-n} \qquad (6.4)$$

For $n = 2$, this expression becomes the true carrier density N. This is also seen experimentally (Figures 6.4(c) and (d)), as the Hall coefficient for most quantum wells converges towards $(eR_H)^{-1} = 6.8 \times 10^{14}$ cm^{-2} in the high T limit.

For $n < 2$, $(eR_H)^{-1}$ is expected to follow a T^{2-n} power law. This is clearly observed above $\approx$100 K for 1 - 4 SrO layer thick quantum wells in SmTiO$_3$, where $(eR_H)^{-1}$ has a well-defined upturn. These are the same samples that have the most pronounced deviations of the resistivity exponent away from $n = 2$.

The exponents shown in Figure 6.5(a) are also consistent with the direct
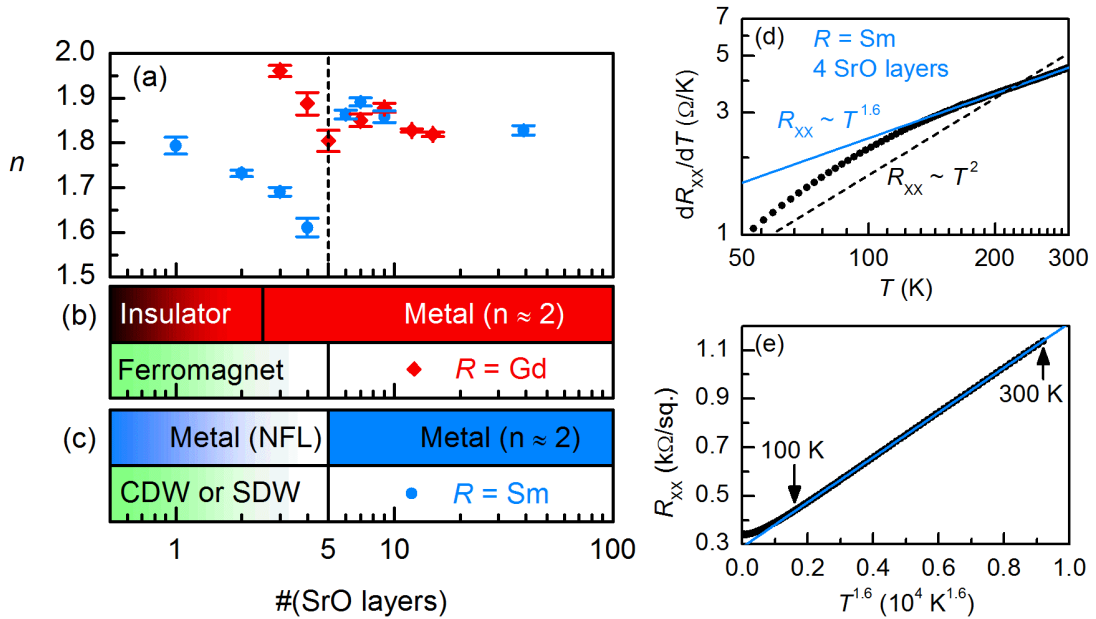
Figure 6.5. (a) Temperature exponents of longitudinal resistivity from fits to data in Figure 6.4. (b,e) Summary of quantum well thickness-induced electronic and magnetic state transitions. (d,e) Representative example of resistivity analysis of a quantum well in the NFL state with $n < 2$. Reprinted with permission from [202]. Copyright 2015, American Physical Society.

analysis of the resistivity data. Figure 6.5(b) shows the data for the 4 SrO layer quantum well embedded in SmTiO$_3$ on a log-log plot of dR_{xx}/dT vs. T, where any power law dependence is expected to appear as a straight line. The blue line illustrates the NFL-type scaling $R_{xx} \sim T^{1.6}$, which accurately describes the resistivity above $\approx$100 K. The progressive deviation at low T corresponds to the low T upturn discussed in Chapter 6.3. The dashed black line illustrates that the T^2 dependence is not appropriate to describe this data. Figure 6.5(c) replots the same data as R_{xx} vs. $T^{1.6}$, highlighting the linearity of this dependence in the 100-300 K range.

While the discussion thus far focused on the high T limit, the opposite low T limit is also of great interest. In the case of Hall effect data, it contains most of the complexity in terms of T and SrTiO$_3$ thickness dependencies. The shape of the $(eR_H)^{-1}(T)$ curves in Figures 6.4(c) and (d) is determined by the progressive transition between the high and low T regimes. In the $T = 0$ limit, $(eR_H)^{-1}$ contains only the carrier density and the ratio of the T independent residuals:

$$\frac{1}{eR_H(T=0)} = N \cdot \frac{\mu_{xx}(T=0)}{\mu_H(T=0)} = \frac{H}{e}\frac{C}{R_0} \tag{6.5}$$

Figure 6.6 summarizes the low T Hall coefficients and longitudinal and Hall residuals extracted from fitting of the data in Figure 6.4. Figure 6.6(a) shows the measured $(eR_H)^{-1}$ at 2 K (lowest measured T) and $HC/(eR_0)$ (same phys-

ical quantity, value extracted from fitting). The two quantities track each other closely for both $R =$ Gd and Sm. The most notable feature of this plot is the divergence near the 5 SrO layer thickness. Within the picture of scattering rate separation, this is driven by the dissimilarity of the longitudinal and Hall residuals, with $\tau_{xx}(T = 0) > \tau_H(T = 0)$. This leads to the increase in the measured $(eR_H)^{-1}$ up to $\approx 1.5 \times 10^{15}$ cm^{-2}, far above the true carrier density $N = 6.8 \times 10^{14}$ cm^{-2}.

Figures 6.6 (b) and (c) show the individual residuals R_0 and C. The quantity R_0 monotonously increases as the SrTiO$_3$ quantum well thickness is decreased. This is expected for ultrathin quantum wells, due to the increased role of interface roughness scattering. The Hall residual C is similarly increased at low SrTiO$_3$ thicknesses. There is, however, an additional divergent contribution near the QCP at 5 SrO layers. The contrast is particularly evident when R_0 and C are multiplied by the quantum well thickness t_{QW}, removing the approximately linear increase due to roughness scattering (see insets in Figures 6.6 (b) and (c)). It should be noted that t_{QW} is defined as the entire SrTiO$_3$ thickness, including the adjacent TiO$_2$ planes (see Figure 6.1). The increase of $R_0 t_{QW}$ and $C t_{QW}$ at high t_{QW} is most likely only apparent due most of the 2DELs not extending fully across the SrTiO$_3$ well thickness.

Based on the discussion above, scattering rate separation manifests itself in
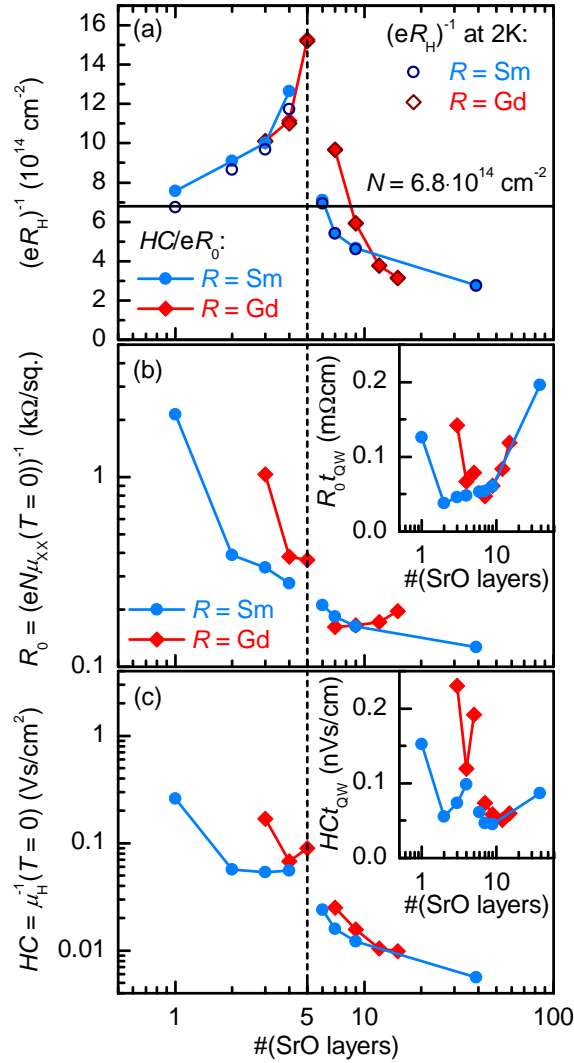
Figure 6.6. Summary of $T = 0$ scattering rate residuals from analysis of data in Figure 6.4. (a) Hall effect in the low T limit, comparing the ratio of fitting residuals (full symbols) with the measured value at $T = 2$ K (open symbols). (b,c) individual values for the residuals R_0 and C. The insets show the same quantities multiplied by the quantum well thickness. Reprinted with permission from [202]. Copyright 2015, American Physical Society.

176
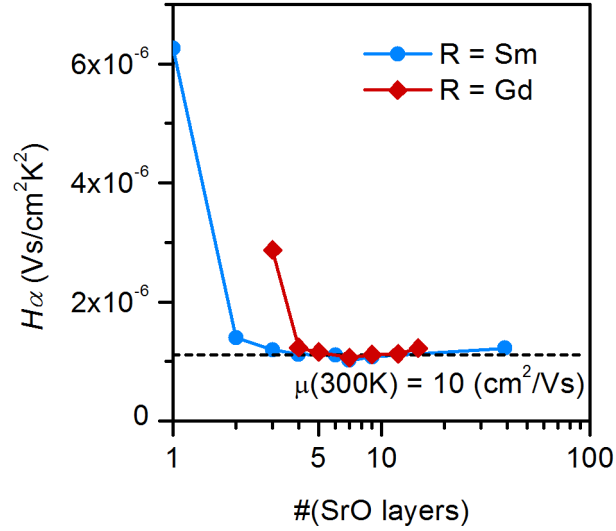
Figure 6.7. The T^2 Hall scattering rate amplitude extracted from analysis of data in Figure 6.4. Reprinted with permission from [202]. Copyright 2015, American Physical Society.

proximity of the QCP at 5 SrO layers in the temperature exponent of τ_{xx} and in the residuals of the Hall scattering rate. In contrast, the slope coefficient of the Hall scattering rate (α) is continuous as a function of SrTiO$_3$ thickness, as shown in Figure 6.7. There is no sign of a discontinuity at the QCP. With the exception of the thinnest quantum wells, α is also approximately constant as a function of SrTiO$_3$ thickness. This is consistent with the discussion in Chapter 5, which presented evidence for a carrier density independent scattering rate in uniformly doped SrTiO$_3$. The sharp increase of α at 3 SrO layers ($R = Gd$) corresponds to proximity to the metal-insulator transition discussed above to be

driven by propagation of the octahedral distortion from $GdTiO_3$ into ultrathin $SrTiO_3$ [336].

Interpretation of the slope coefficient of τ_{xx} is not trivial because of the variable values of the exponent n. The coefficient A defined in Equation 6.1 has the units of Ω/K^n. The evolution of A with $SrTiO_3$ thickness appears discontinuous because n enters its units (see Figure 6.8). This is also the case for the quantity $A^{1/n}$ with units of $\Omega^{1/n}/K$. One can convert A into a temperature scale $T_0 = (R_0/A)^{1/n}$ by re-writing Equation 6.1 as:

$$R_{xx} = R_0 \cdot (1 + (T/T_0)^n) \tag{6.6}$$

This variant of the temperature slope definition has the advantage of not including n in its units, although it does implicitly contain the residual resistivity R_0. As shown in Figure 6.8, T_0 does not appear to show any discontinuous or anomalous behavior in vicinity of the QCP at 5 SrO layers.

Therefore, the fit parameters affected by proximity to the QCP are n and C. The non-Fermi liquid n is reminiscent of many other quantum critical systems, where exponent deviations away from $n = 2$ are usually the strongest in direct proximity of quantum criticality (see Chapter 4.5). In the present case, it is important to note that the behavior of this exponent is sensitive to the proximal magnetism. For $SrTiO_3$ embedded in ferrimagnetic $GdTiO_3$, there is clear

178
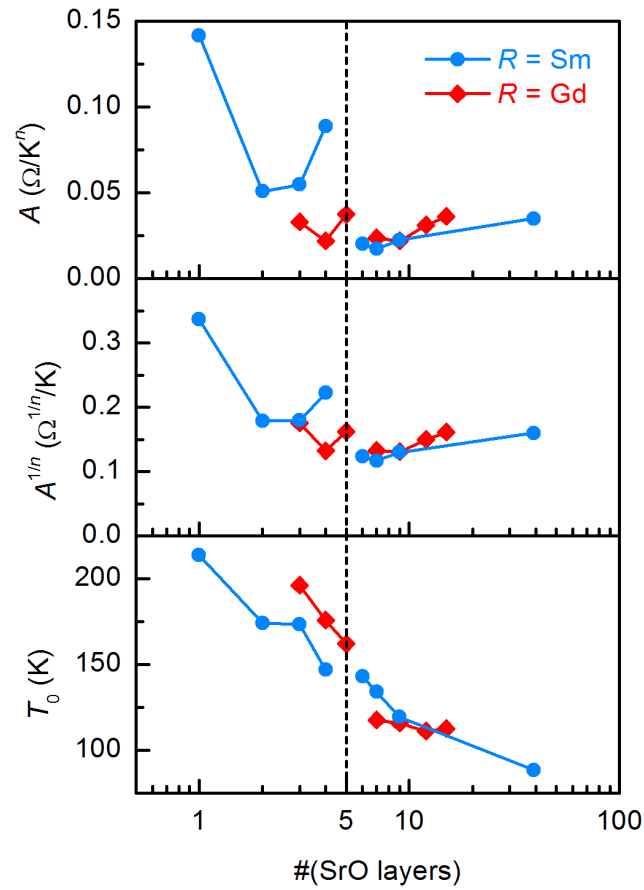
Figure 6.8. The T^n longitudinal scattering rate amplitude extracted from analysis of data in Figure 6.4. Reprinted with permission from [202]. Copyright 2015, American Physical Society.

evidence for ferromagnetic order within the quantum well [333], [334], which appears to prevent n from taking anomalous values. Instead it remains close to $n \approx 2$ in the ultrathin limit.

The magnetic ground state of ultrathin $SrTiO_3$ in $SmTiO_3$ is at present unclear. Bulk $SmTiO_3$ is an antiferromagnet with an ordering temperature near $T_N = 50$ K [216], [221]. One can make an argument by analogy with the quantum wells in $GdTiO_3$: ultrathin $SrTiO_3$ might adopt the itinerant antiferromagnetic ordering of $SmTiO_3$ via a similar proximity effect. This would be consistent with the general trends for NFL behavior, as it is often observed near antiferromagnetic QCPs and many microscopic theories link it to scattering off antiferromagnetic fluctuations.

One experimental set of information on this ground state came from a tunnel junction study [335] by Patrick Marshall et al. It was based on vertical tunneling between 2DELs confined in quantum wells and Pt metal contacts, separated by an epitaxial $SrZrO_3$ tunnel barrier. The vertical current at small voltages in such tunnel junctions is governed by the single particle density of states (DOS). For 2 and 5 SrO layer thicknesses of $SrTiO_3$ in $SmTiO_3$, a pseudogap phase was observed. This refers to a partial depletion of the single-particle DOS near the Fermi level. It is reminiscent of very similar features in other strongly correlated systems, most notably the underdoped cuprates. While their origin is

still actively debated, they are generally considered to be a precursor phase for strongly correlated and quantum critical phenomena.

An important aspect of the pseudogap for 2DELs in $SmTiO_3$ was the presence of coherence peaks, i.e. the buildup of DOS at the edges of the pseudogap. Similar peaks are seen in density wave systems [299], [337]. This suggests that the low-temperature ground state of ultrathin quantum wells in $SmTiO_3$ is indeed an ordered phase, such as a spin or charge density wave. However, this experiment cannot discriminate between these two possibilities.

In this context it is relevant to mention that the Hall effect data for 1-4 SrO layer thick quantum wells in $SmTiO_3$ are the only ones in this study to contain a feature that is not captured by Equation 6.3. Below $T = 50$ K, these samples show a downturn in $(eR_H)^{-1}$ below the fit curve (≈ 10 % reduction). An intuitive explanation is a reduction of the true carrier density N, which would be consistent with an opening of a charge density wave gap in the band structure.

In contrast to the NFL behavior in the exponent n, the scattering rate separation in the T-independent residuals is a very unique behavior, which to the extent of our knowledge has not been reported previously. In cuprates, several extensive studies looked at the influence of isovalent impurity doping (e.g. substitution of Zn for Cu in $YBa_2Cu_3O_7$). C was found to scale straightforwardly

with disorder similarly to R_0, and no separation between residuals in τ_H and τ_{xx} was noted [307], [311].

Figure 6.6 makes a clear a case for an overlap between standard scaling of residuals with disorder and a divergent contribution that only appears in $\tau_H(T=0)$ near the QCP. While the microscopic mechanisms for this divergence is unclear, several constraints can be formulated:

- Given the monotonous continuity of R_0 across the entire SrTiO$_3$ thickness range, conventional disorder scattering can be assumed to also continuously increase in the ultrathin limit and not be affected by the QCP.

- As R_0 also contains the size of the Fermi surface, its continuity also suggests that no dramatic Fermi surface reconstructions take place near the QCP

- Divergent C is consistent with a divergent scattering length. A divergent length scale is implied for a QPT and a quantum critical correction to the residual conductivity is an appealing explanation. It is, however, unclear why this correction only applies to τ_H and not τ_{xx}.

It is important to highlight another broader implication of this study: the combination of separation in the exponents and the residuals makes a com-

pelling argument for the existence of two physically different scattering rates postulated by the two lifetime ansatz, as opposed to an apparent separation induced by anisotropy of scattering across the Fermi surface contour [325], [326]. The two lifetime framework is successful in describing the entire T range for the Hall effect in Figure 6.4, including the transition between the low and high T limits. This implies that the two scattering rates indeed enter into the Hall effect as a well-defined ratio (τ_{xx}/τ_H). As discussed in Chapter 4.6, the framework of anisotropic scattering implies deviations from this simple mathematical form in the presence of disorder and "hot spot" broadening. This is not compatible with the experimental situation: the trends in R_0 imply a significant increase in interface roughness scattering as a function of $SrTiO_3$ thickness (Figure 6.6) which does not alter the mathematical form of scattering rate separation (Equation 6.3).

An alternative framework to explain the T dependence of the Hall effect in Figure 6.4 is multiband transport. Indeed, these high electron density systems have complex band structures with multiple d_{xy} and $d_{xz,yz}$-derived bands [238]. In the case where carriers within these subbands have different mobilities, the measured Hall effect at low B becomes:

$$R_H = -\frac{\sum\limits_i N_i \mu_i^2}{e \sum\limits_i (N_i \mu_i)^2},$$

(6.7)

where i is the subband index. The main difficulty for this model is in describing the very high values of $(eR_H)^{-1}$ near the QCP. A discrepancy in mobilities between the subbands can only make the measured Hall $(eR_H)^{-1}$ lower than the true carrier density N. Given that the polar discontinuity cannot provide more than 0.5 electrons per lateral unit cells (6.8×10^{14} cm^{-2}), it is difficult to rationalize the measured $(eR_H)^{-1} \approx 1.5 \times 10^{15}$ cm^{-2} in ultrathin SrTiO$_3$ quantum wells within the multiband model. The only possible exception would involve the presence of hole pockets, in which case the multiband $(eR_H)^{-1}$ can increase above the true carrier density. The existence of such hole subbands is, however, not supported by either numerical calculations of quantum well band structures [338], [339], or by angle-resolved x-ray photoemission spectrosopy (ARPES) measurements on similar interface systems [340].

6.2 Tuning of the T^n resistivity by electrostatic gating

This Chapter will present an electrostatic gating experiment on a SrTiO$_3$ quantum well in proximity of quantum criticality. It will focus on the corresponding trends in non-Fermi liquid behavior.

The device structure and its basic characteristics are shown in Figure 6.9. It is based on the following epitaxial stack grown by MBE: LSAT / $SmTiO_3$ (10 nm) / $SrTiO_3$ (2 SrO layers) / $SmTiO_3$ (1.2 nm) / $SrZrO_3$ (6 nm). This structure is designed to enable electrostatic gating in a quantum well that shows non-Fermi liquid behavior (see Figure 6.2). The addition of the 6-nm thick $SrZrO_3$ gate insulator was intended to reduce the gate leakage.

The gated Hall bar device was processed using standard contact photolithography techniques. An optical image of the finished device is shown in Figure 6.9(b). The process involved four steps:

1. Negative resist step for lift-off for the 100×300 μm gate contact deposited by e-beam evaporation of 100 nm thick Pt.

2. Positive resist step for mesa definition with a dry etch. The etch was performed using an inductively coupled plasma in a BCl_3 gas atmosphere. A portion of the Pt gate contact was used as a hard mask to ensure correct alignment with the mesa.

3. Negative resist step for the ohmic etch. $SrZrO_3$ was selectively removed with a 5 second etch in HF diluted 1:10 in water

4. Negative resist step for lift-off of the ohmic contacts deposited by e-beam evaporation of Ti (400 nm) / Au (3000 nm).
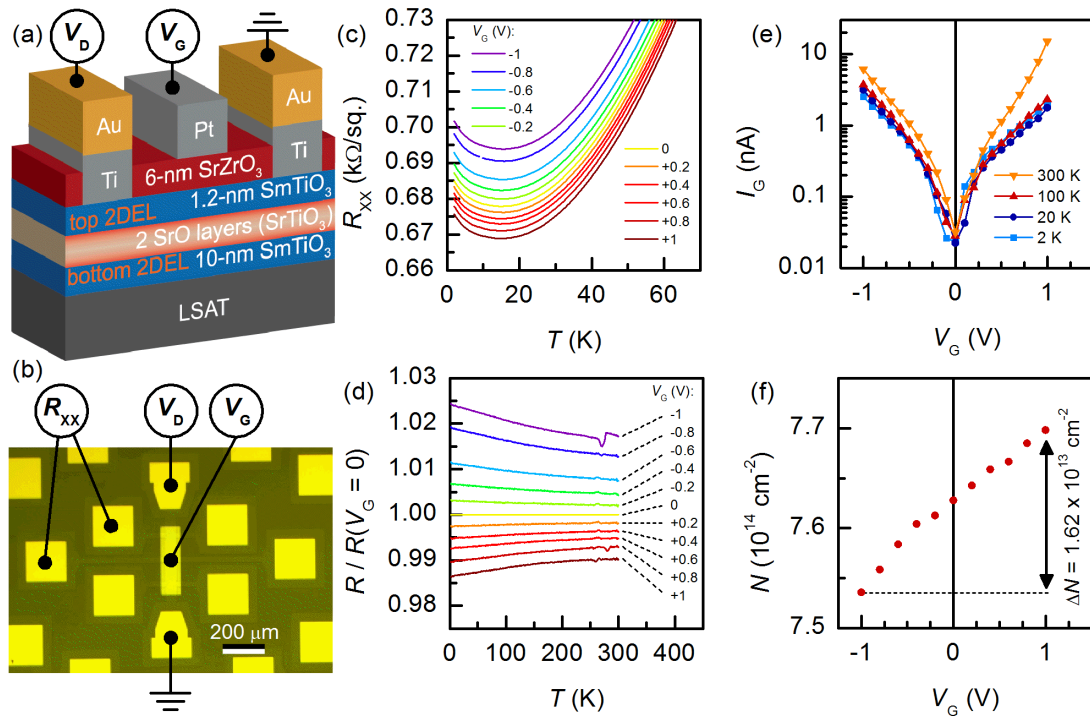
Figure 6.9. (a) Schematic cross section and (b) top view optical image of the gated quantum well device. (c) Longitudinal sheet resistance as a function of gate voltage and temperature. (d) Resistance normalized to $V_G = 0$. (e) Gate leakage at several temperatures. (f) Carrier density measurement by Hall effect as a function of gate voltage ($T = 100$ K). Reprinted from [203], licensed under CC BY 4.0.

Figure 6.9 shows that application of a gate voltage V_G to the Pt top electrode results in a systematic and reversibly volatile modulation of the in-plane sheet resistance R_{xx} of the Hall bar (Figure 6.9(b, c)). The measurement consisted of temperature sweeps from 300 to 2 K at different gate voltages. The gate leakage current I_G was only weakly rectifying, but in all cases it was strongly non-linear and orders of magnitude lower than the source-drain excitation current of 40 μA (Figure 6.9(e)). The systematic decrease of R_{xx} for positive V_G is consistent with accumulation of electrons in the conducting channel.

This electrostatic modulation can be tracked directly through Hall effect. The change in carrier density as a function of V_G at 100 K is shown in Figure 6.9(f). The total modulation between V_G = -1 and +1 (V) is $\Delta N = 1.62 \times 10^{13}$ cm^{-2}. This modulation is fairly large in comparison to typical gated structures with high-k dielectrics (see e.g. [341], [342]). In general, the potential of high-k dielectrics with $\varepsilon_r \approx$ 10-25 (such as SrZrO$_3$) as gate insulators is limited in terms of maximum achievable modulation to $\approx$ 1-5 $\times$ 10^{13} cm^{-2}. Therefore, the carrier density modulation demonstrated here is reasonably close to the maximum achievable with this type of stack design. It is, however, very small when compared to the total sheet density $N \approx 7 \times 10^{14}$ cm^{-2}, which is intrinsic to this quantum well structure. The fractional modulation of N is only 2.1 %. While it does not have a significant effect in terms of altering the electronic state

of the quantum well, it is sufficient to look into the slope and scaling of NFL state properties with carrier density.

The discussion below relies on the fitting of $R_{xx} - T$ curves at different gate voltages to the standard NFL expression:

$$R_{xx} = R_0 + AT^n \qquad (6.8)$$

A representative example ($V_G = 0$ V) is shown in Figure 6.10 in the form of both R_{xx} vs. T and dR_{xx}/dT vs. T plots. The fit range was 150-250 K, and a power law description with $n = 1.645$ was appropriate in the 100-300 K range. The low T range (below 100 K) was excluded in order to avoid interference from the low-T upturn, which can be clearly seen in the dR_{xx}/dT vs. T plot. Both the choice of the fitting range and the value of the exponent are consistent with the description of ungated quantum wells discussed in the previous Chapter.

Figure 6.11 shows the NFL fitting parameters extracted for all gate voltages. The extracted exponent $n = 1.645$ was independent of V_G within experimental noise. The change of R_{xx} with V_G was fully accounted for by the decrease of R_0 and A with V_G. Figure 6.11(d) compares their scaling to the N^{-1} dependence expected for carrier density independent scattering rates by plotting the quantities R_0, A and N^{-1} normalized to their $V_G = 0$ values. The overlap of A and N^{-1} in this plot suggests $A \sim 1/N$. In contrast, the scaling of R_0 is approximately
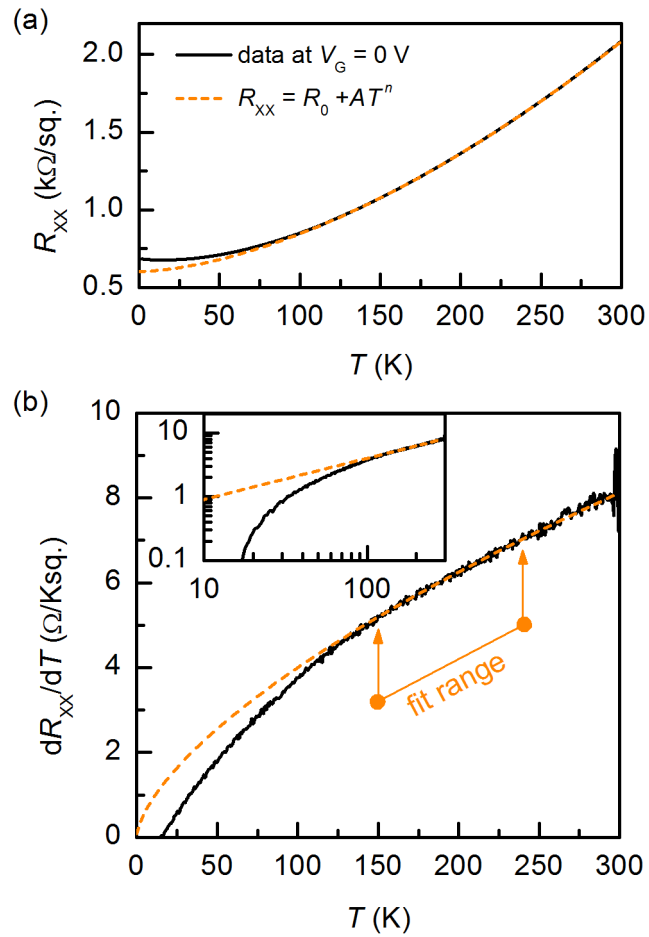
Figure 6.10. Non-Fermi liquid fit (Equation 6.8) to longitudinal resistance at zero gate bias. (a) $R_{xx} - T$ plot, (b) temperature derivative plot, the inset is on a log-log scale. Reprinted from [203], licensed under CC BY 4.0.
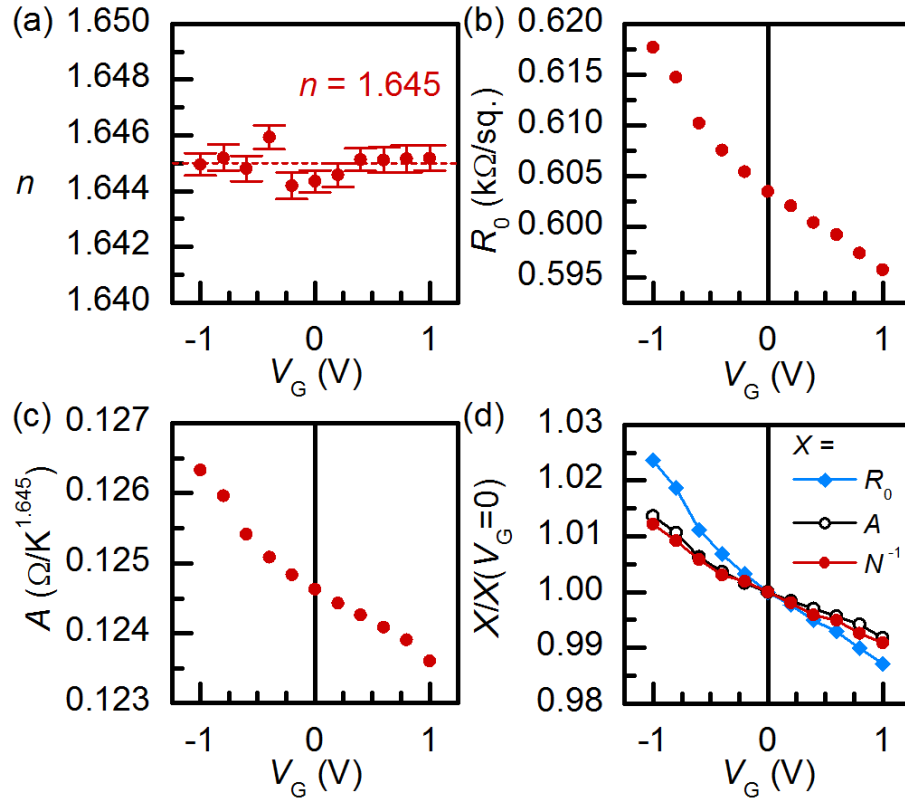
Figure 6.11. Gate voltage dependence of adjustable parameters in the fits to Equation 6.8. (a) Temperature exponent, (b) residual resistance, (c) scattering amplitude. (c) Normalized gate bias dependence of R_0, A, and inverse carrier density N^{-1}. Reprinted from [203], licensed under CC BY 4.0.
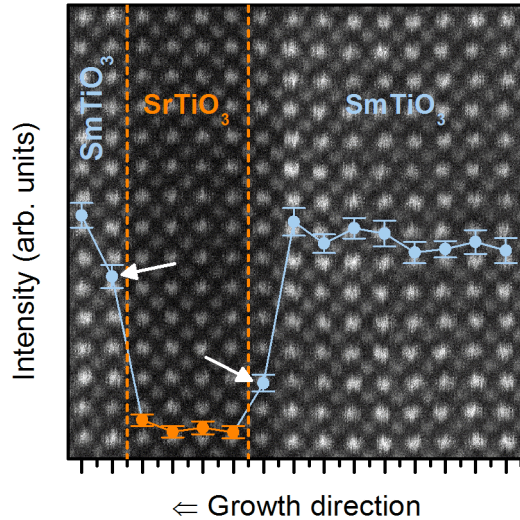
Figure 6.12. HAADF STEM cross section of a 4 SrO layer thick quantum well in SmTiO$_3$. The overlay shows the integrated intensities of each atomic plane. The interface planes are indicated with white arrows, with the top interface being sharper. Reprinted from [203], licensed under CC BY 4.0.

two times stronger than the naive expectation that $R_0 = m^* \Gamma_0 / N e^2$, where Γ_0 is the disorder scattering rate. This implies that Γ_0 is enhanced when $V_G < 0$ (depletion of carriers in the quantum well).

This can be explained by invoking the asymmetry of interface roughness in SmTiO$_3$/SrTiO$_3$/SmTiO$_3$ quantum wells. Figure 6.12 illustrates a general trend observed in such structures: the bottom SmTiO$_3$/SrTiO$_3$ interface has higher roughness in comparison to the top SrTiO$_3$/SmTiO$_3$ interface. It shows a high-

angle annular dark-field scanning transmission electron microscopy (HAADF-STEM) cross-section image (courtesy of Jack Zhang) of a 4 SrO layer thick quantum well embedded in $SmTiO_3$. The overlaid points represent intensities of atom columns, averaged across each atomic plane parallel to the interface. These intensities are approximately constant within the $SrTiO_3$ well and both $SmTiO_3$ layers. The interface roughness can be compared by looking at the column intensities for the interface atomic planes (marked by arrows). The distinctly higher column intensity at the top interface plane indicates a smoother interface. Such interface roughness asymmetries are common in superlattices [343], [344].

For electrostatic modulation with a top gate, the resulting carrier density profile is likely to be asymmetric, in particular given the very small screening length inherent to very high carrier densities. The accumulation and depletion of carriers will thus disproportionately affect the smoother top interface. Given that the predominant disorder scattering mechanism in ultrathin quantum wells is interface roughness [332], accumulation at the top interface will increase the proportion of carriers with reduced disorder scattering (in comparison to the bottom interface). This will reduce Γ_0, the integrated disorder scattering rate for the entire quantum well (as observed experimentally).

In conclusion of this Chapter, the implications of the $A \sim 1/N$ trend within
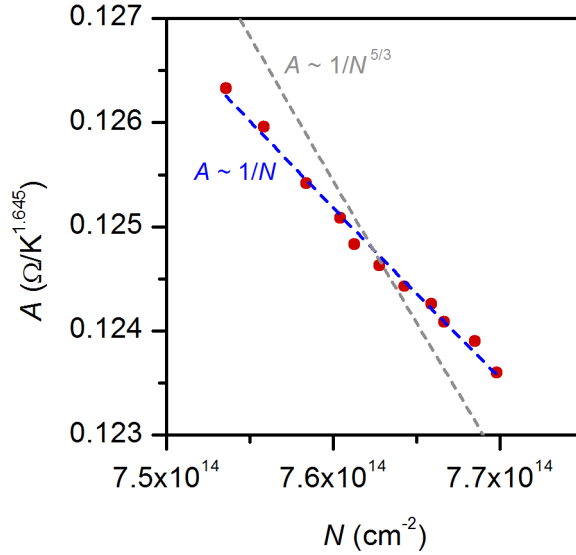
Figure 6.13. Carrier density dependence of the T^n scattering magnitude A. The blue dashed line is the $A \sim N^{-1}$ scaling of a carrier density-independent scattering rate. The grey dashed line is the $A \sim N^{-5/3}$ scaling from [262], [330]. Reprinted from [203], licensed under CC BY 4.0.

the NFL region ($n \approx 1.6$) are discussed. This scaling is identical to the one discussed in Chapter 5 for the T^2 resistivity of uniformly doped SrTiO$_3$. This implies similarity and a common origin for the T^n power law resistivity in SrTiO$_3$ with a carrier density independent scattering rate, for both the cases of $n = 2$ (Fermi liquid-like) and $n < 2$ (NFL). This is complemented by the similar values of α (Hall scattering rate) in Figures 6.1 and 6.7.

By analogy with Equations 5.6 and 5.7, the dimensional analysis of a the T^n

resistivity for the case of an arbitrary exponent $1 \leq n \leq 2$ leads to:

$$AT^n = \frac{m^*}{Ne^2} \cdot \Gamma(T^n) \tag{6.9}$$

$$\Gamma(T^n) = B \cdot \frac{(k_B T)^n}{\hbar E^{n-1}}. \tag{6.10}$$

As discussed in the case of bulk SrTiO$_3$, $A \sim N^{-1}$ implies that both Γ and E are independent of carrier density. This is, again, inconsistent with the Fermi liquid theory prediction that the energy scale is the Fermi energy.

The appearance of the energy scale as E^{n-1} is required to satisfy the units of the scattering rate. It is instructive to consider the limiting non-Fermi liquid exponent case $n = 1$, which is the T-linear resistivity commonly observed in the cuprates and heavy fermion materials (see Chapter 4.5). The energy scale E vanishes in the corresponding scattering rate:

$$\Gamma(T) = B \cdot \frac{k_B T}{\hbar}. \tag{6.11}$$

In addition, it has been experimentally demonstrated that $B \approx 1$ in such systems [331], i.e. the scattering rate $\Gamma = k_B T/\hbar$ is independent of any microscopic processes in the system and temperature is the only energy scale. This is often attributed to the disappearance of all other energy scales near a quantum critical point [272].

Equation 6.10 represents an intermediate situation where the energy scale

E is still relevant because of the fractional exponent value $n \approx 1.6 - 2$, even in very close proximity to the QCP.

The nature of the energy scale is at present an open question. The lack of carrier dependence across many magnitude rules out its traditional assignment in materials with T^2 resistivity as the Fermi energy. It is unclear whether the electron-electron scattering theory can be adjusted to include a different energy scale, e.g. by considering higher order scattering events or mediation of the electron-electron interaction by other quasiparticles.

Previous proposals for SrTiO$_3$ include mediation of the electron-electron interaction by phonons or disorder [206], [329]. For the phonon mediated mechanism proposed in [206] the energy scale is a renormalized Fermi energy, which is again inconsistent with the carrier density independence. Disorder mediation is also unlikely, given that E also appears to be largely insensitive to impurity doping (Figure 5.4) or interface scattering (Figures 6.6 and 6.7). It is also appears to be independent of the choice of material synthesis technique, which do not yield similar disorder levels (Figure 5.4).

Alternatively, the trend for carrier density independence can be argued as suggestive of a magnetic energy scale. While pure SrTiO$_3$ is paramagnetic, the possibility of an intrinsic incipient magnetic order has been suggested in some

experiments [345]–[348]. In this context, it should be noted that for a ferromagnet below its ordering temperature, scattering between electrons and magnons (quasiparticles incorporating collective excitations of electron spins) can yield a well-defined T^2 resistivity that saturates at T_C [349]–[352]. These treatments, however, do not have any straightforward application to SrTiO$_3$, where the T^2 resistivity can extend well above 300 K, far above any known ferromagnetic ordering temperature [333].

Another intriguing option to consider is the possibility of hydrodynamic bounds for conductivity, which have been explored as descriptions for non-Fermi liquids near quantum critical points and incoherent transport [353]–[357].

It should also be emphasized that any potential explanation for the T^2 scattering rate will need to have wide applicability and cannot be a narrow specialized model. The discussion above focused on SrTiO$_3$ and power law resistivity is well-defined across very wide range of doping and disorder. This is the case both in proximity and far removed from magnetic order. It is also robust to structural distortions and modifications of the $d_{xy,yz,xz}$ energy levels.

Another important aspect of the low carrier density regime is the eventual crossover to a non-degenerate semiconductor state, where the Fermi level is below the conduction band and there is no Fermi surface. Resistivity of SrTiO$_3$ is

metallic and Hall effect does not show signs of low temperature carrier freeze-out even for $N \approx 10^{16}$ cm^{-3} [214]. However, thermopower measurements suggest that SrTiO$_3$ is degenerate at 300 K for below $N \approx 10^{20}$ cm^{-3} [211], [358], [359]. This can be rationalized as a consequence of a large dielectric constant, resulting in a large Bohr radius and overlapping donor impurity wave functions even at very low carrier densities [214], producing metallic conductivity even in the non-degenerate regime. Robust T^2 resistivity can thus be found in both the degenerate and non-degenerate limits of SrTiO$_3$ and does not appear to be sensitive to this crossover.

The need for generality in any microscopic description of this scattering mechanism is also emphasized by observations of T^2 resistivity in a number of other d-orbital perovskites: SrNbO$_3$, SrMoO$_3$, (Ca,Sr)VO$_3$, (K,Ba)TiO$_3$, (Ca,Y)TiO$_3$ [360], [361], RNiO$_3$ (R = La, Pr, Nd) [362]–[364]. Many of these cases appear to also follow the trend of carrier density independent scattering rate [361]. Another possible analogy is with the overdoped cuprates, that also show robust T^2 resistivity up to very high temperatures [304], [305], [307], [315].

6.3 Discussion of resistivity upturns at low temperature

One notable aspect left out of the above discussions of temperature dependence of resistivity was the low temperature limit. In all plots of dR_{xx}/dT against T, a straight line indicative of a power law dependence dominates at high temperature. This is the case above ≈ 20 K for uniformly doped $SrTiO_3$ (see Figure 5.3) and above $\approx 50 - 100$ K for $SrTiO_3$ quantum wells in RTiO$_3$ (see Figures 6.5 and 6.10).

At low T, all these plots show a deviation from the power law scaling in the form of a downturn in dR_{xx}/dT. In many cases, dR_{xx}/dT decreases to zero and switches sign to negative at very low T (not shown in log-log plots of dR_{xx}/dT). Mathematically, this is equivalent to an upturn in resistivity. In the standard Drude picture (Equation 4.5), it corresponds to a decrease of electron mobility at low T or a loss of carriers.

In the scattering mechanism analysis of Chapters 5 and 6, such low T upturns were excluded from modeling and all fits were restricted to intermediate and high temperatures. This choice was made in view of the existence of multiple explanations for the physical origin of this upturn, which could also coexist or

be in competition. No single mechanism for low T upturns provides a good systematic description across all data sets. Good agreement usually requires substantial modification of the models with additional adjustable parameters, leading to concerns about overfitting and overinterpretation.

In the following, the various possibilities are outlined. The simplest explanation involves a **temperature-dependent disorder scattering** contribution $\mu_0(T)$. In this case, Equation 5.1 becomes:

$$\mu^{-1}(T) = \mu_0^{-1}(T) + \alpha T^2 + \mu_{LO}^{-1}(T) \tag{6.12}$$

A positive temperature dependence of μ_0 is part of some notable treatments of impurity scattering mechanisms. This is the case of the Cornwell-Weisskopf [365] and Brooks-Herring formulas [366] derived for classic semiconductors Si and Ge using the Born approximation (see Chapter 4.4.5 for the discussion of its applicability to SrTiO$_3$). Both give $\mu_0(T) \sim T^{3/2}$ as the dominant scaling at low T. The origin of this temperature dependence in these treatments comes from accounting for the competition between the Coulomb potential of the impurities and thermal activation. This leads to a reduced scattering cross section at finite temperature.

Figure 6.14 illustrates the likely temperature dependence of μ_0 in the case of uniformly doped La:SrTiO$_3$. It plots the measured Hall mobility μ, the αT^2

contribution, and the subtracted residual $\Delta\mu^{-1}(T) \equiv \mu^{-1}(T) - \alpha T^2$. The quantity $\Delta\mu^{-1}(T)$ is defined to include all scattering mechanisms that are not described by the T^2 scaling.

At high T, $\Delta\mu^{-1}(T)$ is the LO phonon scattering (Equation 5.2). At intermediate T, it is equivalent to a fit residual for the T^2 dependence. The trends in this region are essentially meaningless, since $\mu \ll \Delta\mu$ and $(\alpha T^2)^{-1} \ll \Delta\mu$.

Below ≈ 20 K, $\Delta\mu$ is expected to be equivalent to the impurity scattering contribution μ_0. It has a positive temperature dependence, which can be empirically
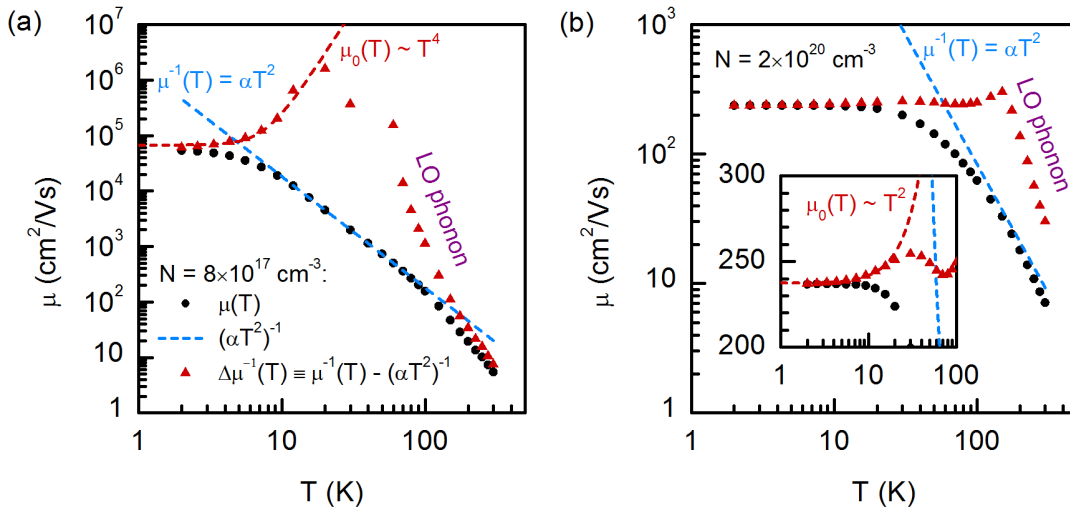
Figure 6.14. Hall mobility of (a) low and (b) highly doped La:SrTiO$_3$. The blue dashed lines are the T^2 contribution. Red triangles are $\Delta\mu$, the residual from the T^2 fit. Red dashed lines illustrate approximate power law dependencies for the temperature-dependent impurity scattering.

described by fairly sharp power laws: $\mu_0(T) = \mu_0(0) + K_0 T^m$, with $m \approx 1.5 - 5$. Such quantitative modeling of $\mu_0(T)$ is, however, very sensitive to even minor adjustments of the prior fit of mobility to the T^2 power law.

It is, however, fairly clear that under the assumption of a monotonous $\mu \sim T^{-2}$ scattering, μ_0 has a positive T dependence. It is only detectable at low T where $\mu \approx \mu_0$. The most sensitive signature for a T-dependent μ_0 is in the logarithmic derivative plots ($dR_{xx}/dT - T$), where it manifests itself as a downturn at low T (see Figures 5.3, 6.5 and 6.10).

From the point of microscopic mechanism for $\mu_0(T)$, it is unlikely that the results of [365], [366] are directly applicable to SrTiO$_3$. As discussed in Chapter 4.4.5, a particularly non-trivial question is the choice of dielectric constant values for impurity potential screening. One can in principle justify adopting any value between $\varepsilon_r = 4$ (high frequency response) and $\approx 10^4$ (static response at low T). The latter value is also strongly temperature dependent. Additional complications discussed in [3], [258] are related to polaronic distortions, likely resulting in crossovers between static and high frequency-like screening. Consequently, this is a complex problem that is extremely difficult to accurately describe without overfitting.

The resistivity upturns at low T are particularly pronounced in ultrathin

quantum well heterostructures with high disorder scattering (see Figures 6.4 6.5 6.9). In this setting another possible contribution to the upturn comes from a **decrease in carrier density at low** T.

The extensive discussion of the Hall effect in Chapter 6 concluded that the trends in Hall effect with temperature are not linked to any changes in the physical carrier density, and can be described by the separation of longitudinal and Hall scattering rates. A notable exception to this statement is the downturn of the measured $(eR_H)^{-1}$ below the fit curve at $T < 50$ K in Figure 6.4. This was most pronounced in ultrathin quantum wells in SmTiO$_3$. It is likely connected to an actual decrease in carrier density, which should also translate into an increased longitudinal resistivity.

A normalized decrease of N can be obtained from the Hall effect by taking the ratio of measured $(eR_H)^{-1}$ to the two-lifetime fit curve (Equation 6.2). This quantity is shown in Figure 6.15. It can be empirically described as:

$$F(T) = \frac{N(T)}{N_{2DEL}} = \frac{eR_H(\text{fit})}{eR_H(T)} = 1 - B\exp\left(-\frac{T}{T_g}\right) \tag{6.13}$$

where B and T_g are adjustable parameters, and $N_{2DEL} = 6.8 \times 10^{14}$ cm^{-2} is the 2DEL carrier density at high T. The longitudinal resistance from Equation 6.1 is thus modified as follows:

$$R_{xx}(T) = \frac{1}{e\mu_{xx}(T)N(T)} = \frac{F^{-1}(T)}{e\mu_{xx}(T)N_{2DEL}} = F^{-1}(T)(R_0 + AT^n) \tag{6.14}$$

This creates an upturn in $R_{xx}(T)$ at low T. Figure 6.15(b) compares the measured R_{xx}, the standard non-Fermi liquid fit to Equation 6.1 and the same fit including the correction for F^{-1} from Figure 6.15(a). It illustrates that F^{-1} only partially accounts for the upturn. The measured increase of R_{xx} is approximately two times greater, which implies coexistence with another mechanism. One possibility is the T-dependent disorder scattering discussed above. Three additional options commonly evoked in similar contexts are weak localization, electron interactions and the Kondo effect.
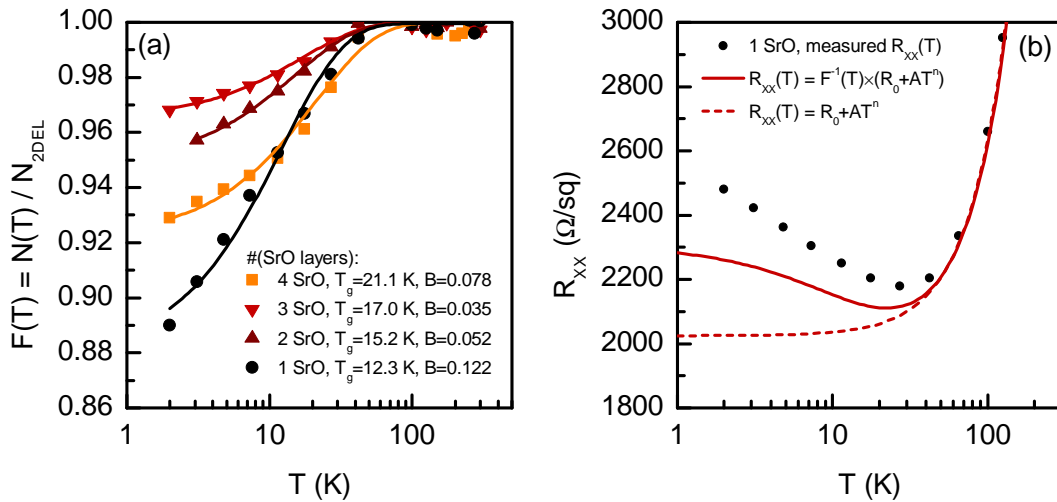
Figure 6.15. (a) Normalized loss of carrier density (see Equation 6.13) below 50 K for ultrathin SrTiO$_3$ quantum wells embedded in SmTiO$_3$, based on data and fitting from Figure 6.4. (b) Corresponding contribution to the resistivity upturn for the 1 SrO layer thick quantum well.

Weak localization [367], [368] is a quantum correction to conductivity in disordered systems. It arises from quantum interference effects in diffusive electron transport which are not accounted for in classical calculations. In the case of a two-dimensional thin film, this leads to the well-known logarithmic correction at low temperature:

$$\sigma_{xx}(T) = \sigma_0 + \frac{p}{2} \cdot e^2 \hbar \pi^2 \ln\left(\frac{T}{T_{WL}}\right) \tag{6.15}$$

where σ_0 is the residual conductivity, $p = 1.5 - 3$ is a scattering mechanism-dependent index and T_{WL} is an energy scale (it is mathematically lumped with σ_0).

The **Kondo effect** refers to scattering of itinerant carriers in a system with dilute magnetic impurities. The Kondo treatment of this problem [369] is valid in the low T limit, i.e. below the Kondo temperature scale T_K. It manifests itself as a nearly logarithmic resistivity upturn that saturates at low T. The relevance of the Kondo effect for SrTiO$_3$ was suggested by ionic liquid gating experiments on undoped single crystals [345], where large upturns were successfully modeled as:

$$R_K(T) = R_K(0) \cdot \left(\frac{T_{K*}^2}{T^2 + T_{K*}^2}\right) \tag{6.16}$$

$$T_{K*} \equiv \frac{T_K}{(2^{1/s} - 1)^{1/2}} \tag{6.17}$$

where $s \approx 0.2$ [370], [371]. Within the framework of a single power law resis-

tivity, the Kondo upturn can be incorporated as:

$$R_{xx} = R_0 + AT^n + R_K(T) \tag{6.18}$$

Figure 6.16 shows a longitudinal resistance measurement extended to $T = 440$ mK for a 2 SrO layer thick $SrTiO_3$ quantum well in $SmTiO_3$. Fits to Equations 6.15 and 6.18 are shown.

Reasonable fits to the Kondo model can be obtained with $T_K \approx 10 - 20$ K. However, the experimental data does not show any appreciable sign of the characteristic saturation of the logarithmic dependence.
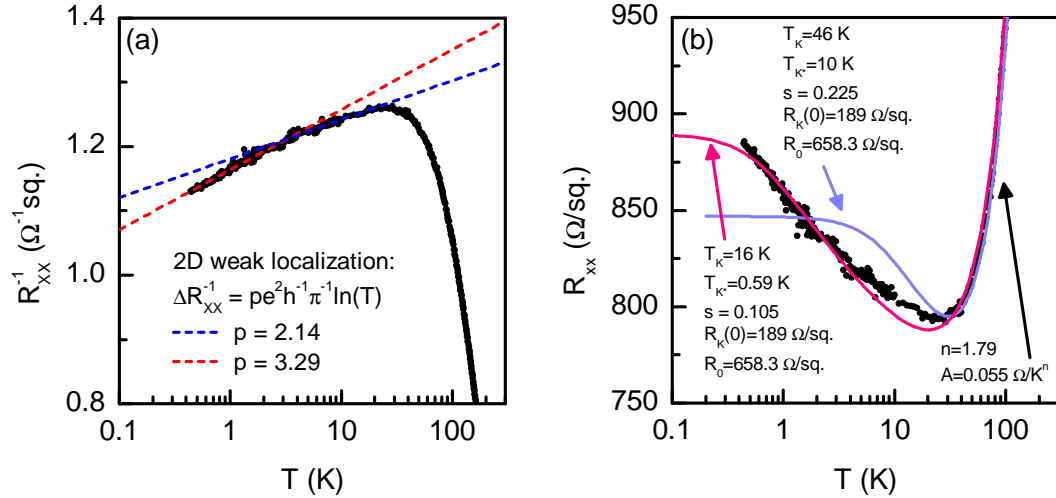
Figure 6.16. Longitudinal resistance of a 2 SrO layer thick quantum well in $SmTiO_3$ at low T. (a) Fits to 2D weak localization (Equation 6.15). (b) Fits to the Kondo effect (Equation 6.18).

The same temperature can be reasonably explained as the $R_{xx}^{-1} \sim \ln(T)$ scaling characteristic of weak localization. The slopes of the plotted fits correspond to $p = 2.14$ and 3.29, indicating realistic agreement with [367]. It should, however, be emphasized that the weak localization is only expected to occur at very low temperatures [367], [368]. It is quite unusual for it to be active up to $\approx$ 100 K (see Figures 6.5 and 6.10).

Additionally, it has been shown [367], [372] that **electron interaction effects** in disordered systems can produce a logarithmic upturn in resistivity, similarly to the weak localization result in Equation 6.15. A notable difference in the interaction result is the presence of a correction in the Hall constant:

$$\frac{\delta R_H}{R_H} = 2 \times \frac{\delta R_{xx}}{R_{xx}} \tag{6.19}$$

which implies that the upturn in the R_H is expected to be two times larger than in resistivity. For weak localization, one expects $\delta R_H = 0$ [372]. However, as discussed above in the context of figure 6.15, δR_H is actually smaller than δR_{xx} by a factor of two or more.

In conclusion, the low T upturns in R_{xx} (and, equivalently, downturns in dR_{xx}/dT) in conductive $SrTiO_3$ can be reasonably well described using isolated models of temperature-dependent impurity scattering, carrier density loss, weak localization, electron interaction and the Kondo effect. Discriminating between

these possibilities will likely require significant input from theoretical modeling combined with a focused effort on systematic study of disorder effects on resistivity in both bulk and heterostructured $SrTiO_3$. Given the likely coexistence of more than one of the above mechanisms, it is extremely difficult to construct an accurate description of the upturn without overfitting.

Therefore, the decision was made to exclude the upturn from the fits to power law resistivity that dominates at higher temperatures. All fitting ranges for T^2 and T^n resistivity in Chapter 5 and 6 were intentionally chosen to be above the downturn in dR_{xx}/dT.

Chapter 7

Conclusions and future directions

7.1 Tunable dielectrics

Chapter 2 provided a demonstration of $(Ba,Sr)TiO_3$ thin films with very high
performance in terms of dielectric tunability and loss. This was achieved by
combining the use of an epitaxial Pt bottom electrode with the low energy de-
position of $(Ba,Sr)TiO_3$ by MBE. Optimization of the structural quality of the
parallel plate capacitor stack yielded dielectric performance Figures of merit
that are orders of magnitude greater than in previous reports.

The main shortcoming of this study was the comparatively low frequency
of operation (1 MHz), limited by the parallel plate capacitor geometry and the

208

thickness of the bottom Pt electrode. One way to extend the operational frequency into the practically desired GHz range is to use a planar device geometry. This was demonstrated in a recent study by Meyers et al. [373], which used (Ba,Sr)TiO$_3$ grown by MBE on an insulator (LaAlO$_3$) and epitaxial top contacts to minimize parasitic interface capacitance (as discussed in Chapter 3). The top Pt contact fabrication procedure was similar to the one described in Chapter 3.2. Operation at 1 GHz with $Q = 205$, $\eta = 1.9$, and CQF $= 7000$ was achieved.

Another route towards high frequency operation is by minimizing series resistances in the parallel-plate capacitor geometry. This can be done by optimizing thicker bottom Pt electrodes, which are less structurally stable at the high temperatures and UHV pressures of the MBE growth environment. Operational frequency can also be extended by device design optimization: downscaling of lateral dimensions, inclusion of dielectric encapsulation, and addition of thick Au layers to the non-buried sections of the bottom electrode as a final processing step [14].

Within the context of practical applications, another potential direction is integration with conventional semiconductors, such as Si or Ge. While such heteroepitaxial growth is extremely challenging, considerable progress has been made in the growth of oxide perovskites with lattice constants in the 3.9-4 Å range, in particular by using ultrathin SrTiO$_3$ template layers on Si [374],

[375]. Growth of $SrTiO_3$ on Si using the hybrid MBE method has been recently reported in [376]. In the context of planar geometries, one can envision constructing stacks of $(Ba,Sr)TiO_3$ on Si or Ge, including low loss buffer layers. It is, however, still an open question whether the structural quality of titanate perovskites can be preserved to the point where dielectric performance is not considerably degraded.

7.2 Resistive switching devices

Chapter 3 established the importance of metal/oxide interface quality in the hysteretic current-voltage phenomena in $SrTiO_3$/Pt Schottky junctions. In particular, the magnitude of the switching effect was shown to be governed by the interface capacitance. In the case of generic low-temperature grown metal contacts, it is dominated by unintentional factors, such as contamination, growth-induced damage and disorder. The uncontrolled nature of these structural imperfections results in a large statistical scatter of resistive switching parameters and poor device reproducibility.

The use of high quality epitaxial contacts offers a route towards reproducible resistive switching by intentionally setting the interface capacitance magnitude. This method enables isolation of switching effects based on intentional place-

ment of structural defects. A proof of concept demonstration using non-stoichiometric SrTiO$_3$ interlayers was presented.

This work offers a template for follow up studies, concisely summarized in Equation 3.8: $\Delta\phi_B \sim \Delta Q_T/C_i$. This expression emphasizes that in a resistive switching device one needs to simultaneously control a dominant trapping center population and the interface capacitance. Future studies are needed to select the best way to reliably control trapped charge density Q_T. In particular, doping with Cr or Fe in SrTiO$_3$ and SrZrO$_3$ were highlighted as promising candidates based on previous reports using low-quality contacts [166], [196]–[200].

Additionally, the framework developed in Chapter 3 implies that the magnitude of resistive switching is sensitive to the placement of charge trapping centers within the vertical stack of the Schottky junction, see Figure 3.8(b) and Equation 3.7. It also predicts a possibility of enhancing the switching magnitude through heterostructuring with epitaxial low dielectric constant layers (such as SrZrO$_3$, LaAlO$_3$). For instance, if X is the intentional trapping center ($X =$ Cr, Fe, Sr excess), an intriguing heterostructure is Nb:SrTiO$_3$ /X:SrTiO$_3$ /SrZrO$_3$ /Pt(001). In this case, the low capacitance of the SrZrO$_3$ can act as an amplifier for the voltage drop projected by the trapped charge.

It is also important to note that while Chapter 3 discussed the resistive

switching in SrTiO$_3$ in terms of the most likely charge trapping mechanism, its results are largely agnostic to the exact microscopic processes. The conclusions about the importance of interface capacitance and the necessity for control of relevant defect populations will remain valid for any mechanism that results in alteration of the charge profile in a Schottky junction. This includes most proposals based on ionic electromigration (see e.g. [107], [108], [113]), particularly of planar interface type. They provide a completely different microscopic description of the process kinetics, but ultimately also result in a voltage-induced modification of the charged defect distribution .

In the context of practical applications, an important question is whether similar high-quality structures can be produced using low temperature deposition methods of amorphous materials on conventional semiconductors. A combination of high temperatures and presence of oxygen so far appears to be necessary to obtain clean interfaces with oxides [173], [174]. An alternative route is the use of an in-situ ozone or plasma cleaning procedure with the metal contact deposition [15], [16], [176]. This does not require high temperatures and has the potential to substantially reduce unintentional contributions to interface capacitance.

7.3   Identification of scattering mechanisms in SrTiO$_3$

Chapters 5 and 6 presented a unified picture of scattering mechanisms in uniformly doped SrTiO$_3$, 2DELS at SrTiO$_3$/RTiO$_3$ interfaces and 2DELs confined in narrow RTiO$_3$/SrTiO$_3$/RTiO$_3$ quantum wells.

The main result is the prevalence of a well-defined T^n power law scattering rate in all these systems, with $n = 2$ in most cases. It was shown to be inconsistent with the traditional assignment as electron-electron scattering within a Fermi liquid [206], [329]. This conclusion was based on the lack of carrier dependence of the scattering rate, its extension to temperatures far exceeding the Fermi energy scale, and its occurrence at low carrier densities, where SrTiO$_3$ is a non-degenerate semiconductor and momentum relaxation through Umklapp or multi-band processes is not possible.

Future studies will need to address the microscopic nature of this T^n scattering process and the corresponding energy scale $E \approx 10$ meV $\neq E_F$. Considerable theoretical input is needed. Proposed possibilities worth exploring include higher order electron-electron interactions mediated by other quasiparticles (e.g. polarons), hidden magnetic energy scales, and intrinsic hydrodynamic bounds.

Another aspect requiring follow up studies is the low temperature limit of

disorder scattering. As discussed in Chapter 6.3, the current lack of understanding of the resistivity upturn at low temperature was a strongly limiting factor for studying transport in SrTiO$_3$. Input from theoretical modeling is required for understanding the complex problem of impurity scattering in SrTiO$_3$. This is challenging in view of numerous complexities involved with the screening of impurity potential in the presence of a dielectric constant that is highly sensitive to temperature, electric fields, global strain and local structural distortions.

Disentangling the origin of the low temperature resistivity upturn is likely to require a systematic experimental study considering all viable possibilities: temperature-dependent impurity scattering, loss of mobile carriers, weak localization and the Kondo effect. In particular, accounting for the last possibility encourages a systematic comparison between impurities with and without magnetic moment.

7.4 Quantum critical phenomena in SrTiO$_3$

Chapter 6 made the case for the existence of a quantum critical point tuned by quantum well thickness in RTiO$_3$/SrTiO$_3$/RTiO$_3$ heterostructures. It is located at 5 SrO layers for the two presented cases of R = Gd and Sm. It corresponds to the emergence of ordered phases in SrTiO$_3$ in the ultrathin limit: ferromag-

netism for R = Gd [333] and a charge or spin density wave for R = Sm [335].

Non-Fermi liquid exponents of the T^n resistivity at the QCP ($n \approx 1.6$ for R = Sm) are one transport signature of quantum criticality. Secondly, a very well-defined pattern of longitudinal and Hall scattering rate separation was documented near the QCP. In particular, a very unique trend for residual ($T = 0$) scattering rate separation was presented. It is consistent with a quantum critical correction to the Hall scattering rate that is divergent at the QCP.

Many important open questions remain. For instance, what exactly is the driving force for the emergence of a quantum phase transition tuned by $SrTiO_3$ thickness? One possibility is the purely electrostatic effect of overlap between two 2DELs at the boundaries of the quantum well. With the majority of the carrier spreading across the first few unit cells of $SrTiO_3$, it is attractive to identify the QCP at 5 SrO layers as the point where the two 2DELs start to overlap significantly.

Additionally, previous theoretical modeling of 2DELs in $SrTiO_3$ [238] suggested significant modification of orbital degeneracy upon confinement (d_{xy} being pushed down with respect to $d_{yz,xz}$). Consequently, a band structure reconstruction effect near the QCP, leading to a Lifshitz transition is a possibility. Valuable information in this context can be provided by ARPES [340]. Such

measurements on buried layers are very challenging, however, and require extremely thin top RTiO$_3$ layers, which are in turn associated with 2DEL carrier density depletion.

Consequently, an important question that needs to be addressed by both future experiments and theory is the exact nature of the non-thermal tuning parameter for the observed QPT and what critical scaling relations are appropriate.

Another currently unresolved scaling puzzle is related to longitudinal magnetoresistance and the applicability of Kohler scaling. This is the classical band theory prediction that magnetoresistance scales as:

$$\frac{\rho(B)}{\rho(B=0)} = F\left(\frac{B}{\rho(B=0)}\right) \tag{7.1}$$

In the context of quantum criticality in cuprates and heavy fermions, pronounced deviations and modifications of the Kohler scaling were observed near QCPs [275], [285], [377]. This lead to numerous proposals of modified Kohler-like and quantum critical scaling of magnetoresistance [285], [377]–[380]. Confined SrTiO$_3$ show a similar type of positive magnetoresistance at temperatures where non-Fermi liquid power laws dominate the resistivity. However, within preliminary investigations with fields up to 9 Tesla, its magnitude is very small ($< 0.1\%$), preventing reliable scaling analysis. A systematic study at high fields is needed. Additionally, it is likely that the magnitude of the magnetoresistance

effect can be enhanced by reducing the residual resistivity [381], [382] through improvements of material quality.

Chapter 6.2 demonstrates the possibility of electrostatic gating in this quantum critical system that is based on a thin film heterostructure (as opposed to bulk single crystal settings). It also highlighted the major challenge associated with the very high carrier densities intrinsic to these double-2DEL structures. Gated structures combining quantum wells with high-k dielectrics (such as the epitaxial SrZrO$_3$ used in this work) will be limited to modulating at most several percents of the total sheet density. While this can give valuable information about the slope of quantum critical states with carrier density, a more exciting prospect is to electrostatically alter the quantum critical state or cross transition boundaries. This requires larger modulation in the $\Delta N \approx 10^{14} - 10^{15}$ cm^{-2} range.

One route towards modulating very high carrier densities is to use SrTiO$_3$ as the gate insulator. For instance, $\Delta N \approx 1.5 \times 10^{14}$ cm^{-2} has been demonstrated [383]–[386] in single 2DEL structures such as LSAT / RTiO$_3$ / SrTiO$_3$ / Pt. However, this approach is not compatible with maintaining quantum confinement of the 2DEL. As discussed in [387], large modulation requires thick SrTiO$_3$ in order to mitigate parasitic capacitance at the interface with the metal. The alternative of incorporating SrTiO$_3$ as a gate insulator on top of a RTiO$_3$/SrTiO$_3$/RTiO$_3$

quantum well results in formation of additional unconfined 2DELs that screen out the electrostatic modulation. Another alternative is to use ionic liquid gating. This approach has been shown to result in very high carrier density modulation in $SrTiO_3$ [345], [388], but is associated with a major challenge of avoiding electrochemical modification of the channel material [388]–[390].

Advances in the understanding of the physics of confined 2DELs are likely to come from careful and systematic study of electrical transport in reduced lateral dimensions. For instance, lateral tunneling into quantum dots and quantum point contacts can be used as probes for the electronic band structure, including sensitivity magnetic ordering and superconducting electron pairing [391], [392]. Measurements of electronic noise [393]–[395], universal conductance fluctuations [396], [397], and current-voltage non-linearity [398] in mesoscopic devices are also promising directions to gain more insights into the quantum critical state of confined 2DELs.

Bibliography

[1] M. Schmidbauer, A. Kwasniewski, and J. Schwarzkopf, "High-precision absolute lattice parameter determination of $SrTiO_3$, $DyScO_3$ and $NdGaO_3$ single crystals," *Acta Crystallographica Section B*, vol. 68, no. 1, p. 8, 2012.

[2] K. van Benthem, C. Elssser, and R. H. French, "Bulk electronic structure of $SrTiO_3$: experiment and theory," *Journal of Applied Physics*, vol. 90, no. 12, p. 6156, 2001.

[3] H. P. R. Frederikse and W. R. Hosler, "Hall mobility in $SrTiO_3$," *Physical Review*, vol. 161, p. 822, 1967.

[4] K. A. Müller and H. Burkard, "$SrTiO_3$: an intrinsic quantum paraelectric below 4 K," *Physical Review B*, vol. 19, p. 3593, 1979.

[5] H.-M. Christen, J Mannhart, E. Williams, and C. Gerber, "Dielectric properties of sputtered $SrTiO_3$ films," *Physical Review B,* vol. 49, no. 17, p. 12095, 1994.

[6] A. Tagantsev, V. Sherman, K. Astafiev, J. Venkatesh, and N. Setter, "Ferroelectric materials for microwave tunable applications," *Journal of Electroceramics,* vol. 11, no. 1, p. 5, 2003.

[7] A. Antons, J. B. Neaton, K. M. Rabe, and D. Vanderbilt, "Tunability of the dielectric response of epitaxially strained $SrTiO_3$ from first principles," *Physical Review B,* vol. 71, p. 024102, 2005.

[8] G. D. Wilk, R. M. Wallace, and J. M. Anthony, "High-k gate dielectrics: current status and materials properties considerations," *Journal of Applied Physics,* vol. 89, no. 10, p. 5243, 2001.

[9] J. Robertson, "High dielectric constant gate oxides for metal oxide Si transistors," *Reports on Progress in Physics,* vol. 69, no. 2, p. 327, 2006.

[10] M. A. Saifi and L. Cross, "Dielectric properties of strontium titanate at low temperature," *Physical Review B,* vol. 2, no. 3, p. 677, 1970.

[11] G. Rupprecht and R. O. Bell, "Dielectric constant in paraelectric perovskites," *Physical Review,* vol. 135, A748, 3A 1964.

[12] O. G. Vendik, E. K. Hollmann, A. B. Kozyrev, and A. M. Prudan, "Ferro-electric tuning of planar and bulk microwave devices," *Journal of Super-conductivity*, vol. 12, no. 2, p. 325, 1999.

[13] O. G. Vendik, L. T. Ter-Martirosyan, and S. P. Zubko, "Microwave losses in incipient ferroelectrics as functions of the temperature and the biasing field," *Journal of Applied Physics*, vol. 84, no. 2, 1998.

[14] R. A York, "Tunable dielectrics for RF circuits," in, M. Steer and W. D. Palmer, Eds. SciTech, 2009.

[15] S. Suzuki, T. Yamamoto, H. Suzuki, K. Kawaguchi, K. Takahashi, and Y. Yoshisato, "Fabrication and characterization of $Ba_{1-x}K_xBiO_3$/Nb-doped $SrTiO_3$ all-oxide-type Schottky junctions," *Journal of Applied Physics*, vol. 81, no. 10, 1997.

[16] T. Yamamoto, S. Suzuki, K. Kawaguchi, and K. Takahashi, "Temperature dependence of the ideality factor of $Ba_{1-x}K_xBiO_3$/Nb-doped $SrTiO_3$ all-oxide-type Schottky junctions," *Japanese Journal of Applied Physics*, vol. 37, no. 9R, p. 4737, 1998.

[17] P. A. Fleury, "The effects of soft modes on the structure and properties of materials," *Annual Review of Materials Science*, vol. 6, no. 1, p. 157, 1976.

[18] Nakanishi, N., Nagasawa, A., and Murakami, Y., "Lattice stability and soft modes," *Journal de Physique Colloques*, vol. 43, p. 35, 1982.

[19] H. Wu and W. Z. Shen, "Soft mode behavior and phase transition in $Ba_xSr_{1-x}TiO_3$," *Applied Physics Letters*, vol. 87, no. 25, p. 252906, 2005.

[20] N. A. Pertsev, A. G. Zembilgotov, and A. K. Tagantsev, "Effect of mechanical boundary conditions on phase diagrams of epitaxial ferroelectric thin films," *Physical Review Letters*, vol. 80, p. 1988, 9 1998.

[21] K. J. Choi, M. Biegalski, Y. L. Li, A. Sharan, J. Schubert, R. Uecker, P. Reiche, Y. B. Chen, X. Q. Pan, V. Gopalan, L.-Q. Chen, D. G. Schlom, and C. B. Eom, "Enhancement of ferroelectricity in strained $BaTiO_3$ thin films," vol. 306, no. 5698, p. 1005, 2004.

[22] A. von Hippel, "Ferroelectricity, domain structure, and phase transitions of barium titanate," *Reviews of Modern Physics*, vol. 22, p. 221, 3 1950.

[23] K. Bethe, "Uber das mikrowellenverhalten nichtlinearer dielektrika," *Philips Research Report Supplement*, 1970.

[24] K. Bethe and F. Welz, "Preparation and properties of $(Ba,Sr)TiO_3$ single crystals," *Materials Research Bulletin*, vol. 6, no. 4, p. 209, 1971.

[25] H. Wu and W. Z. Shen, "Dielectric and pyroelectric properties of $Ba_xSr_{1-x}TiO_3$: quantum effect and phase transition," *Physical Review B*, vol. 73, p. 094115, 2006.

[26] N. A. Pertsev, A. K. Tagantsev, and N. Setter, "Phase transitions and strain-induced ferroelectricity in $SrTiO_3$ epitaxial thin films," *Physical Review B*, vol. 61, R825, 2000.

[27] J. Haeni, P. Irvin, W. Chang, R. Uecker, P. Reiche, Y. L. Li, S. Choudhury, W. Tian, M. Hawley, B. Craigo, A. K. Tagantsev, X. Q. Pan, S. K. Streiffer, L. Q. Chen, S. W. Kirchoefer, J. Levy, and D. G. Schlom, "Room-temperature ferroelectricity in strained $SrTiO_3$," *Nature*, vol. 430, no. 7001, p. 758, 2004.

[28] A. Verma, S. Raghavan, S. Stemmer, and D. Jena, "Ferroelectric transition in compressively strained $SrTiO_3$ thin films," *Applied Physics Letters*, vol. 107, no. 19, 192908, 2015.

[29] R. C. Haislmaier, R. Engel-Herbert, and V. Gopalan, "Stoichiometry as key to ferroelectricity in compressively strained $SrTiO_3$ films," *Applied Physics Letters*, vol. 109, no. 3, 032901, 2016.

[30] S. M. Sze, *Physics of semiconductor devices*. John Wiley & Sons, 1981.

[31] L. Brillson, "The structure and properties of metal−semiconductor interfaces," *Surface Science Reports*, vol. 2, no. 2, p. 123, 1982.

[32] R. T. Tung, "Recent advances in Schottky barrier concepts," *Materials Science and Engineering: R: Reports*, vol. 35, no. 13, p. 1, 2001.

[33] E. H. Rhoderick, "Metal-semiconductor contacts," *IEE Proceedings I - Solid-State and Electron Devices*, vol. 129, no. 1, p. 1, 1982.

[34] T. Shimizu, N. Gotoh, N. Shinozaki, and H. Okushi, "The properties of Schottky junctions on Nb-doped SrTiO$_3$ (001)," *Applied Surface Science*, vol. 117, p. 400, 1997.

[35] H. C. Card and E. H. Rhoderick, "Studies of tunnel MOS diodes I. Interface effects in silicon Schottky diodes," *Journal of Physics D: Applied Physics*, vol. 4, no. 10, p. 1589, 1971.

[36] P. Chattopadhyay and B. RayChaudhuri, "Frequency dependence of forward capacitance−voltage characteristics of Schottky barrier diodes," *Solid-State Electronics*, vol. 36, no. 4, p. 605, 1993.

[37] C. Crowell and V. Rideout, "Normalized thermionic-field (T−F) emission in metal-semiconductor (Schottky) barriers," *Solid-State Electronics*, vol. 12, no. 2, p. 89, 1969.

[38] A. Ruotolo, C. Y. Lam, W. F. Cheng, K. H. Wong, and C. W. Leung, "High-quality all-oxide Schottky junctions fabricated on heavily doped Nb:SrTiO$_3$ substrates," *Physical Review B*, vol. 76, p. 075122, 7 2007.

[39] A. Turut, N. Yalcin, and M. Saglam, "Parameter extraction from non-ideal C-V characteristics of a Schottky diode with and without interfacial layer," *Solid-State Electronics*, vol. 35, no. 6, p. 835, 1992.

[40] A. Cho and J. Arthur, "Molecular beam epitaxy," *Progress in Solid State Chemistry*, vol. 10, p. 157, 1975.

[41] W. P. McCray, "MBE deserves a place in the history books," *Nature Nanotechnology*, vol. 2, no. 5, p. 259, 2007.

[42] D. G. Schlom, "Perspective: oxide molecular−beam epitaxy rocks!" *APL Materials*, vol. 3, no. 6, 062403, 2015.

[43] J. J. Cuomo, D. L. Pappas, J. Bruley, J. P. Doyle, and K. L. Saenger, "Vapor deposition processes for amorphous carbon films with sp^3 fractions approaching diamond," *Journal of Applied Physics*, vol. 70, no. 3, 1991.

[44] J. Y. Tsao, *Materials Fundamentals of Molecular Beam Epitaxy*. Academic Press, 1993.

[45] B. Jalan, P. Moetakef, and S. Stemmer, "Molecular beam epitaxy of SrTiO$_3$ with a growth window," *Applied Physics Letters*, vol. 95, no. 3, 032906, 2009.

[46] F. Briones, D. Golmayo, L. Gonzalez, and J. L. D. Miguel, "Surface stoichiometry and morphology of MBE grown (001)GaAs through the analysis of RHEED oscillations," *Japanese Journal of Applied Physics*, vol. 24, no. 6A, p. L478, 1985.

[47] C. Theis, J Yeh, D. Schlom, M. Hawley, and G. Brown, "Adsorption-controlled growth of PbTiO$_3$ by reactive molecular beam epitaxy," *Thin Solid Films*, vol. 325, no. 12, p. 107, 1998.

[48] C. M. Brooks, L. F. Kourkoutis, T. Heeg, J. Schubert, D. A. Muller, and D. G. Schlom, "Growth of homoepitaxial SrTiO$_3$ thin films by molecular−beam epitaxy," *Applied Physics Letters*, vol. 94, no. 16, 162905, 2009.

[49] M. E. Klausmeier-Brown, J. N. Eckstein, I. Bozovic, and G. F. Virshup, "Accurate measurement of atomic beam flux by pseudodoublebeam atomic absorption spectroscopy for growth of thinfilm oxide superconductors," *Applied Physics Letters*, vol. 60, no. 5, 1992.

[50] J. Haeni, C. Theis, and D. Schlom, "RHEED intensity oscillations for the stoichiometric growth of $SrTiO_3$ thin films by reactive molecular beam epitaxy," *Journal of Electroceramics*, vol. 4, no. 2, p. 385, 2000.

[51] B. Jalan, R. Engel-Herbert, N. J. Wright, and S. Stemmer, "Growth of high$-$quality $SrTiO_3$ films using a hybrid molecular beam epitaxy approach," *Journal of Vacuum Science Technology A*, vol. 27, no. 3, 2009.

[52] D. C. Bradley, "Metal alkoxides as precursors for electronic and ceramic materials," *Chemical Reviews*, vol. 89, no. 6, p. 1317, 1989.

[53] K. L. Siefering and G. L. Griffin, "Growth kinetics of CVD TiO_2: influence of carrier gas," *Journal of The Electrochemical Society*, vol. 137, no. 4, p. 1206, 1990.

[54] C. P. Fictorie, J. F. Evans, and W. L. Gladfelter, "Kinetic and mechanistic study of the chemical vapor deposition of titanium dioxide thin films using tetrakis$-$(isopropoxo)$-$titanium(IV)," *Journal of Vacuum Science Technology A*, vol. 12, no. 4, p. 1108, 1994.

[55] E. Mikheev, J. Hwang, A. P. Kajdos, A. J. Hauser, and S. Stemmer, "Tailoring resistive switching in $Pt/SrTiO_3$ junctions by stoichiometry control," *Scientific Reports*, vol. 5, 11079, 2015.

227

[56] T. Ohnishi, K. Shibuya, T. Yamamoto, and M. Lippmaa, "Defects and transport in complex oxide thin films," *Journal of Applied Physics*, vol. 103, no. 10, 103703, 2008.

[57] J. Neave and B. Joyce, "Structure and stoichiometry of (100) GaAs surfaces during molecular beam epitaxy," *Journal of Crystal Growth*, vol. 44, no. 4, p. 387, 1978.

[58] C. Deparis and J. Massies, "Surface stoichiometry variation associated with GaAs (001) reconstruction transitions," *Journal of Crystal Growth*, vol. 108, no. 1, p. 157, 1991.

[59] A. P. Kajdos and S. Stemmer, "Surface reconstructions in molecular beam epitaxy of $SrTiO_3$," *Applied Physics Letters*, vol. 105, no. 19, 191901, 2014.

[60] D. G. Schlom, L.-Q. Chen, X. Pan, A. Schmehl, and M. A. Zurbuchen, "A thin film approach to engineering functionality into oxides," *Journal of the American Ceramic Society*, vol. 91, no. 8, p. 2429, 2008.

[61] P. Moetakef, T. A. Cain, D. G. Ouellette, J. Y. Zhang, D. O. Klenov, A. Janotti, C. G. Van de Walle, S. Rajan, S. J. Allen, and S. Stemmer, "Electrostatic carrier doping of $GdTiO_3/SrTiO_3$ interfaces," *Applied Physics Letters*, vol. 99, no. 23, 232116, 2011.

[62] E. J. Monkman, C. Adamo, J. A. Mundy, D. E. Shai, J. W. Harter, D. Shen, B. Burganov, D. A. Muller, D. G. Schlom, and K. M. Shen, "Quantum many-body interactions in digital oxide superlattices," *Nature Materials*, vol. 11, no. 10, p. 855, 2012.

[63] P. Moetakef, D. G. Ouellette, J. Y. Zhang, T. A. Cain, S. J. Allen, and S. Stemmer, "Growth and properties of $GdTiO_3$ films prepared by hybrid molecular beam epitaxy," *Journal of Crystal Growth*, vol. 355, no. 1, p. 166, 2012.

[64] P. Moetakef, J. Y. Zhang, S. Raghavan, A. P. Kajdos, and S. Stemmer, "Growth window and effect of substrate symmetry in hybrid molecular beam epitaxy of a mott insulating rare earth titanate," *Journal of Vacuum Science Technology A*, vol. 31, no. 4, 041503, 2013.

[65] P. Xu, D. Phelan, J. Seok Jeong, A. Mkhoyan, and B. Jalan, "Stoichiometry-driven metal-to-insulator transition in $NdTiO_3$/$SrTiO_3$ heterostructures," *Applied Physics Letters*, vol. 104, no. 8, 082109, 2014.

[66] Y. Matsubara, K. S. Takahashi, Y. Tokura, and M. Kawasaki, "Single-crystalline $BaTiO_3$ films grown by gas-source molecular beam epitaxy," *Applied Physics Express*, vol. 7, no. 12, p. 125502, 2014.

[67] S. Raghavan, J. Y. Zhang, O. F. Shoron, and S. Stemmer, "Probing the metal-insulator transition in BaTiO$_3$ by electrostatic doping," *Physical Review Letters*, vol. 117, p. 037602, 3 2016.

[68] R. C. Haislmaier, E. D. Grimley, M. D. Biegalski, J. M. LeBeau, S. Trolier-McKinstry, V. Gopalan, and R. Engel-Herbert, "Unleashing strain induced ferroelectricity in complex oxide thin films via precise stoichiometry control," *Advanced Functional Materials*, n/a, 2016.

[69] A. P. Kajdos, D. G. Ouellette, T. A. Cain, and S. Stemmer, "Two-dimensional electron gas in a modulation-doped SrTiO$_3$/Sr(Ti,Zr)O$_3$ heterostructure," *Applied Physics Letters*, vol. 103, no. 8, 082120, 2013.

[70] A. Prakash, J. Dewey, H. Yun, J. S. Jeong, K. A. Mkhoyan, and B. Jalan, "Hybrid molecular beam epitaxy for the growth of stoichiometric BaSnO$_3$," *Journal of Vacuum Science Technology A*, vol. 33, no. 6, 060608, 2015.

[71] C. Eaton, J. A. Moyer, H. M. Alipour, E. D. Grimley, M. Brahlek, J. M. LeBeau, and R. Engel-Herbert, "Growth of SrVO$_3$ thin films by hybrid molecular beam epitaxy," *Journal of Vacuum Science Technology A*, vol. 33, no. 6, 061504, 2015.

[72] G. Subramanyam, M. W. Cole, N. X. Sun, T. S. Kalkur, N. M. Sbrockey, G. S. Tompa, X. Guo, C. Chen, S. P. Alpay, G. A. Rossetti, K. Dayal, L.-

Q. Chen, and D. G. Schlom, "Challenges and opportunities for multi-functional oxide thin films for voltage tunable radio frequency/microwave components," *Journal of Applied Physics*, vol. 114, no. 19, 191301, 2013.

[73] E. Mikheev, A. P. Kajdos, A. J. Hauser, and S. Stemmer, "Electric field-tunable $Ba_xSr_{1-x}TiO_3$ films with high figures of merit grown by molecular beam epitaxy," *Applied Physics Letters*, vol. 101, no. 25, 252906, 2012.

[74] P Bao, T. J. Jackson, X Wang, and M. J. Lancaster, "Barium strontium titanate thin film varactors for room-temperature microwave device applications," *Journal of Physics D: Applied Physics*, vol. 41, no. 6, p. 063001, 2008.

[75] T. J. Jackson and I. P. Jones, "Nanoscale defects and microwave properties of $(BaSr)TiO_3$ ferroelectric thin films," *Journal of Materials Science*, vol. 44, no. 19, p. 5288, 2009.

[76] L. Kong, S. Li, T. Zhang, J. Zhai, F. Boey, and J. Ma, "Electrically tunable dielectric materials and strategies to improve their performances," *Progress in Materials Science*, vol. 55, no. 8, p. 840, 2010.

[77] I. B. Vendik, O. G. Vendik, and E. L. Kollberg, "Commutation quality factor of two-state switchable devices," *IEEE Transactions on Microwave Theory and Techniques*, vol. 48, no. 5, p. 802, 2000.

[78] K. F. Astafiev, V. O. Sherman, A. K. Tagantsev, N. Setter, T. Kaydanova, and D. S. Ginley, "Crossover between extrinsic and intrinsic dielectric loss mechanisms in $SrTiO_3$ thin films at microwave frequencies," *Applied Physics Letters*, vol. 84, no. 13, 2004.

[79] K. F. Astafiev, A. K. Tagantsev, and N. Setter, "Quasi-Debye microwave loss as an intrinsic limitation of microwave performance of tunable components based on $SrTiO_3$ and $Ba_xSr_{1-x}TiO_3$ ferroelectrics," *Journal of Applied Physics*, vol. 97, no. 1, 014106, 2005.

[80] D. Galt, J. C. Price, J. A. Beall, and R. H. Ono, "Characterization of a tunable thin film microwave $YBa_2Cu_3O_{7-x}/SrTiO_3$ coplanar capacitor," *Applied Physics Letters*, vol. 63, no. 22, 1993.

[81] W. Chang, J. S. Horwitz, A. C. Carter, J. M. Pond, S. W. Kirchoefer, C. M. Gilmore, and D. B. Chrisey, "The effect of annealing on the microwave properties of $Ba_{0.5}Sr_{0.5}TiO_3$ thin films," *Applied Physics Letters*, vol. 74, no. 7, 1999.

[82] H. T. Su, M. J. Lancaster, F. Huang, and F. Wellhofer, "Electrically tunable superconducting quasilumped element resonator using thin-film ferroelectrics," *Microwave and Optical Technology Letters*, vol. 24, no. 3, p. 155, 2000.

[83] S. V. Razumov, A. V. Tumarkin, M. M. Gaidukov, A. G. Gagarin, A. B. Kozyrev, O. G. Vendik, A. V. Ivanov, O. U. Buslov, V. N. Keys, L. C. Sengupta, and X. Zhang, "Characterization of quality of $Ba_xSr_{1-x}TiO_3$ thin film by the commutation quality factor measured at microwaves," *Applied Physics Letters*, vol. 81, no. 9, 2002.

[84] P. M. Suherman, T. J. Jackson, Y. Koutsonas, R. A. Chakalov, and M. J. Lancaster, "On-wafer measurements of tuneability in $Ba_{0.5}Sr_{0.5}TiO_3$ thin films," *Integrated Ferroelectrics*, vol. 61, no. 1, p. 133, 2004.

[85] P. M. Suherman, T. J. Jackson, Y. Y. Tse, I. P. Jones, R. I. Chakalova, M. J. Lancaster, and A. Porch, "Microwave properties of $Ba_{0.5}Sr_{0.5}TiO_3$ thin film coplanar phase shifters," *Journal of Applied Physics*, vol. 99, no. 10, 104101, 2006.

[86] W. Chang, S. W. Kirchoefer, J. A. Bellotti, S. B. Qadri, J. M. Pond, J. H. Haeni, and D. G. Schlom, "In-plane anisotropy in the microwave dielec-

tric properties of SrTiO$_3$ films," *Journal of Applied Physics*, vol. 98, no. 2, 024107, 2005.

[87] X.-Y. Zhang, P. Wang, S. Sheng, F. Xu, and C. K. Ong, "Ferroelectric Ba$_x$Sr$_{1-x}$TiO$_3$ thin-film varactors with parallel plate and interdigital electrodes for microwave applications," *Journal of Applied Physics*, vol. 104, no. 12, 124110, 2008.

[88] C.-H. Lee, N. D. Orloff, T. Birol, Y. Zhu, V. Goian, E. Rocas, R. Haislmaier, E. Vlahos, J. A. Mundy, L. F. Kourkoutis, Y. Nie, M. D. Biegalski, J. Zhang, M Bernhagen, N. A. Benedek, Y. Kim, J. D. Brock, R. Uecker, X. X. Xi, V. Gopalan, D. Nuzhnyy, S. Kamba, D. A. Muller, I. Takeuchi, J. C. Booth, C. J. Fennie, and D. G. Schlom, "Exploiting dimensionality and defect mitigation to create tunable microwave dielectrics," *Nature*, vol. 502, no. 7472, p. 532, 2013.

[89] A. Vorobiev, P. Rundqvist, K. Khamchane, and S. Gevorgian, "Microwave loss mechanisms in Ba$_{0.25}$Sr$_{0.75}$TiO$_3$ thin film varactors," *Journal of Applied Physics*, vol. 96, no. 8, 2004.

[90] M. W. Cole, C. V. Weiss, E. Ngo, S. Hirsch, L. A. Coryell, and S. P. Alpay, "Microwave dielectric properties of graded barium strontium titanate films," *Applied Physics Letters*, vol. 92, no. 18, 182906, 2008.

[91] H.-C. Li, W. Si, A. D. West, and X. X. Xi, "Near single crystal-level dielectric loss and nonlinearity in pulsed laser deposited $SrTiO_3$ thin films," *Applied Physics Letters*, vol. 73, no. 2, 1998.

[92] J. Im, O. Auciello, P. K. Baumann, S. K. Streiffer, D. Y. Kaufman, and A. R. Krauss, "Composition-control of magnetron - sputter - deposited $(Ba_xSr_{1-x})Ti_{1+y}O_{3+z}$ thin films for voltage tunable devices," *Applied Physics Letters*, vol. 76, no. 5, 2000.

[93] T. R. Taylor, P. J. Hansen, N. Pervez, B. Acikel, R. A. York, and J. S. Speck, "Influence of stoichiometry on the dielectric properties of sputtered strontium titanate thin films," *Journal of Applied Physics*, vol. 94, no. 5, 2003.

[94] N. K. Pervez, P. J. Hansen, and R. A. York, "High tunability barium strontium titanate thin films for rf circuit applications," *Applied Physics Letters*, vol. 85, no. 19, 2004.

[95] S. S. Gevorgian, T. Martinsson, P. L. J. Linner, and E. L. Kollberg, "CAD models for multilayered substrate interdigital capacitors," *IEEE Transactions on Microwave Theory and Techniques*, vol. 44, no. 6, p. 896, 1996.

[96] J. Krupka, R. G. Geyer, M. Kuhn, and J. H. Hinken, "Dielectric properties of single crystals of Al_2O_3 , $LaAlO_3$, $NdGaO_3$, $SrTiO_3$, and MgO

at cryogenic temperatures," *IEEE Transactions on Microwave Theory and Techniques*, vol. 42, no. 10, p. 1886, 1994.

[97] M. T. Lanagan, "Microwave dielectric properties of antiferroelectric lead zirconate," PhD thesis, The Pennsylvania State University, 1987.

[98] H. Alexandru, C. Berbecaru, F. Stanculescu, A. Ioachim, M. Banciu, M. Toacsen, L. Nedelcu, D. Ghetu, and G. Stoica, "Ferroelectric solid solutions (Ba,Sr)TiO$_3$ for microwave applications," *Materials Science and Engineering: B*, vol. 118, no. 13, p. 92, 2005.

[99] A. K. Tagantsev and K. F. Astafiev, "Quasi-debye microwave loss in perovskite ferroelectrics," *Integrated Ferroelectrics*, vol. 39, no. 1-4, p. 251, 2001.

[100] A. K. Jonscher, "Dielectric relaxation in solids," *Journal of Physics D: Applied Physics*, vol. 32, no. 14, R57, 1999.

[101] N. K. Pervez, J. Park, J. Lu, S. Stemmer, and R. A. York, "High frequency loss modeling using dielectric relaxation," *Integrated Ferroelectrics*, vol. 77, no. 1, p. 87, 2005.

[102] J. Son, J. Cagnon, and S. Stemmer, "Strain relaxation in epitaxial Pt films on (001) SrTiO$_3$," *Journal of Applied Physics*, vol. 106, no. 4, 043525, 2009.

[103] X. M. Xu, J. Liu, Z. Yuan, J. Weaver, C. L. Chen, Y. R. Li, H. Gao, and N. Shi, "Single crystalline highly epitaxial Pt thin films on (001) $SrTiO_3$,"

[104] N. K. Pervez, "Investigation of loss mechanisms in thin film barium strontium titanate capacitors," PhD thesis, University of California, Santa Barbara, 2006.

[105] E. Mikheev, B. D. Hoskins, D. B. Strukov, and S. Stemmer, "Resistive switching and its suppression in Pt/Nb:$SrTiO_3$ junctions," *Nature Communications*, vol. 5, 2014.

[106] R. Waser and M. Aono, "Nanoionics-based resistive switching memories," *Nature Materials*, vol. 6, no. 11, p. 833, 2007.

[107] A. Sawa, "Resistive switching in transition metal oxides," *Materials Today*, vol. 11, no. 6, p. 28, 2008.

[108] R. Waser, R. Dittmann, G. Staikov, and K. Szot, "Redox-based resistive switching memories nanoionic mechanisms, prospects, and challenges," *Advanced Materials*, vol. 21, no. 25-26, p. 2632,

[109] C. Kügeler, R. Rosezin, E. Linn, R. Bruchhaus, and R. Waser, "Materials, technologies, and circuit concepts for nanocrossbar-based bipolar RRAM," *Applied Physics A*, vol. 102, no. 4, p. 791, 2011.

[110] I. Valov, R. Waser, J. R. Jameson, and M. N. Kozicki, "Electrochemical metallization memoriesfundamentals, applications, prospects," *Nanotechnology*, vol. 22, no. 25, p. 254003, 2011.

[111] D. Strukov and H. Kohlstedt, "Resistive switching phenomena in thin films: materials, devices, and applications," *MRS Bulletin*, vol. 37, no. 2, p. 108, 2012.

[112] H. S. P. Wong, H. Y. Lee, S. Yu, Y. S. Chen, Y. Wu, P. S. Chen, B. Lee, F. T. Chen, and M. J. Tsai, "Metal-oxide RRAM," *Proceedings of the IEEE*, vol. 100, no. 6, p. 1951, 2012.

[113] J. J. Yang, D. B. Strukov, and D. R. Stewart, "Memristive devices for computing," *Nature Nanotechnology*, vol. 8, no. 1, p. 13, 2013.

[114] D. B. Strukov and R. S. Williams, "Four-dimensional address topology for circuits with stacked multilayer crossbar arrays," *Proceedings of the National Academy of Sciences*, vol. 106, no. 48, p. 20155, 2009.

[115] V. V. Zhirnov, R. Meade, R. K. Cavin, and G. Sandhu, "Scaling limits of resistive memories," *Nanotechnology*, vol. 22, no. 25, p. 254027, 2011.

[116] J. S. Lee, S. Lee, and T. W. Noh, "Resistive switching phenomena: a review of statistical physics approaches," *Applied Physics Reviews*, vol. 2, no. 3, 031303, 2015.

[117] X. T. Zhang, Q. X. Yu, Y. P. Yao, and X. G. Li, "Ultrafast resistive switching in SrTiO$_3$:Nb single crystal," *Applied Physics Letters*, vol. 97, no. 22, 222117, 2010.

[118] F. Alibart, L. Gao, B. D. Hoskins, and D. B. Strukov, "High precision tuning of state for memristive devices by adaptable variation-tolerant algorithm," *Nanotechnology*, vol. 23, no. 7, p. 075201, 2012.

[119] M. Prezioso, F. M. Bayat, B. Hoskins, K. Likharev, and D. Strukov, "Self-adaptive spike-time-dependent plasticity of metal-oxide memristors," *Scientific reports*, vol. 6, 2016.

[120] F. Alibart, E. Zamanidoost, and D. B. Strukov, "Pattern classification by memristive crossbar circuits using ex situ and in situ training," *Nature Communications*, vol. 4, 2013.

[121] M. Prezioso, F. Merrikh-Bayat, B. D. Hoskins, G. C. Adam, K. K. Likharev, and D. B. Strukov, "Training and operation of an integrated neuromorphic network based on metal-oxide memristors," *Nature*, vol. 521, no. 7550, p. 61, 2015.

[122] J. J. Yang, I. H. Inoue, T. Mikolajick, and C. S. Hwang, "Metal oxide memories based on thermochemical and valence change mechanisms," *MRS Bulletin*, vol. 37, no. 2, p. 131, Feb. 2012.

[123] W. Lu, D. S. Jeong, M. Kozicki, and R. Waser, "Electrochemical metal-lization cellsblending nanoionics into nanoelectronics?" *MRS Bulletin*, vol. 37, no. 2, p. 124, Feb. 2012.

[124] J. J. Yang, M. D. Pickett, X. Li, D. A. A. Ohlberg, D. R. Stewart, and R. S. Williams, "Memristive switching mechanism for metal/oxide/metal nanodevices," *Nature Nanotechnology*, vol. 3, no. 7, p. 429, 2008.

[125] M.-J. Lee, C. B. Lee, D. Lee, S. R. Lee, M. Chang, J. H. Hur, Y.-B. Kim, C.-J. Kim, D. H. Seo, S. Seo, U.-I. Chung, I.-K. Yoo, and K. Kim, "A fast, high-endurance and scalable non-volatile memory device made from asymmetric Ta_2O_{5-x}/TaO_{2-x} bilayer structures," *Nature Materials*, vol. 10, no. 8, p. 625, 2011.

[126] A. A. Bessonov, M. N. Kirikova, D. I. Petukhov, M. Allen, T. Ryhanen, and M. J. A. Bailey, "Layered memristive and memcapacitive switches for printable electronics," *Nature Materials*, vol. 14, no. 2, p. 199, 2015.

[127] H. Sim, H. Choi, D. Lee, M. Chang, D. Choi, Y. Son, E.-H. Lee, W. Kim, Y. Park, I.-K. Yoo, and H. Hwang, "Excellent resistance switching charac-teristics of Pt/$SrTiO_3$ Schottky junction for multi-bit nonvolatile memory application," in *IEEE International Electron Devices Meeting, 2005. IEDM Technical Digest.*, IEEE, 2005, p. 758.

[128] M. Hasan, R. Dong, H. J. Choi, D. S. Lee, D.-J. Seong, M. B. Pyun, and H. Hwang, "Effect of ruthenium oxide electrode on the resistive switching of Nb-doped strontium titanate," *Applied Physics Letters*, vol. 93, no. 5, 052908, 2008.

[129] C. Park, Y. Seo, J. Jung, and D.-W. Kim, "Electrode-dependent electrical properties of metal/Nb-doped $SrTiO_3$ junctions," *Journal of Applied Physics*, vol. 103, no. 5, 054106, 2008.

[130] H. Kim, C. Park, S. Lee, and D.-W. Kim, "Inhomogeneous barrier and hysteretic transport properties of Pt/$SrTiO_3$ junctions," *Journal of Physics D: Applied Physics*, vol. 42, no. 5, p. 055306, 2009.

[131] D.-W. Kim, M. Gwon, E. Lee, A. Sohn, and E. Mostafa Bourim, "Doping-level Dependences of Switching Speeds and the Retention Characteristics of Resistive Switching Pt/$SrTiO_3$ Junctions," *Journal of Korean Physical Society*, vol. 57, p. 1432, Dec. 2010.

[132] D. Kan, K. Ito, and Y. Shimakawa, "Local conduction in junctions composed of Pt and single-crystalline Nb-doped $SrTiO_3$," *Thin Solid Films*, vol. 518, no. 12, p. 3246, 2010.

[133] E. Lee, M. Gwon, D.-W. Kim, and H. Kim, "Resistance state-dependent barrier inhomogeneity and transport mechanisms in resistive-switching

Pt/SrTiO$_3$ junctions," *Applied Physics Letters*, vol. 98, no. 13, 132905, 2011.

[134] J. Li, N. Ohashi, H. Okushi, and H. Haneda, "Temperature dependence of carrier transport and resistance switching in Pt/SrTi$_{1-x}$Nb$_x$O$_3$ Schottky junctions," *Physical Review B*, vol. 83, p. 125317, 12 2011.

[135] N. Ohashi, H. Yoshikawa, Y. Yamashita, S. Ueda, J. Li, H. Okushi, K. Kobayashi, and H. Haneda, "Determination of schottky barrier profile at Pt/SrTiO$_3$:Nb junction by x-ray photoemission," *Applied Physics Letters*, vol. 101, no. 25, 251911, 2012.

[136] Q. Gao, B. Chen, Q. Yu, X. Zhang, and H. Zhu, "Influence of thermal treatment on the resistance switching of SrTiO$_3$:Nb single crystal," *Journal of Alloys and Compounds*, vol. 569, p. 62, 2013.

[137] E. M. Bourim and D.-W. Kim, "Conductance spectroscopy of resistive switching Pt/Nb:STO single crystal schottky junctions in air and vacuum," *Current Applied Physics*, vol. 13, no. 3, p. 505, 2013.

[138] D. Kan and Y. Shimakawa, "Transient behavior in Pt/Nb-doped SrTiO$_3$ Schottky junctions," *Applied Physics Letters*, vol. 103, no. 14, 142910, 2013.

[139] C Rodenbucher, W Speier, G Bihlmayer, U Breuer, R Waser, and K Szot, "Cluster-like resistive switching of $SrTiO_3$:Nb surface layers," *New Journal of Physics*, vol. 15, no. 10, p. 103017, 2013.

[140] S. Lee, J. S. Lee, J.-B. Park, Y. Koo Kyoung, M.-J. Lee, and T. Won Noh, "Anomalous effect due to oxygen vacancy accumulation below the electrode in bipolar resistance switching Pt/Nb:$SrTiO_3$ cells," *APL Mater.*, vol. 2, no. 6, 066103, 2014.

[141] J. Park, D.-H. Kwon, H. Park, C. U. Jung, and M. Kim, "Role of oxygen vacancies in resistive switching in Pt/Nb-doped $SrTiO_3$," *Applied Physics Letters*, vol. 105, no. 18, 183103, 2014.

[142] Y. Yang, W. Lu, Y. Yao, J. Sun, C. Gu, L. Gu, Y. Wang, X. Duan, and R. Yu, "In situ TEM observation of resistance switching in titanate based device," *Scientific Reports*, vol. 4, 2014.

[143] C. Baeumer, N. Raab, T. Menke, C. Schmitz, R. Rosezin, P. Muller, M. Andra, V. Feyer, R. Bruchhaus, F. Gunkel, C. M. Schneider, R. Waser, and R. Dittmann, "Verification of redox-processes as switching and retention failure mechanisms in Nb:$SrTiO_3$/metal devices," *Nanoscale*, vol. 8, p. 13967, 29 2016.

[144] D. S. Shang, J. R. Sun, L. Shi, and B. G. Shen, "Photoresponse of the schottky junction Au/SrTiO$_3$:Nb in different resistive states," *Applied Physics Letters*, vol. 93, no. 10, 102106, 2008.

[145] D. S. Shang, J. R. Sun, L. Shi, J. Wang, Z. H. Wang, and B. G. Shen, "Electronic transport and colossal electroresistance in SrTiO$_3$:Nb-based Schottky junctions," *Applied Physics Letters*, vol. 94, no. 5, 052105, 2009.

[146] K. G. Rana, V. Khikhlovskyi, and T. Banerjee, "Electrical transport across Au/Nb:SrTiO$_3$ schottky interface with different Nb doping," *Applied Physics Letters*, vol. 100, no. 21, 213502, 2012.

[147] R. Buzio, A. Gerbi, A. Gadaleta, L. Anghinolfi, F. Bisio, E. Bellingeri, A. S. Siri, and D. Marre, "Modulation of resistance switching in Au/Nb:SrTiO$_3$ schottky junctions by ambient oxygen," *Applied Physics Letters*, vol. 101, no. 24, 243505, 2012.

[148] J. X. Shen, H. Q. Qian, G. F. Wang, Y. H. An, P. G. Li, Y. Zhang, S. L. Wang, B. Y. Chen, and W. H. Tang, "Temperature-dependent resistive switching behavior in the structure of Au/Nb:SrTiO$_3$/Ti," *Applied Physics A*, vol. 111, no. 1, p. 303, 2013.

[149] Y. H. Wang, K. H. Zhao, X. L. Shi, G. L. Xie, S. Y. Huang, and L. W. Zhang, "Investigation of the resistance switching in Au/SrTiO$_3$:Nb: heterojunctions," *Applied Physics Letters*, vol. 103, no. 3, 031601, 2013.

[150] X.-B. Yin, Z.-H. Tan, and X. Guo, "The role of schottky barrier in the resistive switching of SrTiO$_3$: direct experimental evidence," *Physical Chemistry Chemical Physics*, vol. 17, p. 134, 1 2015.

[151] T. Fujii, M. Kawasaki, A. Sawa, H. Akoh, Y. Kawazoe, and Y. Tokura, "Hysteretic currentvoltage characteristics and resistance switching at an epitaxial oxide Schottky junction SrRuO$_3$ / SrTi$_{0.99}$Nb$_{0.01}$O$_3$," *Applied Physics Letters*, vol. 86, no. 1, 012107, 2005.

[152] T. Fujii, M. Kawasaki, A. Sawa, Y. Kawazoe, H. Akoh, and Y. Tokura, "Electrical properties and colossal electroresistance of heteroepitaxial SrRuO$_3$ / SrTi$_{1-x}$Nb$_x$O$_3$ $(0.0002{\leqslant}x{\leqslant}0.02)$ Schottky junctions," *Physical Review B*, vol. 75, p. 165101, 16 2007.

[153] H. J. Zhang, X. P. Zhang, J. P. Shi, H. F. Tian, and Y. G. Zhao, "Effect of oxygen content and superconductivity on the nonvolatile resistive switching in YBa$_2$Cu$_3$o$_{6+x}$/Nb-doped SrTiO$_3$ heterojunctions," *Applied Physics Letters*, vol. 94, no. 9, 092111, 2009.

[154] A. Asamitsu, Y. Tomioka, H. Kuwahara, and Y. Tokura, "Current switching of resistive states in magnetoresistive manganites," *Nature*, vol. 388, no. 6637, p. 50, 1997.

[155] A. Sawa, T. Fujii, M. Kawasaki, and Y. Tokura, "Hysteretic currentvoltage characteristics and resistance switching at a rectifying Ti/Pr$_{0.7}$Ca$_{0.3}$Mno$_3$ interface," *Applied Physics Letters*, vol. 85, no. 18, 2004.

[156] ——, "Interface resistance switching at a few nanometer thick perovskite manganite active layers," *Applied Physics Letters*, vol. 88, no. 23, 232112, 2006.

[157] B. J. Choi, D. S. Jeong, S. K. Kim, C. Rohde, S. Choi, J. H. Oh, H. J. Kim, C. S. Hwang, K. Szot, R. Waser, B. Reichenberg, and S. Tiedke, "Resistive switching mechanism of TiO$_2$ thin films grown by atomic-layer deposition," *Journal of Applied Physics*, vol. 98, no. 3, 033715, 2005.

[158] T. Yanagida, K. Nagashima, K. Oka, M. Kanai, A. Klamchuen, B. H. Park, and T. Kawai, "Scaling effect on unipolar and bipolar resistive switching of metal oxides," *Scientific Reports*, vol. 3, p. 1657, 2013.

[159] S. B. Lee, S. C. Chae, S. H. Chang, J. S. Lee, S. Seo, B. Kahng, and T. W. Noh, "Scaling behaviors of reset voltages and currents in unipolar

resistance switching," *Applied Physics Letters*, vol. 93, no. 21, 212105, 2008.

[160] D. R. Wolters and J. J. van der Schoot, "Kinetics of charge trapping in dielectrics," *Journal of Applied Physics*, vol. 58, no. 2, 1985.

[161] J. R. Jameson, W. Harrison, P. B. Griffin, and J. D. Plummer, "Double-well model of dielectric relaxation current," *Applied Physics Letters*, vol. 84, no. 18, 2004.

[162] J. R. Jameson, P. B. Griffin, J. D. Plummer, and Y. Nishi, "Charge trapping in high-k gate stacks due to the bilayer structure itself," *IEEE Transactions on Electron Devices*, vol. 53, no. 8, p. 1858, 2006.

[163] Y. Hirose and H. Hirose, "Polarity-dependent memory switching and behavior of ag dendrite in agphotodoped amorphous As_2S_3 films," *Journal of Applied Physics*, vol. 47, no. 6, 1976.

[164] M. N. Kozicki, M. Balakrishnan, C. Gopalan, C. Ratnakumar, and M. Mitkova, "Programmable metallization cell memory based on Ag-Ge-S and Cu-Ge-S solid electrolytes," in *Symposium Non-Volatile Memory Technology 2005.*, 2005, 7 pp.

[165] D. Jana, S. Roy, R. Panja, M. Dutta, S. Z. Rahaman, R. Mahapatra, and S. Maikap, "Conductive-bridging random access memory: challenges and

opportunity for 3D architecture," *Nanoscale Research Letters*, vol. 10, no. 1, p. 1, 2015.

[166] M. Janousch, G. Meijer, U. Staub, B. Delley, S. Karg, and B. Andreasson, "Role of oxygen vacancies in Cr-doped $SrTiO_3$ for resistance-change memory," *Advanced Materials*, vol. 19, no. 17, p. 2232, 2007.

[167] A. Chanthbouala, A. Crassous, V. Garcia, K. Bouzehouane, S. Fusil, X. Moya, J. Allibe, B. Dlubak, J. Grollier, S. Xavier, C. Deranlot, A Moshar, R. Proksch, N. D. Mathur, M. Bibes, and A. Barthélémy, "Solid-state memories based on ferroelectric tunnel junctions," *Nature Nanotechnology*, vol. 7, no. 2, p. 101, 2012.

[168] A. Chanthbouala, V. Garcia, R. O. Cherifi, K. Bouzehouane, S. Fusil, X. Moya, S. Xavier, H. Yamada, C. Deranlot, N. D. Mathur, M. Bibes, A. Barthélémy, and J. Grollier, "A ferroelectric memristor," *Nature Materials*, vol. 11, no. 10, p. 860, 2012.

[169] V. Garcia and M. Bibes, "Ferroelectric tunnel junctions for information storage and processing," *Nature Communications*, vol. 5, 2014.

[170] C.-H. Chen, E. L. Hu, W. V. Schoenfeld, and P. M. Petroff, "Metallization-induced damage in III-V semiconductors," *Journal of Vacuum Science Technology B*, vol. 16, no. 6, 1998.

[171] Y Takai and M Sato, "Epitaxial growth of platinum thin films on (100) MgO by pulsed laser deposition," *Superconductor Science and Technology*, vol. 12, no. 8, p. 486, 1999.

[172] M. Yoshimoto, H. Ohkubo, N. Kanda, and H. Koinuma, "Two-dimensional epitaxial growth of $SrTiO_3$ films on carbon-free clean surface of Nb-doped $SrTiO_3$ substrate by laser molecular beam epitaxy," *Japanese Journal of Applied Physics*, vol. 31, no. 11R, p. 3664, 1992.

[173] J. Baniecki, M Ishii, K Kurihara, K Yamanaka, T Yano, K Shinozaki, T Imada, and Y Kobayashi, "Chemisorption of water and carbon dioxide on nanostructured $BaTiO_3$-$SrTiO_3$ (001) surfaces," *Journal of Applied Physics*, vol. 106, no. 5, p. 4109, 2009.

[174] B. Jalan, J. Cagnon, T. E. Mates, and S. Stemmer, "Analysis of carbon in $SrTiO_3$ grown by hybrid molecular beam epitaxy," *Journal of Vacuum Science Technology A*, vol. 27, no. 6, 2009.

[175] P. A. Kollensperger, W. J. Karl, M. M. Ahmad, W. T. Pike, and M Green, "Patterning of platinum (Pt) thin films by chemical wet etching in Aqua Regia," *Journal of Micromechanics and Microengineering*, vol. 22, no. 6, p. 067001, 2012.

[176] T. Shimizu and H. Okushi, "The properties of a metal/oxide semiconductor junction prepared using a high-purity ozone surface treatment," *Applied Physics Letters*, vol. 67, no. 10, 1995.

[177] ——, "Intrinsic electrical properties of Au/SrTiO$_3$ Schottky junctions," *Journal of Applied Physics*, vol. 85, no. 10, 1999.

[178] M. Stengel and N. A. Spaldin, "Origin of the dielectric dead layer in nanoscale capacitors," *Nature*, vol. 443, no. 7112, p. 679, 2006.

[179] T. M. Shaw, Z. Suo, M. Huang, E. Liniger, R. B. Laibowitz, and J. D. Baniecki, "The effect of stress on the dielectric properties of barium strontium titanate thin films," *Applied Physics Letters*, vol. 75, no. 14, 1999.

[180] S. K. Streiffer, C. Basceri, C. B. Parker, S. E. Lash, and A. I. Kingon, "Ferroelectricity in thin films: the dielectric response of fiber-textured (Ba$_x$Sr$_{1x}$)Ti$_{1+y}$O$_{3+z}$ thin films grown by chemical vapor deposition," *Journal of Applied Physics*, vol. 86, no. 8, 1999.

[181] H. B. Michaelson, "The work function of the elements and its periodicity," *Journal of Applied Physics*, vol. 48, no. 11, 1977.

[182] J Robertson and C. Chen, "Schottky barrier heights of tantalum oxide, barium strontium titanate, lead titanate, and strontium bismuth tantalate," *Applied Physics Letters*, vol. 74, no. 8, p. 1168, 1999.

[183] A. Ohtomo and H. Y. Hwang, "Surface depletion in doped $SrTiO_3$ thin films," *Applied Physics Letters*, vol. 84, no. 10, 2004.

[184] S. Westerlund and L. Ekstam, "Capacitor theory," *IEEE Transactions on Dielectrics and Electrical Insulation*, vol. 1, no. 5, p. 826, 1994.

[185] S. Zafar, A. Callegari, E. Gusev, and M. V. Fischetti, "Charge trapping related threshold voltage instabilities in high permittivity gate dielectric stacks," *Journal of Applied Physics*, vol. 93, no. 11, 2003.

[186] S. Stemmer, S. K. Streiffer, N. D. Browning, and A. I. Kingon, "Accommodation of nonstoichiometry in (100) fiber-textured $(Ba_xSr_{1-x})Ti_{1+y}O_{3+z}$ thin films grown by chemical vapor deposition," *Applied Physics Letters*, vol. 74, no. 17, 1999.

[187] T. Suzuki, Y. Nishi, and M. Fujimoto, "Defect structure in homoepitaxial non-stoichiometric strontium titanate thin films," *Philosophical Magazine A*, vol. 80, no. 3, p. 621, 2000.

[188] A. Janotti, J. B. Varley, M. Choi, and C. G. Van de Walle, "Vacancies and small polarons in $SrTiO_3$," *Physical Review B*, vol. 90, p. 085202, 8 2014.

[189] A. A. Grinberg, S. Luryi, M. R. Pinto, and N. L. Schryer, "Space-charge-limited current in a film," *IEEE Transactions on Electron Devices*, vol. 36, no. 6, p. 1162, 1989.

251

[190] V. Aubry and F. Meyer, "Schottky diodes with high series resistance: limitations of forward I-V methods," *Journal of Applied Physics*, vol. 76, no. 12, 1994.

[191] P. Chattopadhyay, "The effect of shunt resistance on the electrical characteristics of Schottky barrier diodes," *Journal of Physics D: Applied Physics*, vol. 29, no. 3, p. 823, 1996.

[192] T. Horikawa, T. Makita, T. Kuroiwa, and N. Mikami, "Dielectric relaxation of (Ba,Sr)TiO$_3$ thin films," *Japanese Journal of Applied Physics*, vol. 34, no. 9S, p. 5478, 1995.

[193] J. D. Baniecki, R. B. Laibowitz, T. M. Shaw, P. R. Duncombe, D. A. Neumayer, D. E. Kotecki, H. Shen, and Q. Y. Ma, "Dielectric relaxation of Ba$_{0.7}$Sr$_{0.3}$TiO$_3$ thin films from 1 mHz to 20 GHz," *Applied Physics Letters*, vol. 72, no. 4, 1998.

[194] D. P. Almond and C. R. Bowen, "Anomalous power law dispersions in ac conductivity and permittivity shown to be characteristics of microstructural electrical networks," *Physical Review Letters*, vol. 92, p. 157601, 15 2004.

[195] S. Panteny, R. Stevens, and C. R. Bowen, "The frequency dependent permittivity and AC conductivity of random electrical networks," *Ferroelectrics*, vol. 319, no. 1, p. 199, 2005.

[196] A. Beck, J. G. Bednorz, C. Gerber, C. Rossel, and D. Widmer, "Reproducible switching effect in thin oxide films for memory applications," *Applied Physics Letters*, vol. 77, no. 1, 2000.

[197] C. Rossel, G. I. Meijer, D. Bremaud, and D. Widmer, "Electrical current distribution across a metal-insulator-metal structure during bistable switching," *Journal of Applied Physics*, vol. 90, no. 6, 2001.

[198] S. F. Karg, G. I. Meijer, J. G. Bednorz, C. T. Rettner, A. G. Schrott, E. A. Joseph, C. H. Lam, M. Janousch, U. Staub, F. L. Mattina, S. F. Alvarado, D. Widmer, R. Stutz, U. Drechsler, and D. Caimi, "Transition-metal-oxide-based resistance-change memories," *IBM Journal of Research and Development*, vol. 52, no. 4.5, p. 481, 2008.

[199] T. Menke, P. Meuffels, R. Dittmann, K. Szot, and R. Waser, "Separation of bulk and interface contributions to electroforming and resistive switching behavior of epitaxial Fe-doped $SrTiO_3$," *Journal of Applied Physics*, vol. 105, no. 6, 066104, 2009.

[200] S. Cho, W. G. Park, D.-Y. Cho, P. Berthet, and S.-J. Oh, "Effect of Cr concentration on resistance switching in Cr-doped $SrZrO_3$ films and surface accumulation of Cr ions," *Journal of Applied Physics*, vol. 108, no. 10, 103716, 2010.

[201] E. Mikheev, B. Himmetoglu, A. P. Kajdos, P. Moetakef, T. A. Cain, C. G. Van de Walle, and S. Stemmer, "Limitations to the room temperature mobility of two- and three-dimensional electron liquids in $SrTiO_3$," *Applied Physics Letters*, vol. 106, no. 6, 062102, 2015.

[202] E. Mikheev, C. R. Freeze, B. J. Isaac, T. A. Cain, and S. Stemmer, "Separation of transport lifetimes in $SrTiO_3$-based two-dimensional electron liquids," *Physical Review B*, vol. 91, p. 165125, 16 2015.

[203] E. Mikheev, S. Raghavan, J. Y. Zhang, P. B. Marshall, A. P. Kajdos, L. Balents, and S. Stemmer, "Carrier density independent scattering rate in $SrTiO_3$-based electron liquids," *Scientific Reports*, vol. 6, 2016.

[204] L. F. Mattheiss, "Energy bands for $KNiF_3$, $SrTiO_3$, $KMoO_3$, and $KTao_3$," *Physical Review B*, vol. 6, p. 4718, 12 1972.

[205] A. Janotti, D. Steiauf, and C. G. Van de Walle, "Strain effects on the electronic structure of $SrTiO_3$: toward high electron mobilities," *Physical Review B*, vol. 84, p. 201304, 20 2011.

[206] D. van der Marel, J. L. M. van Mechelen, and I. I. Mazin, "Common Fermi-liquid origin of T^2 resistivity and superconductivity in n-type SrTiO$_3$," *Physical Review B*, vol. 84, p. 205111, 20 2011.

[207] M. Imada, A. Fujimori, and Y. Tokura, "Metal-insulator transitions," *Reviews of Modern Physics*, vol. 70, p. 1039, 4 1998.

[208] S. J. Allen, B. Jalan, S. Lee, D. G. Ouellette, G. Khalsa, J. Jaroszynski, S. Stemmer, and A. H. MacDonald, "Conduction-band edge and Shubnikov-de Haas effect in low-electron-density SrTiO$_3$," *Physical Review B*, vol. 88, p. 045114, 4 2013.

[209] X. Lin, G. Bridoux, A. Gourgout, G. Seyfarth, S. Krämer, M. Nardone, B. Fauqué, and K. Behnia, "Critical doping for the onset of a two-band superconducting ground state in SrTiO$_3$," *Physical Review Letters*, vol. 112, p. 207002, 20 2014.

[210] Y. Tokura, Y. Taguchi, Y. Okada, Y. Fujishima, T. Arima, K. Kumagai, and Y. Iye, "Filling dependence of electronic properties on the verge of metal-Mott-insulator transition in Sr$_{1-x}$La$_x$TiO$_3$," *Physical Review Letters*, vol. 70, p. 2126, 14 1993.

[211] C. C. Hays, J.-S. Zhou, J. T. Markert, and J. B. Goodenough, "Electronic transition in La$_{1-x}$Sr$_x$TiO$_3$," *Physical Review B*, vol. 60, p. 10367, 14 1999.

[212] P. Moetakef and T. A. Cain, "Metal insulator transitions in epitaxial Gd$_{1-x}$Sr$_x$TiO$_3$ thin films grown using hybrid molecular beam epitaxy," *Thin Solid Films*, vol. 583, p. 129, 2015.

[213] C. S. Koonce, M. L. Cohen, J. F. Schooley, W. R. Hosler, and E. R. Pfeiffer, "Superconducting transition temperatures of semiconducting SrTiO$_3$," *Physical Review*, vol. 163, p. 380, 2 1967.

[214] A. Spinelli, M. A. Torija, C. Liu, C. Jan, and C. Leighton, "Electronic transport in doped SrTiO$_3$: conduction mechanisms and potential applications," *Physical Review B*, vol. 81, p. 155110, 15 2010.

[215] J. F. Schooley, W. R. Hosler, E. Ambler, J. H. Becker, M. L. Cohen, and C. S. Koonce, "Dependence of the superconducting transition temperature on carrier concentration in semiconducting SrTiO$_3$," *Physical Review Letters*, vol. 14, p. 305, 9 1965.

[216] A. C. Komarek, H. Roth, M. Cwik, W.-D. Stein, J. Baier, M. Kriener, F. Bourée, T. Lorenz, and M. Braden, "Magnetoelastic coupling in RTiO$_3$ (R=La, Nd, Sm, Gd, Y) investigated with diffraction techniques and

thermal expansion measurements," *Physical Review B*, vol. 75, p. 224402, 22 2007.

[217] X. Lin, Z. Zhu, B. Fauqué, and K. Behnia, "Fermi surface of the most dilute superconductor," *Physical Review X*, vol. 3, p. 021002, 2 2013.

[218] J. Appel, "Soft-mode superconductivity in $SrTiO_{3-x}$," *Physical Review*, vol. 180, p. 508, 2 1969.

[219] S. Rowley, L. Spalek, R. Smith, M. Dean, M. Itoh, J. Scott, G. Lonzarich, and S. Saxena, "Ferroelectric quantum criticality," *Nature Physics*, vol. 10, p. 367, 2014.

[220] J. M. Edge, Y. Kedem, U. Aschauer, N. A. Spaldin, and A. V. Balatsky, "Quantum critical origin of the superconducting dome in $SrTiO_3$," *Physical Review Letters*, vol. 115, p. 247002, 24 2015.

[221] H. D. Zhou and J. B. Goodenough, "Localized or itinerant TiO_3 electrons in $RTiO_3$ perovskites," *Journal of Physics: Condensed Matter*, vol. 17, no. 46, p. 7395, 2005.

[222] J. Hubbard, "Electron correlations in narrow energy bands," *Proceedings of the Royal Society of London A: Mathematical, Physical and Engineering Sciences*, vol. 276, no. 1365, p. 238, 1963.

[223] ——, "Electron correlations in narrow energy bands. II. the degenerate band case," *Proceedings of the Royal Society of London A: Mathematical, Physical and Engineering Sciences*, vol. 277, no. 1369, p. 237, 1964.

[224] ——, "Electron correlations in narrow energy bands. III. an improved solution," *Proceedings of the Royal Society of London A: Mathematical, Physical and Engineering Sciences*, vol. 281, no. 1386, p. 401, 1964.

[225] M. Heinrich, H.-A. Krug von Nidda, V. Fritsch, and A. Loidl, "Heavy-fermion formation at the metal-to-insulator transition in $Gd_{1-x}Sr_xTiO_3$," *Physical Review B*, vol. 63, p. 193103, 19 2001.

[226] F. Inaba, T. Arima, T. Ishikawa, T. Katsufuji, and Y. Tokura, "Change of electronic properties on the doping-induced insulator-metal transition in $La_{1-x}Sr_xVO_3$," *Physical Review B*, vol. 52, R2221, 4 1995.

[227] J. L. García-Muñoz, M. Suaaidi, M. J. Martínez-Lope, and J. A. Alonso, "Influence of carrier injection on the metal-insulator transition in electron- and hole-doped $R_{1-x}A_xNiO_3$ perovskites," *Physical Review B*, vol. 52, p. 13563, 18 1995.

[228] M. L. Medarde, "Structural, magnetic and electronic properties of $RNiO_3$ perovskites (R = rare earth)," *Journal of Physics: Condensed Matter*, vol. 9, no. 8, p. 1679, 1997.

[229] S. Middey, J. Chakhalian, P. Mahadevan, J. Freeland, A. Millis, and D. Sarma, "Physics of ultrathin films and heterostructures of rare-earth nickelates," *Annual Review of Materials Research*, vol. 46, no. 1, p. 305, 2016.

[230] P. A. Lee, N. Nagaosa, and X.-G. Wen, "Doping a Mott insulator: physics of high-temperature superconductivity," *Reviews of Modern Physics*, vol. 78, p. 17, 1 2006.

[231] J. Mannhart and D. G. Schlom, "Oxide interfaces-an opportunity for electronics," *Science*, vol. 327, no. 5973, p. 1607, 2010.

[232] M. Bibes, J. E. Villegas, and A. Barthélémy, "Ultrathin oxide films and interfaces for electronics and spintronics," *Advances in Physics*, vol. 60, no. 1, p. 5, 2011.

[233] H. Y. Hwang, Y. Iwasa, M. Kawasaki, B. Keimer, N. Nagaosa, and Y. Tokura, "Emergent phenomena at oxide interfaces," *Nature Materials*, vol. 11, no. 2, p. 103, 2012.

[234] J. Chakhalian, J. W. Freeland, A. J. Millis, C. Panagopoulos, and J. M. Rondinelli, "*Colloquium* : emergent properties in plane view: strong correlations at oxide interfaces," *Reviews of Modern Physics*, vol. 86, p. 1189, 4 2014.

[235] C. Noguera, "Polar oxide surfaces," *Journal of Physics: Condensed Matter*, vol. 12, no. 31, R367, 2000.

[236] T. Higuchi and H. Y. Hwang, "General considerations of the electrostatic boundary conditions in oxide heterostructures," in, E. Tsymbal, E. Dagotto, C. Eom, and R. Ramesh, Eds. Oxford University Press, 2011.

[237] P. Moetakef, C. A. Jackson, J. Hwang, L. Balents, S. J. Allen, and S. Stemmer, "Toward an artificial Mott insulator: correlations in confined high-density electron liquids in $SrTiO_3$," *Physical Review B*, vol. 86, p. 201102, 20 2012.

[238] G. Khalsa and A. H. MacDonald, "Theory of the $SrTiO_3$ surface state two-dimensional electron gas," *Physical Review B*, vol. 86, p. 125121, 12 2012.

[239] A. Ohtomo and H. Hwang, "A high-mobility electron gas at the $LaAlO_3$/$SrTiO_3$ heterointerface," *Nature*, vol. 427, no. 6973, p. 423, 2004.

[240] S. Thiel, G. Hammerl, A. Schmehl, C. W. Schneider, and J. Mannhart, "Tunable quasi-two-dimensional electron gases in oxide heterostructures," *Science*, vol. 313, no. 5795, p. 1942, 2006.

[241] M. Huijben, G. Rijnders, D. H. Blank, S. Bals, S. Van Aert, J. Verbeeck, G. Van Tendeloo, A. Brinkman, and H. Hilgenkamp, "Electronically coupled

complementary interfaces between perovskite band insulators," *Nature Materials*, vol. 5, no. 7, p. 556, 2006.

[242] M. Huijben, A. Brinkman, G. Koster, G. Rijnders, H. Hilgenkamp, and D. H. A. Blank, "Structure-property relation of $SrTiO_3$/$LaAlO_3$ interfaces," *Advanced Materials*, vol. 21, no. 17, p. 1665, 2009.

[243] P. Moetakef, J. Y. Zhang, A. Kozhanov, B. Jalan, R. Seshadri, S. J. Allen, and S. Stemmer, "Transport in ferromagnetic $GdTiO_3$/$SrTiO_3$ heterostructures," *Applied Physics Letters*, vol. 98, no. 11, 112110, 2011.

[244] T. A. Cain, P. Moetakef, C. A. Jackson, and S. Stemmer, "Modulation doping to control the high-density electron gas at a polar/non-polar oxide interface," *Applied Physics Letters*, vol. 101, no. 11, 111604, 2012.

[245] H. J. H. Ma, Z. Huang, W. M. L, A. Annadi, S. W. Zeng, L. M. Wong, S. J. Wang, T. Venkatesan, and Ariando, "Tunable bilayer two-dimensional electron gas in $LaAlO_3$/$SrTiO_3$ superlattices," *Applied Physics Letters*, vol. 105, no. 1, 011603, 2014.

[246] G. Herranz, M. Basletić, M. Bibes, C Carrétéro, E. Tafra, E Jacquet, K. Bouzehouane, C Deranlot, A. Hamzić, J.-M. Broto, *et al.*, "High mobility in $LaAlO_3$/$SrTiO_3$ heterostructures: origin, dimensionality, and perspectives," *Physical review letters*, vol. 98, no. 21, p. 216803, 2007.

[247] Y. Z. Chen, N. Bovet, F. Trier, D. V. Christensen, F. M. Qu, N. H. Andersen, T. Kasama, W. Zhang, R. Giraud, J. Dufouleur, T. S. Jespersen, J. R. Sun, A. Smith, J. Nygard, L. Lu, B. Buchner, B. G. Shen, S Linderoth, and N. Pryds, "A high-mobility two-dimensional electron gas at the spinel / perovskite interface of γ-Al$_2$O$_3$ / SrTiO$_3$," *Nature Communications*, vol. 4, p. 1371, 2013.

[248] S. W. Lee, Y. Liu, J. Heo, and R. G. Gordon, "Creation and control of two-dimensional electron gas using Al-based amorphous oxides/SrTiO$_3$ heterostructures grown by atomic layer deposition," *Nano Letters*, vol. 12, no. 9, p. 4775, 2012.

[249] S. W. Lee, J. Heo, and R. G. Gordon, "Origin of the self-limited electron densities at Al$_2$O$_3$/SrTiO$_3$ heterostructures grown by atomic layer deposition - oxygen diffusion model," *Nanoscale*, vol. 5, p. 8940, 19 2013.

[250] N. W. Ashcroft and N. D. Mermin, *Solid state physics*. Saunders College Publishing, 1976.

[251] D. C. Look, *Electrical characterization of GaAs materials and devices*. John Wiley & Sons, 1989.

[252] L Van der Pauw, "A method of measuring specific resistivity and Hall effect of discs of arbitrary shape," *Philips Research Reports*, vol. 13, p. 1, 1958.

[253] R. Chwang, B. Smith, and C. Crowell, "Contact size effects on the van der Pauw method for resistivity and Hall coefficient measurement," *Solid-State Electronics*, vol. 17, no. 12, p. 1217, 1974.

[254] W. G. Baber, "The contribution to the electrical resistance of metals from collisions between electrons," *Proceedings of the Royal Society of London A: Mathematical, Physical and Engineering Sciences*, vol. 158, no. 894, p. 383, 1937.

[255] J. Bass, W. P. Pratt, and P. A. Schroeder, "The temperature-dependent electrical resistivities of the alkali metals," *Reviews of Modern Physics*, vol. 62, p. 645, 3 1990.

[256] A. G. Beattie and G. A. Samara, "Pressure dependence of the elastic constants of $SrTiO_3$," *Journal of Applied Physics*, vol. 42, no. 6, 1971.

[257] M. Ahrens, R. Merkle, B. Rahmati, and J. Maier, "Effective masses of electrons in n-type $SrTiO_3$ determined from low-temperature specific heat capacities," *Physica B: Condensed Matter*, vol. 393, no. 12, p. 239, 2007.

[258] A. Verma, A. P. Kajdos, T. A. Cain, S. Stemmer, and D. Jena, "Intrinsic mobility limiting mechanisms in lanthanum-doped strontium titanate," *Physical Review Letters*, vol. 112, p. 216601, 21 2014.

[259] F. E. Low and D. Pines, "Mobility of slow electrons in polar crystals," *Physical Review*, vol. 98, p. 414, 2 1955.

[260] W. G. Spitzer, R. C. Miller, D. A. Kleinman, and L. E. Howarth, "Far infrared dielectric dispersion in $BaTiO_3$, $SrTiO_3$, and TiO_2," *Physical Review*, vol. 126, p. 1710, 5 1962.

[261] D. Eagles, "Polaron coupling coustants in $SrTiO_3$," *Journal of Physics and Chemistry of Solids*, vol. 26, no. 3, p. 672, 1965.

[262] W. E. Lawrence and J. W. Wilkins, "Electron-electron scattering in the transport coefficients of simple metals," *Physical Review B*, vol. 7, p. 2317, 6 1973.

[263] A. H. MacDonald, R. Taylor, and D. J. W. Geldart, "Umklapp electron-electron scattering and the low-temperature electrical resistivity of the alkali metals," *Physical Review B*, vol. 23, p. 2718, 6 1981.

[264] H. Pal, V. Yudson, and D. Maslov, "Resistivity of non-Galilean-invariant Fermi- and non-Fermi liquids," *Lithuanian Journal of Physics*, vol. 52, p. 142, 2 2012.

[265] S. N. Klimin, J. Tempere, D. van der Marel, and J. T. Devreese, "Microscopic mechanisms for the Fermi-liquid behavior of Nb-doped strontium titanate," *Physical Review B*, vol. 86, p. 045113, 4 2012.

[266] O. N. Tufte and P. W. Chapman, "Electron mobility in semiconducting strontium titanate," *Physical Review*, vol. 155, p. 796, 3 1967.

[267] J. Son, P. Moetakef, B. Jalan, O. Bierwagen, N. J. Wright, R. Engel-Herbert, and S. Stemmer, "Epitaxial SrTiO$_3$ films with electron mobilities exceeding 30,000 cm^{2}V^{-1} s^{-1}," *Nature Materials*, vol. 9, no. 6, p. 482, 2010.

[268] T. A. Cain, A. P. Kajdos, and S. Stemmer, "La-doped SrTiO$_3$ films with large cryogenic thermoelectric power factors," *Applied Physics Letters*, vol. 102, no. 18, 182101, 2013.

[269] G. R. Stewart, "Non-Fermi-liquid behavior in d- and f-electron metals," *Reviews of Modern Physics*, vol. 73, p. 797, 4 2001.

[270] M. Vojta, "Quantum phase transitions," *Reports on Progress in Physics*, vol. 66, no. 12, p. 2069, 2003.

[271] H. v. Lohneysen, A. Rosch, M. Vojta, and P. Wolfle, "Fermi-liquid instabilities at magnetic quantum phase transitions," *Reviews of Modern Physics*, vol. 79, p. 1015, 3 2007.

[272] S. Sachdev, *Quantum Phase Transitions*. Cambridge University Press, 2011.

[273] H. E. Stanley, "Scaling, universality, and renormalization: three pillars of modern critical phenomena," *Reviews of Modern Physics*, vol. 71, S358, 2 1999.

[274] A. J. Schofield, "Non-Fermi liquids," *Contemporary Physics*, vol. 40, no. 2, p. 95, 1999.

[275] S. Nair, S. Wirth, S. Friedemann, F. Steglich, Q. Si, and A. J. Schofield, "Hall effect in heavy fermion metals," *Advances in Physics*, vol. 61, no. 5, p. 583, 2012.

[276] P Coleman, C Pepin, Q. Si, and R Ramazashvili, "How do Fermi liquids get heavy and die?" *Journal of Physics: Condensed Matter*, vol. 13, no. 35, R723, 2001.

[277] P. Coleman and A. J. Schofield, "Quantum criticality," *Nature*, vol. 433, no. 7023, p. 226, 2005.

[278] P. Gegenwart, Q. Si, and F. Steglich, "Quantum criticality in heavy-fermion metals," *Nature Physics*, vol. 4, no. 3, p. 186, 2008.

[279] J. A. Hertz, "Quantum critical phenomena," *Physical Review B*, vol. 14, p. 1165, 3 1976.

[280] T. Moriya, "Theory of itinerant electron magnetism," *Journal of Magnetism and Magnetic Materials*, vol. 100, no. 1, p. 261, 1991.

[281] A. J. Millis, "Effect of a nonzero temperature on quantum critical points in itinerant fermion systems," *Physical Review B*, vol. 48, p. 7183, 10 1993.

[282] T. Moriya and T. Takimoto, "Anomalous properties around magnetic instability in heavy electron systems," *Journal of the Physical Society of Japan*, vol. 64, no. 3, p. 960, 1995.

[283] T. Graf, J. D. Thompson, M. F. Hundley, R. Movshovich, Z. Fisk, D. Mandrus, R. A. Fisher, and N. E. Phillips, "Comparison of $CeRh_2Si_2$ and $CeRh_{2-x}Ru_xSi_2$ near their magnetic-nonmagnetic boundaries," *Physical Review Letters*, vol. 78, p. 3769, 19 1997.

[284] H. v. Löhneysen, T. Pietrus, G. Portisch, H. G. Schlager, A. Schröder, M. Sieck, and T. Trappmann, "Non-Fermi-liquid behavior in a heavy-fermion alloy at a magnetic instability," *Physical Review Letters*, vol. 72, p. 3262, 20 1994.

[285] Y. Nakajima, H. Shishido, H. Nakai, T. Shibauchi, K. Behnia, K. Izawa, M. Hedo, Y. Uwatoko, T. Matsumoto, R. Settai, Y. nuki, H. Kontani, and Y. Matsuda, "Non-fermi liquid behavior in the magnetotransport of $CeMIn_5$

(M: Co and Rh): striking similarity between quasi two-dimensional heavy fermion and high-T_c cuprates," *Journal of the Physical Society of Japan*, vol. 76, no. 2, p. 024703, 2007.

[286] M. Lenkewitz, S. Corsepius, G.-F. v. Blanckenhagen, and G. R. Stewart, "Heavy non-Fermi-liquid behavior in nearness to ferromagnetism in $Th_{1-x}UCu_2Si_2$s," *Physical Review B*, vol. 55, p. 6409, 10 1997.

[287] C. Pfleiderer, M. Uhlarz, S. Hayden, R. Vollmer, H. v. Lohneysen, N. Bernhoeft, and G. Lonzarich, "Coexistence of superconductivity and ferromagnetism in the d-band metal $ZrZn_2$," *Nature*, vol. 412, no. 6842, p. 58, 2001.

[288] R. Smith, M. Sutherland, G. Lonzarich, S. Saxena, N. Kimura, S. Takashima, M. Nohara, and H. Takagi, "Marginal breakdown of the Fermi-liquid state on the border of metallic ferromagnetism," *Nature*, vol. 455, no. 7217, p. 1220, 2008.

[289] R. Ritz, M. Halder, M. Wagner, C. Franz, A. Bauer, and C. Pfleiderer, "Formation of a topological non-fermi liquid in MnSi," *Nature*, vol. 497, no. 7448, p. 231, 2013.

[290] A. Yeh, Y.-A. Soh, J. Brooke, G. Aeppli, T. Rosenbaum, and S. Hayden, "Quantum phase transition in a common metal," *Nature*, vol. 419, no. 6906, p. 459, 2002.

[291] S. Grigera, R. Perry, A. Schofield, M Chiao, S. Julian, G. Lonzarich, S. Ikeda, Y Maeno, A. Millis, and A. Mackenzie, "Magnetic field-tuned quantum criticality in the metallic ruthenate $Sr_3Ru_2O_7$," *Science*, vol. 294, no. 5541, p. 329, 2001.

[292] C. Huang, D. Fuchs, M. Wissinger, R. Schneider, M. C. Ling, M. S. Scheurer, J. Schmalian, and H. V. Lohneysen, "Anomalous quantum criticality in an itinerant ferromagnet," *Nature Communications*, vol. 6, 2015.

[293] A. Rosch, "Interplay of disorder and spin fluctuations in the resistivity near a quantum critical point," *Physical Review Letters*, vol. 82, p. 4280, 21 1999.

[294] E Miranda and V Dobrosavljevic, "Disorder-driven non-Fermi liquid behaviour of correlated electrons," *Reports on Progress in Physics*, vol. 68, no. 10, p. 2337, 2005.

[295] B. Keimer, S. Kivelson, M. Norman, S. Uchida, and J. Zaanen, "From quantum matter to high-temperature superconductivity in copper oxides," *Nature*, vol. 518, no. 7538, p. 179, 2015.

269

[296] A. Chubukov and P. Hirschfeld, "Iron-based superconductors, seven years later," *Physics Today*, vol. 68, no. 6, p. 46, Jun. 2015.

[297] C. C. Homes, T. Timusk, R. Liang, D. A. Bonn, and W. N. Hardy, "Optical conductivity of c axis oriented $YBa_2Cu_3O_{6.70}$: evidence for a pseudogap," *Physical Review Letters*, vol. 71, p. 1645, 10 1993.

[298] A. Puchkov, D. Basov, and T Timusk, "The pseudogap state in high-superconductors: an infrared study," *Journal of Physics: Condensed Matter*, vol. 8, no. 48, p. 10049, 1996.

[299] D. N. Basov, E. J. Singley, and S. V. Dordevic, "Sum rules and electrodynamics of high-T_c cuprates in the pseudogap state," *Physical Review B*, vol. 65, p. 054516, 5 2002.

[300] A. Damascelli, Z. Hussain, and Z.-X. Shen, "Angle-resolved photoemission studies of the cuprate superconductors," *Reviews of Modern Physics*, vol. 75, p. 473, 2 2003.

[301] A. Schilling, M. Cantoni, J. D. Guo, and H. R. Ott, "Superconductivity above 130 K in the Hg-Ba-Ca-Cu-O system," *Nature*, vol. 363, no. 6424, p. 56, 1993.

[302] C. Chu, L. Gao, F. Chen, Z. Huang, R. Meng, and Y. Xue, "Superconductivity above 150 K in HgBa$_2$Ca$_2$Cu$_3$O$_{8+\delta}$ at high pressures," *Nature*, vol. 365, p. 323, 1993.

[303] H. Takagi, B. Batlogg, H. L. Kao, J. Kwo, R. J. Cava, J. J. Krajewski, and W. F. Peck, "Systematic evolution of temperature-dependent resistivity in La$_{2-x}$Sr$_x$CuO$_4$," *Physical Review Letters*, vol. 69, p. 2975, 20 1992.

[304] R. A. Cooper, Y. Wang, B. Vignolle, O. J. Lipscombe, S. M. Hayden, Y. Tanabe, T. Adachi, Y. Koike, M. Nohara, H. Takagi, C. Proust, and N. E. Hussey, "Anomalous criticality in the electrical resistivity of La$_{2-x}$Sr$_x$CuO$_4$," *Science*, vol. 323, no. 5914, p. 603, 2009.

[305] N. Barisic, M. K. Chan, Y. Li, G. Yu, X. Zhao, M. Dressel, A. Smontara, and M. Greven, "Universal sheet resistance and revised phase diagram of the cuprate high-temperature superconductors," *Proceedings of the National Academy of Sciences*, vol. 110, no. 30, p. 12235, 2013.

[306] P. W. Anderson, "Hall effect in the two-dimensional Luttinger liquid," *Physical Review Letters*, vol. 67, p. 2092, 15 1991.

[307] T. R. Chien, Z. Z. Wang, and N. P. Ong, "Effect of Zn impurities on the normal-state Hall angle in single-crystal YBa$_2$Cu$_{3-x}$Zn$_x$O$_{7-\delta}$," *Physical Review Letters*, vol. 67, p. 2088, 15 1991.

[308] P Coleman, A. J. Schofield, and A. M. Tsvelik, "How should we interpret the two transport relaxation times in the cuprates?" *Journal of Physics: Condensed Matter*, vol. 8, no. 48, p. 9985, 1996.

[309] J. M. Harris, Y. F. Yan, and N. P. Ong, "Experimental test of the T^2 law for the hall angle from T_c to 500 k in oxygen-reduced $YBa_2Cu_3O_{6+x}$ crystals," *Physical Review B*, vol. 46, p. 14293, 21 1992.

[310] W. Jiang, J. L. Peng, S. J. Hagen, and R. L. Greene, "Hall-effect studies of $Y_{1-x}Pr_xBa_2Cu_3O_7$ crystals," *Physical Review B*, vol. 46, p. 8694, 13 1992.

[311] G. Xiao, P. Xiong, and M. Z. Cieplak, "Universal hall effect in $La_{1.85}Sr_{0.15}Cu_{1-x}A_xO_4$ systems (A = Fe, Co, Ni, Zn, Ga)," *Physical Review B*, vol. 46, p. 8687, 13 1992.

[312] P. Xiong, G. Xiao, and X. D. Wu, "Hall angle in $YBa_2Cu_3O_{7-\delta}$ epitaxial films: comparison between oxygen reduction and Pr doping," *Physical Review B*, vol. 47, p. 5516, 9 1993.

[313] H. Y. Hwang, B. Batlogg, H. Takagi, H. L. Kao, J. Kwo, R. J. Cava, J. J. Krajewski, and W. F. Peck, "Scaling of the temperature dependent Hall effect in $La_{2-x}Sr_xCuO_4$," *Physical Review Letters*, vol. 72, p. 2636, 16 1994.

[314] Y. Kubo and T. Manako, "T^2-dependence of inverse Hall mobility observed in overdoped Tl-cuprates," *Physica B: Condensed Matter*, vol. 194, p. 2047, 1994.

[315] Y. Ando, Y. Kurita, S. Komiya, S. Ono, and K. Segawa, "Evolution of the Hall coefficient and the peculiar electronic structure of the cuprate superconductors," *Physical Review Letters*, vol. 92, p. 197001, 19 2004.

[316] C. Kendziora, D. Mandrus, L. Mihaly, and L. Forro, "Single-band model for the temperature-dependent Hall coefficient of high-T_c superconductors," *Physical Review B*, vol. 46, p. 14297, 21 1992.

[317] Y. Nakajima, K. Izawa, Y. Matsuda, S. Uji, T. Terashima, H. Shishido, R. Settai, Y. Onuki, and H. Kontani, "Normal-state Hall angle and magnetoresistance in quasi-2d heavy fermion CeCoIn$_5$ near a quantum critical point," *Journal of the Physical Society of Japan*, vol. 73, no. 1, p. 5, 2004.

[318] T. F. Rosenbaum, A. Husmann, S. A. Carter, and J. M. Honig, "Temperature dependence of the Hall angle in a correlated three-dimensional metal," *Physical Review B*, vol. 57, R13997, 22 1998.

[319] P. W. Anderson, "New physics of metals: Fermi surfaces without Fermi liquids," *Proceedings of the National Academy of Sciences*, vol. 92, no. 15, p. 6668, 1995.

[320] R. Hlubina and T. M. Rice, "Resistivity as a function of temperature for models with hot spots on the Fermi surface," *Physical Review B*, vol. 51, p. 9253, 14 1995.

[321] B. P. Stojkovic and D. Pines, "Theory of the longitudinal and Hall conductivities of the cuprate superconductors," *Physical Review B*, vol. 55, p. 8576, 13 1997.

[322] L. B. Ioffe and A. J. Millis, "Zone-diagonal-dominated transport in high-T_c cuprates," *Physical Review B*, vol. 58, p. 11631, 17 1998.

[323] N. P. Ong, "Geometric interpretation of the weak-field Hall conductivity in two-dimensional metals with arbitrary Fermi surface," *Physical Review B*, vol. 43, p. 193, 1 1991.

[324] A Carrington, A. Mackenzie, C. Lin, and J. Cooper, "Temperature dependence of the Hall angle in single-crystal YBa$_2$(Cu$_{1-x}$Co$_x$)$_3$O$_{7-\delta}$," *Physical review letters*, vol. 69, no. 19, p. 2855, 1992.

[325] N. Hussey, "Phenomenology of the normal state in-plane transport properties of high-T$_c$ cuprates," *Journal of Physics: Condensed Matter*, vol. 20, no. 12, p. 123201, 2008.

[326] N. Hussey, "The normal state scattering rate in high-T_c cuprates," *The European Physical Journal B - Condensed Matter and Complex Systems*, vol. 31, no. 4, p. 495, 2003.

[327] M. Abdel-Jawad, M. Kennett, L. Balicas, A. Carrington, A. Mackenzie, R. McKenzie, and N. Hussey, "Anisotropic scattering and anomalous normal-state transport in a high-temperature superconductor," *Nature Physics*, vol. 2, no. 12, p. 821, 2006.

[328] B. Himmetoglu, A. Janotti, H. Peelaers, A. Alkauskas, and C. G. Van de Walle, "First-principles study of the mobility of $SrTiO_3$," *Physical Review B*, vol. 90, p. 241204, 24 2014.

[329] X. Lin, B. Fauqué, and K. Behnia, "Scalable T^2 resistivity in a small single-component Fermi surface," *Science*, vol. 349, no. 6251, p. 945, 2015.

[330] A. H. Thompson, "Electron-electron scattering in TiS_2," *Physical Review Letters*, vol. 35, p. 1786, 26 1975.

[331] J. A. N. Bruin, H. Sakai, R. S. Perry, and A. P. Mackenzie, "Similarity of scattering rates in metals showing T-linear resistivity," *Science*, vol. 339, no. 6121, p. 804, 2013.

[332] A. Gold, "Electronic transport properties of a two-dimensional electron gas in a silicon quantum-well structure at low temperature," *Physical Review B*, vol. 35, p. 723, 2 1987.

[333] P. Moetakef, J. R. Williams, D. G. Ouellette, A. P. Kajdos, D. Goldhaber-Gordon, S. J. Allen, and S. Stemmer, "Carrier-controlled ferromagnetism in SrTiO$_3$," *Physical Review X*, vol. 2, p. 021014, 2 2012.

[334] R. F. Need, B. J. Isaac, B. J. Kirby, J. A. Borchers, S. Stemmer, and S. D. Wilson, "Interface-driven ferromagnetism within the quantum wells of a rare earth titanate superlattice," *Physical Review Letters*, vol. 117, p. 037205, 3 2016.

[335] P. B. Marshall, E. Mikheev, S. Raghavan, and S. Stemmer, "Pseudo-gaps and emergence of coherence in two-dimensional electron liquids in SrTiO$_3$," *Physical Review Letters*, vol. 117, p. 046402, 4 2016.

[336] J. Y. Zhang, C. A. Jackson, R. Chen, S. Raghavan, P. Moetakef, L. Balents, and S. Stemmer, "Correlation between metal-insulator transitions and structural distortions in high-electron-density SrTiO$_3$ quantum wells," *Physical Review B*, vol. 89, p. 075140, 7 2014.

[337] U. Chatterjee, J. Zhao, M. Iavarone, R. Di Capua, J. P. Castellan, G. Karapetrov, C. D. Malliakas, M. G. Kanatzidis, H. Claus, J. P. C. Ruff,

F. Weber, J. van Wezel, J. C. Campuzano, R. Osborn, M. Randeria, N. Trivedi, M. R. Norman, and S. Rosenkranz, "Emergence of coherence in the charge-density wave state of 2H-NbSe$_2$," *Nature Communications*, vol. 6, 2015.

[338] L. Bjaalie, A. Janotti, B. Himmetoglu, and C. G. Van de Walle, "Turning SrTiO$_3$ into a mott insulator," *Physical Review B*, vol. 90, p. 195117, 19 2014.

[339] D. Doennig and R. Pentcheva, "Control of orbital reconstruction in (LaAlO$_3$)$_m$ / (SrTiO$_3$)$_n$ (001) quantum wells by strain and confinement," *Scientific reports*, vol. 5, 2015.

[340] Y. J. Chang, L. Moreschini, A. Bostwick, G. A. Gaines, Y. S. Kim, A. L. Walter, B. Freelon, A. Tebano, K. Horn, and E. Rotenberg, "Layer-by-layer evolution of a two-dimensional electron gas near an oxide interface," *Physical Review Letters*, vol. 111, p. 126401, 12 2013.

[341] M. Hosoda, Y. Hikita, H. Y. Hwang, and C. Bell, "Transistor operation and mobility enhancement in top-gated LaAlO$_3$/SrTiO$_3$ heterostructures," *Applied Physics Letters*, vol. 103, no. 10, 103507, 2013.

[342] P. D. Eerkes, W. G. van der Wiel, and H. Hilgenkamp, "Modulation of conductance and superconductivity by top-gating in LaAlO$_3$/SrTiO$_3$ 2-

dimensional electron systems," *Applied Physics Letters*, vol. 103, no. 20, 201603, 2013.

[343] R. M. Feenstra, D. A. Collins, D. Z. Y. Ting, M. W. Wang, and T. C. McGill, "Interface roughness and asymmetry in InAs/GaSb superlattices studied by scanning tunneling microscopy," *Physical Review Letters*, vol. 72, p. 2749, 17 1994.

[344] S. J. May, A. B. Shah, S. G. E. te Velthuis, M. R. Fitzsimmons, J. M. Zuo, X. Zhai, J. N. Eckstein, S. D. Bader, and A. Bhattacharya, "Magnetically asymmetric interfaces in a $LaMnO_3$/$SrMnO_3$ superlattice due to structural asymmetries," *Physical Review B*, vol. 77, p. 174409, 17 2008.

[345] M. Lee, J. R. Williams, S. Zhang, C. D. Frisbie, and D. Goldhaber-Gordon, "Electrolyte gate-controlled Kondo effect in $SrTiO_3$," *Physical Review Letters*, vol. 107, p. 256601, 25 2011.

[346] J. A. Bert, B. Kalisky, C. Bell, M. Kim, Y. Hikita, H. Y. Hwang, and K. A. Moler, "Direct imaging of the coexistence of ferromagnetism and superconductivity at the $LaAlO_3$/$SrTiO_3$ interface," *Nature Physics*, vol. 7, no. 10, p. 767, 2011.

[347] J. Coey and W. Pickett, "Magnetism at the edge: new phenomena at oxide interfaces," *MRS Bulletin*, vol. 38, no. 12, p. 1040, Dec. 2013.

[348] J. Coey, M Venkatesan, and P Stamenov, "Surface magnetism of strontium titanate," *arXiv:1606.09422*, 2016.

[349] P. D. Gennes, "Inelastic magnetic scattering of neutrons at high temperatures," *Journal of Physics and Chemistry of Solids*, vol. 4, no. 3, p. 223, 1958.

[350] R. Weiss and A. Marotta, "Spin-dependence of the resistivity of magnetic metals," *Journal of Physics and Chemistry of Solids*, vol. 9, no. 3, p. 302, 1959.

[351] D. A. Goodings, "Electrical resistivity of ferromagnetic metals at low temperatures," *Physical Review*, vol. 132, p. 542, 2 1963.

[352] B. Raquet, M. Viret, E. Sondergard, O. Cespedes, and R. Mamy, "Electron-magnon scattering and magnetic resistivity in $3d$ ferromagnets," *Physical Review B*, vol. 66, p. 024433, 2 2002.

[353] S. A. Hartnoll, J. Polchinski, E. Silverstein, and D. Tong, "Towards strange metallic holography," *Journal of High Energy Physics*, vol. 2010, no. 4, p. 1, 2010.

[354] M. Blake and D. Tong, "Universal resistivity from holographic massive gravity," *Physical Review D*, vol. 88, p. 106004, 10 2013.

[355] R. A. Davison, K. Schalm, and J. Zaanen, "Holographic duality and the resistivity of strange metals," *Physical Review B*, vol. 89, p. 245116, 24 2014.

[356] S. A. Hartnoll, "Theory of universal incoherent metallic transport," *Nature Physics*, vol. 11, no. 1, p. 54, 2015.

[357] M. Blake and A. Donos, "Quantum critical transport and the Hall angle in holographic models," *Physical Review Letters*, vol. 114, p. 021601, 2 2015.

[358] R. Moos, A. Gnudi, and K. H. Hardtl, "Thermopower of $Sr_{1-x}La_xTiO_3$ ceramics," *Journal of Applied Physics*, vol. 78, no. 8, 1995.

[359] K. Shirai and K. Yamanaka, "Mechanism behind the high thermoelectric power factor of $SrTiO_3$ by calculating the transport coefficients," *Journal of Applied Physics*, vol. 113, no. 5, 053705, 2013.

[360] I. Nagai, N. Shirakawa, S.-i. Ikeda, R. Iwasaki, H. Nishimura, and M. Kosaka, "Highest conductivity oxide $SrMoO_3$ grown by a floating-zone method under ultralow oxygen partial pressure," *Applied Physics Letters*, vol. 87, no. 2, 024105, 2005.

[361] D. Oka, Y. Hirose, S. Nakao, T. Fukumura, and T. Hasegawa, "Intrinsic high electrical conductivity of stoichiometric $SrNbO_3$ epitaxial thin films," *Physical Review B*, vol. 92, p. 205102, 20 2015.

[362] J.-S. Zhou, J. B. Goodenough, and B. Dabrowski, "Pressure-induced non-Fermi-liquid behavior of $PrNiO_3$," *Physical Review Letters*, vol. 94, p. 226602, 22 2005.

[363] J. Liu, M. Kargarian, M. Kareev, B. Gray, P. J. Ryan, A. Cruz, N. Tahir, Y.-D. Chuang, J. Guo, J. M. Rondinelli, J. W. Freeland, G. A. Fiete, and J. Chakhalian, "Heterointerface engineered electronic and magnetic phases of $NdNiO_3$ thin films," *Nature Communications*, vol. 4, 2013.

[364] E. Mikheev, A. J. Hauser, B. Himmetoglu, N. E. Moreno, A. Janotti, C. G. Van de Walle, and S. Stemmer, "Tuning bad metal and non-Fermi liquid behavior in a Mott material: rare-earth nickelate thin films," *Science Advances*, vol. 1, no. 10, 2015.

[365] E. Conwell and V. F. Weisskopf, "Theory of impurity scattering in semiconductors," *Physical Review*, vol. 77, p. 388, 3 1950.

[366] D. Long and J. Myers, "Ionized-impurity scattering mobility of electrons in silicon," *Physical Review*, vol. 115, p. 1107, 5 1959.

[367] P. A. Lee and T. V. Ramakrishnan, "Disordered electronic systems," *Reviews of Modern Physics*, vol. 57, p. 287, 2 1985.

[368] G. Bergmann, "Weak localization in thin films," *Physics Reports*, vol. 107, no. 1, p. 1, 1984.

[369] J. Kondo, "Resistance minimum in dilute magnetic alloys," *Progress of Theoretical Physics*, vol. 32, no. 1, p. 37, 1964.

[370] D. Goldhaber-Gordon, J. Göres, M. A. Kastner, H. Shtrikman, D. Mahalu, and U. Meirav, "From the Kondo regime to the mixed-valence regime in a single-electron transistor," *Physical Review Letters*, vol. 81, p. 5225, 23 1998.

[371] T. A. Costi, A. C. Hewson, and V Zlatic, "Transport coefficients of the Anderson model via the numerical renormalization group," *Journal of Physics: Condensed Matter*, vol. 6, no. 13, p. 2519, 1994.

[372] B. L. Altshuler, D. Khmelnitzkii, A. I. Larkin, and P. A. Lee, "Magnetoresistance and Hall effect in a disordered two-dimensional electron gas," *Physical Review B*, vol. 22, p. 5142, 11 1980.

[373] C. J. G. Meyers, C. R. Freeze, S. Stemmer, and R. A. York, "(Ba,Sr)TiO$_3$ tunable capacitors with RF commutation quality factors exceeding 6000," *Applied Physics Letters*, vol. 109, no. 11, 112902, 2016.

[374] J. W. Reiner, A. M. Kolpak, Y. Segal, K. F. Garrity, S. Ismail-Beigi, C. H. Ahn, and F. J. Walker, "Crystalline oxides on silicon," *Advanced Materials*, vol. 22, no. 26-27, p. 2919, 2010.

[375] L. Mazet, S. M. Yang, S. V. Kalinin, S. Schamm-Chardon, and C. Dubourdieu, "A review of molecular beam epitaxy of ferroelectric $BaTiO_3$ films on Si, Ge and GaAs substrates and their applications," *Science and Technology of Advanced Materials*, vol. 16, no. 3, p. 036005, 2015.

[376] L. Zhang and R. Engel-Herbert, "Growth of $SrTiO_3$ on Si(001) by hybrid molecular beam epitaxy," *Physica Status Solidi (RRL) Rapid Research Letters*, vol. 8, no. 11, p. 917, 2014.

[377] J. M. Harris, Y. F. Yan, P. Matl, N. P. Ong, P. W. Anderson, T. Kimura, and K. Kitazawa, "Violation of kohler's rule in the normal-state magnetoresistance of $YBa_2Cu_3O_{7-x}$ and $La_2Sr_xCuO_4$," *Physical Review Letters*, vol. 75, p. 1391, 7 1995.

[378] G. Kotliar, A. Sengupta, and C. M. Varma, "Hall effect and magnetoresistance in copper oxide metals," *Physical Review B*, vol. 53, p. 3573, 6 1996.

[379] M. K. Chan, M. J. Veit, C. J. Dorow, Y. Ge, Y. Li, W. Tabis, Y. Tang, X. Zhao, N. Barisic, and M. Greven, "In-plane magnetoresistance obeys

kohler's rule in the pseudogap phase of cuprate superconductors," *Physical Review Letters*, vol. 113, p. 177005, 17 2014.

[380] I. M. Hayes, R. D. McDonald, N. P. Breznay, T. Helm, P. J. Moll, M. Wartenbe, A. Shekhter, and J. G. Analytis, "Scaling between magnetic field and temperature in the high-temperature superconductor $BaFe_2(As_{1-x}P_x)_2$," *Nature Physics*, 2016.

[381] X. H. Chen, Y. S. Wang, Y. Y. Xue, R. L. Meng, Y. Q. Wang, and C. W. Chu, "Correlation between the residual resistance ratio and magnetoresistance in MgB_2," *Physical Review B*, vol. 65, p. 024502, 2 2001.

[382] Y. L. Wang, L. R. Thoutam, Z. L. Xiao, J. Hu, S. Das, Z. Q. Mao, J. Wei, R. Divan, A. Luican-Mayer, G. W. Crabtree, and W. K. Kwok, "Origin of the turn-on temperature behavior in WTe_2," *Physical Review B*, vol. 92, p. 180402, 18 2015.

[383] M. Boucherit, O. F. Shoron, T. A. Cain, C. A. Jackson, S. Stemmer, and S. Rajan, "Extreme charge density SrTiO3/$GdTiO_3$ heterostructure field effect transistors," *Applied Physics Letters*, vol. 102, no. 24, 242909, 2013.

[384] M. Boucherit, O. Shoron, C. A. Jackson, T. A. Cain, M. L. C. Buffon, C. Polchinski, S. Stemmer, and S. Rajan, "Modulation of over $10^{14} cm^{-2}$

electrons in $SrTiO_3/GdTiO_3$ heterostructures," *Applied Physics Letters*, vol. 104, no. 18, 182904, 2014.

[385]   A. Verma, S. Raghavan, S. Stemmer, and D. Jena, "Au-gated $SrTiO_3$ field-effect transistors with large electron concentration and current modulation," *Applied Physics Letters*, vol. 105, no. 11, 113512, 2014.

[386]   A. Verma, K. Nomoto, W. S. Hwang, S. Raghavan, S. Stemmer, and D. Jena, "Large electron concentration modulation using capacitance enhancement in $SrTiO_3/SmTiO_3$ Fin-field effect transistors," *Applied Physics Letters*, vol. 108, no. 18, 183509, 2016.

[387]   E. Mikheev, S. Raghavan, and S. Stemmer, "Dielectric response of metal / $SrTiO_3$ / two-dimensional electron liquid heterostructures," *Applied Physics Letters*, vol. 107, no. 7, 072905, 2015.

[388]   P. Gallagher, M. Lee, T. A. Petach, S. W. Stanwyck, J. R. Williams, K. Watanabe, T. Taniguchi, and D. Goldhaber-Gordon, "A high-mobility electronic system at an electrolyte-gated oxide surface," *Nature Communications*, vol. 6, 2015.

[389]   J. Jeong, N. Aetukuri, T. Graf, T. D. Schladt, M. G. Samant, and S. S. P. Parkin, "Suppression of metal-insulator transition in VO_2 by electric

field-induced oxygen vacancy formation," *Science,* vol. 339, no. 6126, p. 1402, 2013.

[390] S. Bubel, A. J. Hauser, A. M. Glaudell, T. E. Mates, S. Stemmer, and M. L. Chabinyc, "The electrochemical impact on electrostatic modulation of the metal-insulator transition in nickelates," *Applied Physics Letters*, vol. 106, no. 12, 122102, 2015.

[391] P. Gallagher, M. Lee, J. R. Williams, and D. Goldhaber-Gordon, "Gate-tunable superconducting weak link and quantum point contact spectroscopy on a strontium titanate surface," *Nature Physics*, vol. 10, no. 10, p. 748, 2014.

[392] G. Cheng, M. Tomczyk, S. Lu, J. P. Veazey, M. Huang, P. Irvin, S. Ryu, H. Lee, C.-B. Eom, C. S. Hellberg, *et al.*, "Electron pairing without superconductivity," *Nature*, vol. 521, no. 7551, p. 196, 2015.

[393] Y. Blanter and M. Buttiker, "Shot noise in mesoscopic conductors," *Physics Reports*, vol. 336, no. 12, p. 1, 2000.

[394] A. A. Balandin, "Low-frequency 1/f noise in graphene devices," *Nature Nanotechnology,* vol. 8, no. 8, p. 549, 2013.

[395] P. J. Wheeler, R. Chen, and D. Natelson, "Noise in electromigrated nanojunctions," *Physical Review B*, vol. 87, p. 155411, 15 2013.

[396] D. Rakhmilevitch, M. Ben Shalom, M. Eshkol, A. Tsukernik, A. Palevski, and Y. Dagan, "Phase coherent transport in $SrTiO_3$/$LaAlO_3$ interfaces," *Physical Review B*, vol. 82, p. 235119, 23 2010.

[397] S. W. Stanwyck, P. Gallagher, J. R. Williams, and D. Goldhaber-Gordon, "Universal conductance fluctuations in electrolyte-gated $SrTiO_3$ nanostructures," *Applied Physics Letters*, vol. 103, no. 21, 213504, 2013.

[398] W. J. Hardy, H. Ji, E. Mikheev, S. Stemmer, and D. Natelson, "Nanostructure investigations of nonlinear differential conductance in $NdNiO_3$ thin films," *Physical Review B*, vol. 90, p. 205117, 20 2014.